RUSSIAN ACADEMY OF SCIENCES

NATIONAL GEOPHYSICAL COMMITTEE

РОССИЙСКАЯ АКАДЕМИЯ НАУК

НАЦИОНАЛЬНЫЙ ГЕОФИЗИЧЕСКИЙ КОМИТЕТ

NATIONAL SEISMOLOGICAL REVIEW OF RUSSIA

for the

International Association of Seismology
and Physics of the Earth's Interior

of the

International Union of Geodesy and Geophysics

2007–2010

НАЦИОНАЛЬНЫЙ СЕЙСМОЛОГИЧЕСКИЙ ОБЗОР РОССИИ

Международной ассоциации сейсмологии
и физики недр Земли
Международного
геодезического и геофизического союза

2007–2010

Москва 2011 Moscow

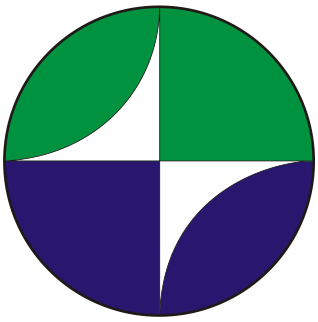

Presented to the XXV General Assembly
of the
International Union of Geodesy and Geophysics

К XXV Генеральной ассамблее
Международного геодезического и геофизического
союза

RUSSIAN ACADEMY OF SCIENCES

National Geophysical Committee

NATIONAL SEISMOLOGICAL REVIEW OF RUSSIA

for the

International Association of Seismology
and Physics of the Earth's Interior

of the

International Union of Geodesy and Geophysics

2007–2010

Presented to the XXV General Assembly

of the

IUGG

2011

Moscow

In the National Seismological Review major results are given of research conducted by Russian scientists in 2007-2010 on the topics of the International Association of Seismology and the Physics of the Earth's Interior (IASPEI) of the International Union of Geodesy and Geophysics (IUGG). The structure of seismic observation stations network of the Russian Federation is given and its prospects are outlined in the report. The results of research in strong and perceptible earthquakes in Russia in 2007-2010 are presented as well as the results obtained in seismic danger and risk assessment, the physics of seismic process, and earthquake prediction. Major achievements in the physics of the Earth, geodynamics, and physical properties of geomaterial are featured. Information on constructing geoinformation systems in geophysics, and on pit seismicity monitoring is given. The results of research in artificial intelligence application in geophysics are. All the required references are given.

Author's Team (in alphabetical order)

Adushkin V. V.
Agayan S. M.
Arefiev S. S.
Bogoutdinov S. R.
Butyrin P. G.
Diament M.
Dyagilev R. A.
Fedotova Yu. V.
Frolova N. I.
Gitis V. G.
Gorbatikov A. V.
Gvishiani A. D.
Kireenkova S. M.
Kiseleva E. A.
Klyuchevskii A. V.
Kocharyan G. G.
Kosarev G. L.
Kossobokov V. G.
Kozhevnikov V. M.
Kozyrev A. A.
Lukhnev A. V.
Malovichko A. A.
Malovichko D. A.
Matsiyevsky S. A.
Mikhailov V. O.
Mordvinova V. V.
Nazaryan A. N.
Nikolaev A. V.
Panin V. I.
Pavlyukova E. R.
Ponomarev A. V.
Rogozhin E. A.
Saltykov V. A.
Sanina I. A.
Sankov V. A.
Shapiro N.
Shaumyan A. V.
Shulakov D. Y.
Sidorov R.
Smol'yaninova E. I.
Sobolev G. A.
Solovei O. A.
Soloviev A. A.
Starovoit O. E.
Timoshkina E. P.
Treussov A.V.
Trubitsyn V. P.
Turuntaev S. B.
Ulomov V. I.
Usoltseva O. A.
Vinnik L. P.
Zavyalov A.D.

DOI: 10.2205/2011-IUGG-NRR2007-2010

ISBN: 978-5-904509-03-3

Contents

Introduction

A. D. Zavyalov, zavyalov@ifz.ru**.** *National Geophysical Committee RAS. Schmidt Institute of the Physics of the Earth RAS. B. Gruzinskaya, 10, Moscow, 123995, GSP-5, Russia.*

This report submitted to the International Association of Seismology and the Physics of the Earth's Interior (IASPEI) of the International Union of Geodesy and Geophysics (IUGG) contains results obtained by Russian geophysicists in 2003-2006. In the report prepared for the XXV General Assembly of IUGG (Australia, Melbourne, June 28 – July 7, 2011), the results are briefly outlined of basic research in seismology, geodynamics, in the studies of physical properties of rocks as well as in some other directions.

The period from 2007 to 2010 was still difficult for Russian geophysics. Owing to economic reasons scientific career is Russia is still believed to be lacking in prestige. Thus recruiting younger scientists for fundamental research in geophysics actually failed. Economic difficulties were redoubled by difficulties arising from ongoing reorganization of the Russian Academy of Sciences, Russian science and the educational system of Russia initiated by the leaders of the country. In spite of the difficulties, Russian scientists participated in practically all conferences of the International Association of Seismology and the Physics of the Earth's Interior (IASPEI), in the General Asssemblies, international projects and international centers.

Even in such difficult conditions high scientific potential, great experience in research and the traditions of Russian geophysics allowed obtaining a number of fundamentally important new results in the period under review. Many of them are presented in the following sections of this report. Each of the sections has a list of the most interesting scientific papers published in 2007–2010 including publications prepared in cooperation of Russian scientists and their colleagues from other countries.

For a number of reasons not all results obtained by Russian scientists on the problems of seismology and physics of the Earth's interior in 2007-2010 are included in the report. At the same time it is hoped that authors may present these results at symposia of IUGG XXV General Assembly.

1. The system of seismic observations in Russia

1.1. Seismic observation network in Russia in 2007-2010

O. E. Starovoit, ostar@gsras.ru**, A. A. Malovichko,** amal@gsras.ru**.** *Geophysical Survey RAS, ul. Lenina, 189, Obninsk, Kaluga Region, 249020, Russia.*

Network of seismic observation in Russia is a permanent seismic monitoring of the territory in the country. Network has a hierarchical three level structure. It includes the teleseismic network and 10 regional seismic networks, which themselves include local area networks. In total, the network employs approximately 300 seismic stations and 10 information-processing centers (IPC) which on a regular basis conduct acquisition and processing of raw data and distribute IPC products (**Fig.1.1.1**).

Geophysical Survey of the Russian Academy of Sciences organizationally unites the network of seismic observation and performs scientific and organizational management. Geophysical Survey annually issues catalogues "The earthquakes of Russia" and "The earthquakes in Northern Eurasia" which contain the results of teleseismic and regional observations for the strong earthquakes on the territory of Russian Federation and CIS countries in hard copy and on CD.

Teleseismic network (Fig.1.1.1). Teleseismic network is a basic network to control seismic activity of Russia in the operational and regular modes.

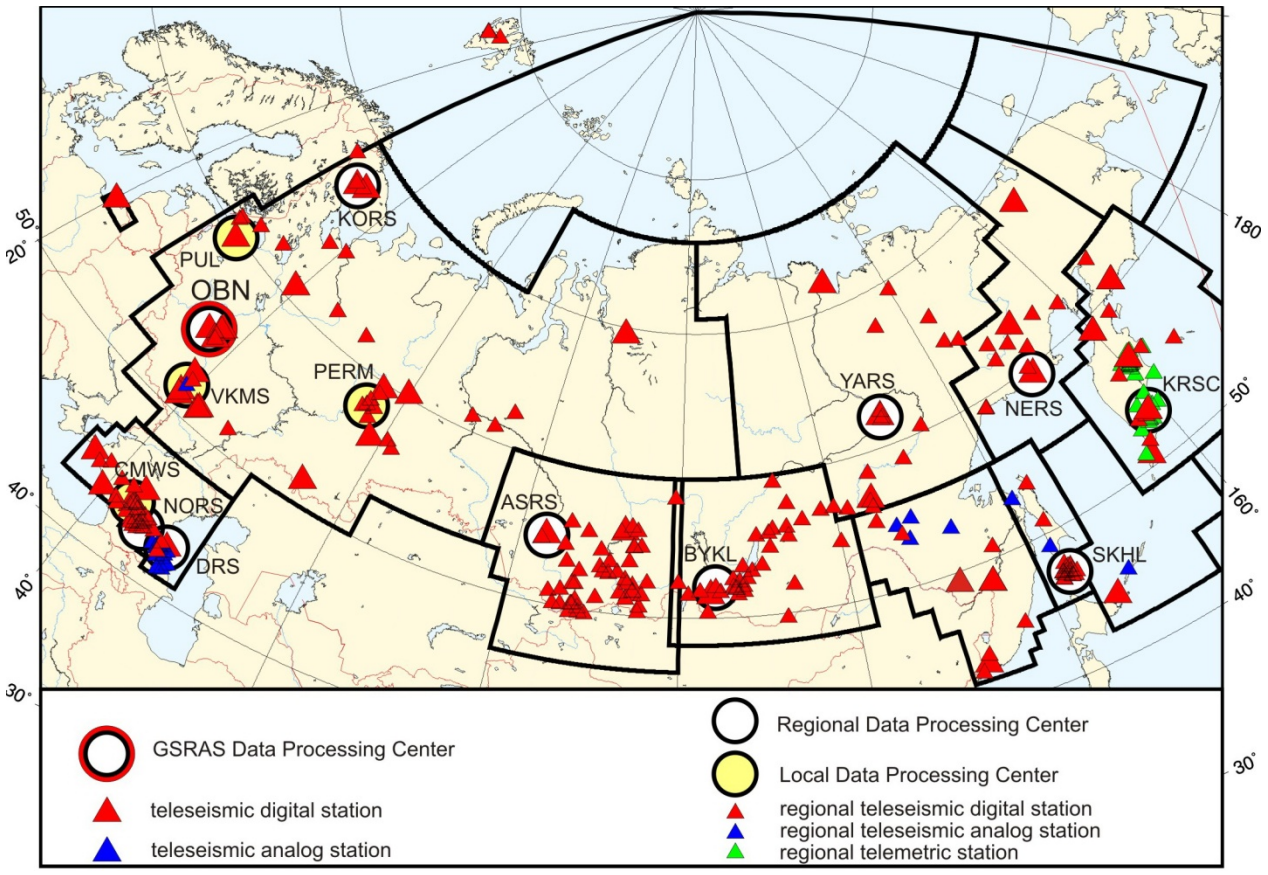

Fig.1.1.1. Russian Seismic Network.

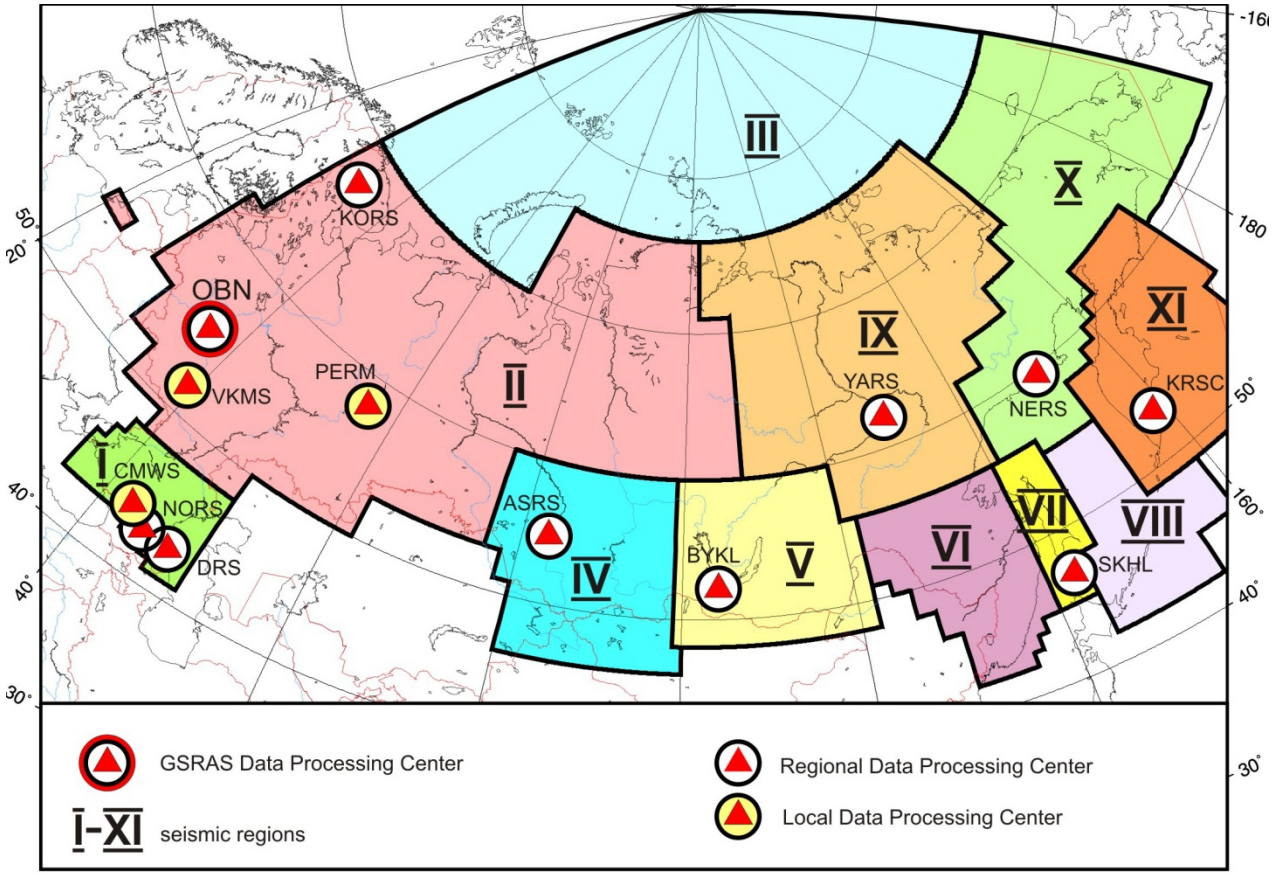

Fig.1.1.2. Russian Seismic Regions.

Teleseismic network includes about 60 stations (international network code OBN). All stations have broadband registration-channels. Digital recording at 12 stations is carried out with the equipment provided by the Corporation of U.S. Seismological Institutes IRIS. These stations are part of the global digital network. Technical parameters of these stations are similar to specifications of the stations which are part of the Global Seismic Network GSN.

Data transmission is implemented through communication channels. Center of teleseismic network in Obninsk operates in near to real-time mode and regularly receives data from more than 60 domestic and foreign stations located in various continents.

Local area network of computers is the central part of the system. The software used by the Center allows to implement the methods of data processing, including data acquisition in different modes, automatic detection and phases association, calculation of events parameters in interactive mode, creation of seismic events bulletin and notification of community with regularly published messages on WEB site of Geophysical Survey (www.gsras.ru and www.ceme.gsras.ru).

Alert Service (AS) is integrated part of the teleseismic network. It operates 24 hours and 7 days a week with the goal to send alert messages to Governmental and other concerned agencies and to submit them immediate information about the main parameters of the strong and sensitive earthquakes occurred (the time of occurrence, the coordinates of the epicenter, focal depth, intensity and potential disastrous consequences). This information is used for taking measures to eliminate the consequences of natural disasters. Efficiency of data acquisition and processing makes from 20-30 min. up to 1-2 hours depending on the priority.

Operation of teleseismic network in the alert mode allows to monitor seismic activity in the whole territory of Russia for magnitudes from 4.5 and in some regions (Northern Caucasus, Baikal Lake and Kamchatka) for M=3.5-4.0.

Regional seismic networks (Fig.1.1.2)

Seismic network of **Altai-Sayan Region (region IV)** (international code of network ASRS) contains 31 seismic stations. All stations are equipped with digital registration systems. Most of these stations operate in frequency band 0.5–20 Hz. Network management is done from Novosibirsk city. Information processing center is located in there, it processes data and issues operation catalogue of the earthquakes with magnitude more than 3.0).

Seismic network of **Baikal Region (V)** (international code of network BYKL) contains 23 digital seismic stations and 7 stations of Burjat branch. All stations of this network are digital with frequency band 0.5–20 Hz and 20 bit analogue digital converters. One broadband station with frequency band 0.003–20 Hz is part of this network. The center of this network is located in Irkutsk city. Summarized processing of seismic events is conducted with data obtained from regional network and «Bulletin of earthquakes of Baikal Region» is issued. The system of emergency and operative data acquisition is done with Internet from 20 seismic stations.

Seismic monitoring at Kamchatka peninsula and Commandor islands is conducted by **Kamchatka Regional Network (XI)** (international code of network KRSC), which contains stationary and radio telemetry (local) networks. The network of stationary seismic stations includes 12 stations equipped with broadband systems of digital registration. All seismic stations conduct permanent digital registration of seismic signals and data are available for processing in a real time mode.

Stations "Kamenskoe" and "Petropavlovsk" have broadband seismic metering channels and operate within the framework of international projects. Network of stations for registering strong motions in Kamchatka contains 20 stations including 14 stations located along the eastern coast of Kamchatka and Bering Island and 6 stations on the territory of Petropavlovsk-Kamchatsky city.

Three local networks were created at Kamchatka with system of radio telemetering acquisition of station data (Petropavlovskaya network – 18 stations, Kozyrevskaya network – 9 stations and Kluchevskaya network – 9 stations), which form the basis of Kamchatka automated regional network. All three local centers communicate via computer channels with regional information-processing center in Petropavlovsk-Kamchatsky city.

IPC operates in alert message mode all day round and calculates automatically hypo centers of

the earthquakes with magnitudes M>4 for Avachinsk Bay and with M>5 for the whole Kamchatka peninsula. Parameters of the earthquakes obtained in regional survey are sent via e-mail, they are available at Web site and sent in form of SMS messages. Operative seismic bulletin is issued regularly for the region of Kamchatka peninsula and Commandor islands. «Petropavlovsk» station is part of tsunami alert system of the Far East.

Seismic monitoring at Sakhalin Island, Kuril Islands and Amur regions is conducted by **Sakhalin Regional Network (VII)** (international code of network SKHL) with center in Yuzhno-Sakhalinsk city. Sakhalin regional network operates more than 30 seismic stations. Southern part of Sakhalin island is provided with monitoring of M>2.0. The rest of this island is monitored with magnitudes M>3,5. Kuril islands are provided with monitoring of magnitudes M>4.0–4.5 **(region VIII)**. Stations «Yuzhno-Sakhalinsk» and «Severo-Kurilsk» participate in tsunami alert system. Operation results of this network are published in quarterly issued catalogue of the earthquakes and in «Seismic Bulletin of Fat East».

North-Eastern regional network (X) (international code of network NERS) conducts seismic monitoring on the territory of Magadan region, Chukotka and shelves of Okhotsk and Bering seas. This network contains 15 digital seismic stations. Most of these stations have short period channels with frequency range 0.5–10 Hz and 24 bit ADC. These stations provide monitoring of magnitudes M>3 on the territory of Magadan region. The rest of this area is monitored for magnitudes M>4.5. Network center is located in Magadan city, it makes summarized processing of data in two modes (operative and alert) and issues monthly catalogue of the earthquakes.

Seismic monitoring in Sakha Republic is conducted by **Yakut Regional Network (IX) (**international code of network YARS). Network center is located in Yakutsk city. This network operates 19 permanently working stations equipped with digital registration systems. The results of survey are published in annual catalogue of Yakut earthquakes. Sensitivity of this regional network is between M=2.0–2.5 in the south and M=4.0–4.5 in the north of the region.

Permanent seismic monitoring of **North-Caucasus Region (I)** is done by three networks – **regional network of Caucasus Mineral Waters area** (network code CMWS), **regional network of Northern Osetia-Alania Republic** (international code of network NORS) **and Dagestan regional network** (international code of network DRS). Processing results of these three networks are published by GS RAS in the form of monthly catalogue of seismic events of North Caucasus.

Regional seismic network of **Caucasus Mineral Waters** contains 16 seismic stations located in Stavropol Region and in adjacent territories of Karachaevo-Cherkessk and Kabardino-Balkarsk republics. It provides seismic monitoring for magnitude levels of M=1.5 in central part of Northern Caucasus and accuracy of hypo centers location of approximately 5–10 km. Data from this network are used for detailed investigation of seismic activity.

Regional Seismic Network of North Osetia–Alania Republic of Northern Caucasus has it's center in Vladikavkaz city and contains 12 digital stations SDAS with registration band between 0.5 and 20 Hz. This is one of the most dense seismic networks of Geophysical Survey, it provides seismic monitoring of North Osetia–Alania Republic with magnitude levels of M=1.0 and accuracy of hypo centers location for the earthquakes of approximately 3–5 km. Data from this network are used for detailed investigation of seismic activity.

Seismic monitoring in Dagestan Republic is provided in the eastern part of Northern Caucasus by **Dagestan Regional Network**. It's center is located in Makhachkala city. It contains 16 seismic stations having short period channels with analogue registration. Six seismic stations are equipped with digital registration systems with frequency band of 0.02–20 Hz. In Dagestan Republic this network registers the earthquakes with magnitudes 1.0 (in the region of Chirkeisk hydro power plant) and with 2.5 for the rest of the territory. Location of the earthquakes is determined with accuracy of 10 km and at the borders of the region with accuracy of 30 km.

Seismic network of **East-European Platform** contains 40 seismic stations of Russian Academy of Sciences and Ministry of Education of RF.

At the **central part of Russia** seismic observations are done with three broadband stations of GS RAS (Moscow, Obninsk, Saratov) and with 12-element micro group of Institute of Dynamics of Geospheres RAS.

Stationary network of seismic stations of GS RAS in the region of **Voronezh Crystal Massive** (network code – VKMS) contains five seismic stations. Besides that, two stations make seismic monitoring in the region of Novovoronezh NPP. The results of data processing if these stations are issued in the form of monthly catalogue of the earthquakes.

Seismic monitoring in the **North-West of Russia** is done by six stations of GS RAS and by regional stationary seismic network in **Arkhangelsk Rigion,** which contains eight seismic stations. Three of these stations belong to GS RAS and five stations to Institute of Ecological Problems of the North of RAS. Results of seismic data processing of this network are issued in the form of annual catalogue of the earthquakes.

The works on permanent seismic observations are done on the territory of Kola peninsula, Karelia and Spitsbergen island by **Kola Regional Network (**international code of network KORS).This network includes seismic group located 17 km from Apatiti town; digital three component broadband station ARA in Apatiti town; two digital three component stations at Spitsbergen archipelago. Permanent seismic monitoring is done by station ARA and seismic group ARAO. The center of this network is located in Apatiti town. Results of seismic data processing of this network are published in the form of monthly catalogue of the earthquakes.

GS RAS network of seismic stations in **Urals Region** consists of 13 stations, including 6 GS RAS stations and one micro seismic group of Mountain Institute of Urals Branch of RAS in Perm city. Code of this network – PERM. Results of data processing of this seismic network are published in the form of annual catalogue of the earthquakes.

1.2. A Statistical Estimate of Seismicity Level: The Method and Results of Application to Kamchatka

V. A. Saltykov, salt@emsd.ru**.** *Kamchatka Branch, Geophysical Survey, Russian Academy of Sciences Petropavlovsk-Kamchatsky, 683006 Russia.*

Information on the current seismicity of a region is rather widely required. The persons who are interested include not only members of the seismological community, but also organizations that are professionally involved in the monitoring of the natural environment (in particular, the Ministry of Emergencies and administrative units). A separate problem apart is that of providing earthquake information to residents of seismic regions.

In view of the wide range of potential users, the characteristics used must be, on the one hand, intuitively understandable and, on the other, their definition must be based on quantitative seismicity parameters. Traditionally the solution is to make scales that convert numerical quantities to qualitative characteristics.

A formalized scale of the seismicity level makes for greater terminological definiteness in descriptions of the state of the seismicity in a region and avoids several ambiguities in assessment and comparisons between seismicity in different space–time volumes. In particular, the concept of "seismic background" is formalized thereby.

"The Monitoring and Prediction of Hazardous Geological Phenomena and Processes" state standard [*GOST R 22.1.06-99*, 1999] contains (in the section that regulates earthquake monitoring) the notion of a "level of seismic background" as one of the required parameters. However, the section merely states the subject itself (the "space–time distribution of small earthquakes") without exactly defining the concept. It thus appears that a scale for seismicity level is required for organizations that are responsible for setting up and conducting the seismicity monitoring to meet the requirements of the state standard mentioned above.

Below there is description of the scale for seismicity level that relies on the statistical distribution function of seismic energy as a parameter that characterizes the seismicity level in a

specified space object during a specified time interval. Considering that the basic parameter is statistical in character, the procedure proposed was called *Statistical Estimate of Seismicity Level*, or SESL'09.

The choice of the basic parameter

One important step in developing the scale is the choice of the seismic parameter as the basis for the scale. A general quantitative estimate of the seismicity level in a specified region during a specified time interval frequently uses parameters such as the total energy of earthquakes that have occurred E and their number N, activity A, and the slope of the recurrence curve (the b-value). However, when a qualitative assessment of the seismic regime is required (i.e., when it is necessary to arrive at the conclusion of an abnormally high or low seismicity level or when seismicity is to be compared between two regions), certain difficulties arise, and the straightforward use of the above parameters provides no answer to the question asked. For example, one and the same amount of energy release or seismic activity may be abnormally high for one region but abnormally low for another. We think that the use of absolute parameters is unjustified, but the distribution function of the same parameter will be devoid of this drawback.

It is proposed to characterize the seismicity level in a specified space–time region by using the empirical distribution function of the total seismic energy released E: $F(K) = P(\log E \le K)$ (**Fig.1.2.1**). In that case, assigning threshold values of F, i.e., defining the scale and knowing the energy release E, we can come to a conclusion as to a higher or lower seismic activity in the region. We note here that the calculation of some widely known statistical parameters like the mathematical expectation and variance cannot be used for the goals we set out to achieve for energy E (or for its logarithm or the energy class $K = \log E$), because their distributions are not reducible to the standard ones for which a similar conclusion could well be reached using known statistical tests without constructing the empirical distribution function.

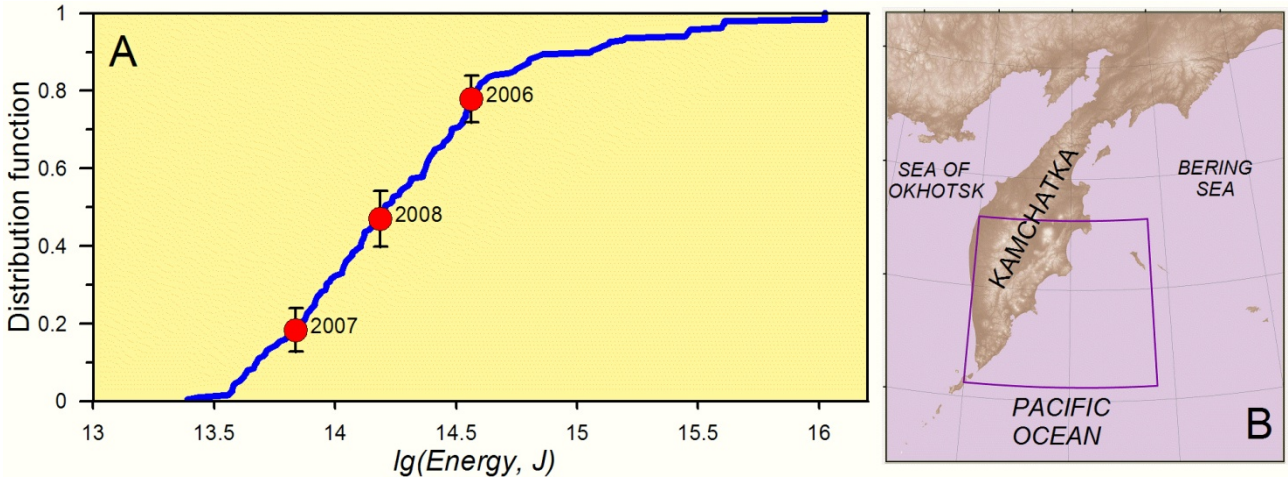

Fig.1.2.1. Empirical distribution function for annual seismic energy (A) for the seismic zone of Kamchatka (B). The points for 2006 – 2008 are plotted. The vertical bars are the *rms* errors of distribution function estimates.

The choice of seismic energy as the basic parameter is due to its greater stability under changes in catalog quality. The use of the earthquake number N or activity A imposes rather stringent requirements on the homogeneity and completeness of the catalog. Energy E behaves in a much more stable manner, because nearly all energy is released by the larger earthquakes.

A scale of seismicity levels

The concept of "background" is associated with the notions of "usual, widely prevalent, and of the most frequent occurrence," in contrast to the notion of an "anomaly," which is observed rather rarely. Bearing this in mind, we propose to define the threshold values of the distribution function F as

follows: F = 0.005, 0.025, 0.15, 0.85, 0.975, and 0.995. The intervals between these values make a scale that contains five seismicity levels:

extremely high, $0.995 \le F$,
high, $0.975 \le F < 0.995$,
background, $0.025 < F < 0.975$,
low, $0.005 < F \le 0.025$,
extremely low, $F \le 0.005$.

According to this scale, seismicity is 95% of the time at the background level, with 2% occurring at high and low levels and 0.5% at extremely high/low levels, which may be defined as seismicity anomalies. To make the division more detailed, the background level can be subdivided into three further sublevels:

lower background, $0.025 < F \le 0.15$,
intermediate background, $0.15 < F < 0.85$,
higher background, $0.85 \le F < 0.975$.

With this refinement, the intermediate background level will occur 70% of the monitoring time, while 12.5% are for the higher/lower background levels.

A nomogram for quantiles in the distribution of seismic energy for various time intervals

In order to be able to use the scale in practice, one need to know the quantiles of the seismic energy distribution corresponding to the threshold values of the probability F for different time intervals. Suppose our task is to estimate the seismicity level for a given space–time region during a time interval $[T_1, T_2]$.

Data from our homogeneous earthquake catalog are used to construct an empirical distribution function $F(K) = P(\log E \le K)$ for the release of seismic energy E in a time window $\Delta T = T_2 - T_1$, which is then used to determine the quantiles of $K(F)$. We suggest the following basic quantiles: $K(0.995)$, $K(0.975)$, $K(0.85)$, $K(0.15)$, $K(0.025)$, and $K(0.005)$. The catalog length T is vastly important.

(1) According to this construction, the lowest value of the empirical distribution function $F\min$ corresponding to the lowest energy for a time interval ΔT equals $\Delta T / T$;

(2) Catalog length affects the accuracy with which the distribution function $F(K)$ and the quantiles $K(F)$ are estimated.

Using the set of distribution functions $F(K)$ for different time intervals ΔT, one can obtain any quantile $K(F)$ as a function of the time window ΔT. The resulting quantiles for a set of ΔT values (7 days to 3 years in our example) are fitted by a monotone curve.

The fitting functions shown in a single plot form a nomogram (**Fig.1.2.2**), which suggests a qualitative estimate of the seismicity for any specified time segment $[T1, T2]$. To do this, we only need the amount of seismic energy E released during that time.

Conclusions

The SESL'09 technique in order to estimate the seismicity level in a specified space–time region in qualitative terms based on a quantitative parameter, viz., the distribution function of seismic energy was developted.

Suggested scale for estimating seismicity levels contains five basic grades and three additional ones.

The main features of this technique and demonstrated certain restrictions on its uses were outlined.

An example of using the technique for one of the most seismically active regions of Russia (Kamchatka) was demonstrated.

An analysis of the uses of this technique for the Kamchatka seismic region based on the regional catalog issued by the Geophysical Survey RAS yields the following conclusions:

(1) The lowest level of completeness for the Kamchatka catalog is sufficient to estimate the seismicity level of the region as a whole in a moving window of at least 7 days;

(2) The estimates based on preliminary data are consistent with those obtained from the final catalog;

(3) When longer time windows are used, it is possible to employ a rougher catalog to obtain adequate estimates.

The technique has been introduced into the practice of the Kamchatka Branch of the Geophysical Survey RAS. Estimates of the current seismicity level are reported on a weekly note to the Kamchatka Branch of the Russian Expert Council for Earthquake Prediction, Assessment of Volcanic Hazards, and Risk and can be found in the Council's conclusions about the seismic situation in the region.

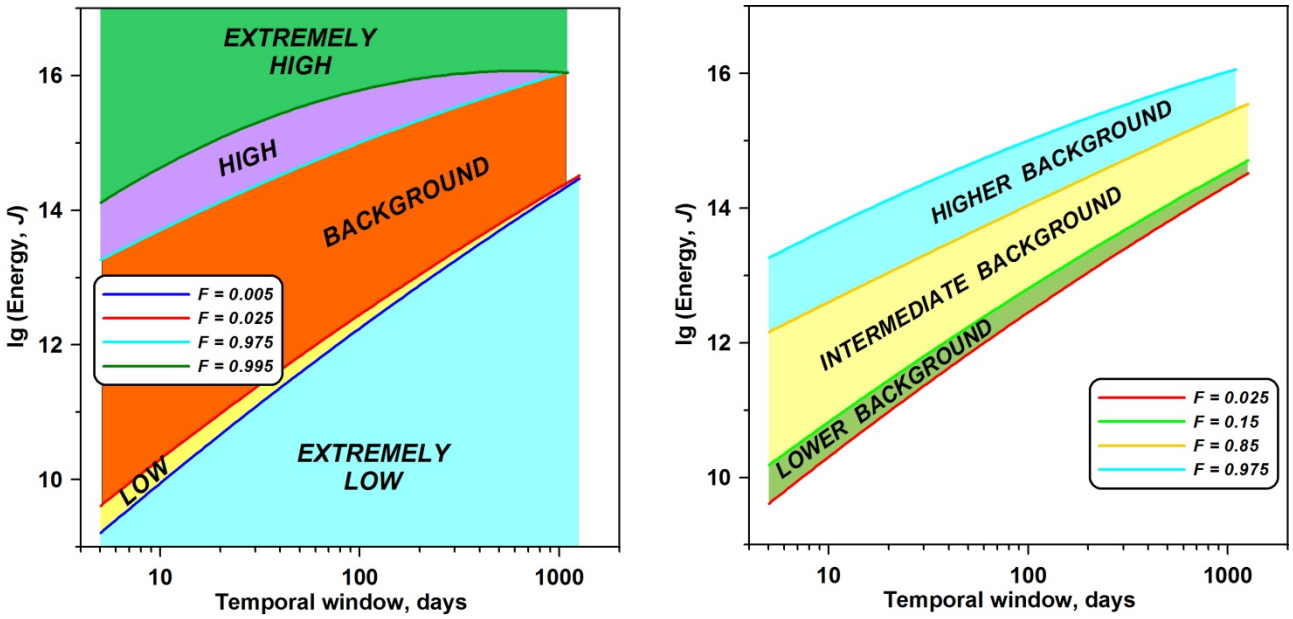

Fig.1.2.1. The SESL'09 nomogram for Kamchatka. The different color denote zones that correspond to different seismicity levels.

References

Saltykov V.A. A statistical estimate of seismicity level: the method and results of application to Kamchatka // Journal of Volcanology and Seismology, 2011, Vol. 5, # 2, pp.123–128. (*Original Russian Text: V.A. Saltykov, 2011, published in Vulkanologiya i Seismologiya, 2011, No. 2, pp. 53–59*). DOI: 10.1134/S0742046311020060.

1.3. Equipment developed by the Institute of Physics of the Earth RAS

S. A. Matsiyevsky, sam49@inbox.ru**.** *Schmidt Institute of the Physics of the Earth RAS. Str. Bol. Gruzinskaya, 10. Moscow 123995, GSP-5, Russia.*

Huge human losses and giant damages caused by earthquakes and tsunamis require urgent measures to be taken with regard to instrumental monitoring of these dreadful natural phenomena. In order to understand the mechanism responsible for formation of strong earthquakes and provide the possibility of their prediction, it is necessary to carry out large-scale studies based on mass networks of instrumental seismological observations. Unfortunately, we have to acknowledge that the existing seismometers for mass (routine) observations which are installed in most stations (both global and regional) of observation networks do not correspond to the current level of seismology development. Although the global geophysical instrument-making is in general a dynamically developing industry, a number of problems connected with release of high-end instruments have been outlined recently:

1. Production of ultra-wideband seismometers of "observatory" class has been completely stopped. The last such instrument was STS-1 withdrawn from production several years ago.

2. Serial-produced single-type three-component mobile (portable) seismometers available from world's manufacturers are essentially inferior to the STS-1 seismometer with regard to a number of parameters in the area of long periods, and limited production capacities do not allow to satisfy the demand in a timely manner.
3. No one of released instruments corresponds to the model of the promising seismometer which can be considered as a basis for modernization of existing mass observation networks. Prototype technical characteristics are discussed from time to time in the international seismological community.

By the beginning of 1970's, it became obvious that the capacitance-type displacement transducer would be a basic means of converting pendulum oscillations into electrical signal for next decades [*Kolesnikov et al.*, 1978]. No one other transducer allowed to achieve such resolution capability along with amazing technological simplicity and minimum cost. In the same period, talented engineer I.I. Rogatnev developed a capacitance-type transducer with resolution of 10^{-5} μm [*Volkov et al.,* 1985]. This resolution was sufficient enough to make relatively wide-band seismometers based on light, short-period pendulums with the natural period of 1-2 s. This can be easily confirmed if we remember that pendulum sensitivity to accelerations for the periods greater than suspension natural period T_0 is constant and determined by the ratio $\Delta x/\Delta g=(T_0/2\pi)^2$, [m/m/s^2].

The theoretical prerequisites for engineer developments supported by new technological capabilities led to mass making of mobile seismometers based on short-period pendulums (the abovementioned mobile seismometers are referred to this type). In Russia, the seismometers of the seismic monitoring network station which have been released in a small lot can fall into this class of instruments [*Rybkin et al.,* 1984]. Now, this direction, as far as we can see, has got up to the limit of current technological capabilities: each new instrument replicates characteristics of the previously developed one. The small inertia moment of these seismometers limits capabilities of instrument amplitude-frequency characteristic extension toward long periods (up to 1000 s) and achievement of the sensitivity threshold that is required in this area and corresponds to the known seismic noise model, NLNM [*Peterson*, 1993]. In the mean time, world's leading seismologists believe that long-wave studies are an important factor of the nearest and future discoveries, while there are almost no instrumental means that support these studies. Global enthusiasm for engineering achievements in the field of mobile seismometer making was to the prejudice of development of high-end "observatory-type" instruments; as a result, no one model competitive with the STS-1 seismometer with regard to long periods came on the world market in the last 15 years.

In order to achieve progress in solving the problems related to prediction and search of forerunners and improvement of current seismicity monitoring quality, as well as solving fundamental tasks of seismology, it is necessary to improve quality of mass observations by equipping observation posts, stations and observatories with instruments of new generation. The long-standing need for instrumental retrofitting the extensive seismic station network of the Geophysical Survey of RAS has called into existence a number of projects for development of unique seismic instruments. Specialists of IPE of RAS have summed up the experience of the best domestic developments, critically analyzed achievements and problems of modern seismometry and formulated a concept for making an ultra-wideband "observatory-class" seismometer that is capable to constitute a basis for modernization of the existing teleseismic observation network, which is especially important for the country of planetary scale. In 2007, IPE of RAS developed the project, within the framework of which the most economically feasible and fast way of making such an instrument was proposed. This method consisted in upgrading the best routine seismometer and turning it into a unique device. This approach allows to take all advantages of many years' successful experience of the best developments and avoid constructional and technological errors of new, insufficiently proven solutions. The electrodynamic seismometer pendulum has long been improving. Talented mechanics from many countries worked to upgrade its design for many years. A huge amount of work was performed to study physical and chemical properties of new materials, create precision cross bearings of supports, develop optimal methods for astatization and design of new suspension force triangles and elaborate new methods and means of improving stability and noise immunity of the pendulum design. As a result, there were a

number of quite successful instruments for mass observations in the world by the mid 90s. In Russia, such devices are represented by the KSESh seismometer pendulum developed by *A.V. Rykov* in IPE of RAS early in the 90s [*Rykov, Bashilov,* 1997]. The pendulum of the KSESh seismometer has unique capabilities to increase the natural period up to 58 s. Large inertia moment, the highest one of all modern seismometers, provides good matching of intrinsic instrumental noises with NLNM seismic interference background for long and ultra-long periods. Supposedly, ultra-wideband seismometers with velocimeter characteristic up to 540 s periods can be designed based on this pendulum. Now, there are no instruments of such class in the world. It has been of great practical interest within the new project to combine the best mechanical suspension with the latest technological and circuitry achievements in electronic engineering.

At the first stage of work on this project, integrated studies of pendulum construction elements were carried out in order to identify the resources of their constructional and technological improvement. Among other things, this included physical and chemical studies of high-stable alloys from the elinvar group and their comparison with the best foreign alloys. A unique Russian technique for manufacture of a coiled cylindrical spring with zero initial length was restored and improved. Various designs of precision frictionless cross bearings of supports were studied in order to find out how they influence on the attenuation and natural period of the mechanical suspension. The pendulum design was modified based on the results of the studies. The two-spring suspension design was substituted by the single-spring one with higher frequency of the first spurious mechanical resonance; cross bearings of supports were replaced in order to increase the natural period of the pendulum; a new spring tension assembly was developed for the vertical pendulum; a new capacitance-type transducer was installed.

At the next stage, the design and electrical schematic diagram of the ultrasensitive capacitance-type displacement transducer with resolution of 10^{-5} μm were developed.

The final stage of work comprised comparative studies of circuit designs for the force-balance wide-band seismometer, as well as development and manufacture of original electronic assemblies with use of components having extreme characteristics (intrinsic noises, operating temperature range). At the present time, certain unanimity of views on the approach to design of wide-band seismometers has surfaced in the world's geophysical instrument-making industry. A force-balance velocimeter circuit has acquired the best reputation from among many circuit designs proposed for implementation in electronic seismometers since the mid 1960s [*Wielandt,* 1982; *Matsievsky,* 1993]. Generally speaking, all modern wide-band seismometers are constructed based on this circuit. The developed universal electronic module contains all the components required for formation of velocimeter characteristic using deep negative feedback ($K\beta>1000$), as well as a microprocessor controller for automated control of calibration and recentering. The automatic correction of seismometer mechanical zero position (recentering) is provided by short-term actuation of an electro-mechanical drive, if necessary. The drive operation causes change of an adjustment mechanism position and induces the return of inertia mass into the state corresponding to the mechanical zero of the pendulum.

Fig.1.3.1 shows the experimental amplitude-frequency characteristic of the considered instrument that has been obtained using the conventional generator method of calibration. **Table 1.3.1** presents key specifications of the seismometer. A preliminary report on the results of this development can be found in [*Vasilyev et al.,* 2009].

The work on refinement of seismometer self-noises in the maximally wide range of operating frequencies is carried out now. At the same time, the instrument design is improved in order to make a pilot sample suitable for serial production.

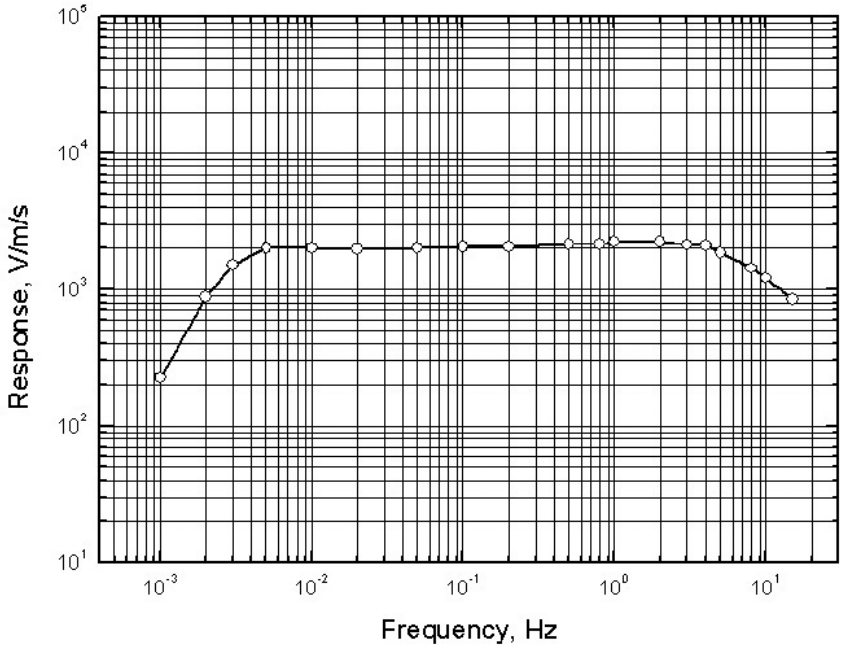

Fig.1.3.1. The experimental frequency response of the seismometer.

Table 1.3.1. Technical specifications

Configuration	Three individual components, one vertical and two horizontal
Feedback	Force balance with capacitive transducer
Standard velocity output band	0.0028 Hz – 15 Hz
Output sensitivity	2000 V/m/s
Dynamic range	> 130 dB (0,01 – 0,2 Hz)
Peak velocity output	± 20 V, differential
Output impedance	100 Ом
Linearity	< -80 dB
Cross-axis rejection	< 0,05%
Supply voltage	9–18 V DC
Power consumption	0.5W (one component)
Mass centering	Automatic motorized re-centering
Lowest spurious resonance	> 25 Hz
Operating temperature	-5°C – +40°C

Bibliography

Peterson J. Observations and Modeling of Background Seismic Noise // Open File Report 93-322, U. S. Geological Survey, Albuquerque, New Mexico, 1993, 94 p.

Rykov A.V., Bashilov I.P. A Very-Broadband Digital Set of Seismometers // Seismic Instruments, 1997, Vol. 27, P.1-4.

Vasilyev I.M., Kozhevnikov Yu.P., Matsiyevskiy S.A., Mezhberg V.G., Rykov A.V., Ulomov I.V. The Prospects for Modernizing Very Broadband Seismometers // Seismic Instruments, 2009, Vol. 45, No. 1, P.60-68.

Wielandt E., Streckeisen G. The Leaf-Spring Seismometer. Design and Performance // Bull. Seismol. Soc. Amer. 1982, Vol. 72, No. 6, P.2349-2367.

Volkov V.A., Iordanov N.D., Rogatnev I.I. Preliminary Results of Observations using a Capacitance-Type Seismogravimeter // Earth's Slow Deformations and Rotation. M.: Radio i Svyaz (Radio and Telecommunication), 1985. P.91-97 (in Russian).

Kolesnikov Yu.A., Matsievsky S.A. Use of Capacitance-Type Linear Displacement Transducers in Seismometry // Issues of Earthquake Prediction and Earth Structure. M.: Nauka (Science), 1978. P.142-179. (Computational Seismology; Issue 11) (in Russian).

Matsievsky S.A. Method for Analysis of STS-1 Seismometer Transfer Functions // Instrumental Studies and Acquisition Trials in Seismometry. M.: United Institute of Physics of the Earth of RAS, 1993. P.121-129. (Seismic Instruments; Issue 24) (in Russian).

Rybkin I.S., Trifonov N.V. Issues of Seismic Monitoring Network Station Construction // Instrumental Study of Seismic Oscillations. M.: Nauka (Science), 1984. P.125-128. (Seismic Instruments; Issue 16) (in Russian).

1.4. Actual Methods and Tools for Geo-ecological Monitoring

E. R. Pavlyukova, e.pavl@mail.ru. *Schmidt Institute of the Physics of the Earth RAS. B. Gruzinskaya, 10. Moscow 123995, GSP-5, Russia.*

The problems of geo-ecological monitoring, prediction and early warning of catastrophic events (earthquakes, tsunami, etc.) become more and more actual because of intensive industry development and so because of increasing danger of man-caused accidents. For solution of these problems industrially advanced countries, such as India, Japan, Russia, USA, etc., have National programs on development of the networks for monitoring seismic events including catastrophic phenomena warning systems.

To obtain comprehensive data about precursors of the catastrophic event and disaster itself, such networks should be based on modern instruments and equipment (like ocean bottom seismic stations and observatories) possessing long-time complex geo-ecological monitoring and reliable online data transmission. Taking into account the fact, that the earthquake focus is placed under ocean bottom in most cases, it is important to place components of the network not only at the dry-land but at the ocean bottom as well [*Bashilov*, 2008].

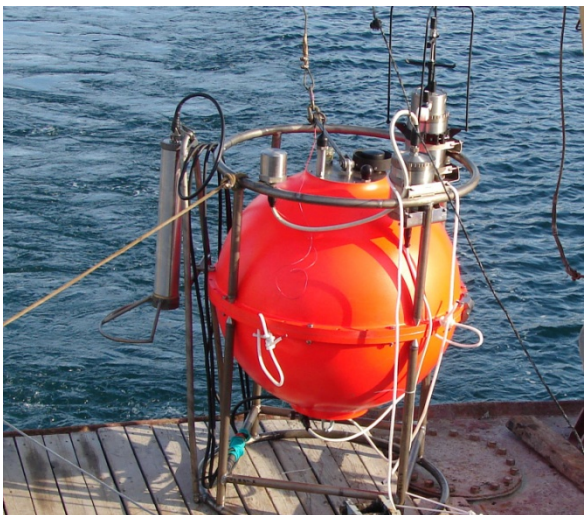

Fig.1.4.1. Underwater Geophysical Observatory (UGO).

Fig.1.4.2. Sea trials of UGO at the Black Sea.

One of the recent developments of the specialists from Schmidt Institute of Physics of the Earth RAS (IPE RAS) and Experimental Design Bureau of Oceanological Engineering RAS (EDBOE RAS) jointly with the specialists from National Institute of Ocean Technology (Chennai, India) in the framework of State Contract with "ROSNAUKA" (2007-2009) is the experimental prototype of underwater geophysical observatory (UGO) of new generation with operating depth till 6000 meters

and with on-line data access for long-term integrated geo-ecological monitoring in the World Ocean (**Fig.1.4.1**). Mentioned operating depth provides the implementation of UGO practically at any point of the World Ocean because of the areas with depths up to 6 000 m take 95% of the World Ocean and bathymetric lows take 15% only.

UGO is a set of oceanological measuring instruments, combined in the modular construction. UGO contains: Seismic module (3-D seismometer), Seismoacoustic module, Hydrophysical module (CTD), Sensor of magnetic field (magnetometer), Acoustic Doppler current profiler, Sensors of hydrochemical parameters, Bottom pressure sensor, Data acquisition system, Hydroacoustic communication link modems, Hydroacoustic ballast switch, radio beacon, light beacon. Significant positive buoyancy of rugged housing (titanium spherical shell, diameter - 1 m) allows to install at the external frame standard instruments and sensors all types, to extend considerably the autonomous operation period at the sea-floor and provides reliable surfacing from depth up to 6000 m.

UGO allows to realize the investigations in the near-bottom zone at new qualitative level, which gives the possibility, not only to register geophysical, hydrochemical, hydrophysical and hydroacoustic characteristics, but to consider their interaction.

Implementation of UGO allows to solve successfully the following scientific and applied problems:

- study of the Earth's crust structure in the World Ocean;
- investigation of superposition of geophysical fields in zones of tectonic fractures directly on the ocean bottom;
- investigation of the state of marine environment in the near-bottom zone and its interaction with tectonic processes;
- geophysical and geo-ecological monitoring of the complex hydrotechnical constructions;
- on-line analysis of seismic and hydrodynamic status of the regions and forecast of possible seismic and ecological after-effects;
- exploration of marine gas-hydrate deposits;
- detecting of seismic, geophysical and geochemical precursors of catastrophic earthquakes, with the sources situated under the ocean floor;
- monitoring of stress changes in Earth's crust in the shelf zone near the development of oil and gas deposits, caused by the extraction of hydrocarbons, peripheral injection of water and other artificial influence on the hydrocarbon layer;
- selection of environmentally safe regimes of deposit exploitation;
- forecast of evolution of Earth's crust structure deformations and induced seismicity;

UGO has been developed using state-of-the-industry high-strength materials and alloys that has allowed to reduce considerably weight of a system and to provide high strength and corrosion stability. UGO surpasses in the principal characteristics well known foreign analogues and has no analogues among autonomous self-surfacing systems. The sea trials of the UGO (experimental prototype) have been successfully executed at the Black Sea in November, 2008 (**Fig.1.4.2**).

One of the significant advantages of UGO is the compatibility with Data-buoys which are produced by National Institute of Ocean Technology (India) and used at the Indian Seismological Network and so in Indian Tsunami Early Warning System. On the base of the UGO the networks of geophysical observations can be created in the World Ocean [*Pavlyukova*, 2009]. The results of this joint project were presented at the Second Science Conclave of Nobel Laureates (Allahabad, India, December, 2009).

The Microseismic sounding method (passive seismic method) is actively developing at the Schmidt Institute of Physics of the Earth RAS for the investigation of deep structures of the Earth crust and indication seismogenerating structures. The main idea of the developing approach is the following: the geological heterogeneities have the effect of anomalies of microseismic wave field on the surface of the Earth. Thus, the approach is based on allocation of anomalies in a spectrum of the deep microseismic wave field around the geological heterogeneities in the Earth crust. The heterogeneities distort the spectrum of low-frequency microseismic field in their vicinity, and namely on the Earth surface above high velocity heterogeneities spectral amplitudes of definite frequency f are decreasing,

but above low velocity ones – are increasing. Method is realized under assumption that vertical component of microseismic field is mainly determined by fundamental modes of Rayleigh surface waves of various frequencies [*Gorbatikov*, 2008, 2010].

The essential advantage of this approach is in using natural seismicity of the Earth as the sources of sounding signals and so it is not necessary to use artificial sources of seismic signals (vibrators, guns, etc.).

Proposed approach can be successfully applied also for exploration of fluidsaturated horisons and underground reservoirs (oil, gas, steam, ground and underground water) and estimation of its reserves for the purpose of industrial deployment as well as [*Nikolaev*, 2010], [*Gorbatikov*, 2010].

Fig.1.4.3. Arkitsa region (Greece). Preparing of the equipment for the field tests, July 2010.

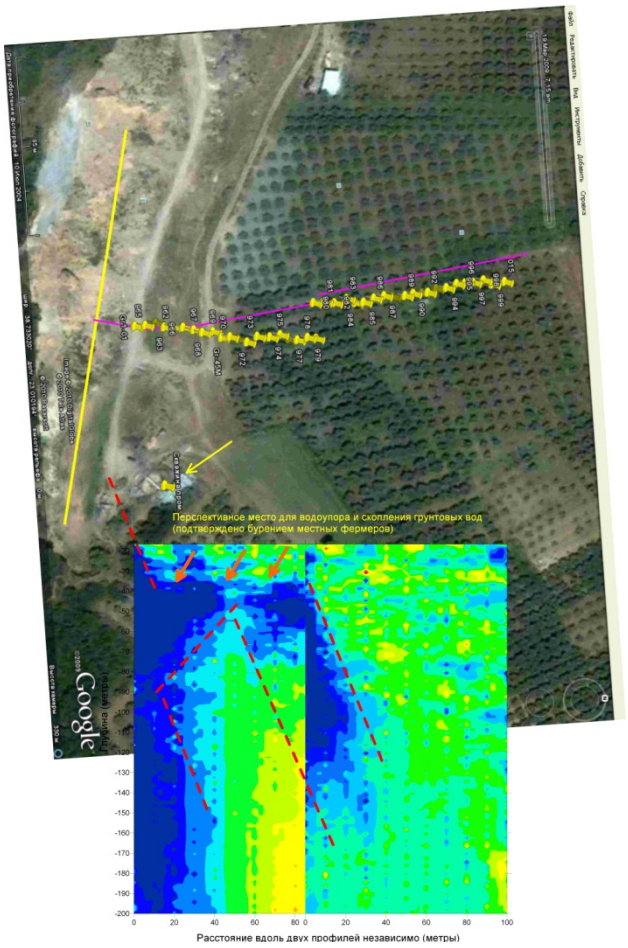

Fig.1.4.4. Method of Microsismic Sounding: results (obtained in Arkitsa, Greece, 2010).

Mentioned approach was successfully tested in Greece (Arkitsa reg.) in March-October, 2010 jointly with the specialists from the Institute of Geodynamics National Observatory of Athens for the survey of aquifers and underground reservoirs under complex geological conditions (**Fig.1.4.3, 1.4.4**). The developed method can be applied in historically densely populated areas with complex geological and geomorphological conditions, where the problems regarding providing by the fresh water for domestic water supply system and for technical purposes are very actual and where the traditional methods (for example, geoelectric prospecting) are complicated or are impossible because of complexity of a relief or a complicated structure of subsurface. The results of the joint project were presented at the following International conferences and exhibitions: X Ecological Forum "Ecology of the Big City" (S-Petersburg, March 17-20, 2010), Russian National Exhibition in Paris (France, June 11-15, 2010, International Conference GEOPETROL-2010 (Krakow, Poland, September 20-22, 2010, [*Pavlyukova*, 2010]), International Seminar "Dynamics of Seismicity: Actual Problems and Applications" (Athens, Greece, October 25, 2010).

One of the actual problems in the World now is the monitoring of cocoon tightness at nuclear power plants. Inspections are executing before start-up and annually in the process of exploitation of the nuclear power plant. The cocoon is rather impressive construction with the volume equal about 60 – 70 thousand cubic meters. The air is injected into the cocoon till the certain pressure and after rather long-term measurements of pressure, temperature and humidity in many points the air weight loss is defined through the equation of state. Tests take about one week and more over and are executed at shutdown reactor, i.e. the power unit is stopped that leads to considerable economic losses. Russian specialists have developed [*Khlestkin*, 2008] express method (which allows to reduce considerably the necessary period for the measurements) and appropriate tools for cocoon tightness inspection and the first industry implementation of the method was executed in January, 2011 at Kudankulam nuclear power plant (India) before start-up (**Fig.1.4.5**) by the specialists from "Sensoris" Ltd. in the framework of the State Contract with ROSATOM State Corporation.

The essence of the method is the following: the control capacity (CC, with the volume about 200 liters, usually is enough) is placed into the cocoon, it is connected with the cocoon through the system of pipelines and cranes, after the completing of the air injection the pressure in the cocoon is equal to the pressure in the CC and at total absence of leakage flow from the cocoon the flow from the CC to the cocoon is absent. If there is the leakage flow from the cocoon to outside the overflow from CC to the cocoon is started and defined by the leakage flow to outside and by the ratio of the volumes. Unfortunately, there are no standard devices, capable to measure this overflow and realization of the idea of the method in practice is not so easy.

For implementation of the developed method for the tests at Kudankulam nuclear power plant it was necessary to provide the sensitivity to low flows about 0,015 SCCM. Honeywell Mass Gas-Flow Sensor AWM42150VH was used as the base, since it is characterized by the high sensitivity and low pressure drop. Connection circuit recommended by producer doesn't satisfy to mentioned above requirements. It was necessary to improve essentially characteristics of the sensor in the range of low flow rates, i.e. to reduce the zero drift. The authors have developed original connection circuit to extend the sensitivity and dynamic range of the sensor, that provides mentioned above sensitivity (**Fig.1.4.6**).

Fig.1.4.5. Kudankulam Nuclear Power Plant (India), January 2011.

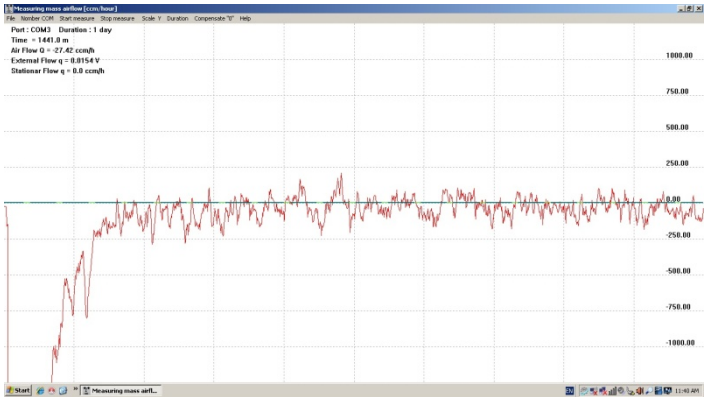

Fig.1.4.6. Measuring mass airflow at Kudankulam NPP on January 28-29, 2011.

The connection circuit developed by the authors can be successfully applied for any other sensors with DC power (not only to Mass Gas-Flow Sensors) to extend the sensitivity and dynamic range of the sensors and be of some interest for the specialists in the fields where it is necessary to measure low gas flow rates.

The development of the new innovative approach for geo-ecological monitoring will allow to improve the ecological safety of the objects having rather high technogenic hazard (nuclear power plants, hydroelectric power stations, dams, bridges, etc.).

References

Bashilov I.P., Zubko Yu.N., Levchenko D.G., Ledenev V.V., Pavlyukova E.R., Paramonov A.A. Bottom geophysical observatories: methods of designing and fields of their application – Nauchnoe Priborostroenie (in Russian), 2008, V 18, # 2, pp.97-108.

Gorbatikov A.V. et al. Microseismic field affected by local geological heterogeneities and microseismic sounding of the medium, Izvestiya RAS. Physics of the Solid Earth, 2008, V 44, # 7, pp.577-592.

Gorbatikov A.V. et al. New technology of microseismic sounding for the problems of the deposit (oil, gas) deep structure investigations, "Neftyanoe hozyaistvo, # 6, 2010, pp.15-17 (in Russian).

Gorbatikov A.V. et al. Numerical simulation of Rayleigh Waves Interaction with Compact Deepened Velocity Heterogeneities, Proc. 4th International Conference and Exhibition EAGE-2010, Saint-Petersburg, Russia, April 5-8, 2010, p.123.

Gorbatikov A.V. et al. Particularities of Astrakhan gas field deep structure resulting from microseismic sounding technique application, Proc. 4th International Conference and Exhibition EAGE-2010, Saint-Petersburg, Russia, April 5-8, 2010, p.105.

Khlestkin D.A., Safarov N.A., Vinogradov V.A. Comparison of efficiency and reliability of the measurement techniques for the integrated leakages in the cocoon of the nuclear power stations. Izvestiya RAS. Energetics. 2008, # 3, pp.52-62 (in Russian).

Nikolaev A.V. Non-typical methods of basins exploration – priority of geophysics the 21 century. X Annual International Conference "Galperin readings-2010 commemorating 90 year anniversary of Y.I. Galperin, pp.144-146.

Pavlyukova E.R., Antonenko M.N. Actual methods and tools for integrated geo-ecological monitoring, Proc. Int. Conf. "Fluxes and Structures in Fluids: Physics of Geospheres", Moscow, 2009, V 1, pp.183-184.

Pavlyukova E.R., Nikolaev A.V., Gorbatikov A.V. New geophysical methods for the survey of fluid saturation levels and underground reservoirs under complex geological conditions, Proc. International Conference "GEOPETROL, 2010", Krakow, 2010, Poland, pp.525-527.

2. The strong earthquakes in the territory of Russia in 2007-2010 and their seismotectonics

S. S. Arefiev, sserg@ifz.ru, **E. A. Rogozhin,** eurog@ifz.ru**.** *Schmidt Institute of Physics of the Earth RAS. B. Gruzinskaya, 10, Moscow 123995, GSP-5, Russia.*

In 2007-2010 several strong earthquakes occurred in the territory of Russia. Fortunately earthquakes were located in thinly populated areas and did not lead to human life loss. The map of earthquakes in Russia and adjacent areas is shown in **Fig.2.1**; stars indicate the most important earthquakes with M>6.0 that occurred from 2007 to 2010 and are briefly discussed in this section. Note that we define the degree of earthquake significance not only from its magnitude but from the region of its location, degree of unexpectedness, social significance and other features as well.

The strongest earthquake occurred on January 13, 2007 in the region of the Kurile-Kamchatka arc. Mw=8.1. The earthquake is interesting due to its location on the eastern oceanic slope of trench bounding the Kurile Island arc from the east. The source mechanism is normal faulting, which is typical for this active zone [*Informatsionnoe* ..., 2007], but is untypical for subduction. Geophysical studies carried on in the South Kurile region revealed the system of active normal faults NE striking and abruptly dipping towards the trench [*Stroenie* ..., 1981]. The seismic source was apparently related to one of these normal faults. These dislocations are developed on the oceanic slope of the trench as well as the shallow dipping thrusts are typical on the continental slope of the Kurile and Japan arcs [*Huene et al.*, 1994].

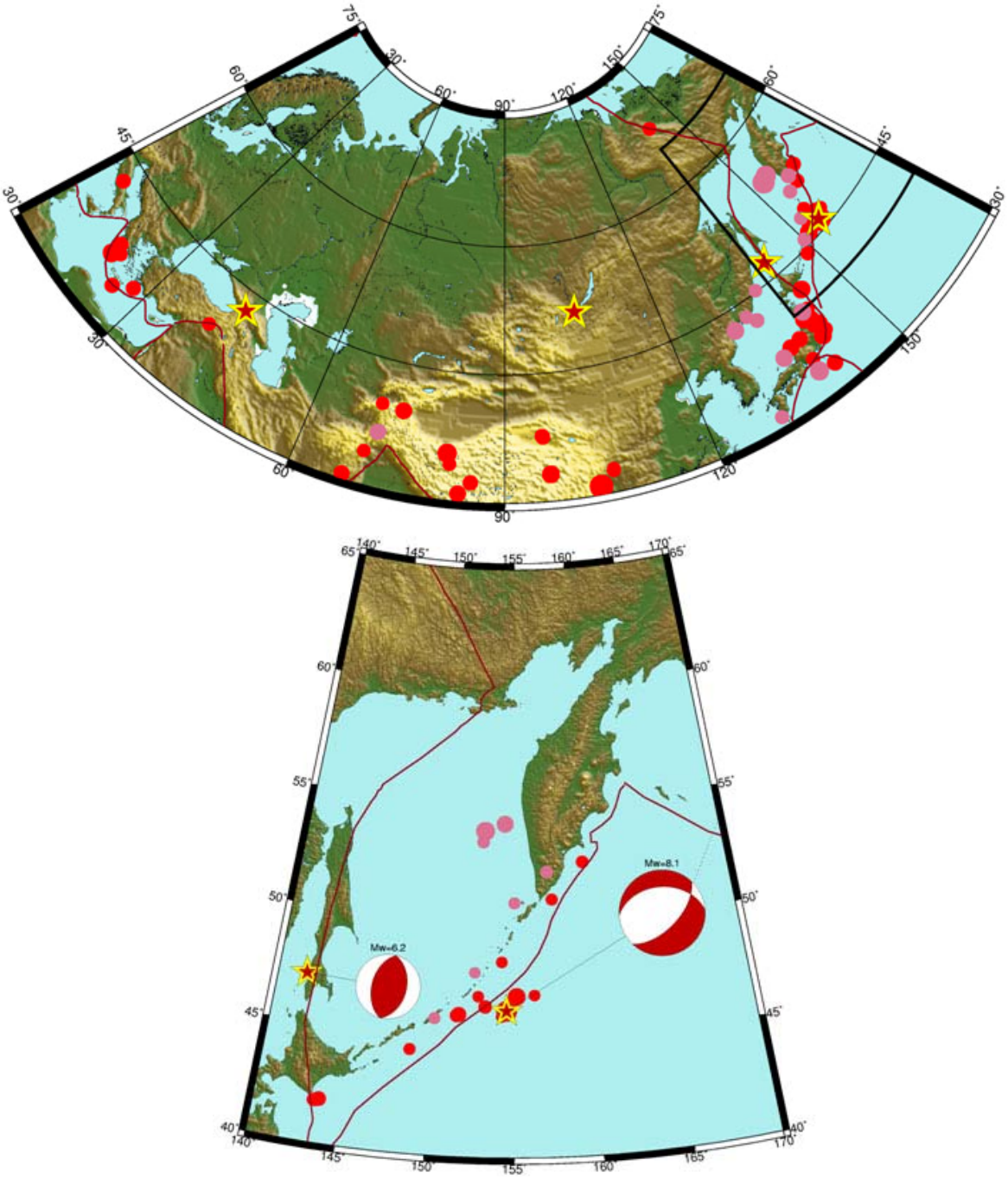

Fig.2.1. Earthquakes with M>6.0 (circles) and more detailed examined earthquakes (stars).

The earthquake can be regarded as conjugate with the strongest earthquake (M=8.3) that occurred in the Central Kurile region on November 15, 2006.

The 2007 shock was accompanied by numerous aftershocks with epicenters located in the thalweg and both slopes of the trench. The shaking was felt from Kamchatka to Japan and over all Kurile Islands with the following intensities: in Severo-Kurilsk of 5-6, in Kurilsk of 4-5, in Petropavlovsk of 3-4, in Yuzhno-Kurilsk and Malokurilsk of 3, according to MSK-64 scale. Tsunami warning was declared for all Kurile Islands and Hokkaido, Japan, however tsunami did not occur [Informatsionnoe …, 2007].

Coseismic deformations were recorded by the network of regional GPS stations on Kurile Islands working since 2006. According to these data, horizontal NE displacements were about 8 mm on Iturup, Shikotan and Kunashir Islands, NNW displacements were 10 mm on Urup Island, and

northern displacements were 4-5 mm in the region of Petropavlovsk-Kamchatsky and 3-4 mm in Yuzhno-Sakhalinsk [Steblov, 2008].

2.1. The Kultuk earthquake, August 27, 2008, Southern Baikal

The earthquake on August 27, 2008 (Mw=6.3) in the southern part of the Baikal Lake is the second by magnitude event after the Srednebaikalsk earthquake of August 19, 1959, M=6.8 that occurred during the period of instrumental observations. It exceeded the magnitude of Yuzhnobaikalsk earthquake (February 25, 1999, M=6.0). The 1999 earthquake was accompanied by the intense aftershock swarm, therefore at the beginning of work on the Kultuk earthquake we expected the greater volume of data than it was recorded. The Kultuk aftershocks rather rapidly attenuated, although the swarm of spatially distant aftershocks was observed.

The region studied is the southeastern part of the Siberian platform bounded from southeast by the Baikal Lake and from southwest by the mountain part of Eastern Sayan including the system of Tunkin rift depressions and territory of the North Mongolia. The Eastern Transbaikalia territory adjoins the southeastern coast of the Baikal Lake.

Fig.2.2 shows the map of epicenters of aftershocks of the Kultuk earthquake and mechanisms obtained by different agencies.

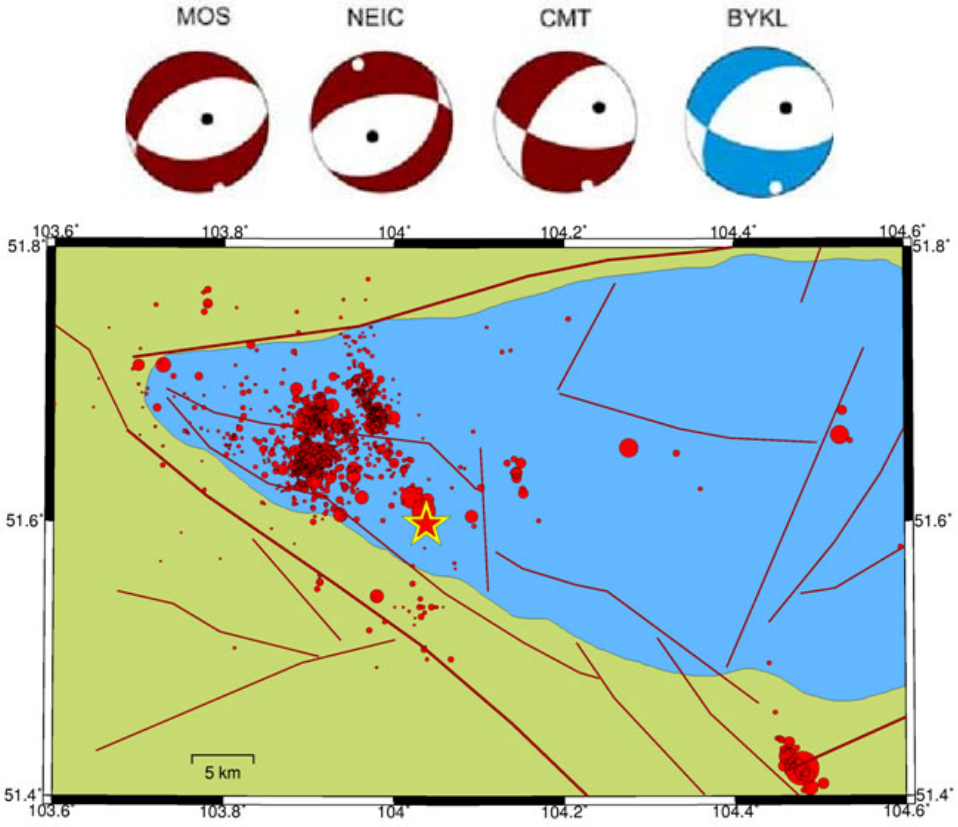

Fig.2.2. Map of epicenters of aftershocks of the Kultuk earthquake

2.2. The earthquake on September 7, 2009, Central Caucasus

On September 7, 2009 the earthquake occurred in the central part of the Greater Caucasus, Mw=6.0 (Ms=6.1-6.2) [Informatsionnoe..., 2009; http://neic.usgs.gov]. The epicenter was located in the highland north of Georgia at a depth of 10 km and distance of 27 km to northwest from Kvaisa (South Ossetia), of 40 km to north-northeast from Sachhere (Georgia), of 68 km to northwest from Tshinval (capital of South Ossetia), of 155 km to northwest from Tbilisi (capital of Georgia), and of 93 km to south-southwest from Nalchik (Russia). The earthquake was felt on the territory of South Ossetia and in the Oni region (Georgia) with the intensity to 7-8 MSK-64 scale and on the territory of

North Ossetia-Alania and in the central part of Georgia with the intensity of 3-5 MSK-64 scale. The shaking was also felt in Armenia, in particular, in towns of Gumri, Vanadzor, and Alaverdi, as well as in Tovuz, Gazah, Agstafa, and Shamkir regions of Azerbaidjan, in Abhazia, and in Turkey. On the territory of Russia, the earthquake was felt in North Ossetia, Chechnya, Ingushetia, Kabardino-Balkaria and Stavropol Territory. Sesimotectonic study of seismic dislocations was operatively carried out in autumn of 2009 and was continued in 2010. Seismic source did not reach the surface. Surface dislocations were secondary and mainly seismogravitational; they were manifested as rare landslides, numerous talus on mountain slopes and mudflows at small rivers and streams. Jigging slopes along the sides of rivers are widely represented.

The zone near the mainshock epicenter in the Kvaisa town vicinities was mostly affected.

The limited instrumental field observations were organized to study the aftershock process. From September 14 till the end of October, 2009, 5 temporary seismic stations of the Institute of Physics of the Earth, RAS, continuously recorded seismic events. Aftershock activity attenuated rather rapidly, however, we recorded about 100 aftershocks during the period indicated. 25 aftershocks (**Fig.2.3**) were of Mb magnitude from 3.7 to 5.1 [Informatsionnoe …, 2009].

It is interesting to compare this new earthquake with the strong Racha, 1991, earthquake [Rogozhin et al., 1993; Arefiev et al., 2006]. Its epicentral zone was essentially larger than in 2009. Various agencies give different epicenter locations. In **Fig.2.3** green star indicate its location according to USGS, and blue star, according to the Center of Seismic Monitoring of Georgia [http://www.seismo.ge].

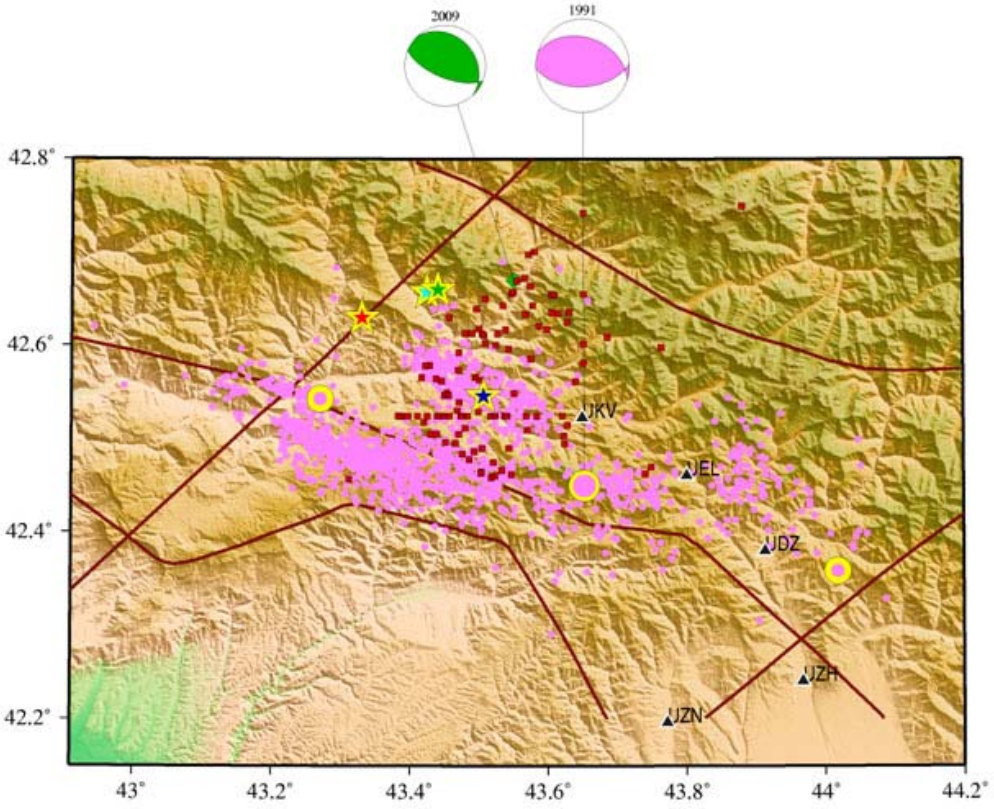

Fig.2.3. The map of epicenters of strong shocks and aftershocks in the Central Caucasus. Rose circles are aftershocks of the Racha, 1991, earthquake, large yellow and rose circles are the main shock and strongest aftershocks of 1991, red squares are 2009 aftershocks, stars are the main shock of 2009 according to various data, diamond is the CMT centroid, triangles indicate the temporary seismic network of 2009.

We constructed the model of the source assuming its complexity (existence of three subsources) and calculated the full tensor of seismic moment. The results of this modeling reveal large values of isotropic component, which can be difficultly interpreted in seismotectonic conditions

observed. Instability of the solution and absence of additional data does not allow making the final choice. Although we can definitely state that this model consisting of three subsources provides the most adequate description of the 2009 source. The solution yielding the best fit of synthetic to observed waveforms is shown in **Fig. 2.4**. As seen, the strongest subsource is close to the CMT solution, but two other subsources significantly differ from it. In other words, the source was firstly realized as thrust-strike-slip NE striking and almost perpendicular to the main acting surface of fault plane (this direction corresponds to the striking of the known Rioni-Kazbek fault, **Fig.2.3**), secondly as the rupture in the main NW direction (the largest in energy), and finally as a normal faulting along the plane of the same striking and somewhat smaller in energy.

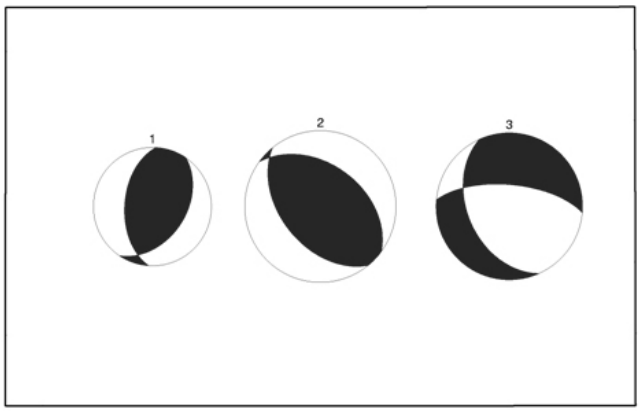

Fig.2.4. Focal solutions for subsources of the September 7, 2009, earthquake, Central Caucasus.

2.3. The Sakhalin high-magnitude swarm of earthquakes, 2007

On August 02, 2007 in 02:37 GMT (13:37 local time) the strong earthquake (M=6.2) occurred near the southwestern coast of the Sakhalin Island. It caused victims and destructions. The epicenter (star in **Fig.2.5**) was located in the Tatar Strait about 7 km to west from Nevelsk and 80 km to southwest from Yuzhno-Sakhalinsk [Informatsionnoe …, 2007].To August 6 (four days and 5 hours since the main shock), GS RAS recorded 19 aftershocks with M≥4 including four shocks with magnitude exceeding 5 (5.2-5.8), **Fig 2.5**.

According to data of seismic station "Yuzhno-Sakhalinsk", the earthquake was felt in Nevelsk with intensity 6, in Kholmsk, 5, and Yuzhno-Skhalinsk, 4. The earthquake caused the small local tsunami up to 20 cm. The aftershock at 05:22 GMT, M=5.7, was felt in Yuzhno-Sakhalinsk with intensity 4, in Ogonki, 3. The aftershock at 08:06 GMT, M=5.6, was felt in Yuzhno-Sakhalinsk, Nevelsk, and Kholmsk with intensity of 4. The aftershock at 10-37 GMT, M=5.6, was felt in Gornozavodsk, Korsakov and Krillion with intensity of 3.

According to distribution of aftershock epicenters the main source was related to the zone of the West Sakhalin fault of near meridional orientation

The fault plane solution of the main shock calculated by CMT method is shown in **Fig.2.5**. The rupture (thrust faulting) occurred under the action of dominant compression stresses nearly EW oriented. Both nodal planes demonstrate close striking (near meredional) and dip by about 45°; one of the planes, to west, and other, to east. According to the distribution of aftershock hypocenters, the acting plane should dip to west.

Measurements of the Earth's surface before and after the Nevelsk earthquake obtained from the Japanese satellite ALOS involving radar interferometry made it possible to construct the dislocation model of the source taking into account seismic and geological data [Nevelskoe …, 2009]. According to this model, the vertical lift of the bottom in the source zone of the main shock was 15-40 cm, and amplitude of horizontal eastward displacements at the east coast of Sakhalin was 15-20 cm from all strong earthquakes of the swarm.

Seismic dislocations in the epicentral part of Sakhalin were secondary. The methane emissions were observed, a series of landslides on steep mountain slopes were revived, and vibration cracks were formed on unstable soils.

The most spectacular manifestation of primary seismic dislocations is almost instantaneous uplift of three coastal linear parts of rock bottom (benches) along the eastern coast of the island with a total length of 5.5 km and amplitude from 0.5 to 1.5 m. These benches stand out above the water level in the strait. The height of their elevation decreases towards the east, and thus, the northern bench is a newly formed island. This system of deformations can be interpreted as uplift (similar to anticline) of the main shock that did not reach the surface over the edge of the acting plane.

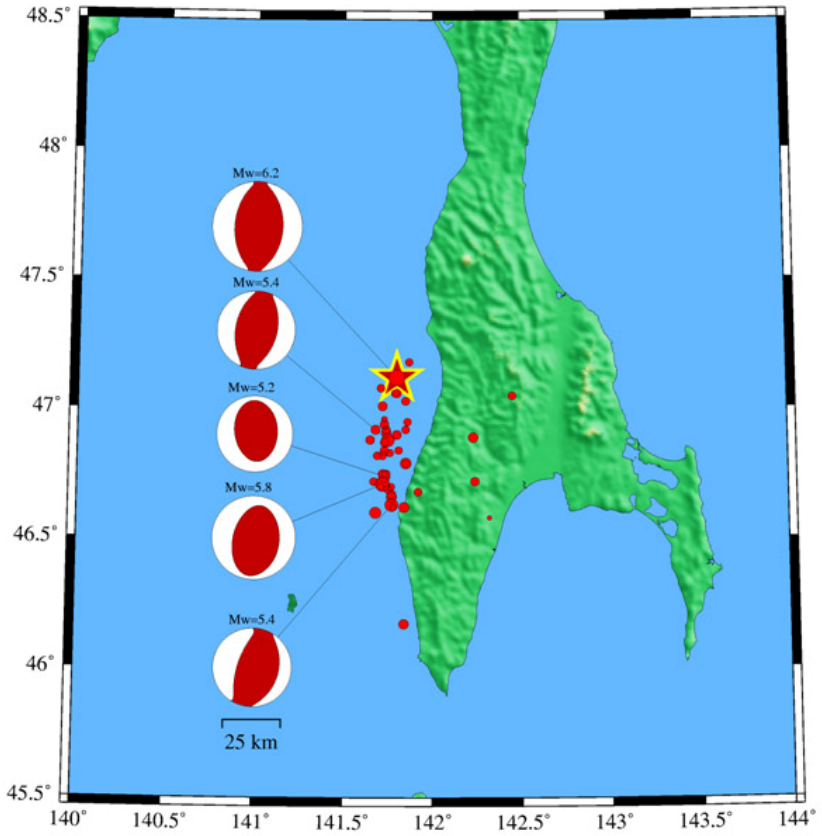

Fig.2.5. Epicenters of the Nevelsk earthquake (star) and its aftershocks (circles). Fault plane solutions are shown for the strongest events of seismic swarm.

References

Arefiev S.S., Rogozhin E. A., Bykova V.V., Dorbath C. Deep Structure of the Racha Earthquake Source Zone from Seismic Tomography Data. Izvestiya, Physics of the Solid Earth, 2006, Vol. 42, # 1, pp.27–40.

Huene von R., Klaeschen D., Cropp B., Miller J. Tectonic structure across the accretionary and erosional parts of the Japan Trench margin // Journal of Geophysical Research. 1994. v.99, # B11, pp.22349-22361.

Informatsionnoe soobshenie o silnom zemletriasenii u zapadnogo poberezhia ostrovs Sahkalin, Rossia, 02 avgusta 2007 // http://www.ceme.gsras.ru/cgi-bin/info_quake.pl?mode=1&id=98

Informatsionnoe soobshenie o silnom zemletriasenii v tsentralnoi chasti Kurilskoi griady 13 ianvaria 2007 // http://www.ceme.gsras.ru/cgi-bin/info_quake.pl?mode=1&id=92

Informatsionnoe soobshenie ob oshutimom zemletriasenii v Gruzii 7 sentiabria 2009 // http://www.ceme.gsras.ru/cgi-bin/info_quake.pl?mode=1&id=136

Nevelskoe zemletriasenie i tsunami 2 avgusta 2007, o.Sakhalin. M.: Ianus-K, 2009, 204 p. (in Russian).

Rogozhin E.A., Arefiev S.S., Bogachkin B.M., et al. Combined Analysis of Geological and Seismological Data and the Seismotectonic Reconstruction of the Racha Earthquake Source // Fiz. Zemli, # 3, 70–77.

Steblov G.M., Grekova T.A., Vasilenko N.F., Prytkov A.S., Frolov D.I. Dinamika Kurilo-Kamchatskoi zony subduktsii po dannym GPS// Tectonofzika I aktualnye voprosy nauk o Zemle. 2008, v. 2, p. 331-333 (in Russian).
Stroenie dna Okhotskogo moria. M: Nauka, 1981, 176 p. (in Russian).

3. Structural seismology of the Earth's interior

3.1. Developments in the studies of the Earth with receiver functions

L. P. Vinnik, vinnik@ifz.ru**.** *Schmidt Institute of the Physics of the Earth, RAS. B. Gruzinskaya, 10, Moscow 123995, GSP-5, Russia.*

P and S receiver functions were applied in many Earth's regions. New evidence of low velocity layers in the mantle transition zone was obtained in several regions. There are numerous indications of a low S velocity atop the 410-km discontinuity and in a depth range between 450 and 520 km. The low velocity layer atop the 410-km discontinuity a few tens kilometers thick has been found by analysis of recordings of the global network in 10 regions [*Vinnik and Farra*, 2007]. In most cases the layer has been found in association with either Cenozoic or Mesozoic mantle upwellings and plumes. In particular, evidence of this layer has been found in the East and West Siberia, Northern and Southern China, Northern Africa and Antarctica. A detailed analysis of structure of this layer has been conducted in California by using a network of almost 50 stations (*Vinnik et al.*, 2010]. Previously obtained evidence for this layer is southern Africa has been verified by the analysis of P and S receiver functions from a local network of 80 stations [*Vinnik et al.*, 2009]. It has been found that, owing to the low velocity layer, the S velocity contrast at the 410-km discontinuity is 40% larger than the norm. The S350p and P350s phases converted from the top of the layer display a dependence on the azimuth, which can be caused by azimuthal anisotropy in the layer atop the 350-km discontinuity.

The low-velocity layer between 450 and 520 km depths has been reported first time in 2004, and in the last few years this first observation has been verified in several other regions [*Vinnik and Farra*, 2006; *Vinnik et al.*, 2009; *Silveira et al.*, 2010]. The clearest indications of this layer were found beneath hotspots in the Atlantic (Iceland and Azores). This layer is found only in the nearest vicinities of the islands and there are reasons to believe that the origin of these islands is somehow related to it.

The method of joint inversion of the P and S receiver functions was improved and used in several Earth' regions for obtaining velocity models of the crust and upper mantle up to a depth of ~200 km. The method has been used in the Tien-Shan, Himalaya, Tibet, southern Africa, Azores and a few other locations. It has been shown that, with this method, one can evaluate Vp/Vs ratio as a function of depth which is either difficult or impossible with other data. In the Tien-Shan the results of these studies suggested an explanation of the regularity of occurrences of large earthquakes [*Vinnik et al.,* 2006]. These earthquakes are known only near the southern and northern borders of the Tien Shan, but never between them. The crustal S velocity in the central Tien-Shan appeared to be very low with implications that the crust is mechanically weak and it is deformed by creep rather than by violent earthquakes.

In the Indian shield the major result of these studies is an S velocity in the subcrustal lithosphere, a few percent lower than in other shields of comparable age [*Kiselev et al.,* 2008]. The crust and mantle velocity models for the Himalaya and Tibet [*Oreshin et al.*, 2008] reveal previously unknown details with important implications for processes in the continental collision zones. In the Azores the analysis of recordings of several local stations provided a detailed characterization of the crust and mantle up to a depth of several hundred kilometers. The receiver functions reveal in this region a division of the subsurface medium into four distinctly different zones: the crust with a Vp/Vs velocity ratio of 1.9 in the lower crust, the high-velocity mantle lid with a velocity ratio of 1.6-1.7, the low velocity zone with a velocity ratio of 1.9 and the underlying upper-mantle layer with a standard velocity ratio. This stratification is consistently found in a few independent data sets. A major boundary with the S velocity contrast of ~1 km/s is found between the upper and the lower crust at a

depth of ~10 km. The ratio of 1.9 is characteristic of mafic and hydrated ultramafic rocks. The thickness of the crust thus determined is near 25 km, about twice thicker than sought previously. The low ratio in the high-velocity lid suggests that it is depleted through the basaltic melt extraction. The LVZ with a reduction of S velocity of nearly 20% is terminated at a depth of ~200 km.

In southern Africa the models obtained by joint inversion of the receiver functions and the teleseismic travel time residuals, the low-velocity zone (LVZ) with the onset of low velocity at the average depth of nearly 140 km is present at most locations. The minimum S velocity in this LVZ is 4.5 km/s. This LVZ is consistent with the S velocity, Vp/Vs velocity ratio and depth range of high-temperature lerzholites in the mantle xenoliths from southern Africa. The most intriguing finding of this study is a very low quality factor Q (on the order of a few tens) in the upper mantle. The high attenuation, the LVZ and the low S velocity atop the 410-km discontinuity can be interpreted jointly as the effects of plume-like phenomena beneath southern Africa.

The other direction of seismic research where the receiver functions play an important role is azimuthal anisotropy. Shear wave splitting in the seismic SKS phase provides a unique possibility to judge on deformations at depths inaccessible for direct observations. However, the SKS technique is notable by a poor depth resolution. To investigate depth dependent azimuthal anisotropy, the SKS particle motions can be inverted jointly with P receiver functions. The technique involves azimuthal filtering of the receiver functions and provides a criterion to discriminate between the effects of azimuthal anisotropy and of lateral heterogeneity of the isotropic medium. This technique was applied to the seismograph network in the Tien Shan [*Vinnik et al.*, 2007]. It has been found previously that the fast direction of azimuthal anisotropy in the Tien Shan is parallel to the trend of the belt, but the depth of the effect was unknown. The results for the network in the Tien Shan reveal a pronounced change in the patterns of azimuthal anisotropy at a depth of 100 km. In the mantle lithosphere (at depths less than 100 km) anisotropy is relatively weak and fast polarization direction varies laterally in a broad range. In the lower layer (asthenosphere) the average azimuth of fast wave polarization is close to the trend of the belt, whereas magnitude of S wave anisotropy is stable and large (5%). This anisotropy is a likely result of recent uniaxial shortening at right angle to the trend of the belt.

A similar analysis has been conducted for station NIL in the western Himalaya [*Vinnik et al.*, 2007b]. Joint inversion of SKS particle motions and P receiver functions revealed a pronounced change in the fast direction of azimuthal anisotropy from 60 degrees at 60-160 km depths to 150 degrees at 160-220 km. The fast direction in the lower layer is parallel to the trend of the Himalaya. The change of deformation regimes at a depth of 160 km suggests that this is the base of the Indian lithosphere. A similar analysis of the data from southern Africa [Obrebski et al., 2010] also demonstrates a difference between the anisotropies in the subcrustal lithosphere and asthenosphere.

The last problem that was addressed with receiver functions is mid-mantle layering [*Vinnik et al.*, 2010b]. Many seismic data on mid-mantle discontinuities are related only to subduction zones. In this paper the problem was investigated with a method which can be applied practically everywhere. The idea is to use SKS-to-P converted phases that are generated in the receiver regions and can be detected in S receiver functions. In two regions (southern Africa and western Europe) the authors have detected apparently the same ‘1200-km’ discontinuity, but at a depth that varies from 1170 km (Africa) to 1240-1270 km (Europe). The S velocity contrast at this discontinuity is ~0.1 km/s, i.e., half of the value in subduction zones. The ‘1200-km’ discontinuity may correspond to the phase transition of SiO_2 from stishovite to $CaCl_2$ structure. The small S velocity contrast is compatible with scenarios in which remnants of old subducted oceanic lithosphere, thermally equilibrated and partly reacted, are finely dispersed in a bulk mantle matrix.

References

Du Z., Vinnik L.P., Fougler G.R. Evidence from P-to-S mantle converted waves for a flat "660-km" discontinuity beneath Iceland // Earth and Planet. Sci. Lett. 2006, V.241, 271-280.

Kiselev S., Vinnik L., Oreshin S., Gupta S., Rai S.S., Singh A., Kumar M.R., Mohan G. Lithosphere of the Dharwar craton by joint inversion of P and S receiver functions // Geophys. J.Int. 2008. V.173, 1106-1118.

Komatitsch D., Vinnik L.P., Chevrot S. SHdiff-SVdiff splitting in an isotropic Earth // J.Geophys.Res.. 2010, V.115. N B07312. Doi:10.1029/2009JB006795.

Obrebski M., Kiselev S., Vinnik L., Montagner J.-P. Anisotropic stratification beneath Africa from joint inversion of SKS and P receiver functions // J. Geophys. Res., 2010, V. 115, N B09313, Doi:10.1029/2009JB006923.

Oreshin S., Kiselev S., Vinnik L., Prakasam S., Rai, S.S., Makeyeva L., Savvin Y. Crust and mantle beneath western Himalaya, Ladakh and western Tibet from integrated seismic data // Earth and Planet. Sci. Lett. 2008, V.271, 75-87.

Silveira G., Vinnik L., Stutzmann E., Farra V., Kiselev S., Morais I. Stratification of the Earth beneath the Azores from P and S receiver functions // Earth and Planet. Sci. Lett. 2010, V. 299, 91-103.

Vinnik L., Farra V. Low S velocity atop the 410 km discontinuity and mantle plumes // Earth and Planet.Sci.Lett.. 2007, V. 262, 398-412.

Vinnik L., Oreshin S., Kosarev G., Kiselev S., Makeyeva L. Mantle anomalies beneath southern Africa: evidence from seismic S and P receiver functions. // Geophys. J. Int., 179(1), 2009, 279-298. Doi:10,1111/j.1365-246X.2009.04261.x

Vinnik L., Oreshin S., Speziale S., Weber M. Mid-mantle layering from SKS receiver functions // Geophys.Res.Lett. 2010, V. 37, N L24302. Doi: 101029/2010GL045323.

Vinnik L., Singh A., Kiselev S., Kumar M.R. Upper mantle beneath foothills of the western Himalaya: subducted lithospheric slab or a keel of the Indian shield? // Geoph. J. Int. 2007, V. 171, 1162-1171.

Vinnik L., Yong Ren, Stutzmann E., Farra V., Kiselev S. Observations of S410p and S530p phases at seismograph stations in California // J.Geophys.Res. 2010. V.115, N B05303. Doi: 101019/20095B006582.

Vinnik L.P., Aleshin I.M., Kaban M.K, Kiselev S.G., Kosarev G.L. et al. Crust and mantle of the Tien Shan from data of the receiver function tomography // Izvestiya Physics of the Solid Earth, 2006, Volume 42, Number 8, Pages 639-651.

Vinnik L.P., Aleshin I.M., Kiselev S.G., Kosarev G.L., Makeyeva L.I. Depth localized azimuthal anisotropy from SKS and P receiver functions: the Tien Shan // Geoph. J. Int. 2007, V. 169, 1289-1299.

Vinnik L.P., Aleshin I.M., Kiselev S.G., Kosarev G.L., Makeyeva L.I. Depth localized azimuthal anisotropy from SKS and P receiver functions: the Tien Shan // Geoph. J. Int. 2007, V. 169, 1289-1299.

Vinnik L.P., Farra V. S velocity reversal in the mantle transition zone. Geoph. Res. Lett. 2006, V.33. L18316. Doi:10.1029/2006GLO227120.

3.2. The practice of application of the receiver functions method to the international teleseismic experiments data in the Central Asia

V. V. Mordvinova, mordv@crust.irk.ru, *The Earth's Crust SB RAS, Lermontov st., 128, Irkutsk, 664033, Russia*; **G. L. Kosarev**, kosarev@ifz.ru, *O. Yu. Shmidt Institute of Physics of the Earth RAS, B. Grusinskaya st., 10, Moscow, 123995, GSP-5, Russia*.

Although a great deal of effort has gone into seismic imaging of the area, many essential points remain unresolved for the scarcity of regional networks, especially the crustal and upper mantle velocity structure beneath the southern Siberian craton, the Sayan-Baikal mountainous terrain and Hangay dome in Central Mongolia. The international teleseismic experiments in the south of Siberia and in Mongolia (PASSCAL 1991–1992 – Program for the Array Seismic Study of Continental Lithosphere и MOBAL 2003 – MOngolian-BAika Lithosphere seismological transect) made more active deep researches (**Fig.3.2.1**). Also essential progress in observations was reached by going of

Siberian and Mongolian seismic stations to a digital equipment and with development of a modern seismic network in China. Accumulated teleseismic recordings are useful the velocity structure of the crust and upper mantle of region by means of a reliable method of receiver function. The receiver function analysis (*Ammon et al.*, 1990; *Burdick and Langston*, 1977; *Kosarev et al.*, 1993; Owens et al, 1984; Vinnik, 1977) was applied in many regions worldwide (for instance, *Bertrand and Deschamps*, 2000; *Gao et al.*, 2004; *Jordi et al*., 2003; *Kind et al.*, 1995; *Liu and Gao*, 2006; *Mordvinova et al.*, 2007; *Zorin et al.*, 2002).

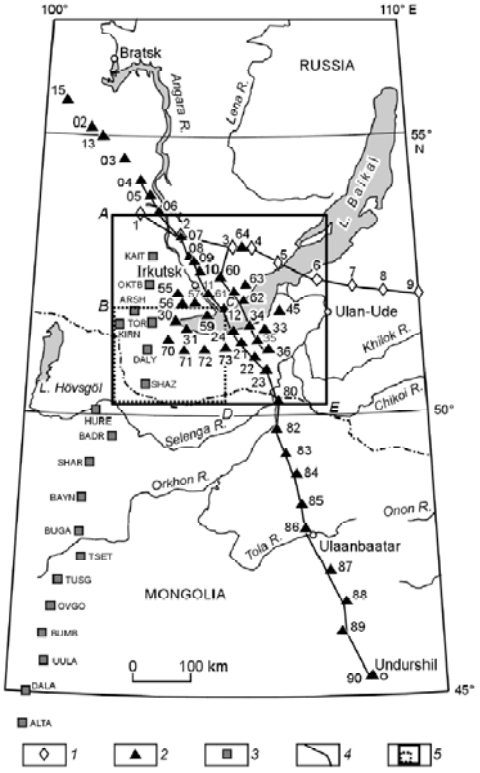

Fig.3.2.1. Location map of seismic stations in teleseismic experiments.
1, 2 - stations of PASSCAL Project of 1991 and 1992, respectively; 3 - stations of MOBAL Project of 2003; 4 - profiles; 5 - area covered by 3D model (dashed line is face of cube chosen for visualization).

With its frequency range from a few hundredths Hz to 1.0 Hz and nearly vertical rays, the method ensures a resolution intermediate between deep seismic sounding (DSS) and regional tomography and has an advantage of imaging fine details of the crust and mantle structure beneath a separate station. It is known to work especially well for profile and uniformly distributed array data. The most reliable are the models calculated by inversion of the P and S waves receiver functions [Vinnik et al., 2006]. In this study we use teleseismic records collected during the international projects PASSCAL 1991–1992 and MOBAL_2003 (Fig. 1). Relatively small amount of the data and a narrow frequency range of many stations have allowed to apply to deep researches in the south of Siberia and in Mongolia only inversion of receiver functions of P waves (receiver function P-to-S).

The *P*-to-*S* receiver function has its origin in the fact that in *P*-wave coda there is a superposition of converted SV waves, are the most highly sensitive to velocity changes at deep structure discontinuities boundaries beneath the observation region. The *P*-to-*S* receiver function method consists in reconstructing the substation isotropic layered velocity structure by fitting theoretical receiver functions to the observed ones defined by converted *SV* arrivals in *P*-wave codas at layer boundaries. The 1D substation velocity and density structure was modeled by iterative minimization of the discrepancy between the observed and synthetic function [Kosarev et al., 1993]. The lateral heterogeneous structure can be presented, from 1D models for several stations, as a mosaic of homogeneous blocks.

Inversion of teleseismic data collected in the PASSCAL 1991–1992 and MOBAL_2003 experiments yielded 1D *Vs(h)* models (**Fig.3.2.2**) which were then employed to simulate the 2D and 3D velocity structure of the crust and upper mantle in the southern Baikal basin and its surroundings (Fig. 3–4) [Mordvinova, Artemyev, 2010]. The models had a resolution for the depths of most

prominent interfaces (of the order of 1 km) and for the lateral patterns comparable with spacing between stations. This accuracy is enough to correlate the velocity pattern with the surface tectonics and to gain more knowledge of the crustal structure and the crust-mantle transition.

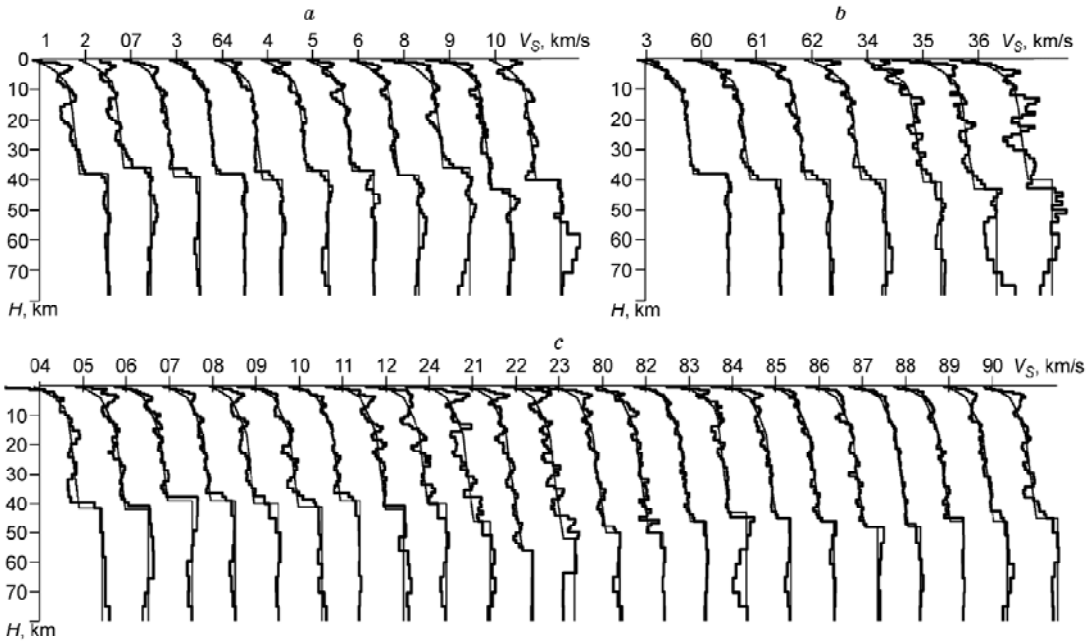

Fig.3.2.2. Velocity models for profile stations, from inversion of receiver functions.
a–c, profiles: W-E (*a*), N–S (seven stations) (*b*), N–S Bratsk–Irkutsk–Ulaanbaatar–Undurshil (*c*). Only the order of stations is shown, their spacing being not to scale. Curves *Vs(h)* are spaced at 1 km/s along velocity axis; bars correspond to *Vs* =3 km/s at H=0, given as velocity tie.

The obtained models have confirmed local crustal thinning beneath the South Baikal basin (34–36 km) relative to that under the adjacent craton margin and foldbelts (46–50 km or more beneath the Khamardaban Range). Low-velocity zones in the uppermost mantle, which have been commonly attributed to asthenospheric upwarps, most often correspond to zones of thickest crust. The obtained 2D and 3D models predict that the asthenospheric upwarps reach the crustal base beneath mountains higher than 1000 km (**Fig.3.2.3–3.2.4**).

Low-velocity zones were revealed in the crust beneath the Baikal rift as well as beneath the folded areas of Transbaikalia and Mongolia, and the Siberian craton. Joint analysis of the receiver-function results with geological and gravity data allowed a hypothesis that most of these low-velocity zones in East Siberia and Mongolia have been produced by alignment of mylonites with large low-angle thrusts (*Zorin et al.*, 2002). The mylonite alignment may cause seismic anisotropy, in which the seismic velocity is slow in the vertical direction and fast in the horizontal direction. Thus, the receiver function method employing nearly vertical rays may be a promising tool to study heterogeneities of this kind.

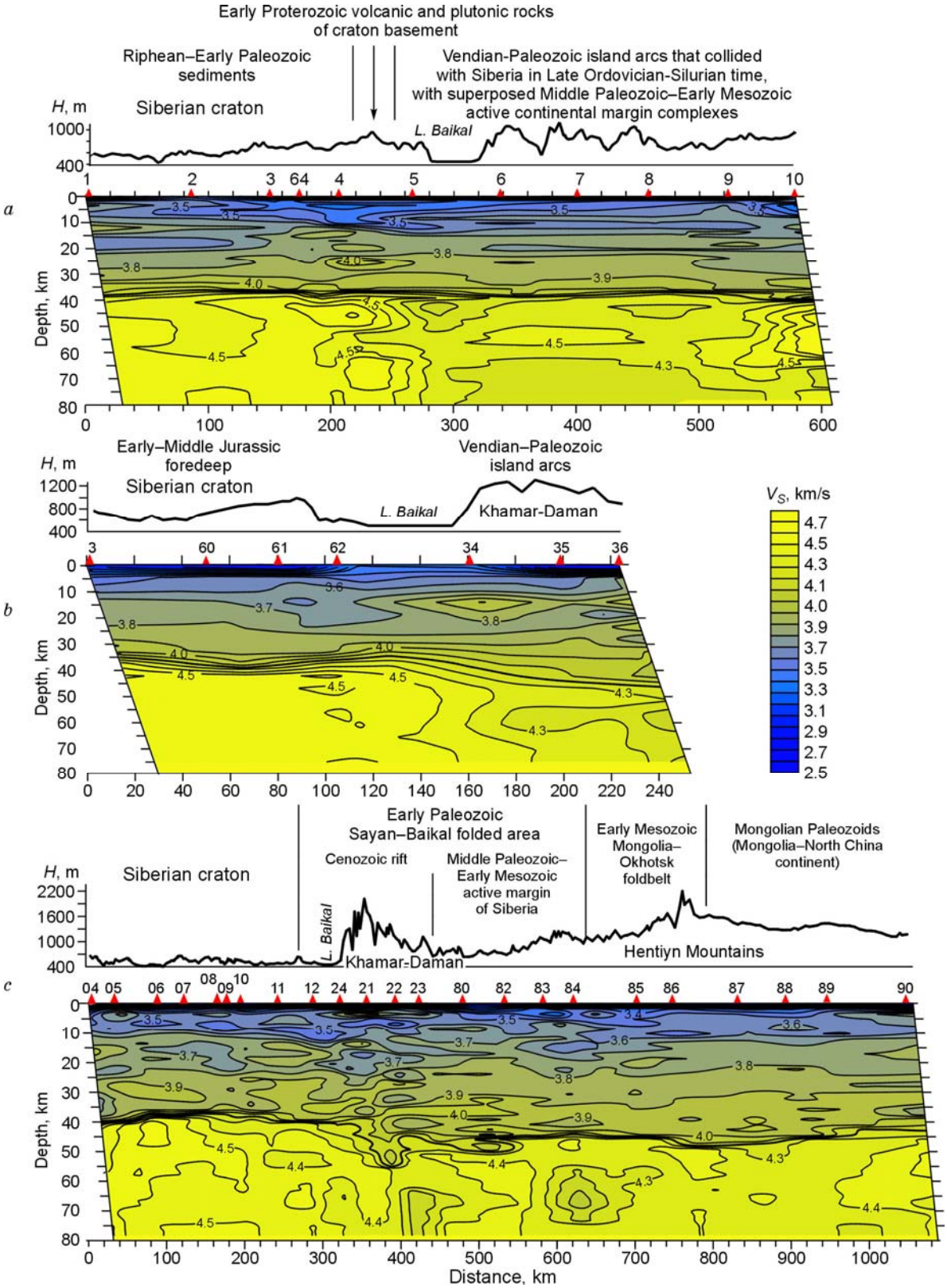

Fig.3.2.3. Smoothed velocity images obtained by inversion of receiver functions P-to-S. Sections are inclined with regard to horizontal scale to an angle corresponding to average ray incidence (20º). Names of tectonic units are according to (*Zorin et al.*, 2002).

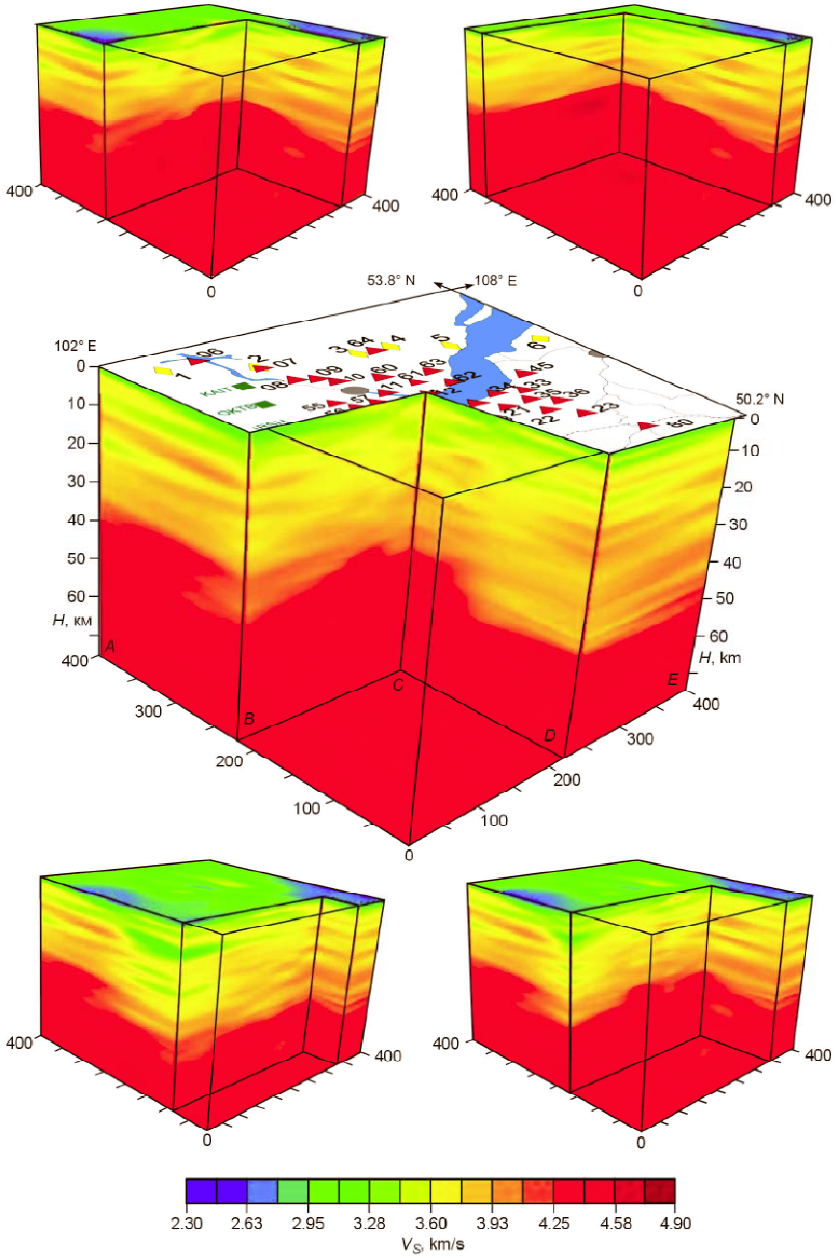

Fig.3.2.4. 3D shear velocity structure.
Sections BC and CD correspond to respective profiles on **Fig.3.2.1**.

The important result obtained from the broadband data are 2D *S* wave velocity sections of the crust and upper mantle along a 1000-km line MOBAL_2003 extending from the Siberian platform to the Gobi-Altai (**Fig.3.2.1, 3.2.5**). These broadband data allow to derive V_S models to a depth of 270 km. The most evident features of the crustal section (**Fig.3.2.5a**) are its abrupt thickening from the Siberian platform to the Sayan dome, the gradient nature of the Moho beneath many stations of the profile, and the lateral division of the section into clearly expressed different zones. The variations in the crustal structure consistent with the change of tectonic regions [*Zorin et al.*, 1993]. For example, a 30-km-thick low velocity crustal layer beneath the Sayan and Khamar-Daban ridges (stations OKTB, ARSH, KIRN and DLY2) gives way in the south to alternating low and high velocity layers and lenses. Higher and lower velocities in the respective depth intervals 12–25 and 20–35 km are observed all along the 500-km Djida fold zone and beneath the eastern Khangai uplift.

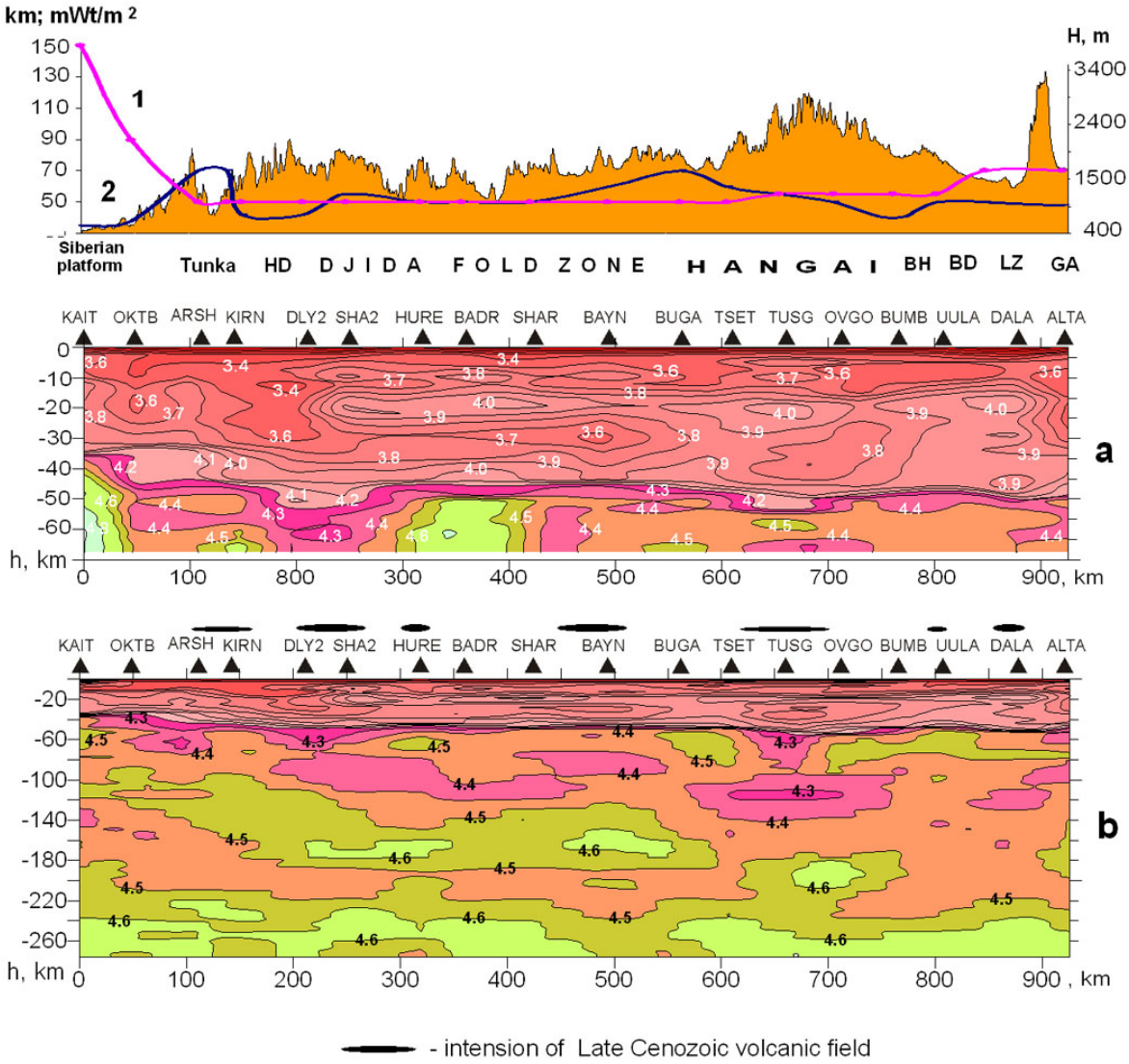

Fig.3.2.5. 2D S wave velocity sections from MOBAL 2003 data in the frequency range 0.01-0.25 Hz. The upper panel of the figure shows the following parameters for the profile (Fig. 1): topography (the height scale is shown to the right); *(1)* lithosphere thickness from gravity data [*Zorin et al.*, 1990]; (2) heat flow [*Lysak and Dorofeeva*, 1997, 2003] (the combined scale of the depth and heat flow is given to the left), (**a**) Velocity section for the depth interval 0–65 km based on the model containing 40 layers (the minimization interval is -5 to 22 s and the $V_s(h)$ dependences for profile stations are linearly interpolated on a 20 x 20 grid), (**b**) Velocity section for the depth interval 0–270 km based on the model with 60 layers (a minimization interval of -5 to 35 s and interpolation on a 30 x 90 grid).

The sections calculated for greater depths (**Fig.3.2.5b**) are similar in crustal velocity structure to the section shown in Figs. 5,a and demonstrate a rather complex V_s distribution in the upper mantle. Being processed by the receiver function method, the MOBAL data image asthenosphere to reach the crustal base in a wedge-shaped upwarp. The upwarp thickens up in the NS direction from 50 km south of the Siberian craton to 150 km north of the Gobi Altai; its west-east extent may be about 400–500 km as inferred from the MOBAL 3D tomography as well as from gravity evidence and the geography of volcanic fields.

Azimuthal seismic anisotropy on the basis of SKS splitting recorded along the MOBAL transect indicates predominant fast direction from NW to SE across the Hangay uplift (*Barruol et al.*, 2008) (**Fig.3.2.6**). The delay of the slow phase along MOBAL is 1.5–2.5 s being much above the Central Asian average. We interpret it as evidence, that dominant Central Asian NW-SE mantle flow comes into particular thick in a zone which we identify with the asthenospheric upwarp.

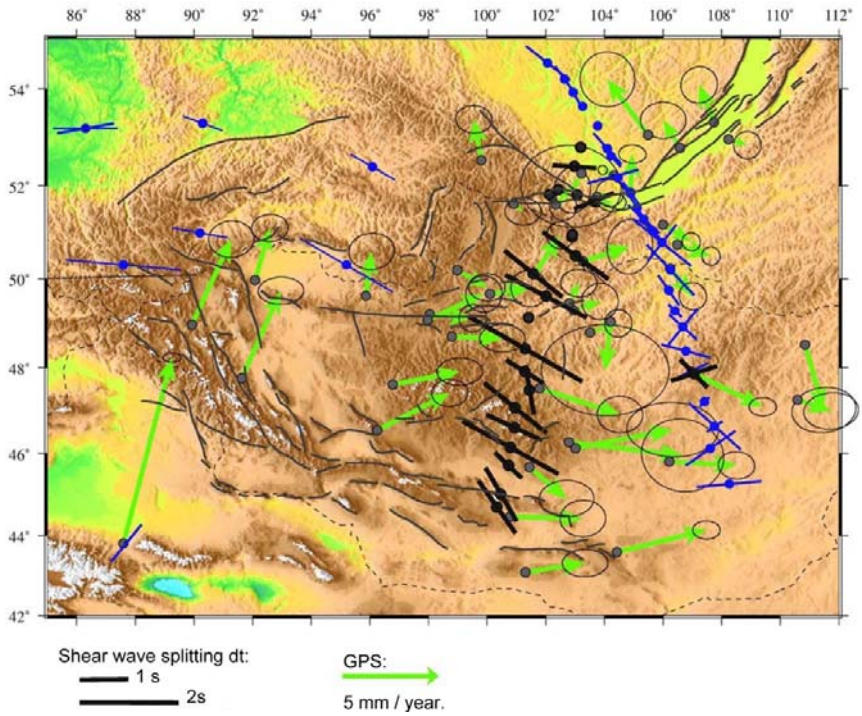

Fig.3.2.6. Topographic map of Mongolia and surrounding areas showing the mean SKS splitting measurements available in the region, together with the GPS vectors and their ellipsoid of uncertainty from Calais et al. (2003). The splitting observations are characterized by their azimuths and the delay time (length of the segment). Black lines represent the data obtained in (*Barruol et al.*, 2008); the blue lines represent splitting measurements previously published by Silver and Chan (1991), *Vinnik et al.* (1992), *Gao et al.* (1994, 1997), and *Dricker et al.* (2002).

The asthenospheric upwarp origin remains uncertain and may be associated with the mantle plume detectable in 2D and 3D tomography images beneath the Hangay or with extrusion of asthenospheric material from the neighbor areas under the joint effect of the India-Eurasia collision and the Pacific subduction.

Anyway, the asthenospheric upwarp produces gravity instability and, according to Yu. *Zorin*, can maintain increasing NW extension [*Zorin, Turutanov*, 2005]. The rising mantle wedge which generates extension stress apparently has been a sort of a barrier to impede transfer of the collisional compression into eastern Central Asia. The existence of such a barrier is consistent with the pattern of abrupt stress change derived from mechanisms of Central Asian earthquakes [*Melnikova et al.*, 2004], as well as in the GPS velocity pattern showing a change from NS compre compression west of the Hangay to WE extension east of it [*Calais et al.*, 2003; *Barruol*, 2008].

References

Ammon, C.J., Randall, G.E. and Zandt, G. On the nonuniqueness of receiver function inversion // J. Geophys. Res., 1990. 95: 15,303–15,318.

Bertrand E., Deschamps A. Lithospheric structure of the southern French Alps inferred from broadband analysis // Physics of the Earth and Planet. Inter., 2000. V. 122. 79–102.

Barruol G., Deschamps A., Déverchère J., Mordvinova V., Ulziibat M., Perrot J., Artemiev A., Dugarmaa T., Bokelmann G. Upper mantle flow beneath and around the Hangay dome, Central Mongolia // Earth and Planet. Science Lett., 2008. V. 274. 221–233. doi:10.1016/epsl.2008.07.027.

Burdick L.J. and C.J. Langston. Modeling crustal structure through the use of converted phases in teleseismic body–wave forms // Bull. Seism. Soc. Am., 1977. 67(3), 677–691.

Calais, E., Vergnolle M., San'kov V., Lukhnev A., Miroshnitchenko A., Amarjargal S., De´verche`re J. GPS measurements of crustal deformation in the Baikal–Mongolia area (1994–2002):

Implications for current kinematics of Asia // J. Geophys. Res., 2003. V. 108(B10). 2501, doi:10.1029/2002JB002373.

Dricker I.G., Roecker S.W., Vinnik L.P., Rogozhin E.A., Makeyeva L.I. Upper mantle anisotropy beneath the Altai–Sayan region of Central Asia // Physics of the Earth and Planet. Inter.,2002. V. 131. 205–223.

Farra V., Vinnik L. Upper mantle stratification by P and S receiver functions // Geophys. J. Int., 2000. V. 141. 699–712.

Gao, S., Liu, K., Chen, C. Significant crustal thinning beneath the Baikal rift zone: New constraints from receiver function analysis // Geophys. Res. Lett., 2004. 31(20)., L20610 – doi:10.1029/2004GL020813.

Gao S.S., Davis P.M., Liu H., Slack P.D., Zorin Yu.A., Mordvinova V.V., Kozhevnikov V.M., Meyer R.P. Seismic anisotropy and mantle flow beneath the Baikal rift zone // Nature, 1994. V. 371. 149–151.

Gao, S., Davis P.M., Liu H., Slack P., Rigor A.W., Zorin Y.A., Mordvinova V.V., Kozhevnikov V.M., Logachev N.A. SKS splitting beneath continental rift zones // J. Geophys. Res., 1997. V. 102. 22,781–22,797.

Kind R., Kosarev G.L., Petersen N.V. Receiver functions at the stations of the German Regional Seismic Network (GRSN) // Geophys. J. Internat., 1995. V.121. 191–202.

Kosarev G.L., Petersen, N.V., Vinnik, L.P., Roecker S.W. Receiver functions for the Tien Shan analog broadband network: Contrasts in the evolution of structures across the Talass–Fergana fault // J. Geophys. Res., 1993. 98 (B3), 4437–4448.

Liu K.H., Gao S.S. Mantle transition zone discontinuities beneath the Baikal rift and adjacent areas // J. Geophys. Res., 2006. V. 111. B11301, doi:10.1029/2005JB004099.

Lysak S.V. and R. P. Dorofeeva Geothermal regime of the upper crust in Southern Eastern Siberia // Dokl. Akad. Nauk, 1997. 352(3), 405–409.

Lysak S.V. and R. P. Dorofeeva Thermal State of Lithosphere in Mongolia // Russ. Geol. and Geophys., 2003. 44(9), 929–941.

Melnikova V.I., et al., Mechanisms of earthquake foci and seismotectonic deformations of the Mongolia region. / Complex geophysical and seismological investigations in Mongolia, 2004. 165–170.

Mordvinova V.V., Deschamps A., Dugarmaa T., et al., Devershere J., Ulziibat M., Artemyev A.A., Sankov V.A., Perro J. Velocity structure of the lithosphere on the 2003 Mongolian-Baikal transect from SV waves // Izv. Phys. Solid Earth, 2007. 43 (2), 119–24.

Mordvinova V.V., Artemyev A.A. The three-dimensional shear velocity structure of lithosphere in the southern Baikal rift system and its surroundings // Russ. Geol. and Geophys., 2010. 51 (6), 694-–707.

Owens, T., Zandt, G. & Taylor, S., Seismic evidence for an ancient rift beneath the Cumberland plateau, Tennessee: a detailed analysis of broadband teleseismic P waveforms // J. geophys. Res., 1984. 89(9), 7783–7795.

Silver P.G., Chan W.W. Shear-wave splitting and subcontinental mantle deformation // Geophys. Res., 1991. V. 96, 16429–16454.

Vinnik L.P. Detection of waves converted from P to S in the mantle // Phys. Earth planet. Inter., 1977. V. 15. 39–45.

Vinnik, L.P., Aleshin, I.M., Kaban, M.K., Kiselev, S.G., Kosarev, G.L., Oreshin, S.I., Reigber, C. Crust and mantle of the Tien Shan from data of the receiver function tomography // Izvestia Phys. Solid Earth, 2006. 42(8), 639–651.

Vinnik L., Farra V. Subcratonic low-velocity layer and flood basalts // Geophys. Res. Lett. – 2002. 29(4), 81–84.

Vinnik L.P., Makeyeva L.I., Milev A., Usenko Yu. Global patterns of azimuthal anisotropy and deformations in the continental mantle // Geophys. J. Int., 1992. V. 111. 433–447.

Zorin Yu.A., V.V.Mordvinova, E.Kh.Turutanov, V.G.Belichenko, A.A. Artemyev, G.L. Kosarev, Gao S.S. Low seismic velocity layers in the Earth's crust beneath Eastern Siberia (Russia) and

Central Mongolia: receiver function data and their possible geological implication // Tectonophysics, 2002. 359(3–4), 307–327.

Zorin Yu.A., Belichenko V.G., Turutanov E.Kh., Kozhevnikov V.M., Ruzhentsev S.V., Dergunov A.B., Filippova I.B., Tomurtogoo O., Arvisbaatar N., Bayasgalan Ts., Biambaa Ch., Khosbayar P. The South–Siberia–Central Mongolia transect // Tectonophysics, 1993. V. 225. 361–378.

Zorin Yu. A., Novoselova M.R., Turutanov E.H., Kojevnikov M.V. Lithospheric Structure of the Mongolian–Siberia mountainous province // J. Geodynam., 1990. 11, 327–342.

Zorin Yu.A., Turutanov E.Kh. Plumes and Geodynamics of the Baikal rift zone // Russ. Geol. and Geoph., 2005. 51, (6).

3.3. Studies of the Lithospheric Structure by Seismic Tomography Methods

I. A. Sanina, irina@idg.chph.ras.ru, **O. A. Usoltseva, A. V. Shaumyan.** *The Institute of the dynamics of the geospheres RAS. Leninskii prospect, 38, korp. 1. Moscow, 119334, Russia.*

With respect to seismic tomography, modern methods of 3D modeling based on body wave data were developed in 2007-2010.

New seismic stations put into operation in the North Caucasus made it possible to study the crustal structure in the region in detail; moreover, it became obvious that velocity models used earlier to determine earthquake coordinates cannot ensure the required accuracy. The paper [*Shaumyan*, 2009] based on the classical seismotomography methods [*Aki*, 1976] studied the crust in the Central and Eastern parts of the North Caucasus and produced an optimal one-dimensional velocity model of the crust, which was later used by the Geophysical Department of the Russian Academy of Sciences (GD RAS) to locate earthquake foci. For the first time ever, a 3D velocity model of the crustal structure was produced for the North Caucasus area in terms of variations in P-wave velocities and the Vp\Vs ratio, consistent with the existing geological views of the crustal structure. The findings proved that it was overall possible to study specific features of the velocity field based on regional observations of earthquakes in the North Caucasus using the existing network of GD RAS stations in the region.

The second paper on the Caucasus [*Usoltseva*, 2010] describes the seismotomography studies of the Southeastern part of the Caucasian crust. A quasi-continuous isotropic velocity model was developed for P-waves where the velocity function has a discontinuity at specific depths but remains continuous in the horizontal direction. A custom-developed algorithm was used to create 3D velocity model for P-waves based on classical seismotomography method for the case when sources and receivers are located within the researched area. According to the algorithm in question, the researched area is divided into Delaunay tetrahedra, and seismic ray paths are calculated by the finite difference method [*Podvin*, 1991]. The paper [*Usoltseva*, 2004] provides a comparative analysis of the above algorithm with other algorithms widely used in the international practice, i.e. Sphypit90 and SimulPS14. The analysis concludes that the custom-developed algorithm is in compliance with the global level yet appears to be more universal, for it is designed not only for 3D continuous velocity modeling, but also for 3D quasi-continuous velocity modeling, whereas Sphypit90 calculates only a block velocity model and Simul PS14 calculates a continuous linear model. A velocity jump in terms of depth is necessary for accurate reconstruction of sharp horizontal boundaries in the crust and those between the crust and the mantle. Horizontal continuity is necessary to reconstruct the nature of velocity heterogeneities in the fracture zone and under hot spots.

The above algorithm was used earlier to reconstruct a 3D velocity model for P-waves in the crust under the Tian Shan Orogen [*Usoltseva*, 2005]. The reconstructed 3D velocity model of the crust under the Tian Shan was used to explain geodynamical relations under the stations in Kyrgyzstan and adjacent regions.

Sensitivity of the available data was checked for the Southeastern part of the Caucasus using the checkerboard test and the above algorithm to find the best reconstruction area of ~400*200 km. The total area of studies is ~600*400 km. Analysis of the findings shows that calculated 3D velocity modes are consistent with the existing views of the regional tectonics.

Surface wave tomography is another rapidly growing field of studies. The paper [*Yanovskaya*, 2008] used the spectral time analysis method to determine phase-velocity dispersion curves for Rayleigh waves on 43 station-to-station routes in the Central Asia region.
The same routes were used to calculate group velocities on the basis of earlier tomographic imaging made by the authors [*Yanovskaya*, 2006] and to determine the average velocity profiles along the routes.

Velocities obtained at fixed depths by 2D tomography were used to assess lateral variations in velocities at such depths, which made it possible to model smoothed vertical velocity profiles at some points within the area. The profiles served as initial approximations for modeling local velocity profiles.

Another paper [*Yanovskaya*, 2009] offers a method of studying the deep mantle structure based on surface waves from remote earthquakes in the areas covered by a dense network of stations. This method was tested on sample models and actual data from a network of stations in Tibet. Advantages of the said method over conventional surface wave tomography were shown.

Practical application of 2D seismic tomography for studying the internal structure of the earth dam/foundation system is described in the paper [*Abramov*, 2007]. Tomograms of longitudinal and transversal seismic waves and the Vs/Vp ratio allow detailed identification of weaker (due to a number of reasons) areas in the structures and their foundations, which is essential for environmental safety of the region.

Studies in the Kamchatka region are also under way. The paper [*Gontovaya*, 2010] examines velocity structure models of the Earth's crust and the upper mantle in Kamchatka produced by classical seismic tomography methods and compares the data with gravimetry data and present-day tectonics.

The paper [*Slavina*, 2009] calculates 3D velocity field for P-waves within a part of the focal area of Kamchatka earthquakes by the inverse wave method [*Slavina*, 2003].

A new approach to seismic tomography inversion was proposed in [*Smaglichenko*, 2007]. It evolves from the papers [*Sanina*, 1982] and proposes to use the probabilistic differential approach in order to find a solution resistant to observation errors. A higher-dimension problem is reduced to a great number of smaller-dimension subproblems that can be solved more accurately and correctly. The final solution is selected from the most probabilistic solutions to smaller subproblems. The next paper [*Smaglichenko*, 2010] proves that it is possible, for seismic tomography problems in the ray approximation for a discrete case, to separate two problems by determining the velocity parameter at a fixed hypocenter location value, if the differential approach is used instead of the conventional method. The findings of the theoretical studies are confirmed by testing seismic data from the Tjornes Fracture Zone.

The paper [*Zerkal*, 2007] discusses how important it is to select proper velocity distribution (null approximation) for seismotomography problems. The paper proposes to consider environments with the quasi-linear velocity/depth function. It provides theoretical description and shows (using a numerical example) how to select the optimal 1D linear velocity model depending on depth only, for a specific seismic experiment at the initial stage.

The papers [*Chebotareva*, 2010a] and [*Chebotareva*, 2010b] contain descriptions and results of the numerical testing of two new seismic emission tomography algorithms that allow to eliminate the screening effect caused by strong coherent noise and imaging of deep weak sources. Both algorithms invoke spatial filters calculated on the basis of singular decomposition of the spectral matrix of the wave field. In practice, the algorithms were used to study the ongoing seismic processes on a producing hydrocarbon deposit in West Siberia. The efficient use of technogenic seismic surveying made it possible to obtain a 3D image of the fracture zone.

References

Abramov N.N., Snezhkova V.E. A Seismotomography Study of the Internal Structure of the Tailings Dam Owned by JSC Apatit // Gornyy Zhurnal (Mining Journal). 2007. No. 12. P. 39 -42.

Aki K., Lee W.H.K. Determination of three-dimensional velocity under a seismic array using first P arrival times from local earthquakes. A homogeneous initial model // JGR, V.81, N.23, P.4381-4399, August 10, 1976

Chebotareva I.Ya. New Algorithms of Emission Tomography for Passive Seismic Monitoring of a Producing Hydrocarbon Deposit. Part I: Algorithms of Processing and Numerical Simulation // Fizika Zemli (Physics of the Earth). 2010a. № 3. P. 7 -19.

Chebotareva I.Ya. New Algorithms of Emission Tomography for Passive Seismic Monitoring of a Producing Hydrocarbon Deposit. Part II: Results of Real Data Processing // Fizika Zemli (Physics of the Earth). 2010b. No. 3. P. 20 -36.

Gontovaya L.I., Popruzhenko S.V., Nizkous I.V. The Structure of the Upper Mantle in the Ocean/Continent Transition Area in the Kamchatka Region // Vulkanologiya i Seismologiya (Volcanology and Seismology). 2010. No. 4. P. 13 -29.

Podvin, P., and I. Lecomte, Finite difference computation of travel times in very contrasted velocity models: a massively parallel approach and its associated tools // Geophys. J. Int. 1991 105, P. 271-284

Sanina I.A., Nikolaev A.V. The Method and Results of the Seismic Survey of the Tian-Shan // Doklady Akademii nauk SSR (Reports of the USSR Academy of Sciences). 1982. Vol. 264. No. 1. P. 69-72.

Slavina L.B., Pivovarova N.B. Methodological Aspects in the Algorithm for Recovering a 3D Velocity Field // Matematicheskie Metody v Geofizike (Mathematical Methods in Geophysics). Novosibirsk, 2003. P. 69-74.

Slavina L.B., Pivovarova N.B., Levina V.I. A Study of the Velocity Structure for the Focal Zone of Kamchatka: The Avacha Bay-Kronotskii Bay Segment // Vulkanologiya i Seismologiya (Volcanology and Seismology). 2009. No. 5. P. 38 -50.

Smaglichenko T.A., Nikolaev A.V. A New Scheme for the Solution of Inverse Problems in Seismic Tomography // Doklady Akademii nauk (Reports of the Academy of Sciences). 2007. Vol. 415. No. 3. P. 399-403.

Smaglichenko T.A., Nikolaev A.V., Yakobi V.R. Separate Determination of the Velocity Structure and Earthquake Hypocenter Parameters Based on a Differential Approach // Doklady Akademii nauk (Reports of the Academy of Sciences). 2010. Vol. 433. No. 4. P. 539-543.

Shaumyan A.V., Sanina I.A., Gabsatarova I.P. A 3D Velocity Model of the North Caucasus Crust Based on Regional Observation Data // Collection of Scientific Papers, Institute of Geosphere Dynamics, Russian Academy of Sciences. Moscow, 2009. P. 160-173.

Usoltseva O.A. 3D Velocity Models of the Tian Shan Crust Based on B-Spline Parametrization and Delaunay Triangulation // Cand. Sc. Thesis in Physics and Mathematics. Institute of Geosphere Dynamics, Russian Academy of Sciences. Moscow, 2004.

Usoltseva O.A., Sanina I.A. A Study of the Tian Shan Crust Based on Seismotomography Data // Dynamic Processes in the System of Internal and External Interactive Geospheres. Moscow, 2005. P. 83-89.

Usoltseva O.A., Kazymova S.E., Kazymov I.E. A Seismotomography Study of the Crust in the Southeastern Part of the Caucasus using the Delaunay Triangulation and P-Wave Travel Time Data // Collection of Scientific Papers, Institute of Geosphere Dynamics, Russian Academy of Sciences. Moscow, 2010. P. 140-147.

Yanovskaya T.B., Kozhevnikov V.M. Anisotropy of the Upper Mantle of the Asian Continent by Group Rayleigh and Love Wave Velocities // Geologiya i Geofizika (Geology and Geophysics). 2006. Vol. 47. No. 5. P. 622-629.

Yanovskaya T.B., Kozhevnikov V.M., Solovey O.A., Akchurin K.R. The Structure of the Upper Mantle in Asia by Phase and Group Rayleigh Wave Velocities // Fizika Zemli (Physics of the Earth). 2008. No. 8. P. 22 -31.

Yanovskaya T.B. Surface Wave Tomography Method Based on Data from Remote Earthquakes // Fizika Zemli (Physics of the Earth). 2009. No. 3. P. 50 -55.

Zerkal S.M., Novokreshchin A.V. The Choice of Initial Approximation (Reference Velocity Distribution) in Iteration Kinematic Seismotomography // Doklady Akademii nauk (Reports of the Academy of Sciences). 2007. Vol. 413. No. 5. P. 679-682.

3.4. Teleseimic tomography at geo transects in Central Asia

V. V. Mordvinova, mordv@crust.irk.ru, *The Earth's Crust SB RAS, Lermontov st., 128, Irkutsk, 664033, Russia*; **A.V. Treussov**, treussov@ifz.ru, *O. Yu. Shmidt Institute of Physics of the Earth RAS, B. Grusinskaya st., 10, Moscow, 123995, GSP-5, Russia*.

The first data on deep velocity structure of the Central Asia have been received by various methods [*Bijwaard et al.*, 1998; *Zhao*, 2004; *Zorin et al.*, 1990]. Models of these works have the low resolution and are insufficiently correlated one with another, as have been based on a poor network of seismic stations. To remedy this, in Eastern Siberia and Mongolia active tomography researches are begun on the basis of special international teleseismic observations PASSCAL_1992 and MOBAL_2003 [*Burkholder et al.*, 1995; *Gao et al.*, 2003; *Mordvinova et al.*, 2000, 2009; *Tiberi*, 2003, 2008; *Zhao et al.*, 2006; *Zorin et al.*, 2003].

We investigate the velocity structure of the southern Siberian craton and its folded surroundings from digital teleseismic P body-wave data collected by the permanent Baikal seismological network and the campaign PASSCAL_1992 and MOBAL_2003 profiles which intersect in the southwestern Baikal region (**Fig.3.4.1**) [*Mordvinova et al.*, 2000, 2009]. The crust and upper mantle structure from 0 to 600 km depth beneath the transects has been modeled with the classical 2D tomography (*Aki, Christofferson, Husebye*, 1977) using P-wave traveltime residuals. The resulted P-velocity anomalies are no more than ±3 % relative to the reference IASP91 model of the Earth. However, as shown by graphical tests, the applied system of teleseismic rays can provide location of mantle anomalies but cannot rigorously constrain their contours and their intensity is half from that in the test model (**Fig.3.4.2**). Consequently, it is possible that at the investigated depth the most velocity anomalies can peak ±5–6 % relative IASP91 V_P model.

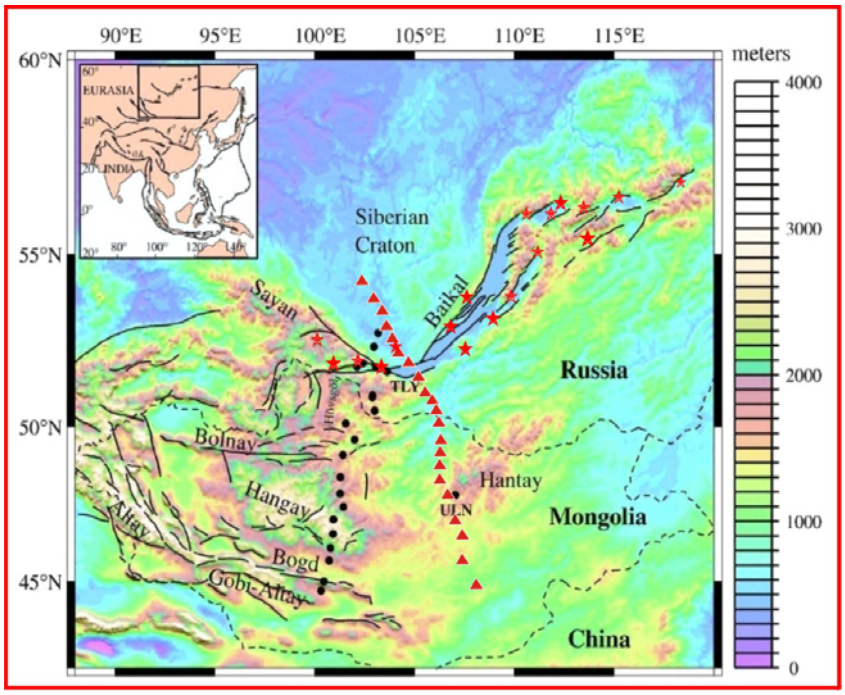

Fig.3.4.1. The seismological network in the region of research [*Mordvinova et al.*, 2009] Asterisks – stations of the permanent Baikal seismological network; triangles – of the compaign PASSSCAL_1992 profile; dots – of the MOBAL_2003 profile.

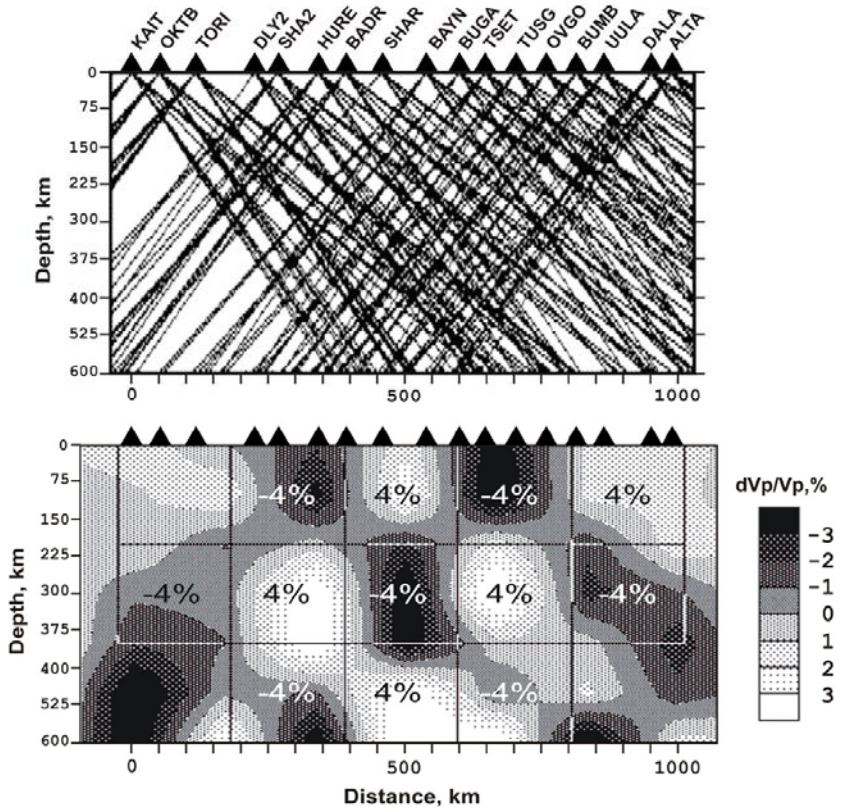

Fig.3.4.2. Rays system sounding the deep structure beneath the MOBAL transect (above) and the chess test of the system resolution (below). The test model is interchange of squares with 4% anomalies: black – lower velocity, white – higher one.

According to 2D tomography evidence from the Baikal network (vertical section, **Fig.3.4.3a**), the central and northeastern Baikal rift system lies over the Siberian craton margin with a 100–200 km thick high-velocity lithosphere [*Mordvinova et al.,* 2009]. This result supports the dedused from surface waves tomography conclusion [*Emmerson et al.,* 2006] that south-east deep-earth boundary of the Siberian platform is detected far southern, than it was established accordingly to the geological and topographic position [*Logatchev & Florensov*]. At the southwestern flank of profile "Baikal rift system" (under the rift valleys and East Sayan mountains) P-tomography reveals a zone of low P velocity in the crust and upper mantle (**Fig.3.4.3a**).

The low-velocity zone is especially well pronounced along the SE-trending PASSCAL_1992 profile traversing the Siberian craton, the southern end of Lake Baikal, and Mongolia (**Fig.3.4.3b**). The most prominent shallow portion of the anomaly falls within the Khamar-Daban foothills south of Baikal rather than into the Baikal basin. This important fact agrees with the results of other works (Burkcholder et al., 1995; Mordvinova et al., 2000; Tiberi et al., 2003).

The tomographic image of the MOBAL_2003 profile along 100°E (**Fig.3.4.3c**) reveals a complex low-velocity structure with its intensity peak between 0 and 200 km beneath the highest elevated uplift of eastern Hangay. The Hangay anomaly is clearly from 600 km and is linked with the southwestern flank of the Baikal rift system at depths 200–300 km.

More detailed P-tomography image till 300 km depth was obtained by a joint inversion of gravity and MOBAL teleseismic P-data (Tibery et al., 2008) (**Fig.3.4.4,a**). Comparison shows good accordance between the most intense V_P anomalies and intense V_S anomalies from the receiver function P-to-S method [Mordvinova et al., 2007] (**Fig.3.4.4a,b**). In turn, on the data of body and surface waves, large-scale Vs anomalies have common configuration (**Fig.3.4.4b,c**) [*Shapiro, Ritzwoller*, 2002]. Unfortunately in Hangay region the most discrepancy between the models 4,b and 4,c is due to absence of seismic observation at Hangay before 2003. In that way, along MOBAL

transect, the independent methods results support one another in spite of its different data and resolution.

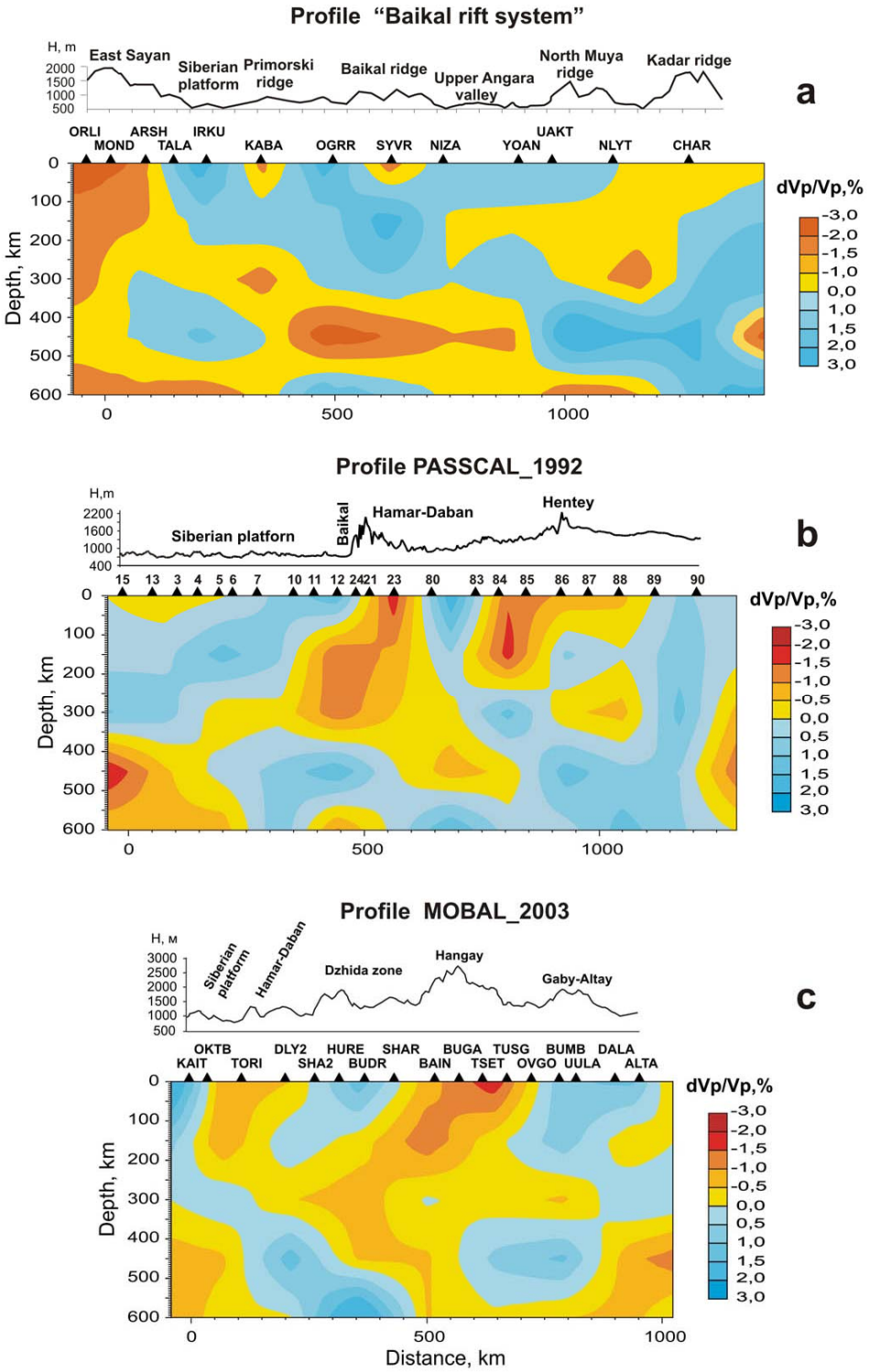

Fig.3.4.3. 2D P-tomography along Baikal rift system (a), along profile PASSCAL_1992 (b) and profile MOBAL_2003 (c) [*Mordvinova et al.*, 2009].

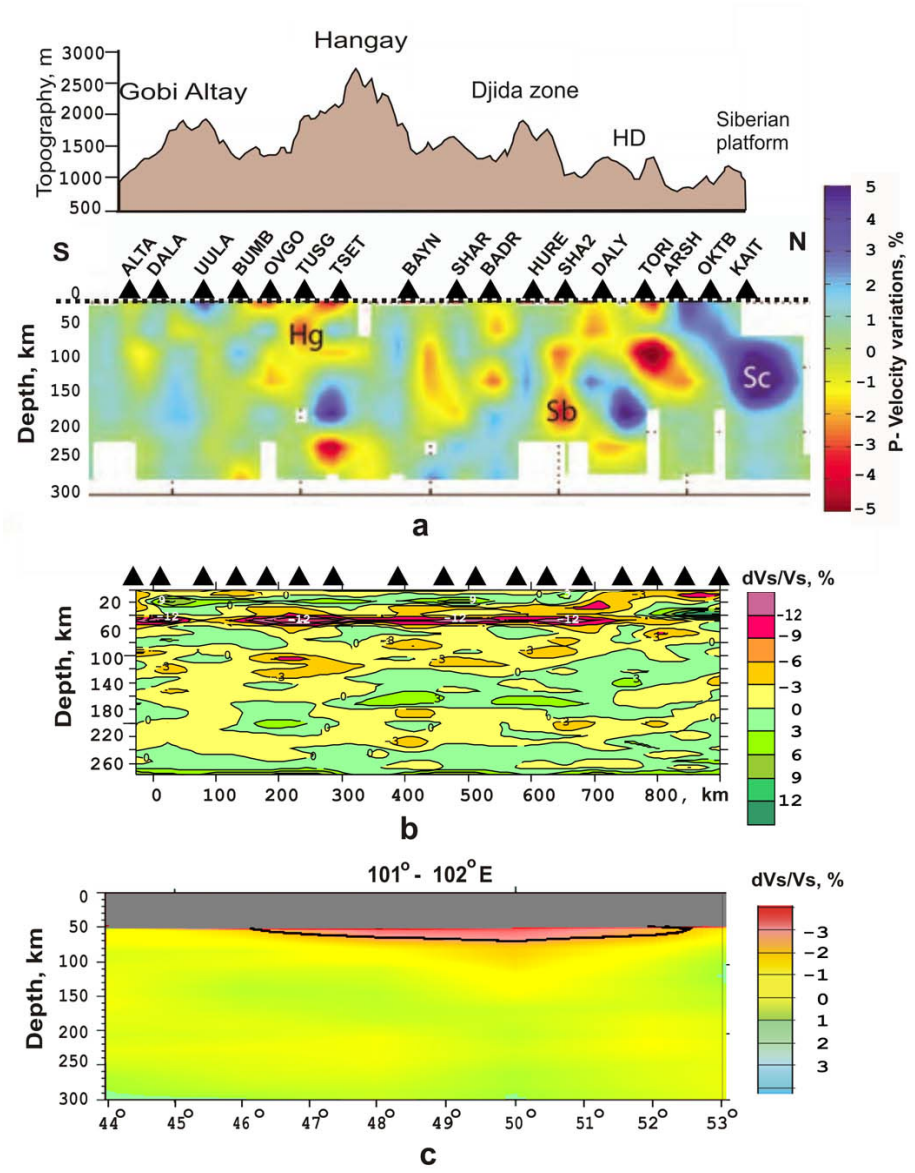

Fig.3.4.4. Models verification: Comparison of Mobal P-velocity anomalies [*Tiberi et al.*, 2008] (a) with S-velocity anomalies of body waves [*Mordvinova et al.,* 2007] (b) and surface wave [*Shapiro, Ritzwoller,* 2002] (c).

As geodynamic implications, we suggest that the low-velocity zone in the southwestern flank of the rift system, which is imaged in the PASSCAL_1992 data to border the steep southern craton edge, may be produced by a mantle flow that rises from beneath the craton.

The MOBAL_2003 velocity pattern over the 600-km depth section, with a branching low-velocity anomaly, fits the plume hypothesis assuming the shallow plume geometry to be controlled by mantle interaction with fluids. Fluids may create conditions for large-scale melting above 200 km (*Letnikov*, 2006) producing hot buoyant material that impinges on the lithospheric base and isostatically maintains the topographic high of the Hangay.

Thus, it is becoming evident that the distant effect from the India-Eurasia collision, hardly could exert major control of Cenozoic rifting in the Baikal region. One possible agent maintaining the Cenozoic mountain growth and rifting in the area is heat and fluids transport associated with the upwelling mantle flow from under the low permeable craton and plume-related fluids percolating through faults in the lithosphere [*Mordvinova et al.,* 2010].

References

Aki K., Christofferson A. and Husebye E. Determination of three-dimensional seismic structure of the lithosphere // J. Geophys. Res., 82, 277–296.

Bijwaard, H., Spakman, W., Engdahl, E.R. Closing gap between regional and globel travel time tomography // J. Geophys. Res., 1998. 103, 30055 – 30078.

Burkholder P.D., Meyer R.P., Delitsin L.L., Davis P.M., Zorin Yu.A. A teleseismic tomography image of the upper mantle beneath the southern Baikal rift zone // Preceeding to IUGG XXI General Assembly. Boulder, 1995. P. 400.

Emmerson B., Jackson J., McKenzie D., Priestley K. Seismicity, structure and rheology of the lithosphere in the lake Baikal region // Geophys. J. Int., 2006. 167, 1233–1272. doi:10.1111/j.1365–246X.2006.03075.x.

Gao S.S., Liu K.H., Davis P.M., Slack P.D., Zorin Y.A., Mordvinova V.V., Kozhevnikov V.M. Evidence for small–scale mantle convection in the upper mantle beneath the Baikal rift zone // J. Geophys. Res., 2003. 108(B4). 2194, doi:10.1029/2002JB002039.

Logatchev, N. & Florensov, N. The Baikal system of rift valleys // Tectonophysics, 1978. 45(1), 1–13.

Letnikov F.A., 2006. Fluid regime of the endogenous processes and the ore genesis problems. Russian Geology and Geophysics, 47, (12).

Mordvinova V.V., Deschamps A., Dugarmaa T., et al., Devershere J., Ulziibat M., Artemyev A.A., Sankov V.A., Perro J. Velocity structure of the lithosphere on the 2003 Mongolian-Baikal transect from SV waves // Izvestia Phys. Solid Earth, 2007. 43 (2).

Mordvinova V.V., Treussov A.V., Sharova E.V., Anan'in L.V. Teleseismical P-tomography beneath the Southern Siberia and Mongolia / Geodinamical evolution of the Central Asia mobile belt lithosphere(proceedings), Irkutsk, 2009. 7(2), 25–27.

Mordvinova V., Treussov A., Tiberi C., Barruol G., Déverchère J., Deschamps 2D P-teleseismic tomography in Southern Siberia and Mongolia: evidence for upwelling mantle flows / Abstract book of Europian Seismological Comission 32nd General Assembly (Montpellier, France), 2010. P. 182.

Shapiro N. M., Ritzwoller M.H. Monte–Carlo inversion for a global shear–velocity model of the crust and upper mantle // Geophys. J. Int., 2002. 151, 88–105.

Tiberi C., Diament M., De´verche`re J., Petit–Mariani C., Mikhailov V., Tikhotsky S., Achauer U. Deep structure of the Baikal rift zone revealed by joint inversion of gravity and seismology // J. Geophys. Res., 2003. V. 108. B3. 2133, 10.1029/2002JB001880.

Tiberi C., Deschamps A., Déverchère J., Petit C., Perrot J., Appriou D., Mordvinova V., Dugaarma T., Ulzibaat M., Artemiev A. Asthenospheric imprints on the lithosphere in Central Mongolia and southern Siberia from a joint inversion of gravity and seismology (MOBAL experiment) // Geophys. J. Intern., 2008. 175, 1283–1297. doi: 10.1111/j.1365–246X. 2008. 03947.x.

Zhao Dapeng. Global tomographic images of mantle plumes and subducting slabs: insight into deep Earth dynamics // Physics of the Earth and Planet. Inter., 2004. 146, 3–34.

Zhao D., Lei J., Inoue T., Yamada A., Gao S. Deep structure and origin of the Baikal rift zone // Earth and Planet. Science Lett., 2006. 243, 681–691.

Zorin Yu.A., M.R. Novoselova, E.Kh. Turutanov and V.M. Kozhevnikov. Sructure of the lithosphere of the Mongolian-Siberian mountainous province // J. Geodinamics, 1990. 11, 327–342.

Zorin Yu.A., E.Kh. Turutanov, V.V. Mordvinova, V.M. Kozhevnikov, T.B. Yanovskaya, A.V. Treussov. The Baikal rift zone: the effect of mantle plumes on older structure // Tectonophysics, 2003. 371, 153–173.

3.5. The three-dimensional velocity structure of upper mantle beneath Central Asia from dispersion of Rayleigh wave phase velocities

V. M. Kozhevnikov, kozh@crust.irk.ru, **O. A. Solovei.** *The Earth's Crust SB RAS, Lermontov st., 128, Irkutsk, 664033, Russia*.

The 3D upper mantle structure beneath Central Asia has been imaged by means of Rayleigh surface-wave tomography using LHZ data of broadband digital GSN stations of the Asian IRIS network.

The Rayleigh phase velocities were calculated within interstation seismic paths, with input wave data of $M \geq 6.0$ earthquakes that occurred mostly at teleseismic distances within basins and islands of the Pacific, Indian and Atlantic oceans, as well as in near-shore areas of North, South, and Central America. The events were selected proceeding from the criteria of (i) being proximal to the great circle arcs across the station pairs and (ii) having the epicentral distance difference between the station pairs commensurate with the station spacing. The epicentral distances in our case varied from 7000 to 15,000 km, and the mantle was imaged to depths about 600-650 km, correspondingly.

The phase velocities were estimated using the frequency- time analysis (FTAN) which is an analog of multichannel narrow-band filtering [*Levshin*, 1972]. With this method, one can calculate the dispersion curves of group velocities directly from input data and find the respective surface-wave modes in the pure form. See **Fig.3.5.1** for an example of such FTAN calculation.

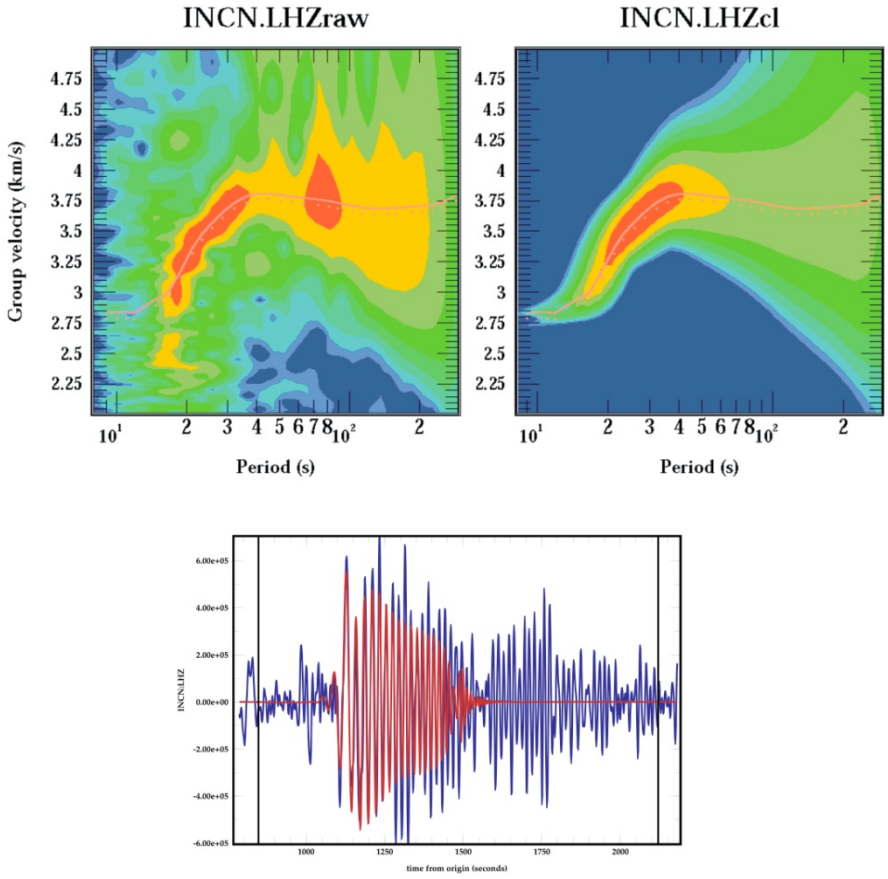

Fig.3.5.1. An example of FTAN processing of Rayleigh wave data from station INCN (South Korea). The upper panels show a FTAN diagram corresponding to raw (left) and filtered (right) data. Red lines are dispersion curves of group velocities. The panel below is the original seismogram (blue) and the Rayleigh main mode (red) obtained by filtering.

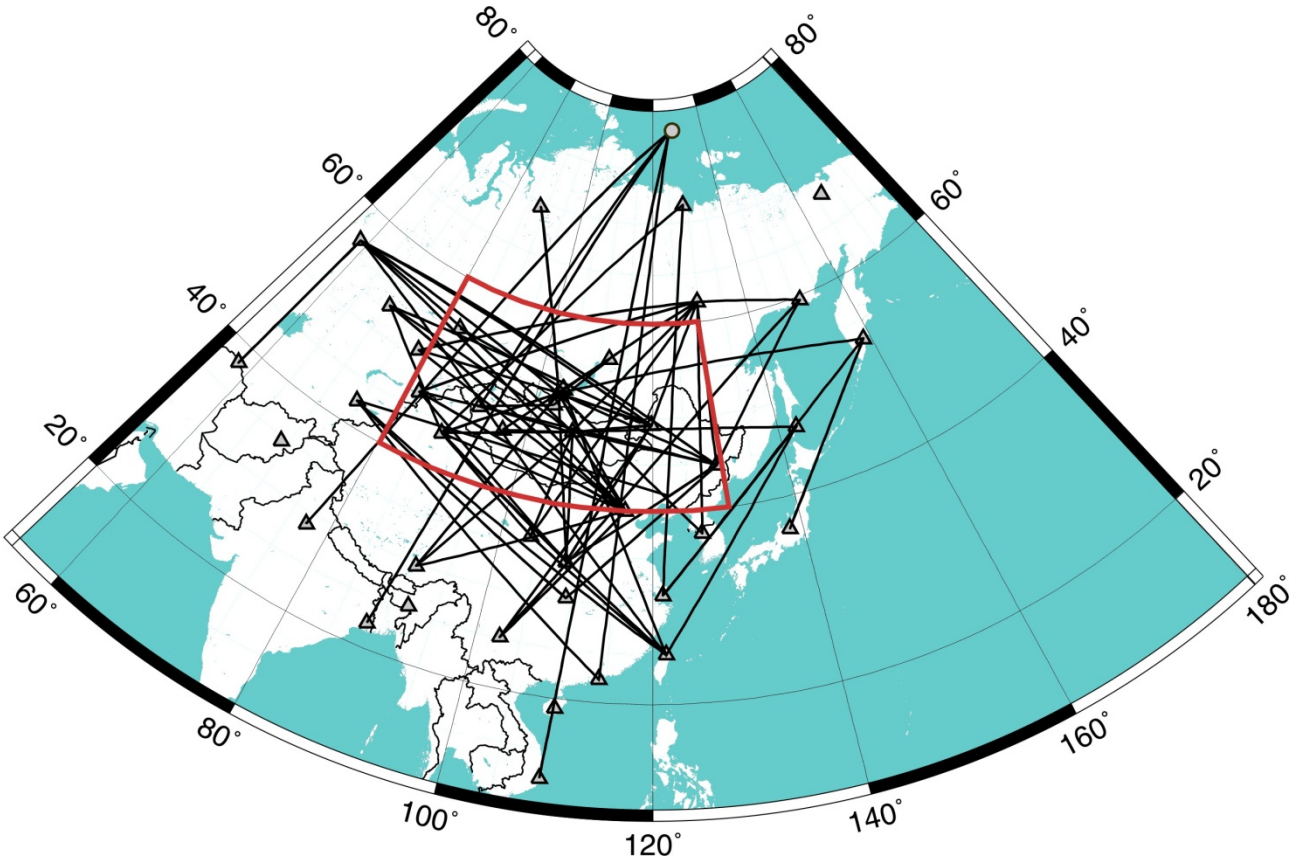

Fig.3.5.2. Locations of interstation seismic paths. Red box frames the area where the 3D shear-wave velocity structure of upper mantle was imaged.

Interstation phase velocities corresponding to the chosen frequency ω_j were calculated as follows. First FTAN was applied to obtain main Rayleigh modes filtered from noise for events recorded at both stations. Then the signals $Y_1(t_i,\omega_j)$ and $Y_2(t_i,\omega_j)$ were presented in 2D in the coordinates of frequency and time for the selected station pairs. That made basis for calculating the phase spectra $\arg[Y_1(t'_i,\omega_j)]$ and $\arg[Y_2(t''_i,\omega_j)]$ for each frequency ω_j and the times t'_i and t''_i , at points that corresponded to peaks in the FTAN diagrams and to the same mode (filtered dispersion of Rayleigh group velocities in that case). Then, the phase velocity between stations 1 and 2, for the frequency ω_j, is given by

$$C(\omega_j) = \frac{\omega_j \times (\Delta_2 - \Delta_1)}{\omega_j \times (t_i'' - t'_i) + \arg[Y_1(t'_i, \omega_j)] - \arg[Y_2(t_i'', \omega_j)] \pm 2\pi N},$$

where Δ_1 and Δ_2 are the epicentral distances to the stations 1 and 2, at $\Delta_2 > \Delta_1$.

Thus we obtained a sample of 198 dispersion curves for 51 interstation seismic paths (**Fig.3.5.2**). The results for each pair were checked for reproducibility through calculating several dispersion curves for events on both sides of the interstation profile, with subsequent averaging and phase velocity correction (**Fig.3.5.3**).

The obtained phase velocity dispersion curves were used for reference in inversion in order to obtain a 3D surface-wave tomographic image of the Asian upper mantle. The inversion method we used is based on solving the 2D tomography problem for a spherical surface and gives the 3D velocity structure from group or phase velocities; the resolution in it can be checked by calculating the effective averaging radius [*Yanovskaya*, 2001; *Yanovskaya*, 2003].

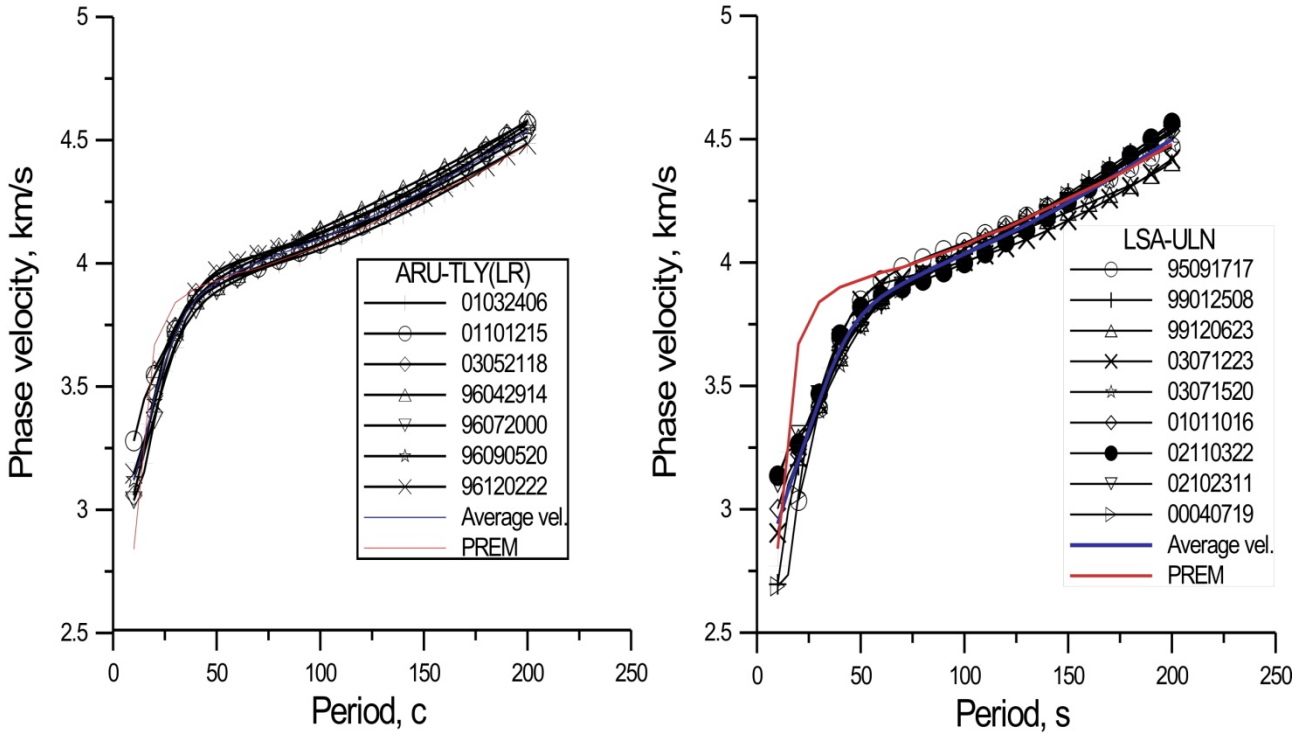

Fig.3.5.3. Example phase velocity dispersion curves for station pairs Arti – Talaya (ARU-TLY) and Lhasa – Ulaan-Baatar (LSA-ULN). Numerals in legend are dates and origin times of earthquakes (year, month, day, hour). Dark blue lines are averaged dispersion curves with velocity errors; red line is dispersion curve obtained from the parameters of the standard Dziewonski-Andersen PREM model.

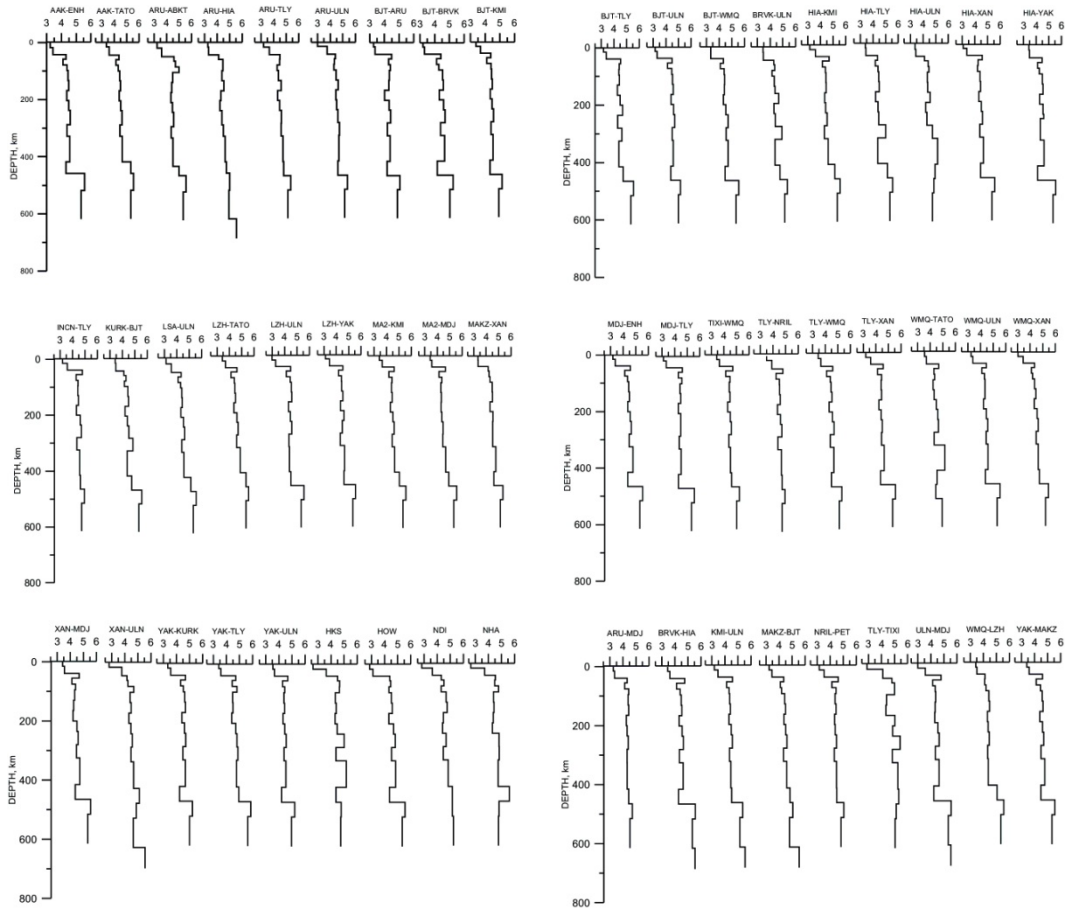

Fig.3.5.4. S-wave velocity profiles that represent the integral mantle structure of each interstation seismic path.

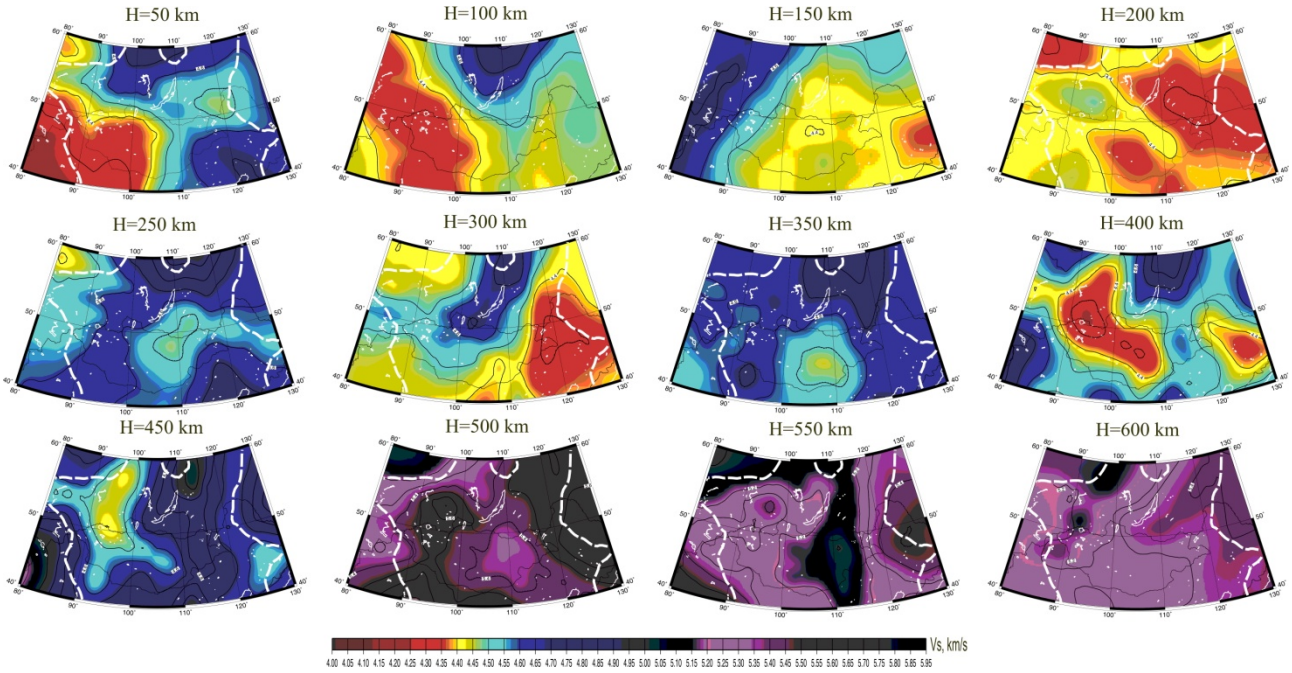

Fig.3.5.5. S-wave velocity patterns in Central Asian upper mantle. H - are the depths of spherical surfaces for which the respective maps were calculated. White dashed line contours domains of reliable mapping results.

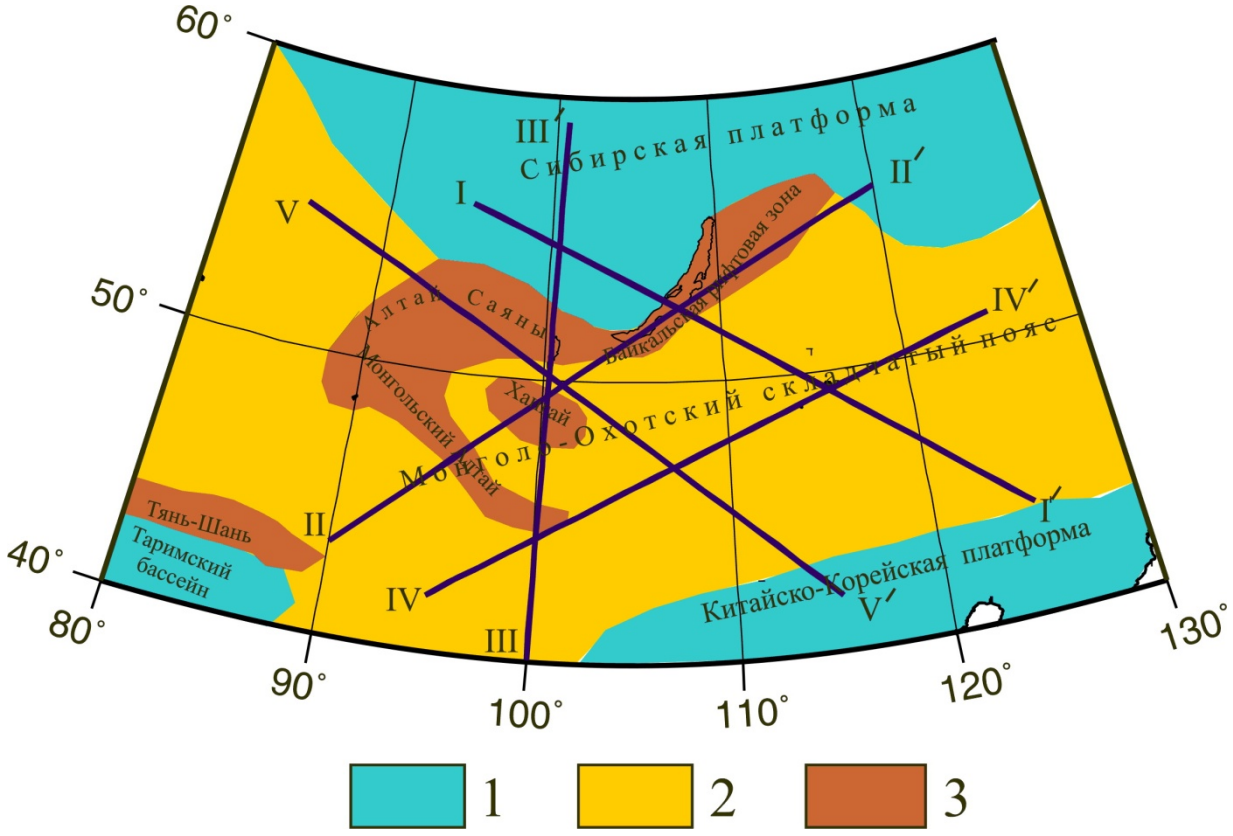

Fig.3.5.6. Locations of seismic profiles (black lines) along which 2D shear-wave cross sections (**Fig.3.5.7**) were obtained. 1 are platforms areas; 2 and 3 are structures of Mongolia-Okhotsk foldbelt, including zones of current rapid mountain growth (3).

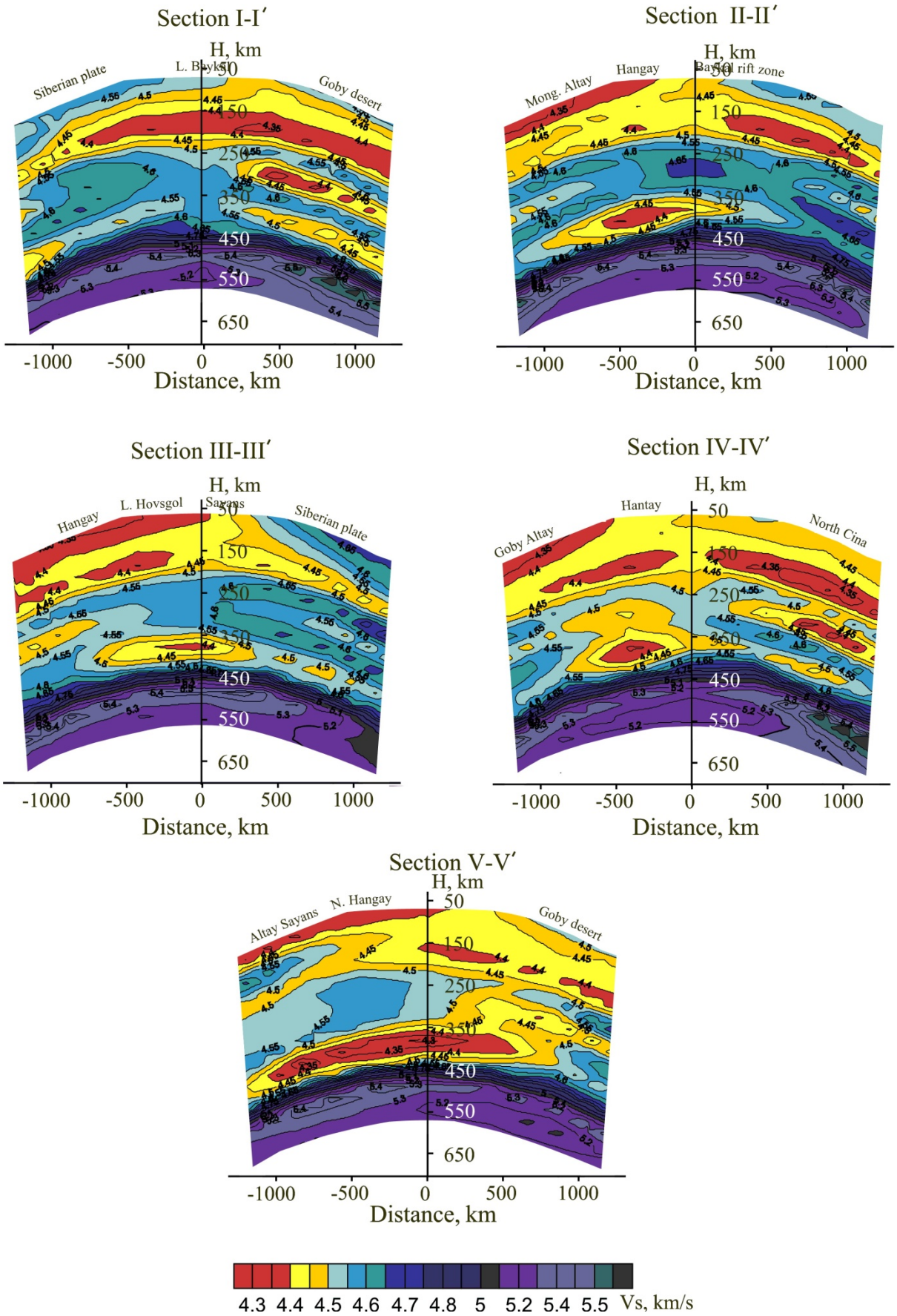

Fig.3.5.7. 2D shear-wave velocity cross sections along profiles of **Fig.3.5.6.**

In the course of 3D mantle structure imaging from phase velocity dispersion, the shear-wave maps were obtained using a special approach because of a limited number of interstation seismic paths. According to this approach, the S-wave velocity profiles which represented an integral mantle structure along the respective paths were calculated for each dispersion curve (**Fig.3.5.4**), and then the velocity curves at given depths within the modeling domain were modeled with the method of surface-wave tomography for spherical surfaces. Altogether we obtained 12 maps of S-wave velocities (**Fig.3.5.5**) at every 50 km between 50 and 600 km depths and 2D velocity sections (**Fig.3.5.6, 3.5.7**) across main tectonic units of the area. The mapping resolution was evaluated in order to specify the limits of the domain where the solutions were accessible, and that domain was assumed to follow the contour line R=1000 km. These limits turned out to include only the best-coverage areas of Central Asia, namely, the eastern and southeastern margins and the central part of the Siberian platform, and the Mongolia-Okhotsk orogen. In the latter they were zones of rapid current mountain growth in southern Siberia and western Mongolia, the zone of slow mountain building in central Mongolia, the Baikal rift zone, and some subplatform areas of Transbaikalia and North China.

As a result, we have imaged the three-dimensional S-wave velocity structure of the upper mantle beneath the main tectonic units of Central Asia from dispersion of Rayleigh phase velocities and arrived at the following inferences [*Kozhevnikov*, 2010].

(1) The upper mantle beneath Central Asia includes large-scale horizontal inhomogeneities as alternating low- and high-velocity zones (layers and lenses) throughout the depth interval to about 400 km.
(2) The lithospheric thickness between different tectonic domains varies broadly from 200-250 km beneath the Siberian craton to ~70 km under areas of current mountain growth in southern Siberia and western Mongolia, and to 100-150 km beneath the Mongolia-Okhotsk belt.
(3) The structures of the Mongolia-Okhotsk belt differ from the Siberian craton in a more developed asthenospheric conduit which is 80-100 km thick beneath the former and about 50 km beneath the craton interior, the lower asthenospheric boundary being at the same depth of ~200 km.

References

Kozhevnikov, V.M., Solovei, O.A., 2010. The 3D mantle structure of Central Asia from dispersion of Rayleigh phase velocities. Vulkanologiya i Seismologiya No. 4, 30-39.

Levshin, A.L., Pisarenko, V.F., Pogrebinsky, G.A., 1972. On a frequency-time analysis of oscillations. Ann. Geophys. 28, 211-218.

Yanovskaya, T.B., 2001. Solving surface-wave tomography problems using the Backus-Gilbert method. Vychislitel'naya Seismologiya Issue 32, 11-26.

Yanovskaya, T.B., Kozhevnikov, V.M., 2003. 3D S-wave velocity pattern in the upper mantle beneath the continent of Asia from Rayleigh wave data. Phys. Earth and Planet. Inter. 138, 263-278.

3.6. Developing of Microseismic sounding Method

A. V. Gorbatikov, avgor70@mail.ru, *O. Yu. Shmidt Institute of Physics of the Earth RAS, B. Grusinskaya st., 10, Moscow, 123995, GSP-5, Russia*.

A microseismic sounding method utilizing of the Rayleigh wave field near the scattering heterogeneities of wavelengths of the same or smaller size was recently developed in the Institute of Physics of the Earth RAS. Initially it was developed as phenomenological and it's phenomenological and experimental validation on test geological objects has been carried out in [*Gorbatikov et al.,* 2008]. The method is based on using the natural microseismic field whose vertical component is mainly determined by the superimposition of the surface Rayleigh wave trains. A simple procedure was proposed for the inversion of the spatial distribution of the measured amplitude of the microseismic

field into the depth section of the medium. This procedure is based on general physical knowledge and verified in a series of test field experiments.

The algorithm of the microseismic sounding method

The phenomenological method of microseismic sounding using the Rayleigh waves is based on the fact that the crustal heterogeneities distort the spectrum of the low frequency microseismic field in the vicinity of the object. Namely, the spectral amplitudes on the Earth's surface at a certain frequency f decrease above high velocity heterogeneities and increase above low velocity objects. The frequency f is related to the depth of the heterogeneity H and the velocity of the fundamental mode Rayleigh wave by the formula $H = KV_R(f)/f$, where K is the numerical coefficient. The method is implemented under a reasonable assumption that the vertical component of the microseismic field is predominantly determined by the contribution of the fundamental Rayleigh modes. The measurement and processing technology includes the following steps.

1) Successive measurements of statistically stable spectra of microseisms in all points of a grid or profile. In order to ensure statistical stability, the microseismic signal is accumulated during the experimentally determined period of signal stationarity (about two hours) [*Gorbatikov and Stepanova*, 2008].

2) Construction of maps or profiles reflecting the distribution of microseismic amplitudes for each spectral frequency.

3) Depth referencing of the obtained map or profile according to the relation

$H(f) = K\lambda(f) = KV_R(f)f$, where $H(f)$ is the depth of the layer for which the image is being constructed; is the wavelength of the fundamental mode Rayleigh wave; is the velocity of the fundamental mode Rayleigh wave at a frequency f; f is the frequency of the microseismic signal for which the calculations are to be conducted; the numerical coefficient K is 0.4–0.5 according to the experimental estimates.

Processing of the data and imaging of the deep structure are as follows. For each frequency f of the spectrum, a spatial profile (map) of the distribution of the variations in the intensity of the microseismic signal is constructed. This profile (map) is tied to depth. Based on the distributions of variations in the intensity, a surface (3D image) is constructed in the coordinates with the horizontal axes being the spatial coordinates and the vertical axis being the depth. The distribution of the intensity variations is determined with respect to the base station that is usually located close to the profile and remains at the same place during the entire measurement cycle. The signals are recorded at the points of the profile (array) by the mobile stations simultaneously with measurements at the base station.

Misroseismic signal properties

The microseismic field is dual in its nature. On the one hand, this field is represented by interference of seismic waves of various types whose propagation mechanism has been well studied. The waves travel as separate trains of a finite length and, within this time interval, realize a deterministic process at each surface point. On the other hand, an observer does not know a priori the relative content of each type of waves, as well as their amplitudes, initial phases, and train lengths. The random nature of these and other parameters makes the microseismic vibration at each point a random process characterized by experimentally determined statistical properties.

Presently, researchers acknowledge a few mechanisms of generation of microseisms, namely, (1) the surf impact, (2) transmission of pressure variations through water to the seafloor with subsequent pressure propagation across a continent, and (3) transmission of pressure variations directly to a solid surface. Pressure variations can be due to the wind effect on the ocean surface and development of swell, the direct impact of variations in the atmospheric pressure on water and land surfaces at centers of large atmospheric vortices, and the generation of internal gravitational waves in oceanic water in regions with an extended shelf.

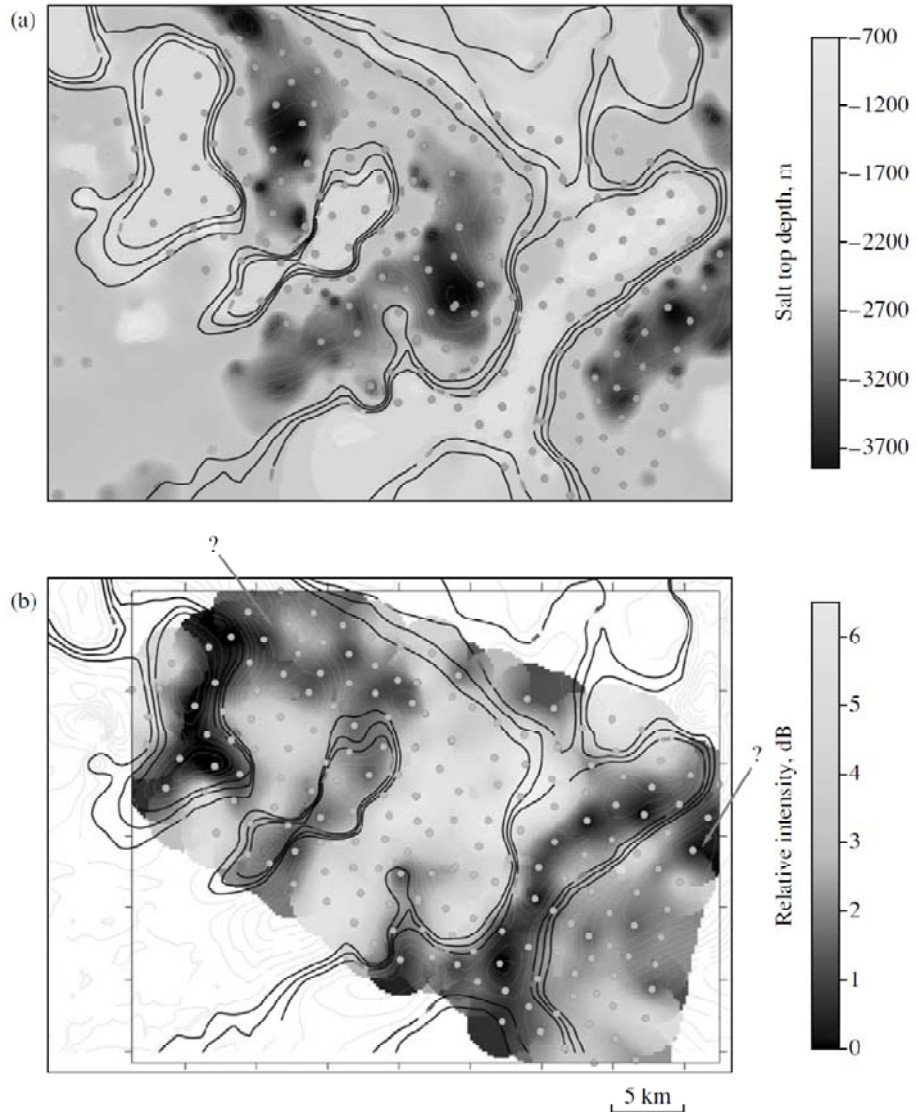

Fig.3.6.1. (a) Schematic map of the roof of salt deposits from data of drilling in the Astrakhan gas condensate deposit. Contours are depth isohypses of 1500, 1750, and 2000 m. (b) Schematic map showing the experimental spatial distribution of the relative intensity of the microseismic signal for the spectral frequency $f = 0.235$ Hz. The gray circles show points of microseismic measurements.

In situ verification of microsesmic sounding phenomenological technique

An testing experiment was planned in which a benchmark heterogeneity was represented by the system of salt domes of the Astrakhan gas condensate field in the Caspian sedimentary basin [*Gorbatikov et al.,* 2008]. This area has been well studied by various geophysical methods, including detailed drilling exploration. The research area has approximate sizes of 40 × 20 km 2 and lies above the Lesser Aral salt dome, which together with the Aksarai and Utigen salt domes forms a salt wall with an elbow-shaped bend and the Aksarai and Southern interdome troughs. The top depth of the salt domes is ~700 m, and they extend downward to depths of about 3800 m. The structural layer overlying salt is composed of two rock complexes aged Triassic– Paleogene and Neogene–Quaternary. The interdome troughs are compensatory structures; have elongated rounded structural shapes; and are composed of Triassic, Jurassic, Cretaceous, and Paleogene deposits. The troughs are distinguished by steep slopes and a sharply decreased thickness of salt-bearing deposits. The intrusion of salt masses into the overlying rock mass fractured the latter, particularly in near-dome zones.

The field works were performed in 2004 and 2005. The deposit area and a part of the adjacent territory were covered by a measuring network consisting of 200 points spaced on average at 2–2.5 km. The measurements were made according to the principle “point after point” with the correction for the reference station. **Fig.3.6.1a** presents a map of the surface of salt deposits obtained from drilling

data. Results of mapping the microseismic field are shown in **Fig.3.6.1b**. Lighter shades here correspond to larger intensities of vibrations, and vice versa. The spectral frequency for which the intensity map of microseismic signals is presented was chosen from the comparison of several maps constructed for different frequencies. It found that the map constructed for f = 0.235 Hz fits best the real configuration of the salt deposits. Taking the Rayleigh wave velocity V_R = 1000 m/s, known characteristic of rocks filling the troughs, and using the relation H=0.5λ, we could estimate the depth of the layer responsible for the formation of the resulting microseismic pattern. We obtained a depth of ~2 km, agreeing well with the real depth of the salt structures within the zone studied.

We can note a good coincidence of the patterns outlined by isohypses and microseismic intensity contours for f = 0.235 Hz, which confirms the hypothesis about the character of the influence of deep heterogeneities on the surface microseismic field. Namely, heterogeneities with higher seismic velocities are observed in the surface microseismic field above them as zones of lower amplitudes and, vice versa, lower velocity heterogeneities are observed as zones of higher amplitudes.

Numerical modeling

Until recent time an actual question remained about the method possible accuracy for the resulting relative velocity pattern and about method resolving capacity. Main difficulties were connected with solution of direct 3-D problem about Rayleigh surface wave propagation complicated by interacting with small size deepened velocity inclusions whose sizes are compared with the wavelength. From one side this problem has no analytic solution. From the other side our several separate successes obtained in 2-D modeling didn't describe many of diffraction phenomena having place in 3-D space. Using only 2-D models one cannot also estimate the superposing effect from many signal sources distributed along the surface which has place while forming the real microseismic field in nature.

To solve the problem in general case we should resort to numerical calculations and conduct a number of numerical experiments in order to establish the forms in dependencies of wave field properties on heterogeneity properties and wavelength. We realized a parallel algorithm using mixed explicit-implicit scheme for finite differences method for solution of the problem about dynamics of elastic heterogeneous half-space with a free surface. Solution for the points on the free surface we found in implicit way utilizing a parallel LUP factorization algorithm adopted for solution of sparse systems of high order. Grid of spatial points was distributed by equivalent size blocks along calculating nodes of the cluster and was processed with explicit scheme. The parallel program complex created during the job advancement utilizes the MPI technology and means to be run on multiprocessor computers with distributed memory [*Gorbatikov and Tsukanov*, 2011].

We have studied the total vector field of oscillations in the near zone of the scattering heterogeneity (**see Fig.3.6.2a,b; Fig.3.6.3; Fig.3.6.4**). The obtained results can be expanded onto a broad class of real geological structures; the validity of such an expansion is supported by numerous field experiments. Using the numerical modeling, we have analyzed a series of regularities in the fundamental mode Rayleigh wave interacting with buried inclusions of different sizes and different velocity contrasts. Our results validate the application of the microseismic sounding technique for the assessment of the structure of a medium that had been previously based exclusively on experimental observations and was thus purely phenomenological.

From results of the modeling we can follow an interesting analogy: the microseismic sounding method relates to the surface wave tomography in the same manner as the seismic reflection technique relates to the refraction technique in seismic prospecting. Based on the results of numerical experiments, we estimated the accuracy and resolution of the method of microseismic sounding. It was shown that two small heterogeneities located at the same depth are horizontally resolved (distinguished as separate structures) when the distance between them is larger than (0.25–0.3)λ, where λ is the effective wavelength (for the given depth). A similar spacing for the vertical resolution is estimated as (0.3–0.5)λ, where λ is the effective wave length for the midpoint between the inclusions. Numerical simulations showed that in the case of distributed sources, small isolated heterogeneities can be identified in the wave field with wavelengths far in excess of the dimensions of the inclusions. In the

ideal conditions of measurement, the horizontal positions of the centers of these objects and the locations of the vertical boundaries of large heterogeneities can be determined exactly. The vertical accuracy is defined by the velocity model applied and is liable to uncertainties because of the coefficient of the depth adjustment. The value of this coefficient depends, inter alia, on the velocity contrast between the inclusion and the host medium. The relationship between the velocity model and the coefficient K in the method of microseismic sounding is assumed to be described by the formula $H = KV_R(f)$, where H is the depth of the heterogeneity, f is frequency, $V_R(f)$ is the dispersion dependency that can be obtained in practice using one of the methods of the surface wave tomography. Therefore, as in the seismic reflection techniques, the accuracy of microseismic sounding in the determination of the vertical location of real objects is to a large extent governed by a priori geological and geophysical information.

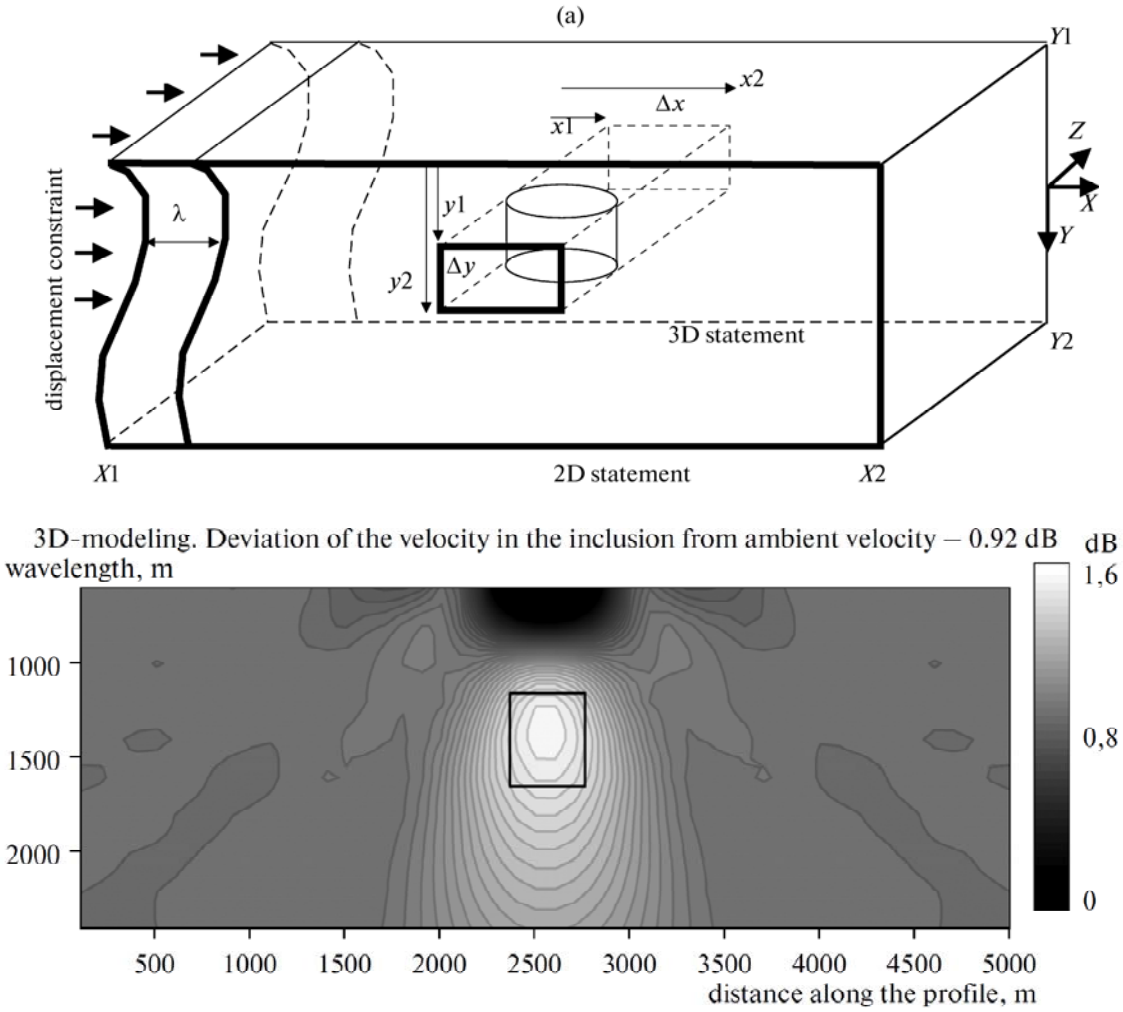

Fig.3.6.2. A scheme illustrating the statement of the problem (a) and the results of the calculation for 3D model (b). Panel (b) displays the results of the combined solution of the inverse and direct problem according to the method of microseismic sounding. The results are presented in the form of distributions of the surface waves' intensity in the "wavelength – distance along profile" coordinates. The rectangular contour outlines the position (in the mentioned coordinates) of the given heterogeneity calculated with K=0.4.

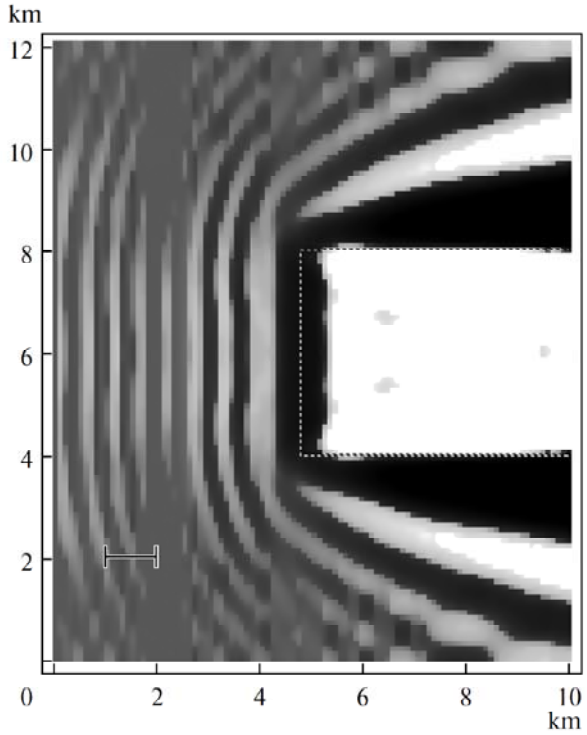

Fig.3.6.3. A section of the surface formed by the variations in the wave field intensity in the case of a large low velocity inclusion illuminated by a plane monochromatic Rayleigh wave. The dashed line outlines the surface projection of the heterogeneity. The wavelength of the sounding wave (1 km) is shown by a line segment. The shown section corresponds to a level of 0 dB.

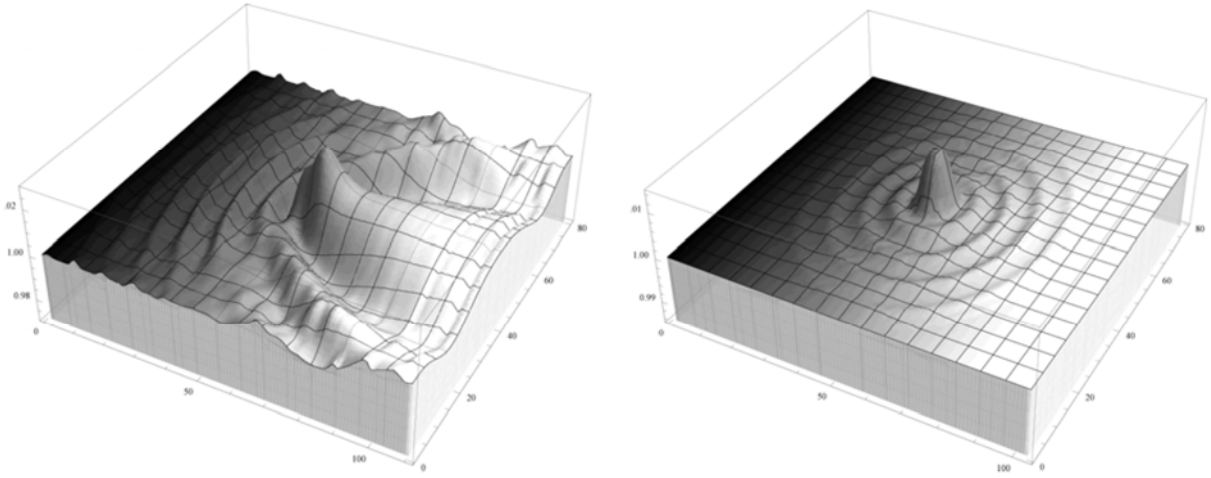

Fig.3.6.4. Comparison between amplitude distributions for small deepened inclusion in the field of surface Rayleigh waves. The left figure exhibits a case of exposing from one side; the right figure when exposing by many sources homogeneously distributed on the surface from all the sides.

References:

Gorbatikov A.V. and Stepanova M.Yu. Statistical Characteristics and Stationarity Properties of Low-Frequency Seismic Signals, Izvestiya, Physics of the Solid Earth, 2008, Vol. 44, # 1, pp.50–59. © Pleiades Publishing, Ltd., 2008., Original Russian Text published in Fizika Zemli, 2008, # 1, pp.57–67.

Gorbatikov A.V., Stepanova M.Yu., and Korablev G.E. Microseismic Field Affected by Local Geological Heterogeneities and Microseismic Sounding of the Medium, Izvestiya, Physics of

the Solid Earth, 2008, Vol. 44, # 7, pp.577–592. © Pleiades Publishing, Ltd., 2008. Original Russian Text published in Fizika Zemli, 2008, # 7, pp.66–84.

Gorbatikov A.V. and Tsukanov A.A. Simulation of the Rayleigh Waves in the Proximity of the Scattering Velocity Heterogeneities. Exploring the Capabilities of the Microseismic Sounding Method, Izvestiya, Physics of the Solid Earth, 2011, Vol. 47, # 4, pp.354–369. © Pleiades Publishing, Ltd., 2011. Original Russian Text published in Fizika Zemli, 2011, # 4, pp.96–112.

4. Seismogeodynamics

4.1. Seismogeodynamics and seismic hazard prediction

V. I. Ulomov, ulomov@ifz.ru**.** *Schmidt Institute of the Physics of the Earth RAS. B. Gruzinskaya, 10. Moscow 123995, GSP-5, Russia.*

4.1.1. Introduction

Beginning in 2010 was marked by a number of natural disasters on a global scale. One after another powerful earthquake in the Solomon Islands (January 3), Haiti (January 12), off the coast of Chile (27 February), on the border of California and Mexico (April 4), China (April 13). Apogee were two very powerful volcanic eruptions. The largest over the past half-century eruption in Chile. Giant eruptions in Iceland suspended for several days, the aviation industry in many countries.

A powerful earthquake struck Haiti on Jan. 12, 2010. His moment magnitude of Mw=7.1. Almost completely destroyed the city of Port-au-Prince - the capital and main port of Haiti. Under the ruins of the city literally disappeared into densely populated neighborhoods. Killed over 270,000 people. Millions of people were left homeless.

One of the largest earthquakes in the past half century occurred off the coast of Chile on Feb. 27, 2010. It had a magnitude of Mw=8.8, accompanied by a tsunami and led to numerous casualties and destruction. Its epicenter was 90 kilometers from the capital of the Bio-Bio Concepcion, the second largest city in the country after Santiago. Magnitude of the strongest aftershocks reached Mw=8.0. The death toll from the tsunami was minimal, since most of the inhabitants managed to escape the coast in the mountains. The earthquake on Feb. 27, 2010 was the largest after the Chilean earthquake of May 22, 1960 with Mw=9.5, occurred at 230 km to the south.

Extremely strong earthquakes continue as at present. The author shows that this global seismogeodynamic activation is not accidental [*Ulomov*, 2007, 2010]. It is also reported of the prediction of strong earthquakes in the North Caucasus [*Ulomov*, 2006].

4.1.2. On the variation of global seismogeodynamics

The results obtained by the author are based on the study of the Earth's seismogeodynamic regime according to which the flow of seismic events is analyzed not integrally but in magnitude intervals reflecting the geodynamics of the hierarchical fault–block structure of the geological medium.

In this section of the report the sequences of large earthquakes that occurred throughout the Earth in the period from January 1996 to May 2010 were the subject of study. These earthquakes were differentiated in the magnitude intervals M=8.5±0.2, M=8.0±0.2, M=7.5±0.2 and M=7.0±0.2, completely overlapping a wide energy range, from M=6.8 to M=8.7. The last interval also included several large earthquakes of M≥8.8. (Further all of the magnitude of M correspond to Ms.).

Fig.4.1.1 shows the position of all seismic sources. Red painted sources, located at the depth of 70 km or less; blue color shows the sources deeper 70 km. These earthquake sources coincide with zones of subduction. Date of show only those earthquakes that are cited in the text. Open circles delineated foci of earthquakes in Alaska (1964) and Chile (1960). Thin red lines - the boundaries between lithospheric plates.

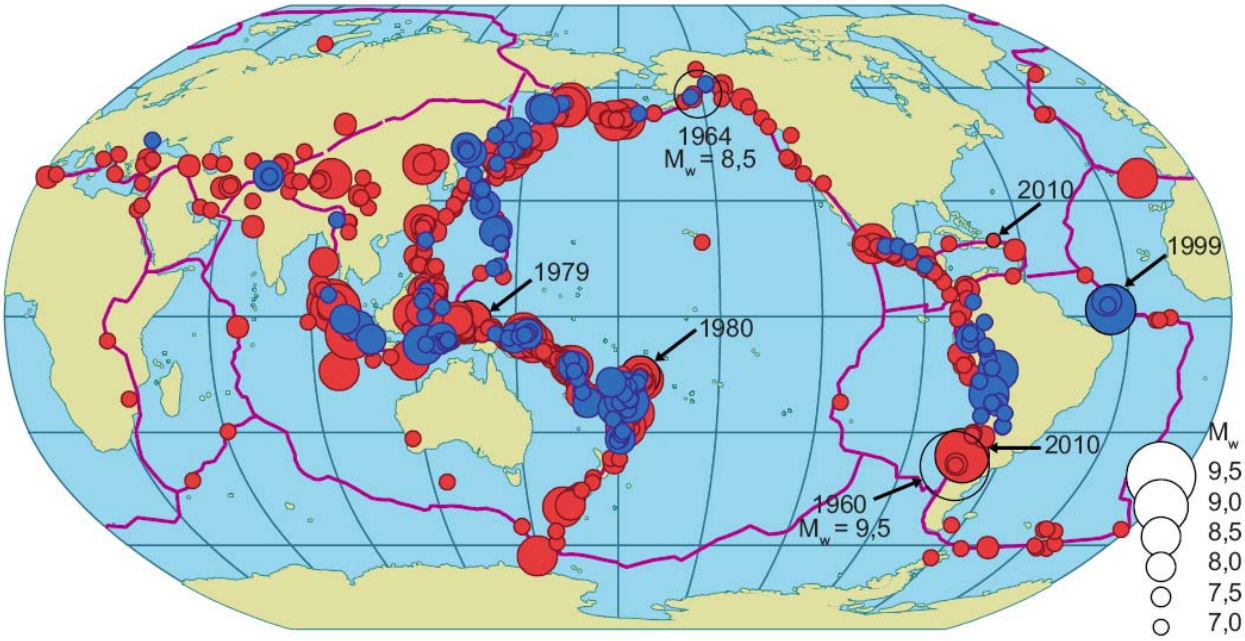

Fig.4.1.1. The epicenters of major earthquakes of the Earth for the period from January 1996 to May 2010. Scale of earthquake magnitude is shown at the bottom to the right [*Ulomov*, 2010].

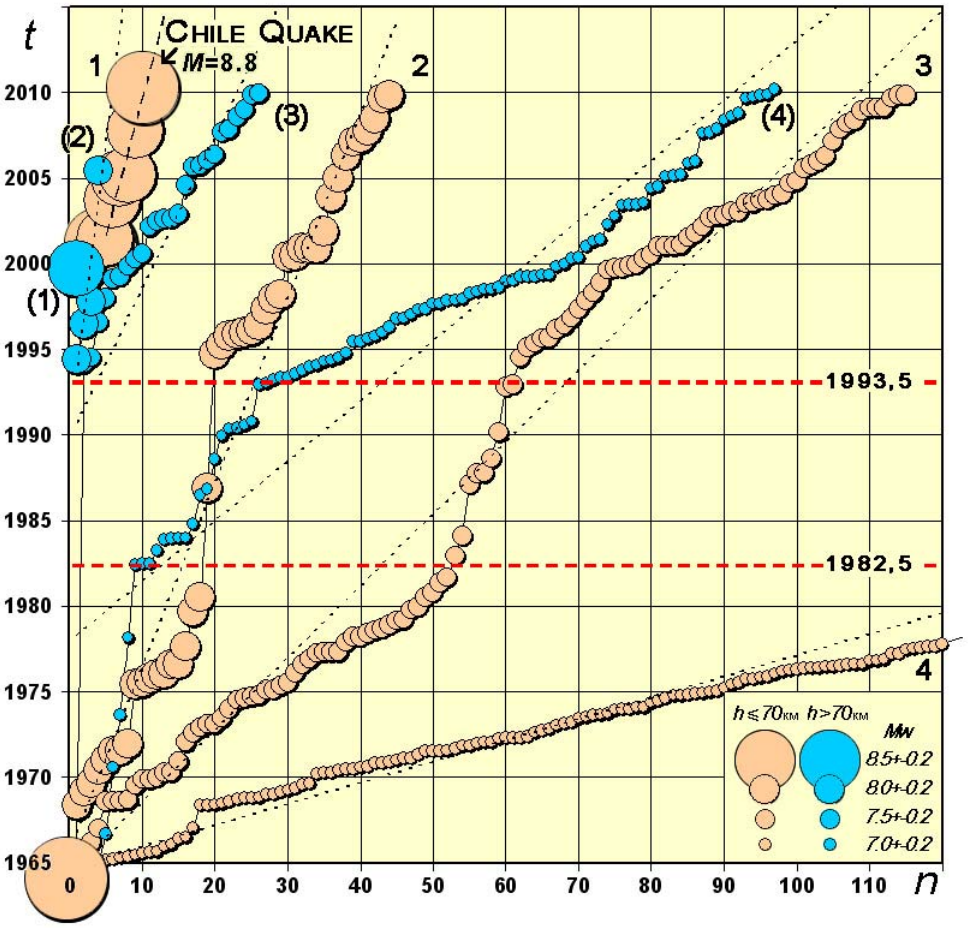

Fig.4.1.2. Cumulative plots of the accumulation of global seismic events with the magnitudes 8.5±0.2, 8.0±0.2, 7.5±0.2, and 7.0±0.2 that occurred in the period from January 1996 to May 2010 [*Ulomov*, 2010]: 1–4 - linear approximation of the occurrence times of earthquakes with hypocenters no deeper than h=70 km; (1) – (4) the same for seismic events with hypocenters at depths h>70 km.

Cumulative plots characterizing the accumulation rate of seismic events all over the Earth in the studied magnitude intervals are presented in **Fig.4.1.2**. It should be noted that this figure, as in **Fig.4.1.1**, borrowed from the paper, which was submitted for the publication in 2007 and in this article is completed until May 2010 [*Ulomov*, 2007, 2010].

In **Fig.4.1.2** the cumulative number of earthquakes and the years of their occurrence are plotted on the abscissa and ordinate axes, respectively. Events with hypocenters in the depth ranges h≤70 km (shallow events) and h>70 km (deep events) are shown by rose and blue color circles, respectively. The linear approximations (dotted lines) are actually everywhere characterized by the high correlation coefficient (0.9 or higher)

Because of a very large number of shallow earthquakes with M=7.0 ±0.2, only the fragment of the corresponding plot is presented in the inset in **Fig.4.1.2** (line 4).

The slopes of the approximating lines characterize the accumulation rates of seismic events of the corresponding magnitudes: the smaller the slope of a line, the higher the rate. A steepness increase reflects a decrease in the recurrence rate of earthquakes. If earthquakes occurred rhythmically, i.e., with the same frequency in each sequence, all their occurrence times, in particular, during the entire period under consideration, would lie exactly on straight lines. However, in reality, deviations from this pattern are caused by a nonlinear development of seismogeodynamic processes affecting the stress–strain state of the medium and, accordingly, seismicity manifestations.

Analysis of the configurations of the cumulative plots revealed an interesting phenomenon reflecting specific features of the temporal evolution of global seismogeodynamic processes. First of all, we mean a substantial slowdown in the recurrence of all shallow earthquakes during the approximately 11-yr time interval (from the middle of 1982 through the middle of 1993) bounded by the horizontal dashed lines in **Fig.4.1.2**. As is seen from the figure, the accumulation rates of events in the considered magnitude intervals change rather rapidly, which is expressed in abrupt bends in all plots at the ends of the anomalous interval (1982.5–1993.5). However, before and after there veiled relative seismic quiescence, the occurrence frequency of shallow earthquakes not only was substantially higher but also was characterized by virtually the same accumulation rate of seismic events.

In order to compare the occurrence frequencies of earthquakes within the magnitude ranges under consideration, the numbers of events in 11-yr time intervals before (1971.5–1982.5), during (1982.5–1993.5), and after (1993.5–2005.5) the seismic quiescence are given in the **Table 4.1.1**.

Table 4.1.1

Hypocentral depths h≤70 km				
Y, годы	M=7.0±0.2	M=7.5±0.2	M=8.0±0.2	M=8.5±0.2
1993.5–2005.5	141	39	17	4
1982.5–1993.5	40	9	1	0
1971.5–1982.5	111	36	12	0
Hypocentral depths h>70 km				
1993.5–2005.5	53	12	4	1
1982.5–1993.5	22	0	0	0
1971.5–1982.5	2	0	0	0

In all cases, the time is measured from the middle of the year, as in the anomalous period of seismic quiescence. It is seen that, in the interval 1982.5–1993.5, earthquakes with M=7.0±0.2 and 7.5±0.2 occurred three to four times, and earthquakes with M=8.0±0.2 ten or more times, less frequently than in the preceding and subsequent 11-yr periods. The largest seismic events with M=8.5±0.2 and more, which were altogether absent during the first two intervals, started to occur nearly annually from 2001 through 2006. They included the catastrophic earthquakes of December 26, 2004, with M=8.8 and March 28, 2005, with M=8.5, which occurred off the Sumatra coast. The previous 1964 Alaska earthquake with M=8.5 was equally large, and the time interval under consideration began actually from this earthquake.

The fact that deep seismic activity began immediately after the general quiescence of the shallow seismicity is no less important (see **Fig. 4.1.2**). No earthquakes with magnitudes M=7.5±0.2 and higher were observed before this period, whereas twelve earthquakes with M=7.5±0.2, four earthquakes with M=8.0±0.2, and one earthquake with M=8.8 occurred in the conclusive time interval. The last earthquake was unique in its magnitude and occurred in the Atlantic Ocean at a depth of about 90 km off the eastern coast of South America (see **Fig.4.1.1**). However, earthquakes with M=7.0±0.2 occurred very seldom up to their conclusive active stage. Thus, while five such earthquakes occurred annually from the middle of 1993 and later, their recurrence rate in the period of seismic quiescence was lower by a factor of 2.5 (and before, even by a factor of 26.5).

It is noteworthy that during this same time period (1982.5-1993.5) were also found abnormal changes in global Ocean level. According to the author, these anomalies were caused by slow deformation of the oceanic lithosphere [*Ulomov*, 2007].

4.1.3. Reflection of the global seismicity at the regional level

No less remarkable that similar anomalies in the seismic regime at the same time interval (1982.5-1993.5 years) we found in the Caspian region [*Ulomov*, 2007], but for smaller magnitudes of local earthquakes (see **Fig.4.1.3**).

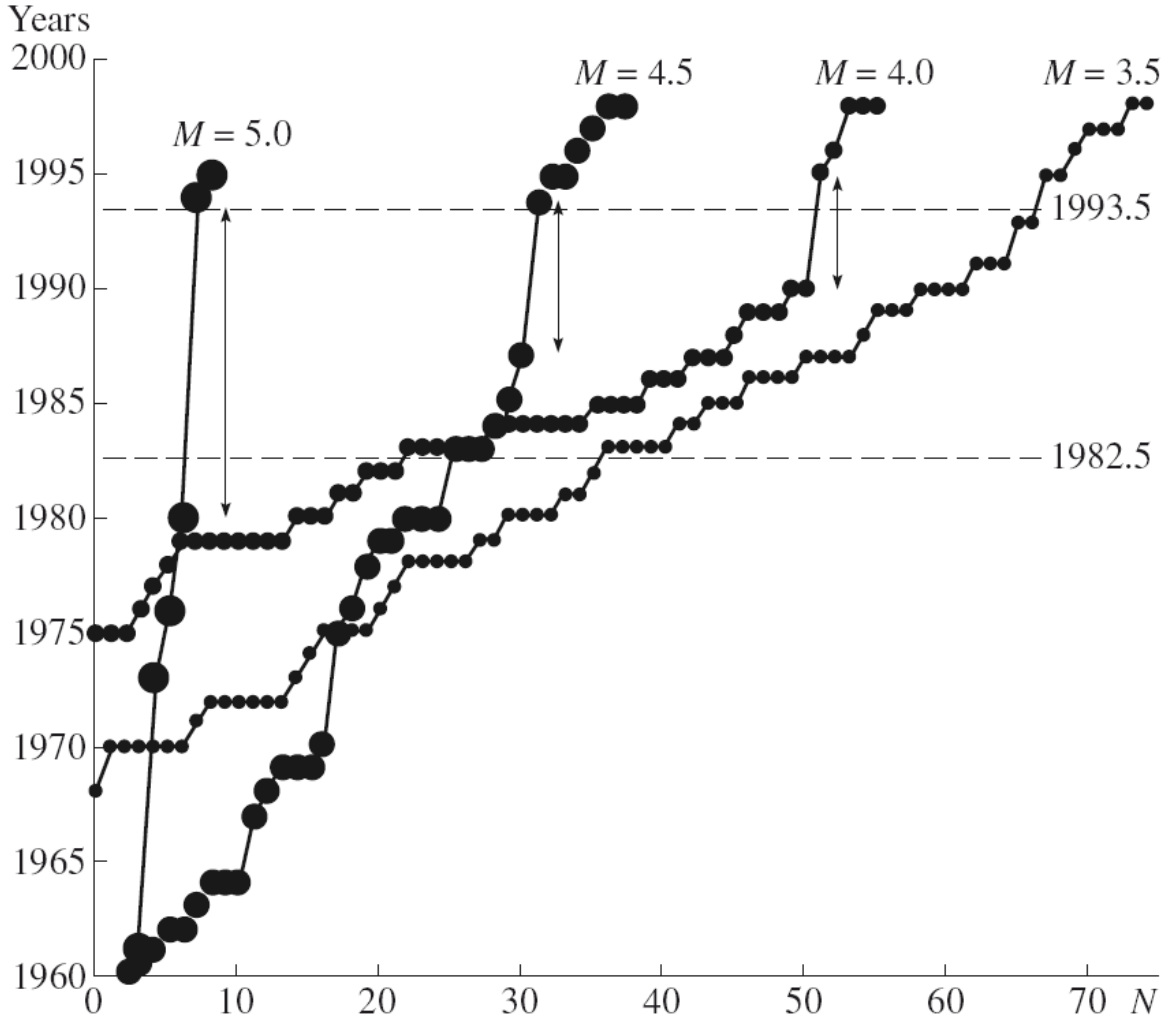

Fig.4.1.3. Sequences of seismic events of moderate and low magnitudes in the subduction zone of the Central Caspian region [Ulomov, 2007]. The time interval 1982.5–1993.5 of the global seismic quiescence is bounded by horizontal dotted lines.

A further search for the correlation between seismogeodynamic and hydrogeodynamic processes in water areas of the Caspian Sea and the Ocean should take into account the dimensions of earthquake sources and their distance from water basins. It cannot be ruled out that powerful global geodynamic processes affected in some way the Iran–Caucasus–Anatolian region, including the closed Caspian basin. One should also pay attention to a certain seismic quiescence in nearly the same time interval (1982.5–1993.5) in relation to moderate and weak earthquakes with M=5.0±0.2, 4.5±0.2, 4.0±0.2, and 3.5±0.2 in the subduction zone of the central Caspian Sea.

With decreasing magnitude, these anomalous zones become gradually less contrasting and even completely disappear in the sequence of the weakest earthquakes (M=3.5±0.2). Incidentally, this fact emphasizes once more that it makes no sense to search for anomalies in the seismic regime of some or other region and the Earth as a whole by summing up the total number of earthquakes without their differentiation by magnitudes because an infinite set of weak seismic events will smooth the general pattern.

4.1.4. The prediction of seismic activity in the North Caucasus

Through our many years of research in the North Caucasus have been identified potential foci of strong earthquakes. The most probable location of one of them was expected in the coming years in the eastern part of the North Caucasus, on the border of Chechnya and Dagestan.

This strong earthquake with the moment magnitude Mw= .9 occurred on Oct. 11, 2008 in the Chechen Republic. It was accompanied by the loss of life and extensive destruction. Presented here (**Fig.4.1.4**) map seismogeodynamics and forecast seismic hazard in the east of the North Caucasus is taken from the publication [*Ulomov*, 2006]. Shown on the map of seismic sources correspond to the Specialized Earthquake Catalog of Northern Eurasia (SECNE, ed. V.I. Ulomov), composed on the basis of unified catalog of earthquakes for the period from ancient times to 2006.

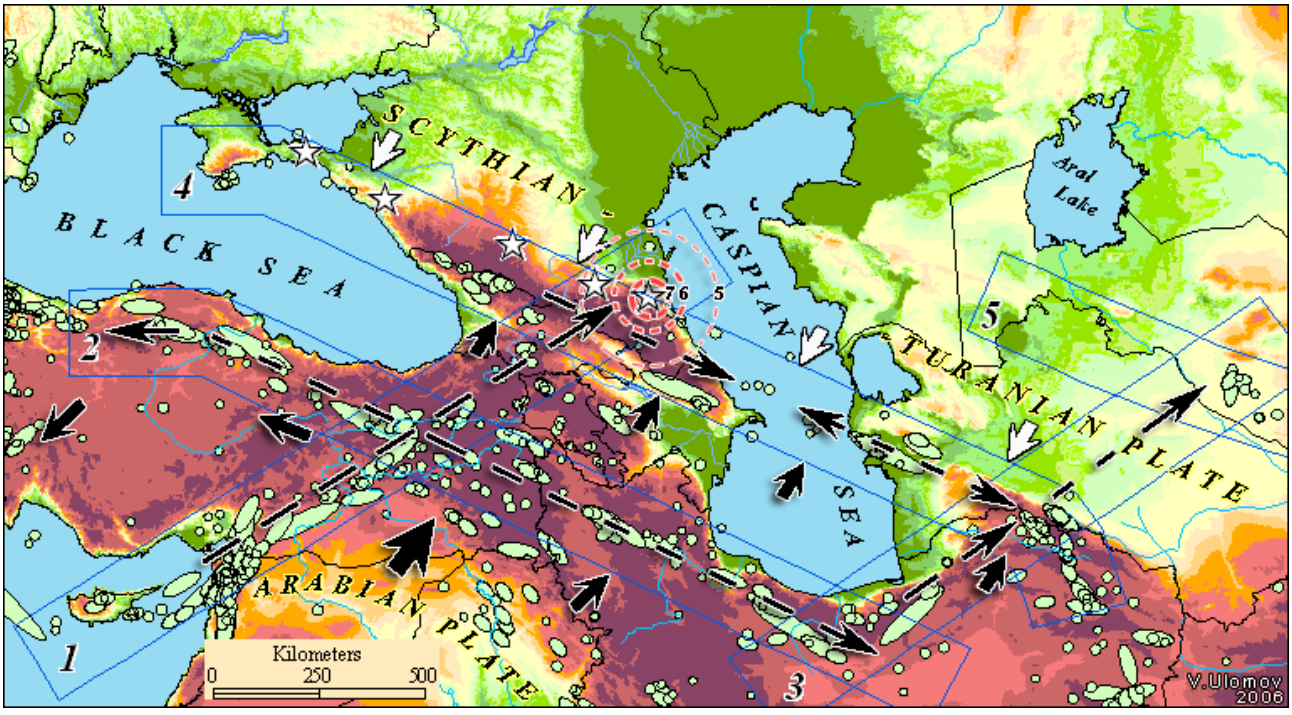

Fig. 4.1.4. The map of prediction of a strong earthquake in the eastern part of the North Caucasus, published in [*Ulomov*, 2007]. Potential sources of earthquakes, the stars are shown.

The Iran-Caucasus-Anatolian region, a fragment of which is shown here on the map represents a single seismogeodynamic system that makes the seismic regime throughout the territory. Studies of spatiotemporal and energy development seismogeodynamic processes along the main seismogenic structures (1. Cyprus-Caucasus, 2. Anatolia-Iran, 3. Iran-Turan, 4. Crimea-Caucasus – Kopet-Dagh) showed distinct patterns in the sequence of seismic events of different magnitudes and in the migration

of seismic activity along each of the featured structures. The direction of migration of earthquakes along the profiles indicated by the dashed arrows. Large arrows illustrate the directions of interaction between the Arabian and Eurasian tectonic plates. Conditional isoseismals in the east of the North Caucasus illustrate published in 2006-2007 [*Ulomov*, 2007]. anticipated effect of seismic intensity of 8-9 points.

4.1.5. Conclusion

The beginning of 2010 marked the intensification of research on the actualization of seismic normative documents in the Russian Federation - namely, building codes and zoning maps of seismic hazard. The initiators of these studies was the Ministry of Regional Development in Russia and Schmidt Institute of Physics of the Earth of Russian Academy of Sciences.

Will be harmonized research on the general, detailed and micro seismic zoning. New maps of general seismic zoning GSZ-2012 will include an assessment of seismic hazard in terms of acceleration of ground strong motion and other quantitative parameters.

The Unified Information System "Seismic Safety of Russia" in the Internet will be created.

References

Ulomov V.I. Global Changes in the Seismic Regime and Water Surface Level of the Earth // ISSN 1069-3513, Izvestiya, Physics of the Solid Earth, 2007, Vol. 43, No. 9, pp.713–725. © Pleiades Publishing, Ltd., 2007. Original Russian Text © V.I. Ulomov, 2007, published in Fizika Zemli, 2007, # 9, pp. 3–17.

Ulomov V.I. On the question of planetary seismic activity // Journal "GeoRisk", № 3, 2010. pp.4-9.

Ulomov V.I. Seismogeodynamics and seismic hazard prediction // National Report of the International Association of Seismology and Physics of the Earth's Interior International Union of Geodesy and Geophysics 2003-2006. 2007. pp.47-51.

4.2. Seismo-geodynamic applications of satellite data

V. O. Mikhailov, mikh@ifz.ru, **A. N. Nazaryan, E. A. Kiseleva, E. I. Smol'yaninova, E. P. Timoshkina**, *Schmidt Institute of the Physics of the Earth RAS. B. Gruzinskaya, 10. Moscow 123995, GSP-5, Russia;* **M. Diament, N. Shapiro,** *IPGP, Paris, France.*

Introduction.

We report the analysis of co-seismic and post-seismic deformations in the region of the Altai (Chuia) earthquake of September 27, 2003. This earthquake is well studied by ground and satellite methods including images of Synthetic Aperture Radar (SAR) interferometry [*Nissen et al.,* 2007; *Barbot et al.,* 2008, *Nazaryan et al.,* 2008, *Mikhailov et al.,* 2010]. In our study, we perform joint inversion of the SAR interferometry and satellite geodesy data published in [Gol'din et al., 2005]. For the purposes of a combined inversion, we developed inversion technique which allows for particular features of the geodetic and SAR interferometry data available.

Altai 27/09/2003 earthquake.

According to the refined data of the Information and Processing Center of the Geophysical Survey of the RAS and the European–Mediterranean Seismological Centre (EMSC) the coordinates the main seismic event epicenter are 49.97°N, 87.77°E. The focal depth was estimated by different seismological centers as 16–18 km and the magnitude of the main shock was 7.0–7.3. The main seismic event was followed by numerous aftershocks. Two large events of 6.2 and 6.6 in magnitude hit the region on the day of the main event and on October 01, 2003 at the northwestern extension of the main rupture [*Starovoit et al.,* 2003; NEIC data]. Analyzing the seismograms, *Nissen et al.* [2007] identified one more seismic event, which occurred presumably south-eastwards of the epicenter of the main event with the magnitude about 6.7 (**Fig.4.2.1**) what was confirmed by the seismotectonic observations and SAR interferometry data.

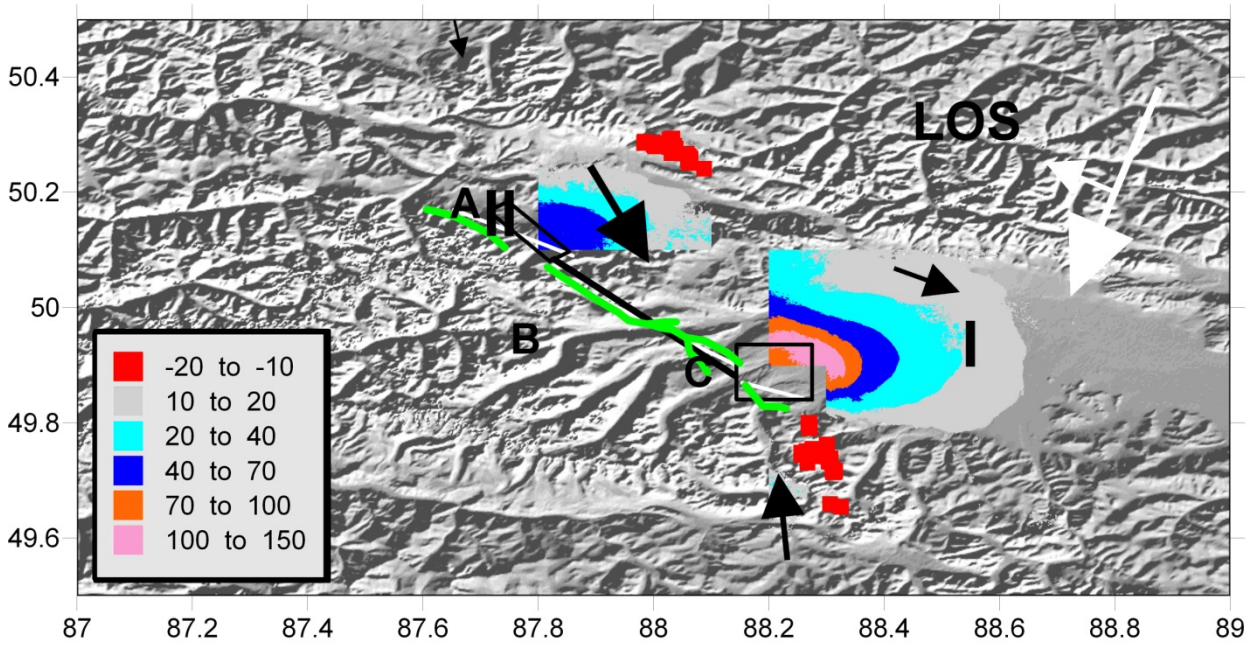

Fig.4.2.1. Colored scale shows the LOS displacement field in cm obtained from images 2–7 for the Chuia (indicated by the numeral I) and 1-4 for the Kurai (indicated by II) depressions (**Table 4.2.1**). Ground projection of the upper edge of the *Nissen et al.* [2007] model is shown by the white lines; their position of the surface rupture is shown by green line. Projection of three rectangles composing our fault plane model is shown by black squares. The larger white arrow in the upper right-hand corner is the satellite flight direction; the smaller arrow indicates LOS direction. The black arrows are the horizontal displacements according to GPS data [*Gol'din et al.,* 2005].

The tectonic rupture on the surface of sedimentary cover has been traced on the southern slopes of the Chuia and Kurai depressions, in the zone of their junction with the North and South Chuia Ranges (**Fig.4.2.1**). It was possible to trace several segments of the rupture as far as 50 km away [*Geodakov et al.,* 2003; *Nissen et al.,* 2007].

SAR interferometry data.

We used ten SAR interferometry images of the ESA ENVISAT satellite (**Table 4.2.1**) under conditions of close Doppler frequency and the baseline not exceeding 600 m. The initial image size is 100 ×100 km, the spatial resolution is about 30 m, the polarization is vertical. Processing of the SAR data was executed using the JPL/Caltech ROI PAC software [Rosen et al. 2004]. For topographic correction we used Shuttle Radar Topographic Mission (SRTM) DEM [*Farr, Kobrick*, 2000]. Precise orbits were uploaded from the open database of the Delft University of Technology (DEOS).

The processing of seven pairs of SAR images provided phase interferograms, which were transformed into the line-of-sight (LOS) displacement field via phase unwrapping employing two algorithms GZW [Goldshtein et al., 1988] and SNAPHU [*Goldshtein et al.,* 1993]. The results yielded by the SNAPHU algorithm for the Altai region appeared to be less dependent on the coherence of images, a more dense coverage of the target region and showed better consistency with the earlier results [*Nissen et al.,* 2007; *Barbot et al.,* 2008]. For more details of data processing see [*Nazaryan*, 2008, *Mikhailov et al.*, 2010].

Fig.4.2.1 depicts the LOS displacements obtained by the superposition of the results of phase unwrapping for the pair 1–4 for the Kurai depression and the pair 2–7 for the Chuia depression (**Table 4.2.1**) as well as two fault plane models and GPS horizontal displacements (see figure captures for details). Reconstruction of the displacement fields from different pairs of images yielded similar results. A distinct interferometric pattern is obtained for the unforested areas with relatively smooth topography of the Kurai and Chuia depressions and for a part of surrounding mountain regions. The

loss in correlation is mostly due to the mountain topography and high-density of forest vegetation on the mountain slopes.

Table 4.2.1.

ENVISAT images used in the analysis of the Altai earthquake of September 27, 2003

Number	Date	Orbit	Track
1	23/08/2003	7731	162
2	08/09/2003	7960	391
3	11/09/2003	8003	434
4	13/10/2003	8461	391
5	16/10/2003	8504	434
6	06/12/2003	9234	162
7	22/12/2003	9463	391
8	25/12/2003	9506	434
9	19/08/2004	12469	391
10	22/06/2004	12512	434

Data inversion.

For mathematical description of deformations caused by low-magnitude earthquakes, the model of rectangular fault in elastic half-space [*Okada*, 1985] is in common use. Rupture surface can be approximated by number of planes. Each plane is characterized by nine parameters: three coordinates, e.g., of one of its corner; the strike and the dip lengths; the strike and the dip angles; and displacement amplitude and rake angle. It is important that some of these parameters can be constrained a priori. Indeed, in order to estimate the average dip and strike angles of the rupture, one may choose a nodal plane that agrees with the position of the seismic rupture on the surface of sedimentary cover (**Fig.4.2.1**). Because the shape of the rupture on the surface of the sedimentary infill is always more complex than its configuration in the underlying crystalline basement, we smoothed the surface trace of the rupture. This also enables reducing the contributions of the second-order processes such as landslides, topography effects, heterogeneities in the physical properties, and variations in the thickness of the sediments.

For numerical solution of the problem we developed a minimization procedure for a functional incorporating weighted misfits of calculated and real SAR and GPS data. The strategy for the solution of the problem is as follows. The rupture is approximated by a set of planes. The parameters of the planes and the components of the displacement vectors are found under the best fit condition. The algorithm implies successive partitioning of each plane into four equal subregions, then into eight, and so on (each subregion with the same dip and strike as the initial plane), until a stable solution and misfit are attained. Such a scheme provides sufficiently detailed solution, but allows avoiding its oversegmentation, which may lead to instability.

Following [*Nilssen et al.*, 2007], we approximated the rupture by three planes. The difficulty of the inversion in this specific case is that almost all of the SAR and GPS data are clustered at north-east of the rupture. As a result, the planes, approximating the rupture surface, may shift southwest to the region of the North and South Chuiskii Ranges. To dispose of this effect, the limits of the possible shift of the planes were fixed in such a way that the planes could not shift far from the outcrop of the seismic rupture. The rest of the parameters were free of any limitations and could vary arbitrarily.

The results of the data inversion are shown in **Fig.4.2.2**. With the properly chosen parameters of smoothing and the weights of the geodetic data, we arrived to a solution that is consistent with all available data. The white and black arrows in **Fig.4.2.2** show GPS and calculated displacements. The red arrows show the calculated displacements of [*Nissen et al.*, 2007] constructed without any geodetic control. Because they had no GPS data in their disposal, the arrows corresponding to their solution are much shorter, and the directions of displacements sometimes disagree with the measured ones. The calculated LOS displacement field (shown in the isolines) is close to those inferred from the SAR data (shown in colored scale). The ruptures detected on the surface of the sedimentary cover (green line in **Fig.4.2.1**) agree with the positions of the planes in our model. Partitioning of any of the initial planes into smaller parts resulted in no improvement of the misfit.

The basic difference of our model against the *Nissen et al.* [2007] one is that the involvement of GPS data resulted in a considerable increase in the estimates of the displacement amplitudes on the rupture (**Table 4.2.2**). *Nissen et al.* [2007] note that their solution provides noticeably underestimated magnitudes of the seismic events, e.g., the magnitude of the main event is estimated as 6.67, against the measured one of 7.1–7.3. Our solution estimates the magnitude of the main event as 7.14, and the aftershocks, as 6.66–6.88 (**Table 4.2.2**), which is consistent with the seismological determinations. Another distinction between the two models is the different positions of the two distal planes (A and C in **Fig.4.2.2**); in our model, these planes dip more gently, compared to the model of *Nissen et al*. The parameters of the intermediate plane that corresponds to the main seismic event are rather similar in both models, although the B plane in our model dips a bit steeper, and its bottom edge lies noticeably deeper. The displacement on the plane B in our model is an almost pure shear with a very small thrust component. On the plane C, an almost pure thrust occurred; and on the plane A, both the shear and thrust components have nearly similar amplitudes.

Table 4.2.2.

Comparison of the solutions obtained from the interferometry data alone [*Nissen et al.,* 2007] and from joint inversion with geodetic data (this study)

Plane		Strike, deg	Dip, deg	Rake deg	Displacement, m	Upper edge, km	Bottom edge, km	Strike length, km	Magnitude
A	[*Nissen et al.*, 2007], model (i)	322	80	145	1.27	1.8	25.9	12.3	6.67
B		305	80	146	1.61	0	9.7	25.3	6.77
C		295	57	96	4.63	1.4	11.4	8.2	6.76
A	our study	285	48	127	1.6	3.9	12.0	21.6	6.66
B		305	87	171	4.1	0	24.6	19.4	7.14
C		302	34	107	5.2	0	12.6	7.0	6.88

In [*Barbot et al.,* 2008], the surface of the rupture is strictly vertical. The displacements all over the studied region correspond to a nearly pure shear, which should result in an even stronger discrepancy with GPS data. Because no numerical parameters of the model were indicated in their paper, no quantitative comparison has been done. It should be noted that, despite the considerably large volume of geophysical data involved in the inversion, some of the rupture parameters are determined still rather poorly. So, for the planes A and C, nearly similar solutions exist at different depths of the upper and lower edges and at different dips of the planes. This is due to the problems of the interferogram unwrapping in regions of strong displacements and with the data clustering north-east of the rupture.

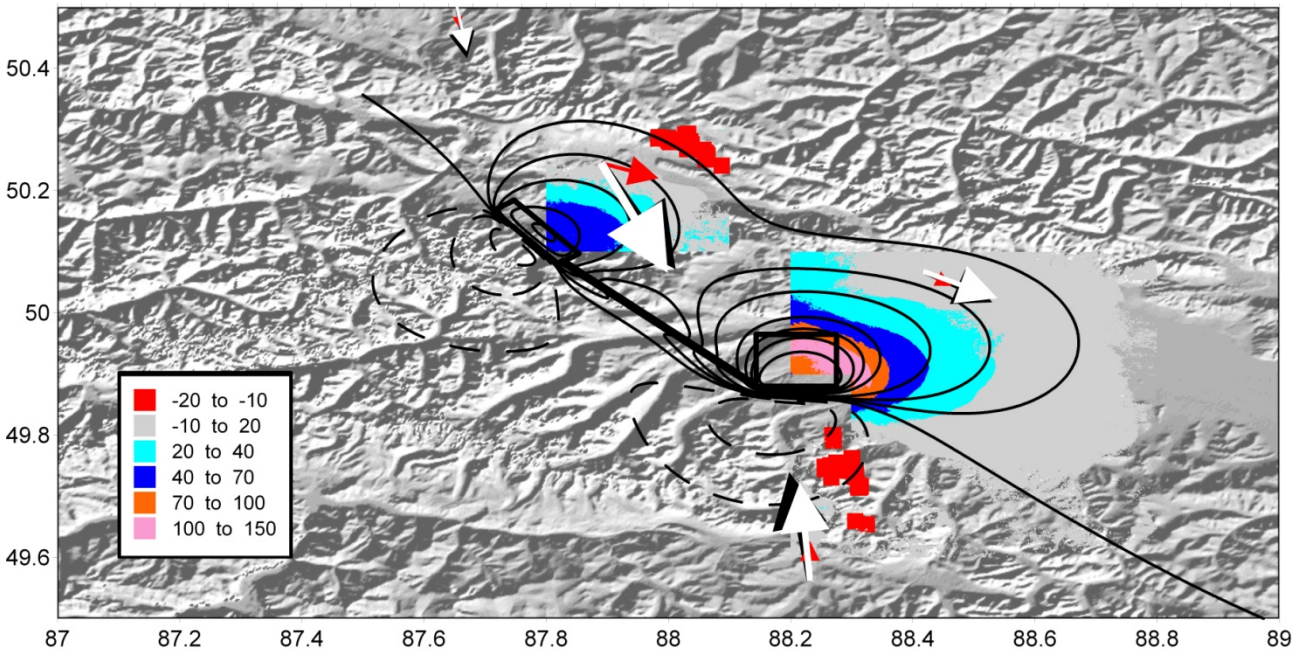

Fig.4.2.2. Comparison of the real and calculated data. The observed data: the LOS displacement field in cm (shown in colored scale); GPS horizontal displacements [*Gol'din et al.*, 2005] are shown by the white arrows Our model: the calculated LOS displacements in cm (isolines); the horizontal displacements at GPS sites (black arrows); the ground projection of our rupture surface model is shown by the squares. The model of *Nissen et al.* [2007]: the calculated horizontal displacements at GPS sites are shown by the red arrows.

On the whole, the data available allow us to construct a detailed rupture model and to reconstruct the amplitude and the direction of displacements on it. The model of displacement on the rupture is in a good agreement with the regional geodynamics.

In [*Mikhailov et al,* 2010] we also performed an analysis of post-seismic SAR and aftershock data which showed that the displacements estimated in our work mainly characterize the processes that took place from the commencement of the rupture surface opening on September 27, through the end of the northwest propagation of the rupture on October 1–2, 2003.

Conclusions.

1. The constructed model of the Altai earthquake agrees well with the entire set of the experimental data available, including the results of the field observations and the regional geodynamic models.

2. In the region of the Altai earthquake, due to the dense forest vegetation and the mountain topography, images of the SAR interferomety characterize the displacements mainly to the northeast of the seismic rupture, which impedes the localization of the rupture surface and the estimations of the displacement field on it. GPS sites of the Altai geodynamical network within the nearby zone (100 km as large) are not numerous and distant from the rupture, however, the joint inversion of the SAR and GPS data in this specific case provides considerably higher accuracy and stability of the solution of the inverse problem.

Acknowledgements. This study was supported by grant of Russian Foundation for Basic research 08-05-00466. SAR data were provided by ESA under research project Category-1 #4254.

References

Barbot S., Hamiel Y., Fialko Y. Space geodetic investigation of the coseismic and postseismic deformation due to the 2003 Mw7.2 Altai earthquake: Implications for the local lithospheric rhe-ology // JGR. 2008. v. 113, (doi:10.1029/2007JB005063).

Farr, T., Kobrick, M., 2000. Shuttle Radar Topographic Mission produces a wealth of data, EOS, Trans. Am. geophys. Un., 81, 583–585.

Geodakov A. R., A. N. Ovsyuchenko, S. G. Platonova, and E. A. Rogozhin, "Preliminary Results of Studying the Strong Earthquake of 2003 in Mountain Altai," Vestn. Otdeleniya nauk o Zemle RAN: Elektr. nauch.-inf. zhurn., # 1 (21), 1−21 (2003) [in Russian].

Gol'din S. V., V. Yu. Timofeev, and D. G. Ardyukov, "Fields of the Earth's Surface Displacement in the Chuya Earthquake Zone in Gornyi Altai," Dokl. Earth Sciences 405 (9), 1408−1413 (2005).

Goldstein R. M., Engelhardt H., Kamp B., Frolisch R. M. Satellite Radar Interferometry for Monitoring Ice Sheet Motion: Application to an Antarctic Ice Stream // Science. 1993. v. 141. pp.1171-1172.

Goldstein R. M., Zebker H. A., Werner C. L., Satellite Radar Interferometry: Two-dimensional Phase Unwrapping // Radio Sci. 1988. v. 23 (4). pp.713-720.

Mikhailov V.O., A.N. Nazaryan, V.B. Smirnov, M. Diament, N. Shapiro, E.A. Kiseleva, S.A. Tikhotskii, S.S. Polyakov, E.I. Smol'yaninova, E.P. Timoshkina, 2010. Joint Inversion of the Differential Satellite Interferometry and GPS Data: a Case Study of Altai (Chuia) Earthquake of September 27, 2003. *Izvestiya*, Physics of the Solid Earth, 2010, Vol. 46, # 2, pp.91–103.

Nazaryan A.N., Mikhailov V.O., E.A. Kiseleva, E.I. Smol'yaninova, E.P. Timoshkina, M. Diament, N. Shapiro, 2008. Studying of the Earth surface deformations using SAR interferometry: A ase study of the Altai 27.09.2003 earthquake. Geofizika, # 5 [in Russian].

NEIC catalogue at http://earthquake.usgs.gov/regional/neic/ .

Nissen E., Emmerson B., Funning G.J., Mistrukov A., Parsons B., Robinson D., Rogozhin E., Wright T. Combining InSAR and seismology to study the 2003 Siberian Altai earthquakes—dextral strike-slip and anticlockwise rotations in the northern India–Eurasia collision zone // Geophys. J. Int. 2007. v. 169. p. 216–232 (doi: 10.1111/j.1365-246X.2006.03286.x)

Okada Y. Surface deformation due to shear and tensile faults in a half-space // BSSA. 1985. v. 75. pp.1135-1154.

Rosen, P.A., Hensley, S., Peltzer, G. and Simons, M., 2004. Updated Repeat Orbit Interferometry package released, EOS, Trans. Am. geophys. Un., 85, 35.

Starovoit O. E., L. S. Chepkunas, and I. P. Gabsatarova, "Parameters of the Altay earthquake on September, 27, 2003 on the instrumental data," Vestn. Otdeleniya nauk o Zemle RAN: Elektr. nauch.-inf. zhurn., # 1 (21), 1-11 (2003) [in Russian].

4.3. Investigations of present-day crustal movements and deformations of Central Asia using GPS geodesy

V. A. Sankov, sankov@crust.irk.ru**, A. V. Lukhnev.** *The Earth's Crust SB RAS, Lermontov str., 128, Irkutsk, 664033, Russia*.

During 2007-20010 the investigations of present-day crustal movements and deformations using GPS geodesy on geodynamic testing grounds of Central Asia were continued. Such testing grounds are three from east to west: Baikal-Mongolia (founded on 1994), Altai (founded on 2000) and Central Asian (founded on 1994). The geodetic networks cover the seismically active regions with different styles of crustal deformations – extension in Baikal rift, strike-slip in Mongolia, Altai and Sayan and compression in Pamir and Tien-Shan.

Current deformation in Pribaikalia, Western and Central Mongolia, and Tuva has been studied from measured horizontal GPS velocities and respective computed strain and rotation rates using 1994–2007 data of the Baikal–Mongolian GPS triangulation network [*Lukhnev et al.,* 2010]. The GPS velocity field shows two main trends: an NE trend within Jonggaria, the Mongolian Altay, and the

Great Lakes Valley and an SE trend in the Hangayn and eastern Gobi Altay mountains, and in the Transbaikalian block of the Amur plate (**Fig.4.3.1**). The velocity magnitudes and vectors are consistent with an SE motion of the Amur plate at a rate of ~2 mm/year. The derived strain pattern includes domains of crustal contraction and extension recognized from the magnitudes of relative strains. Shortening predominates in the Gobi and Mongolian Altay and in the Khamar-Daban Range, where it is at $\varepsilon_2 = (19.2 \pm 6.0) \times 10^{-9}$ yr^{-1} being directed northeastward. Extension domains exist in the Baikal rift and in the Busiyngol–West Hangayn area, where the crust is stretching along NW axes at $\varepsilon_1 = (22.2 \pm 3.1) \times 10^{-9}$ yr^{-1}. The eastern Hangay dome and the Gobi peneplain on its eastern border show low and unstable strain rates. In central and northern Mongolia (Orhon–Selenge basin), shortening and extension are at similar rates. The strain pattern changes notably in the area of the Mogod earthquake of 1967. Most of rotation throughout Central Asia is clockwise at a low rate of about $\Omega = 6 \times 10^{-9}$ deg·yr^{-1}. Two or three times high rates of clockwise rotation are observed in the Hangayn domain, in the Gobi Altay, and in the Orhon–Selenge domain. Counterclockwise rotation is restricted to several domains. One is in western Tuva and northwestern Great Lakes Valley of Mongolia. Two more counterclockwise rotation regions occur on both flanks of the Baikal rift: along the craton edge and in basins of Transbaikalia on the rift eastern border, where rotation rates are as high as $(13.0 \pm 3.9) \times 10^{-9}$ deg·yr^{-1}, while rotation within the Baikal basin does not exceed the measurement error. Another such domain extends from the eastern Hövsgöl area to the Hangayn northern foothills, with the counterclockwise rotation at a highest rate of $(16.3 \pm 2.8) \times 10^{-9}$ deg·yr^{-1}.

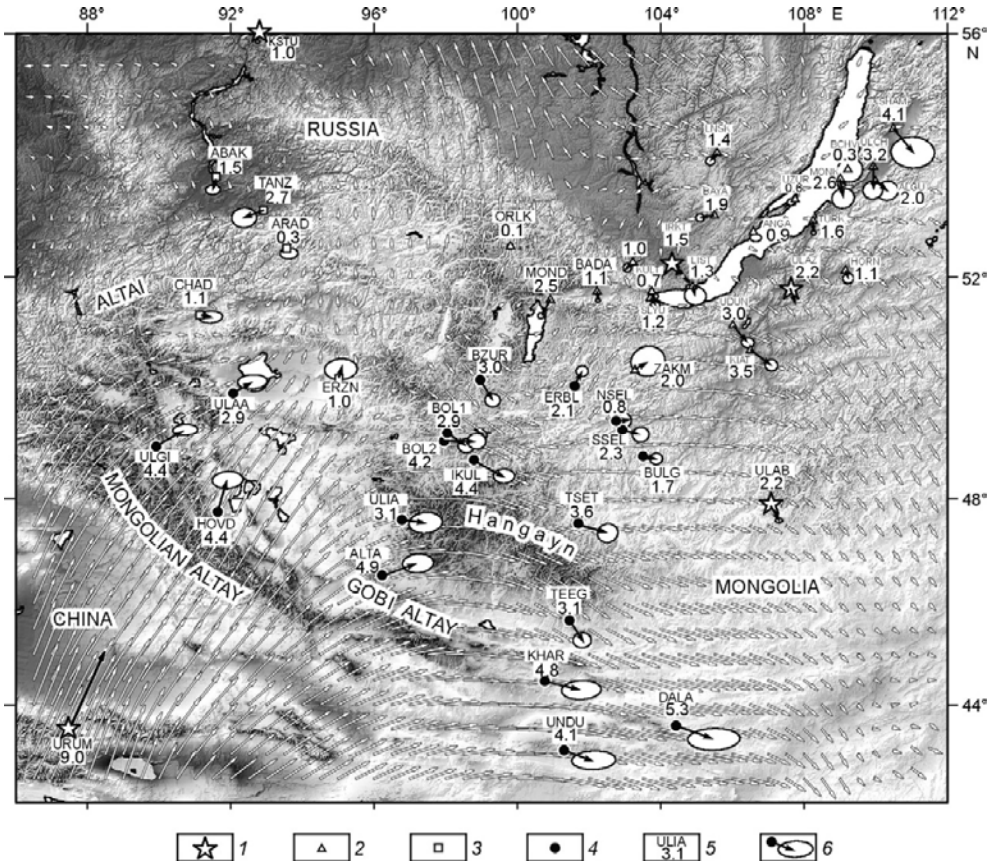

Fig.4.3.1. Field of GPS horizontal velocities with respect to Eurasia, 1994–2007, 95% confidence interval. White arrows are velocities averaged on a 30′ × 30′ uniform grid; black arrows are velocities of GPS stations calculated in this study. 1–4, GPS stations: permanent stations (1) and campaign stations within Baikal (2), Tuva (3), and Mongolia (4) areas; 5, abbreviated station name and velocity in mm per year; 6, direction and magnitude of velocity, 95% confidence interval.

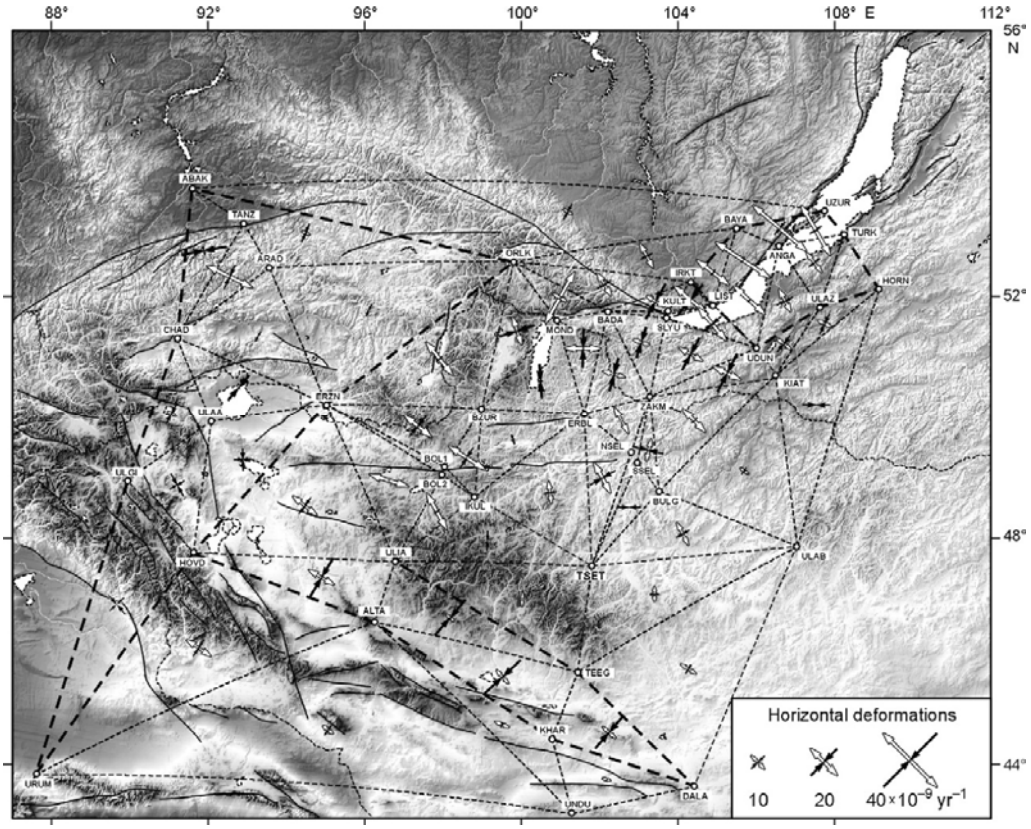

Fig.4.3.2. Relative strain patterns within Baikal–Mongolia GPS network. Black and white lines are principal shortening and extension rate axes, respectively.

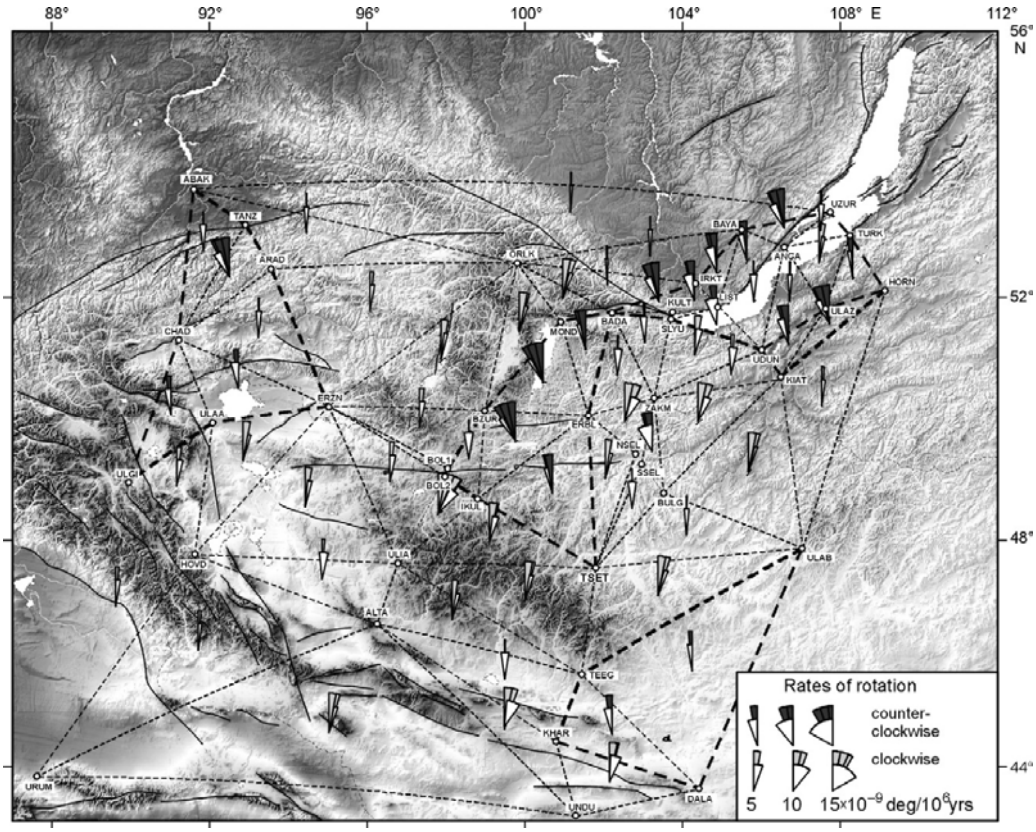

Fig.4.3.3. Rates and sense of rotation within Baikal–Mongolia GPS network. Light gray and dark gray fans show right-lateral (clockwise) and left-lateral (counterclockwise) rotation, respectively.

On the basis of long-term measurements (1994-2007) on the Baikal geodynamic GPS testing ground, the velocity of the Siberian and Transbaikalian block divergence in the direction of 130°. has

been refined [*Sankov et al.,* 2009]. It makes up 3.4 ± 0.7 mm/year at a distance comparable with the width of the zone of the plate boundary dynamic effect (**Fig.4.3.4**). This is consistent with parameters of a long-term (Holocene) constituent of the extension velocity, which are established based on geological data [*San'kov et al.,* 2000], and with the extension direction determined by earthquake focal mechanisms data [*Petit et al.,* 1996; *Radziminovich et al.*, 2006]. The velocity distribution across the rift basin with its gradual growth from one block to another suggests the non-rigid behavior of continental lithospheric plates on the divergent boundary. About 30% (1.0–1.5 mm/year) of the total growth of the velocity falls on the Baikal depression. The rate of strain there reaches $2.1*10^{-8}$ $year^{-1}$ and gradually decreases into both sides across the rift (**Fig.4.3.5**). The data on extension in the Barguzin depression have been obtained for the first time. The average rate of displacement of all the Barguzin polygon stations relative to the Siberian Platform block makes up 4.0 mm/year. As noted for the Baikal depression, there is a tendency to its increase when moving southeastward from the platform (see **Fig.4.3.5**). In general the distribution of the velocity of horizontal movements on the Baikal divergent boundary between the North Eurasian and Amur plates corresponds to the model of passive rifting.

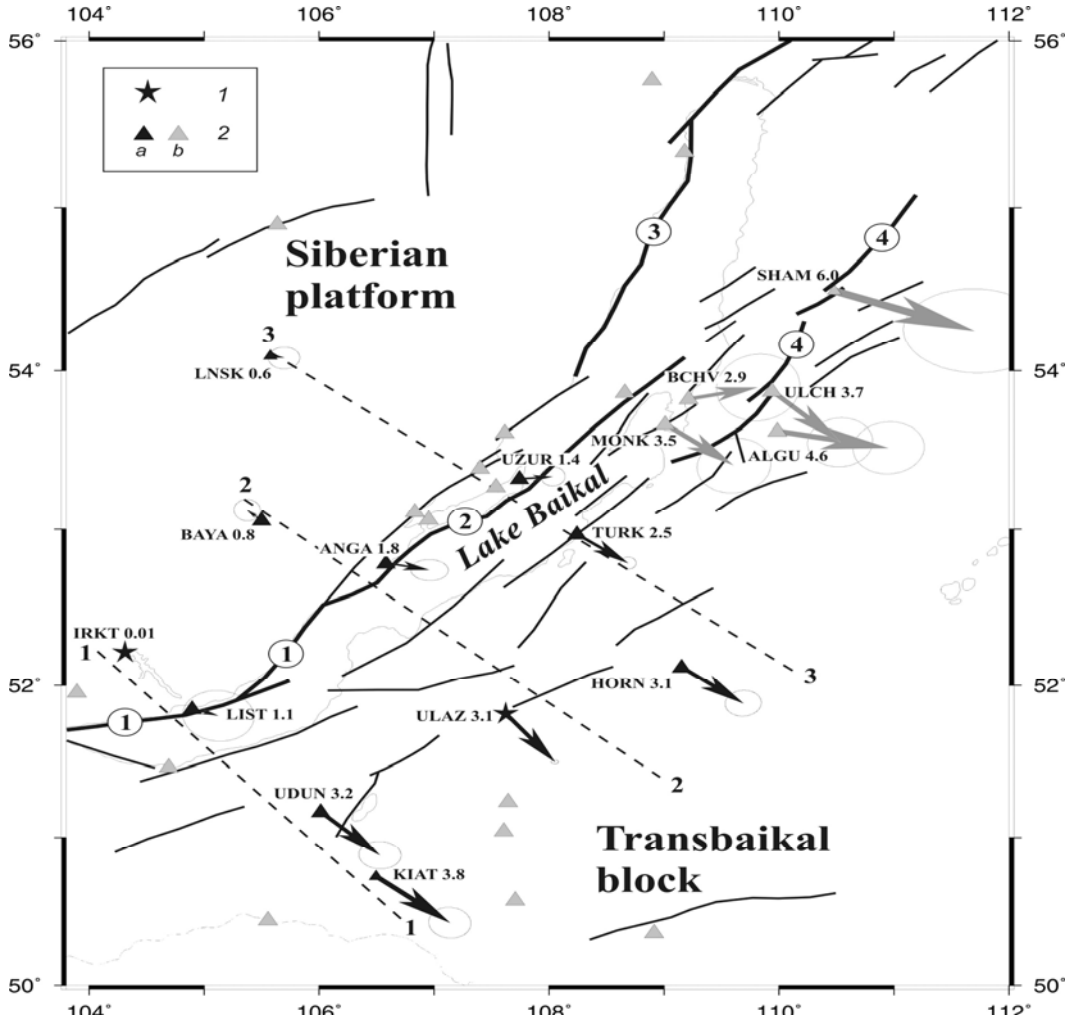

Fig.4.3.4. The field of velocities for present-day horizontal movements of the Baikal depression by data of measurements on the Baikal GPS polygon for 1994–2007. (1) Stations of permanent measurements; (*2*) field stations: (*a*) for long-term measurements, (*b*) for measurements lasting 4 or fewer years. Designated near the stations are abbreviations of their names and motion velocities, mm/year. Velocity vectors for station displacements relative to the Siberian Platform are shown with ellipses of a 95% confidence interval. (1–4) Faults: (1) Obruchev, (2) Morskoi, (3) North-Baikal, (4) Barguzin. (1–1, 2–2, 3–3) profiles shown in **Fig.4.3.5**.

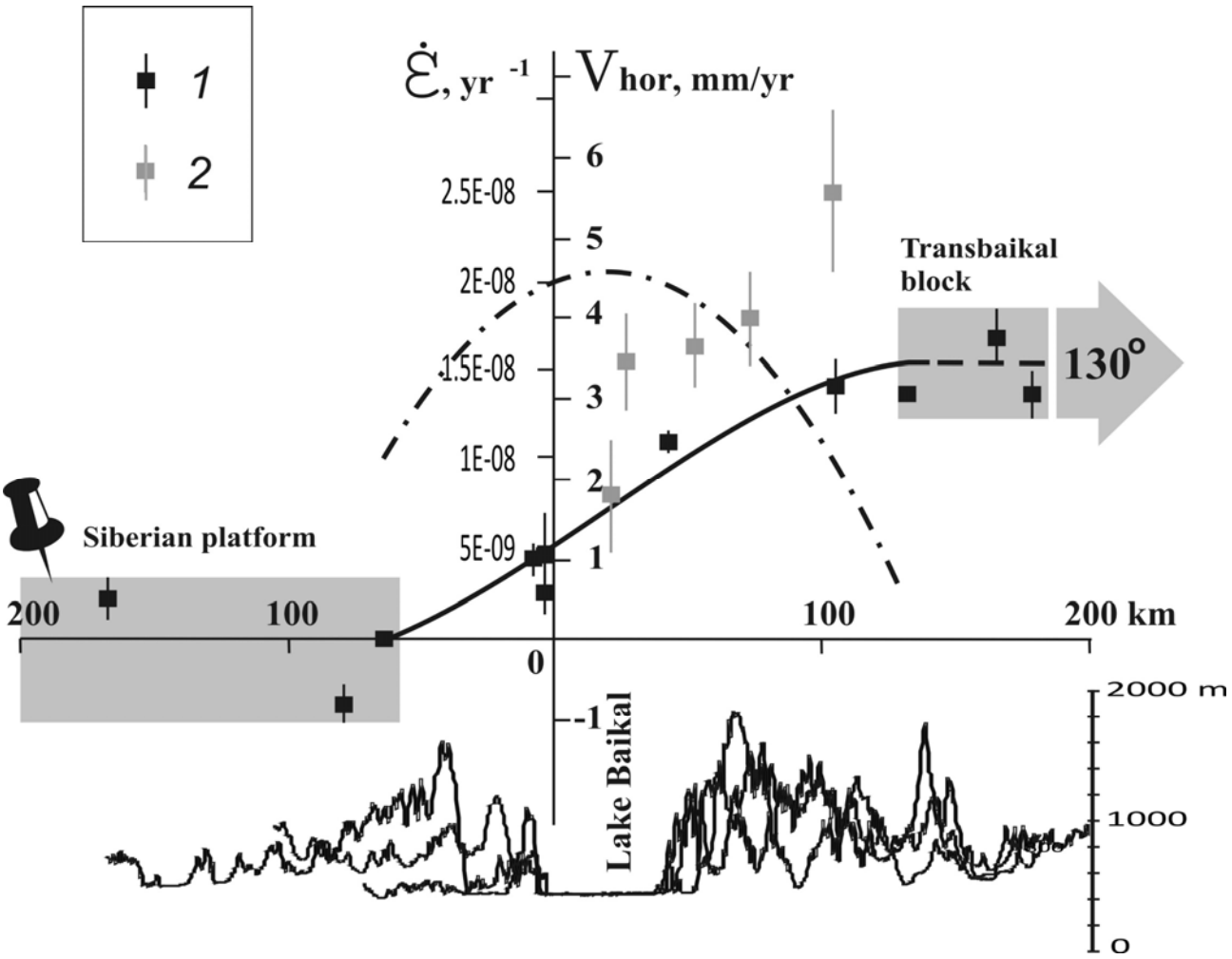

Fig.4.3.5. Diagrams for velocities of horizontal movements (*V*hor, firm line) relative to the Siberian Platform by the azimuth of 130° and velocities of elongation (, dashed line) on the Baikal plate boundary. (*1*) *V*hor values with their errors for stations of long-term measurements in the southern and central parts of the Baikal basin, (*2*) the same, for stations of the Barguzin geodynamic polygon. Given below are superposed sections of the relief by profiles 1–1, 2–2, 3–3 through the Baikal basin (see **Fig.4.3.4**).

According to the map of earthquake epicenters and map of seismic moment relies the most seismic activity concentrates along major fault within the Baikal basin. It is shown [*Sankov, Dobrynina*, 2009] that the scalar moment rates for earthquakes catalogue over 1742-2008 agree, within uncertainties, with the deformation rate of the South Baikal basin determined by space geodesy. Seismic-moment rate have been estimated from an earthquakes catalogue complete for M≥5. Authors use Anderson's (Anderson, 1979) formulation to translate the geodetic strain rate into rate of energy release. On the plot of cumulative seismic-moment release with time one can recognize two stages of activation – in 1742 (Ms=7.7) and in 1862 (Ms=7.5). The last period of strain accumulation exceeds the previous one at the moment. The energy release deficit reaches $2.37*10^{27}$ dyne*cm. It is equal to Mw≈7.5 – a proposed upper bound of current seismic hazard for the region. The largest for Central Baikal rift system during instrumental period 27.08.2008 Kultuk earthquake (Mw=6.2) occurred in the southern part of the South Baikal basin has possibly opened a new stage of seismic activation.

Timofeev V.Yu. and coauthors [*Timofeev et al.,* 2009] used the experimental GPS data on 3D displacements of the Gorny Altai lithosphere for 2000-2007 to find special features of displacement velocity fields for three periods. The first period (2000-2003) represents the field before the Chuya earthquake (**Fig.4.3.6a**). The velocity field of the future epicentral zone has anomalies achieving 5-11 mm in a year. The coseismic displacement field (2003-2004) allows developing the elastic rebound model for the Chuya earthquake, 09.27.2003 (*Ms* = 7.3-7.5) (fig 6b). The measurement results for the

2003-2004 provide the pattern of postseismic displacements, where a right-lateral strike-slip is observed in the epicentral zone. This phenomenon is described using elastic rebound models for 2D- and 3D-displacements of the Earth's crust. The experimental data used within the chosen model allow estimating realized stress (σ=4 MPa), rupture displacement (a=2 m) and rupture length (L=140 km) at the maximum rupture depth (H=16 km). Using the experimental GPS data authors derived the seismic moment ($Mo=0.9\cdot10^{20}$ N·m) and earthquake magnitude (Mw=7.2).

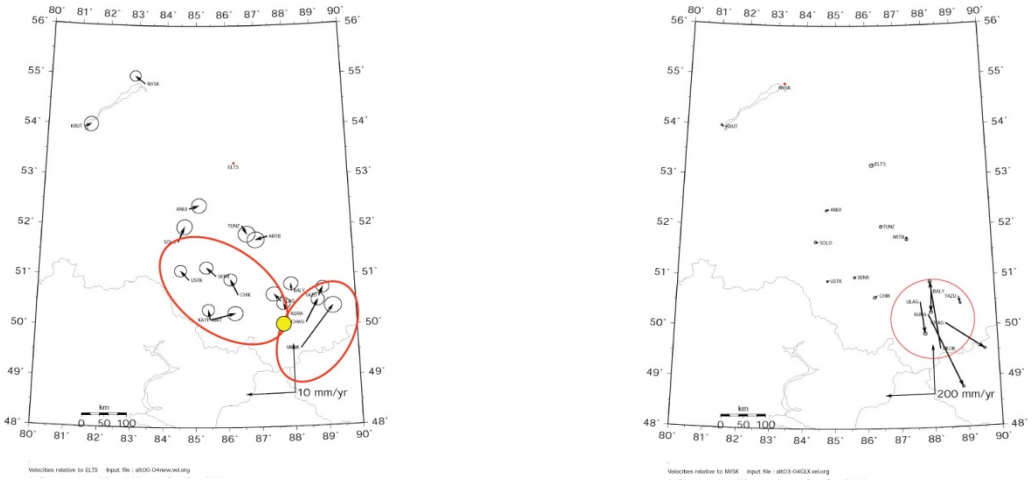

a **b**

Fig.4.3.6. Horizontal velocity field before Chuya earthquake, 09.27.2003 (*M* = 7.3-7.5) (2000-2003) (a) and coseismic movements (2003-2004) for Altai geodetic network (b).

Crustal deformation in the northern Tien Shan as recorded in strain rates derived from earthquake and GPS data were studied within Central Asian testing ground [*Tychkov et al.*, 2008]. It is shown that geodetic strain rates indicate general shortening along the N-S component and agree with Quaternary fault slip rates and with the strain field obtained from earthquake mechanisms, all being signature of overall north-south contraction in the region. The GPS strain field changes quickly in time, especially in the W-E direction, and is produced by a joint effect of elastic, plastic, and quasi-plastic deformation (**Fig.4.3.7**). Author believed that the seismological strain field reflects the effect of external tectonic forces applied to seismogenic crust and the stress change due to crustal heterogeneity. Seismological and GPS strain rates carry information of different kinds. The former reflect formation of local structures mainly in the brittle crust, such as a local pull-apart in the center of the Lake Issyk Kul area, whereas the latter provide clues to mechanisms that drive the geological evolution of the mountain terrain as a whole. The strain field inferred from seismology bears evidence of vertical movements in the lower crust and upper mantle as interplay of upwelling and downwelling south and east of Lake Issyk Kul, respectively. The current evolution may involve the effect of density instability at the lithosphere-asthenosphere boundary [*Tychkov et al.*, 2008].

Zubovich A.V. and Mukhamediev Sh.A. [*Zubovich, Mukhamediev*, 2010] proposed a new method to define piecewise continuous fields of velocity gradients of crustal horizontal movements from spatially discrete data on horizontal velocities of such movements. The method is designed to identify zones of localized deformation and boundaries between areas with different strain rates in considerable detail. It is applied to determine the field of horizontal velocity gradient in the region of the Central Asian GPS network. Calculations are based on GPS survey data obtained at 308 sites from 1995 to 2006 (**Fig.4.3.8**). The resolution of the proposed method is increased by using a triangulation grid which is much denser than a conventional one (**Fig.4.3.9a,b**). As a result, point **x** on the surface under study is covered by several triangles rather than one. Strain characteristics at point **x** are calculated by weighted summation of corresponding characteristics in the cover triangles. Thus, for each point we estimate spin tensor **W,** which defines angular velocity ω, and components of horizontal strain rate tensor **E**. These components provide for direct calculation of orientation of principal axes and invariants of **E**, i.e. maximum stretching E_1, maximum shortening E_2 (**Fig.4.3.10**), velocity divergence $E=E_1+E_2$, and

maximum shear rates. The calculated values are presented in maps which demonstrate that spatial distribution of such values is highly inhomogeneous. Regions with increased values of kinematic characteristics mentioned above stand out sharply against the background. At the same time, spatial distribution of the kinematical characteristics in the Tien Shan region is quite regular: zones of increased absolute values of E_2 are mainly oriented in the ENE direction, while the NNW orientation dominates in zones of increased values of E_1 [*Zubovich, Mukhamediev*, 2010].

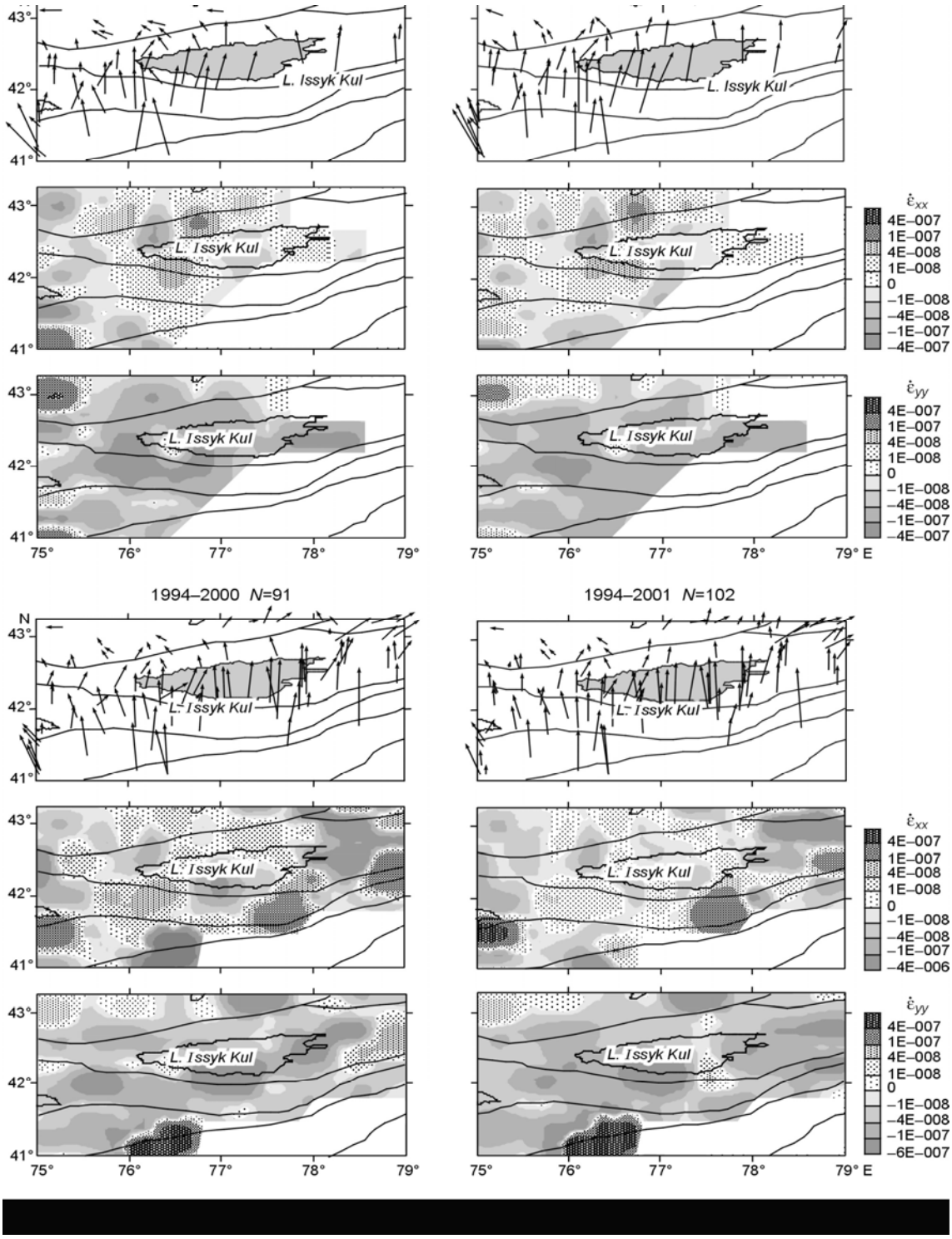

Fig.4.3.7. GPS velocities and respective maps of W-E (E*xx*) and N-S (E*yy*) strains for periods 1994–1998, 1994–1999, 1994–2000, and 1994–2001.

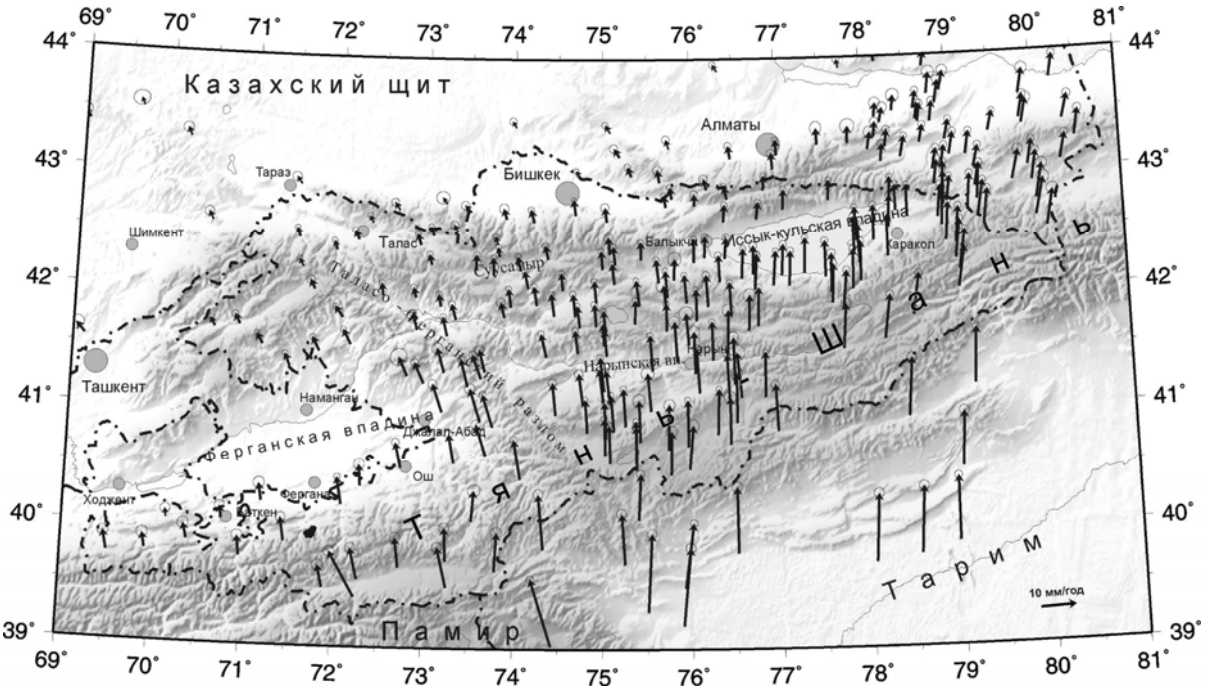

Fig.4.3.8. Recent horizontal velocity pattern of the Tien Shan fragment of the Central Asian GPS network, as calculated relative to stable parts of the Eurasian Plate. Ellipses show 95 percent confidence. Chain lines show state frontiers.

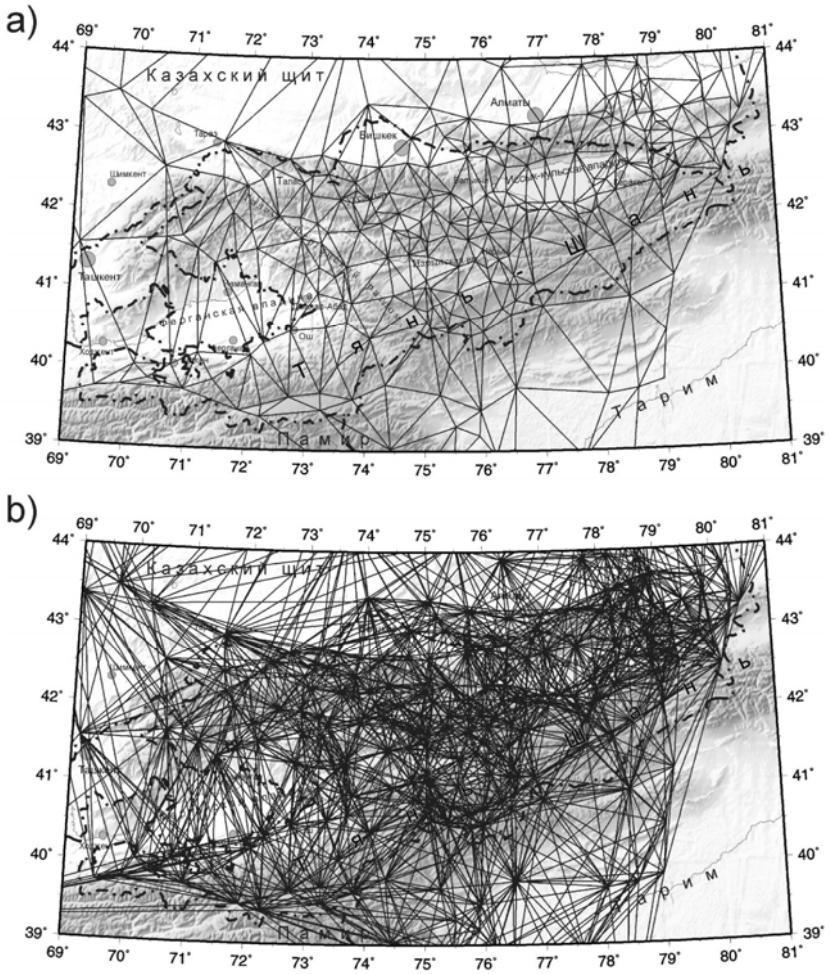

Fig.4.3.9. Triangulation of the Tien Shan fragment of the Central Asian GPS network: *a* – initial Delaunay triangulation (chain lines show frontiers of the Central Asian states); *b* – a set of triangles after initial triangulation is subject to iteration.

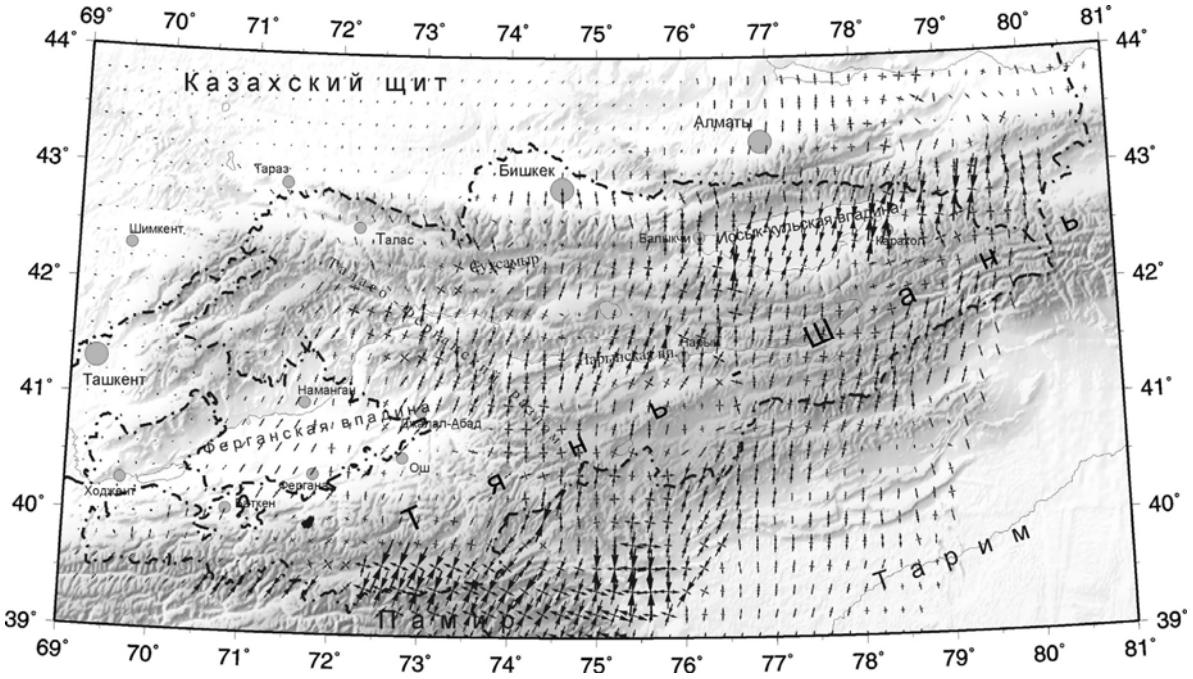

Fig.4.3.10. Pattern of axes of maximum (E_1) and minimum (E_2) stretching. Outward arrows show stretching; inward arrows show shortening. Arrow lengths are proportional to absolute values of corresponding strain rates.

References

Anderson J.G. (1979) Estimating the seismicity from geological structure for seismic-risk studies. Bull. Seism. Soc. Am. V.69. P. 135–158.

Lukhnev A.V., San'kov V.A., Miroshnichenko A.I., Ashurkov S.V., Calais E. (2010) GPS rotation and strain rates in the Baikal–Mongolia region. Russian Geology and Geophysics. V.51. P. 785–793

Petit C., Deverchere J., Houdry F., Sankov V.A., Melnikova V.I., Delvaux D. (1996) Present-day stress field changes along the Baikal rift and tectonic implication. Tectonics. V.15, N6. - P. 1171-1191.

Radziminovitch N., Deverchere J., Melnikova V., San'kov V., Giljova N. (2005) The 1999*M*w 6.0 earthquake sequence in the southern Baikal rift, Asia, and its seismotectonic implications Geophys. J. Int. V.161. P. 387–400.

San'kov V.A., Lukhnev A. V., Miroshnichenko A.I., Ashurkov S.V., Byzov L.M., Dembelov M.G., Calais E., Deverchère J. (2009) Extension in the Baikal Rift: Present-Day Kinematics of Passive Rifting. Doklady Earth Sciences. Vol. 425, No. 2. P. 205–209.

San'kov V., Deverchere J., Gaudemer Y., Houdry F., Filippov A. (2000) Geometry and rate of faulting in the North Baikal Rift, Siberia. Tectonics. V.19, №4. P. 707-722.

Sankov V.A., Dobrynina A.A. Current seismic hazard estimation for South Baikal basin (Baikal rift system, Siberia) using seismicity and GPS data. Geophysical Research Abstracts, Vol. 11, EGU2009-7956, 2009. EGU General Assembly 2009.

Timofeev V.Yu., Ardyukov D.G., Boiko E.V. (2009) Current motions of Gorny Altai. Physical mezomechanics. V 12, № 1. P. 45–54. (in Russian).

Tychkov S.A., Kuchai O.A., Bushenkova N.A., Bragin V.D., Kalmetieva Z.A. (2008) Current crustal deformation in the northern Tien Shan: GPS and seismological data. Russian Geology and Geophysics. V.49. P.280–290.

Zubovich A.V., Mukhamediev Sh.A. (2010) A method of superimposed triangulations for calculation of velocity gradient of horizontal movements: application to the Central Asian GPS network. Geodynamics & Tectonophysics. V. 1. № 2. P. 169–185.

5. Seismic Risk Assessment and Management in the Russian Federation 2007-2010

N. I. Frolova, Frolova@comail.ru**.** *Seismological Center, Institute of Environmental Geosciences, Russian Academy of Sciences, Nikoloyamskaya str., 51, Moscow 109004, Russia.*

Natural disasters including earthquakes are becoming more frequent and devastating. Social and economic losses due to negative events increase annually, which is definitely dealt with evolution of society. Natural hazards identification and analysis, as well natural risk assessment and mapping are the first steps in prevention strategy aimed at saving lives and protecting property against future events. During the past years much attention was paid in Russia to seismic risk and other natural risk reduction within the Russian Federal Program "Natural and Technological Risk Reduction and Management in the Russian Federation up to 2005 and 2010" and Council of Europe Partial Agreement Program on Major Hazards.

The chapter of the report addresses the methodological issues of seismic and integrated natural risk assessment and mapping at different levels. The most hazardous natural processes, which may results in fatalities, injuries and economic loss in the Russian Federation, are considered. They are earthquakes, landslides, mud flows, floods, storms, avalanches. The special GIS project was developed which includes the information about hazards' level and reoccurrence, impact databases for the last 20 years, as well as mathematical models for estimating damage and casualties due to these hazards. The examples of seismic and integrated natural risk estimations and mapping at different levels are given. The results of integrated natural risk assessment are essential (practical) inputs for planning and implementation the preventive measures at national and local authorities levels, as well as by EMERCOM of Russian Federation.

The Extremum System assigned for loss estimations worldwide was improved within the Council of Europe Partial Agreement Program on Major Hazards and the Russian Federal Program "Natural and Technological Risk Reduction and Management in the Russian Federation up to 2010". The examples of expected loss estimations provided by Russian team to Executive Secretariat of Council of Europe and interested countries are presented.

Methodological issues of seismic and natural risk assessment

The section describes the procedures for individual and collective risk assessment due to earthquakes and other natural hazards, such as landslides, mud flows, floods, storms, avalanches, as well as integrated natural risk assessment. For estimation risk indexes and risk mapping the probabilistic approach.

Individual risk due to natural hazards is determined as the probability of death and/or injuries and/or economic loss to population due to possible natural hazards within one year in a given territory. Individual seismic risk [*Methods...,* 2000] may be determined through mathematical expectation of social losses $M(N_j)$ taking into account the number of inhabitants N in the considered settlement and probability of seismic event H

$$R_s = H \cdot V_s\ (I) = H \cdot M(N\ ) / N \tag{5.1}$$

where $V_s(I)$ – vulnerability of population for the considered settlement; H – probability of seismic event per one year; N – the number of inhabitants in the considered settlement.

The mathematical expectation of social losses $M(Nj)$ for the considered settlement taking into account inhabitant migration in the buildings of j type during the day and night is determined by equation

$$M(N_j) = \sum_{j=1}^{n} \iint_{S_c} \int_{0}^{24} \int_{I_{\min}}^{I_{\max}} P_{Cj}(I) \cdot f(x, y, I) \cdot \Psi_j(x, y) \cdot f(t) dI dt dx dy \tag{5.2}$$

where I_{min} и I_{max} – maximum and minimum possible earthquake intensity; S_c – settlement area; n – number of considered building types according to MMSK-86 scale; $P_{Cj}(I)$ – probability of fatalities and injuries under the condition of damage to buildings of j type due to earthquake with intensity I; $\psi_j(x,y)$ – density of population distribution within the considered area in buildings of j-type; $f(x,y,I)$ – density function of earthq0uakes' intensity probabilities within the unit area with coordinates x , y; $f(t)$ – function obtained on the basis of statistical analysis of data on population migration during 24 hours.

Individual risk due to landslides, mud flows, floods, storms, avalanches may be determined using statistical data on negative consequences due to these processes for the area under study by formula

$$R_{ei} = H \cdot P, \tag{5.3}$$

where R_{ei} - individual risk due to i-th emergency situation caused by natural hazard; H - probability of natural hazards per one year; P - probability of unfavorable event under the condition that natural hazard occurred. Dimension of individual risk is 1/year.

Integrated natural individual risk (R_e) may be determined taking into account the probability of death and/or injuries and/or economic loss to population due to all possible natural hazards within one year in the area under consideration by formula

$$R_e = 1 - \prod_{i=1}^{n} (1 - R_{ei}), \tag{5.4}$$

where n – number of considered natural hazards; R_{ei} — individual risk due to i-th natural hazard.

In the present study for estimating integrated individual and collective natural risks from earthquakes, landslides, mud flows, floods, storms, avalanches the assumption is made that all these events are independent.

Collective risk due to natural hazards R_{ec} is determined as expected number of casualties, both fatalities and injuries, as well as number of people who lost their property as a result of natural hazards' occurrence per year.

$$R_{ec} = R_e \cdot N, \tag{5.5}$$

where R_e — integrated individual risk due to natural hazards under consideration, N - number of inhabitants in the area under study.

The estimations of collective seismic and integrated risks were made for the administrative areas of the Russian Federation.

Special GIS project for risk assessment and mapping

In order to estimate risks and construct the maps for the Russian Federation territory the special GIS project was developed in 2009 by Extreme Situations Research Center and laboratory of seismic risk of IGE, RAS. It includes data bases with information which describes the Russian Federation territory, software assigned for hazard and risk indexes' assessment, interface which allows thematic maps and text report to be created according to established forms.

The data bases contain the information describing geographical position of the territory, its structure, main landmarks and boundaries' shape. The main sources of the information are digital and paper maps of average scales, thematic maps with description of zones characterized by different levels of natural hazards, statistical data about natural hazards' impact.

Thematic information about landslides, mud flows, floods, storms, avalanches is presented as vector digital maps with detailed description of zones characterized by different hazard levels and reoccurrence period. The information is developed by the laboratories of geological risk and geoinformatics and computer mapping of IGE RAS. The maps of review seismic zoning of Russian Federation RSZ-97, scale 1:8000000, developed by Institute of Physics of the Earth RAS (http://seismos-u.ifz.ru/zoning.htm) were used as the source of information about seismic hazard levels. **Fig.5.1** shows the special GIS screen assigned to visualize different natural hazards, **Fig.5.2** – integrated indexes of natural hazards for the Russian Federation territory.

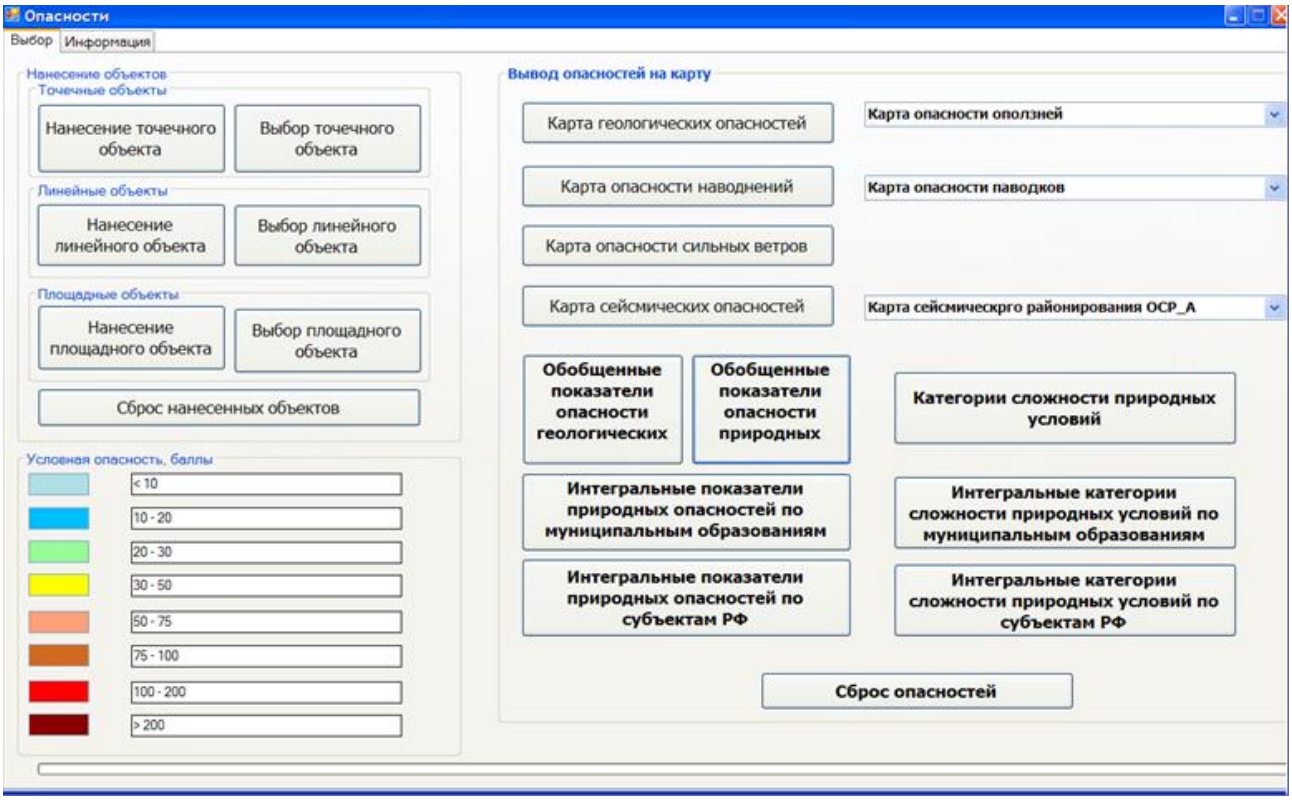

Fig.5.1. Screen of the special GIS for natural hazards visualization.

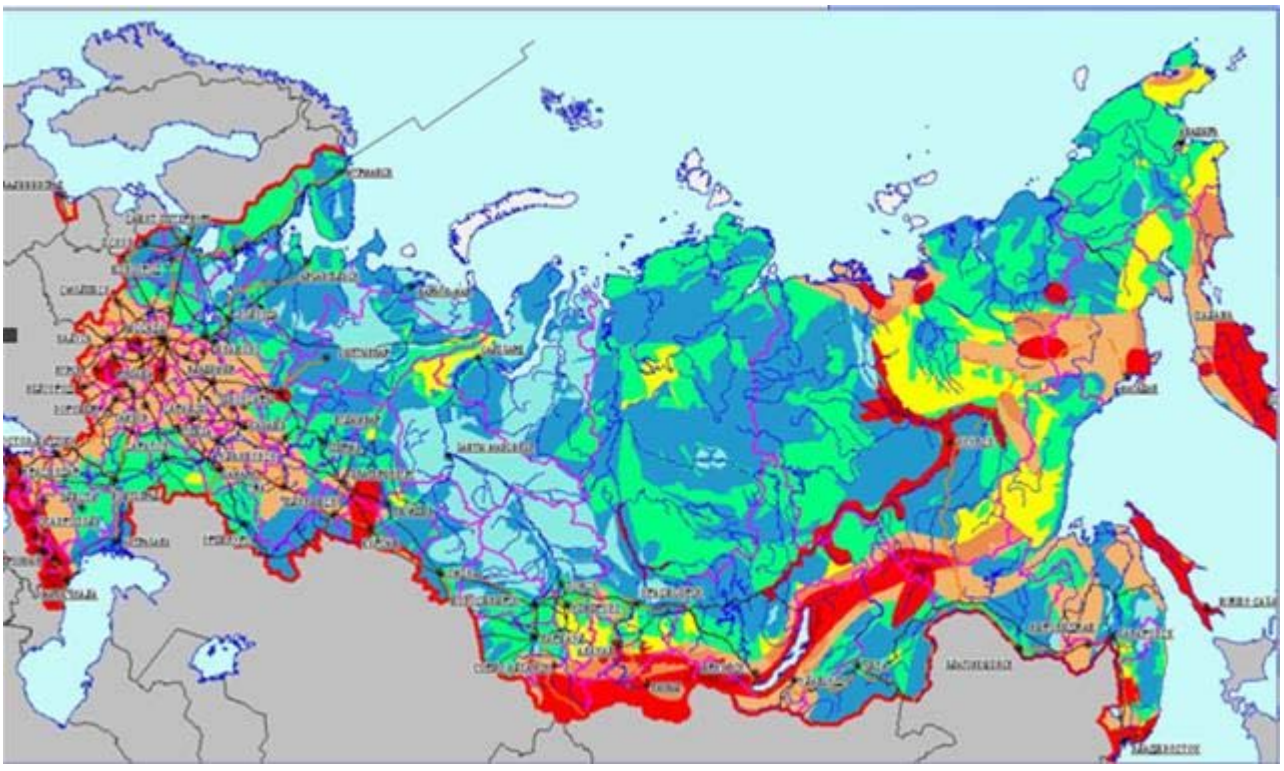

Fig.5.2. Map of integrated natural hazard for the territory of Russian Federation.

The GIS project includes also impact data base which was developed by laboratory of seismic risk of IGE, RAS. It contains brief descriptions about consequences of emergencies caused by natural hazards during the last 20 years from 1991 up to 2010 in the Russian Federation.

GIS project software includes three blocks used for data management, computation of risk indexes and visualization of space information at screen as the thematic maps of fixed scales.

The software allows integrated natural risk levels to be estimated at national level on the basis of statistical information about past events during the last 20 years, as well as separate and integrated natural hazards risk indexes to be evaluated. It allows natural risk evaluations to be visualized for administrative areas and regions of the country. **Fig.5.3** shows visualization of zones characterized by different integrated individual natural risk levels computed using empirical data on past events' consequences.

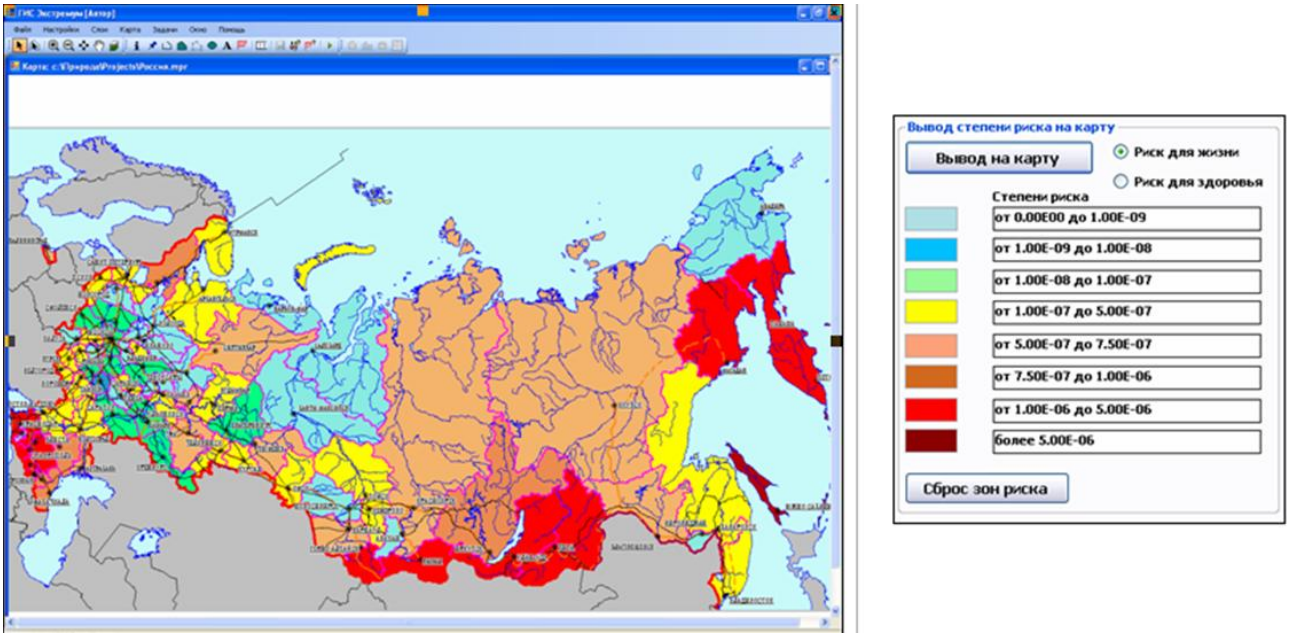

Fig.5.3. Visualization of integrated natural risk.

Zones with level of individual integrated risk from earthquakes, landslides, mud flows, floods, storms, avalanches above 1.0×10^{-6} are shown by red and dark brown colors.

Seismic risk assessment and mapping

Simulation models of special GIS project were used for computation of individual and collective seismic risks for the territory of Russian Federation. Values of seismic risk obtained for separate cities and settlements were averaged within the administrative regions of the country. Three maps of individual seismic risk were constructed: R_s1 – probability of fatalities, R_s2 – probability of fatalities and injuries, R_s3 - probability of fatalities and injuries, economic loss to population due to earthquakes within one year. Three maps of collective seismic risk were constructed as well: $R_{sc}1$ – expected number of fatalities due to earthquakes per year, $R_{sc}2$ – expected number of fatalities and injuries due to earthquakes per year, $R_{sc}3$ – expected number of fatalities and injuries, as well as those who lost their property due to earthquakes per year. **Fig.5.4** shows the map of individual seismic risk zoning R_s2: probability of fatalities and injuries.

Obtained values of individual seismic risk vary from negligible ones close to zero up to rather high values – more than $300 \cdot 10^{-6}$ for the probability of fatalities (map R_s1), more than $1{,}000 \cdot 10^{-6}$ for the probability of fatalities and injuries (map R_s2), more than $1{,}500 \cdot 10^{-6}$ for the probability of fatalities, injuries and economic loss to population caused by earthquakes per year (map R_s3). **Table 5.1** shows size of zones with different levels of individual seismic risk according to maps R_s1, R_s2 and R_s3.

Fig.5.5 shows the map of collective seismic risk zoning $R_{sc}2$: expected number of fatalities and injuries due to earthquakes per one year.

Obtained values of collective seismic risk vary from negligible small ones – less than $1 \cdot 10^{-6}$ up to rather high values – more than $10{,}000 \cdot 10^{-6}$ for expected number of fatalities (map $R_{sc}1$), more than $50{,}000 \cdot 10^{-6}$ for expected number of fatalities and injuries (map $R_{sc}2$) and for expected number of fatalities, injuries and number of persons who lost their property (map $R_{sc}3$). **Table 5.2** shows size of zones with different levels of collective seismic risk according to maps $R_{sc}1$, $R_{sc}2$ and $R_{sc}3$.

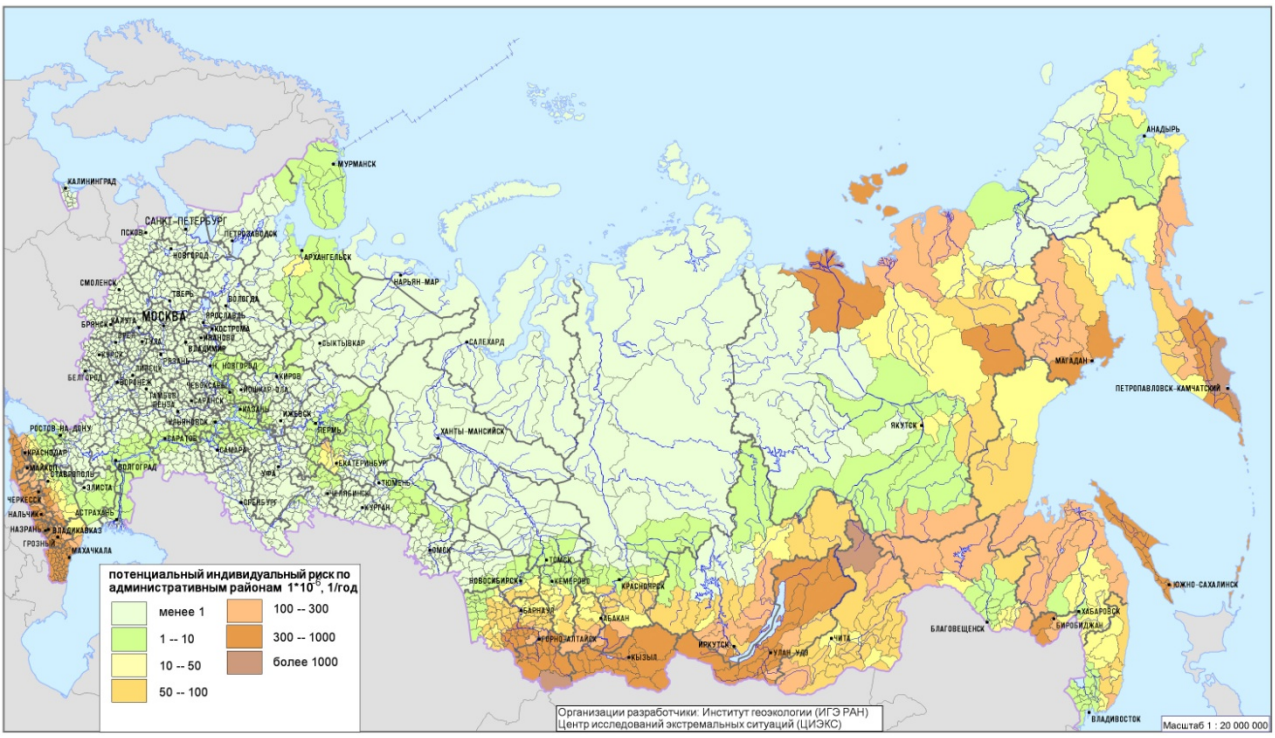

Fig.5.4. Map of individual seismic risk for the territory of Russian Federation.

Table 5.1. Values of individual seismic risk and size of zones with different risk levels.

Risk ranges, 10^{-6},1/year	Qualitative risk characteristics	Square of zones, map R_s1		Square of zones, map R_s2		Square of zones, map R_s3	
		10^6, km^2	%	10^6, km^2	%	10^6, km^2	%
Less than 1	small	8.8	53	8.1	49	7.6	46
1 – 10	moderate	2.5	15	2.9	17	2.2	13
10 – 50	average	2.4	14	1.5	9	1.9	11
50 – 100	high	1.2	7	1.4	8	0.9	5
100 – 300	rather high	1.2	7	1.5	9	1.8	11
300 – 1000	extremely high	0.5	3	1.1	7	1.6	10
1,000 – 1,500		-	-	0.1	1	0.2	1
More than 1,500		-	-	-	-	0.4	2

The computed values of individual seismic risk R_s1 are more than $300 \cdot 10^{-6}$ 1/year for all administrative divisions within Sakhalin area, Republic of Altaj, Tyva, Dagestan and Northern Osetiya. The highest values of individual seismic risk R_s3 are obtained for Kamchatka, near lake Baikal, Republic of Buryatiya, Irkutsk region, Altaj kraj, as well as for Krasnodar region and Chechen Republic.

Integrated risk assessment and mapping

Individual risks from separate natural hazards: landslides, mud flows, floods, storms, avalanches were computed according to equation (3) using regional empirical data about each hazard consequences during the last 20 years. Integrated individual risk from all considered six hazards (earthquakes, landslides, mud flows, floods, storms, avalanches) was computed according to equation (4). Three maps of integrated individual natural risk were constructed: R_e1 – probability of fatalities, R_e2 – probability of fatalities and injuries, R_e3 - probability of fatalities and injuries, economic loss to population due to six hazards within one year. Three maps of integrated collective natural risk were constructed as well: $R_{ec}1$ – expected number of fatalities due to six hazards per year, $R_{ec}2$ – expected

number of fatalities and injuries due to six hazards per year, $R_{ec}3$ – expected number of fatalities and injuries, as well as those who lost their property due to six hazards per year. **Fig.5.6** shows the map of integrated individual natural risk zoning R_e3: probability of fatalities, injuries and economic loss to population due to six hazards within one year.

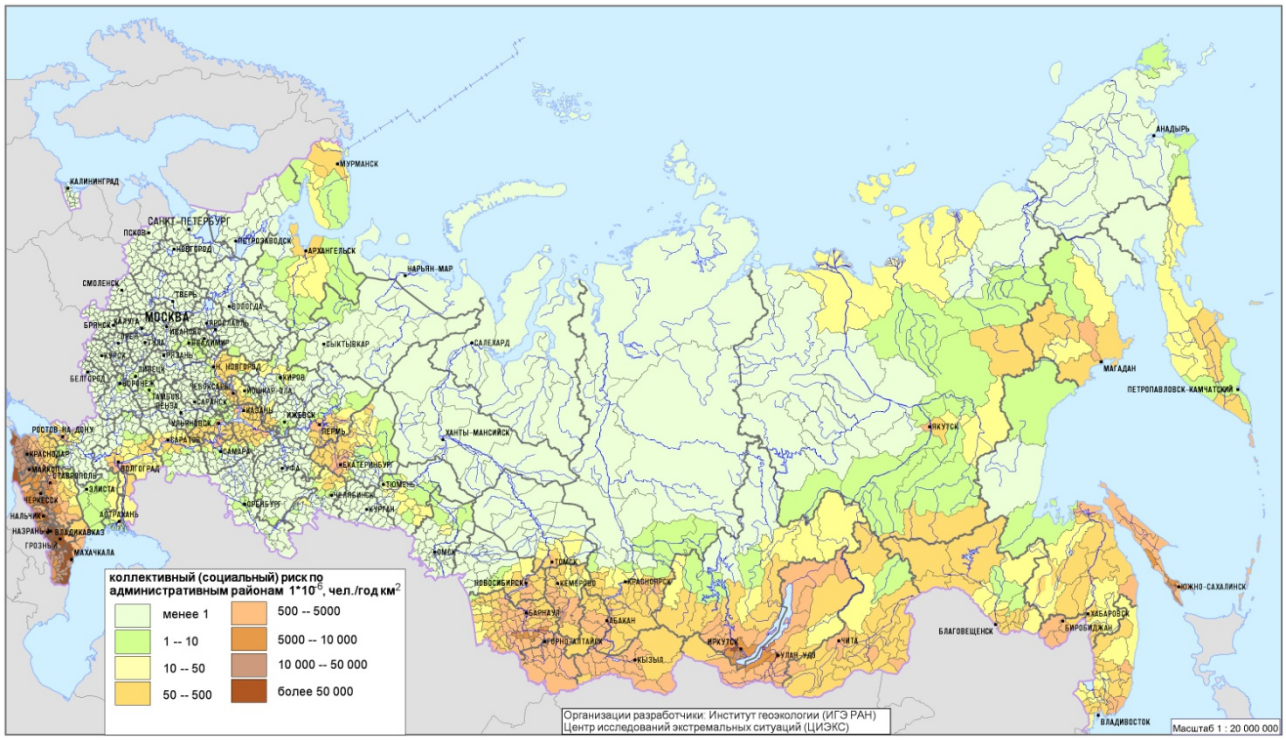

Fig.5.5. Map of collective seismic risk for the territory of Russian Federation.

Table 5.2. Values of collective seismic risk and size of zones with different risk levels.

Risk ranges, 10^{-6} persons/year·km^2	Qualitative risk characteristics	Square of zones, map $R_{sc}1$		Square of zones, map $R_{sc}2$		Square of zones, map $R_{sc}3$	
		10^6, km^2	%	10^6, km^2	%	10^6, km^2	%
Less than 1	small	9.7	58.4	8.9	53.6	8.1	48.8
1 – 10	moderate	2.5	15.1	2.4	14.5	2.8	16.9
10 – 50	average	2.1	12.7	2.0	12.0	1.6	9.6
50 – 500	high	1.7	10.2	2.2	13.3	2.6	15.7
500 – 5000	rather high	0.5	3.0	0.9	5.4	1.2	7.2
5000 – 10000	extremely high	0.06	0.4	0.08	0.5	0.1	0.6
10000 – 50000		0.06	0.4	0.08	0.5	0.1	0.6
More than 50000		-	-	0.04	0.2	0.1	0.6

Obtained values of integrated individual natural risk vary from negligible ones close to zero up to rather high values – more than $300 \cdot 10^{-6}$ for the probability of fatalities (map R_e1), more than $1{,}000 \cdot 10^{-6}$ for the probability of fatalities and injuries (map R_e2), more than $1{,}500 \cdot 10^{-6}$ for the probability of fatalities, injuries and economic loss to population caused by six hazards per year (map Re3). **Table 5.3** shows size of zones with different levels of integrated individual natural risk according to maps Re1, Re2 and Re3.

Table 5.4 shows the number of Russian Federation inhabitants in the zone with different level of integrated natural risk.

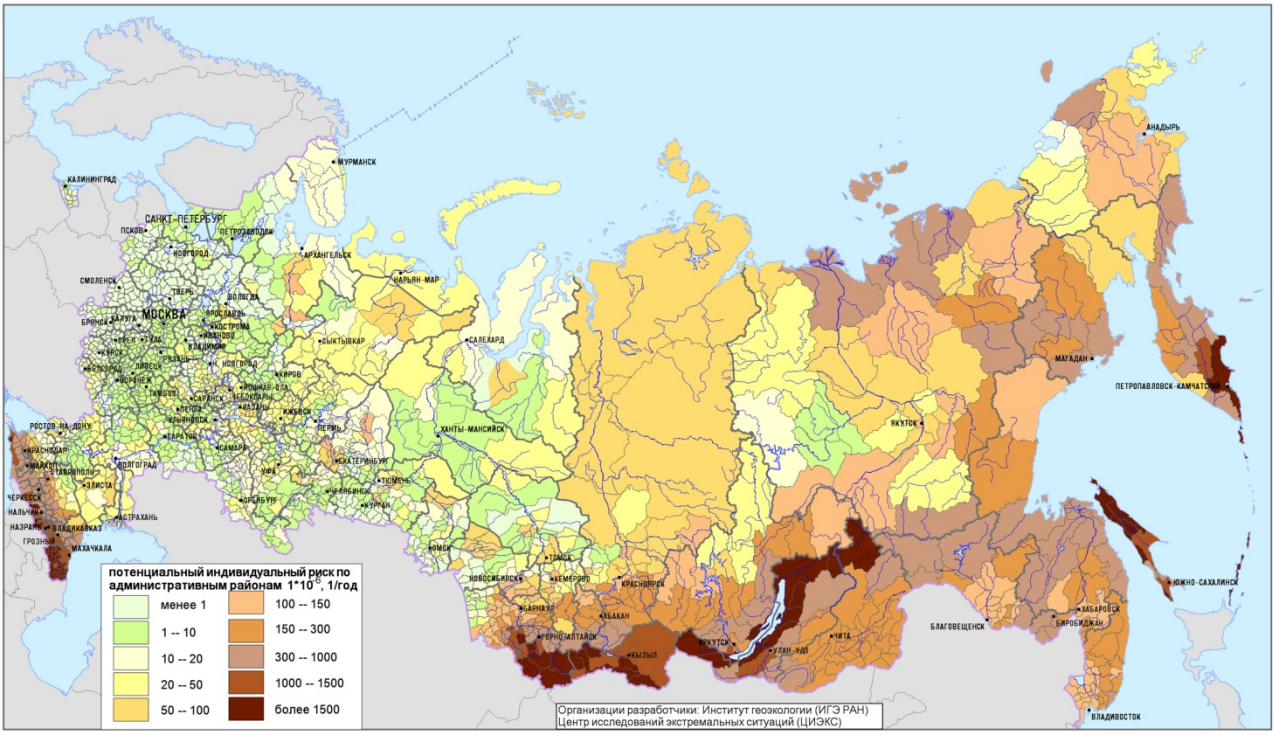

Fig.5.6. Map of integrated individual natural risk for the territory of Russian Federation.

Table 5.3. Values of integrated natural risk and size of zones with different risk levels.

Risk ranges, 10^{-6},1/year	Qualitative risk characteristics	Square of zones, map R_e1		Square of zones, map R_e2		Square of zones, map R_e3	
		10^6, km^2	%	10^6, km^2	%	10^6, km^2	%
Less than 1	small	7.9	48	5.7	34	1	6
1 – 10	moderate	3.3	20	5	30	1.9	11
10 – 20	average	0.9	5	0.5	3	1.6	10
20 – 50		1.6	10	1.2	7	2.6	16
50 – 100	high	1.1	7	1.4	8	3.5	21
100 – 150	rather high	0.5	3	0.4	2	1.6	10
150 – 300		0.7	4	1.1	7	1.6	10
300 – 1,000	extremely high	0.6	4	1.2	7	2.1	13
1,000 – 1,500		-	-	0.1	1	0.2	1
More than 1,500		-	-	-	-	0.5	3

The highest values of integrated individual natural risk R_e1 are obtained for the same areas as for individual seismic risk: Kamchatka, near Lake Baikal, Republic of Buryatiya, Irkutsk region, Altaj kraj, as well as for Krasnodar region and Chechen Republic. It could be explained by the fact that among considered 6 natural hazards earthquake are more often result in fatalities in comparison with landslides, mud flows, floods, storms, avalanches.

In Sakhalin, Republic of Altaj, Tyva, Dagestan, Northern Osetiya computed values of R_e1 exceed 300-400·10-6, 1/year for 70% territory of their administrative divisions.

The highest values of integrated individual natural risk R_e3 are obtained for Kamchatka, Republic of Altaj, Krasnodar area, Baikal area, Republics of Buryatiya and Tyva, Sakhalin and Northern Osetiya.

Fig.5.7 illustrates the contribution of earthquakes to the integrated individual natural risk in the earthquake prone area, Krasnodar region. Contribution of hazards to integrated risk R_e3 are shown in the centers of administrative divisions by circles: red color – contribution of earthquakes, blue color – contribution of landslides, mud flows, floods, storms, avalanches.

Table 5.4. Number of inhabitants in zones with different risk levels.

Risk ranges, 10^{-6},1/year	Number of inhabitants, map R_e1		Number of inhabitants, map R_e2		Number of inhabitants, map R_e3	
	thous., pers.	%	thous., pers.	%	thous., pers.	%
Less than 1	91452	61	73370	49	22566	15
1 – 10	30114	20	46440	31	45957	31
10 – 20	5345	4	1254	1	18514	12
20 – 50	7393	5	8396	6	21940	15
50 – 100	2580	2	4844	3	8496	6
100 – 150	3456	2	737	0	9776	6
150 – 300	5861	4	5299	4	7239	5
300 – 1,000	4786	3	10616	7	9884	7
1,000 – 1,500	-	-	30	0.02	3941	3
More than 1,500	-	-	-	-	2194	1

The obtained estimations of integrated individual and collective natural risk from earthquakes, landslides, mud flows, floods, storms, avalanches are used by EMERCOM of Russian Federation, as well as by other federal and local authorities for planning and implementation the preventive measures aimed at saving lives and protecting property against future events.

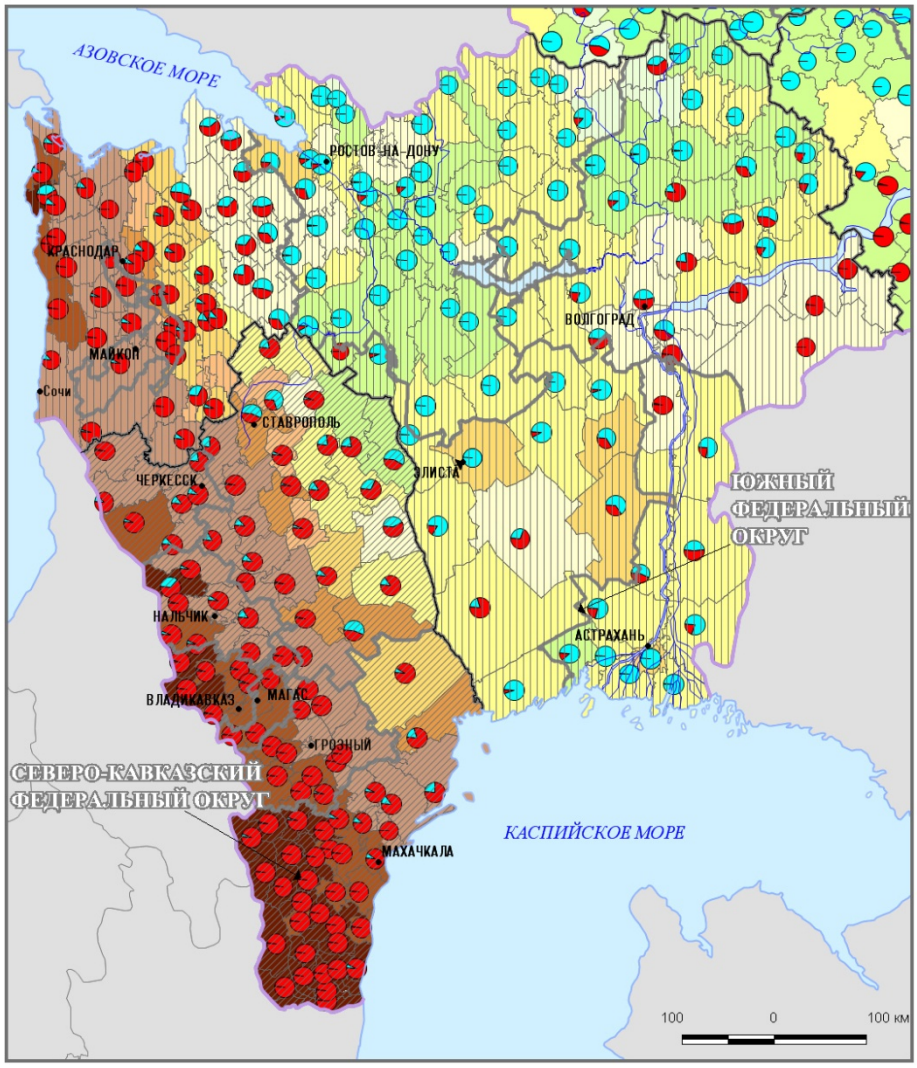

Fig.5.7. Map of integrated individual natural risk R_e3 for the Northern Caucasus.

Extremum System for earthquake loss estimations worldwide

In 2007-2010 the Extremum System mathematical models and databases assigned for loss estimations worldwide were updated within the Council of Europe Partial Agreement Program on Major Hazards and the Russian Federal Program "Natural and Technological Risk Reduction and Management in the Russian Federation up to 2010" by joint efforts of Extreme Situations Research Center, Seismological Center of IGE, RAS and VNII GOChS, EMERCOM of Russia.

The procedure [*Larionov et al.,* 2003a; *Larionov et al.,* 2003b] of expected damage and loss assessment in "emergency mode", using the different system versions, includes:

1. information about the earthquake parameters (origin time, epicenter coordinates, depth, magnitude) is taken automatically from web-sites of seismological surveys, or received by e-mail messages;
2. computation of expected damage extent, social and economic losses (and, eventually, identification of the effective response measures);
3. expert review of the results obtained with the help of a knowledgebase about past events;
4. validation of expected consequences estimation;
5. dissemination of messages about expected damage and losses.

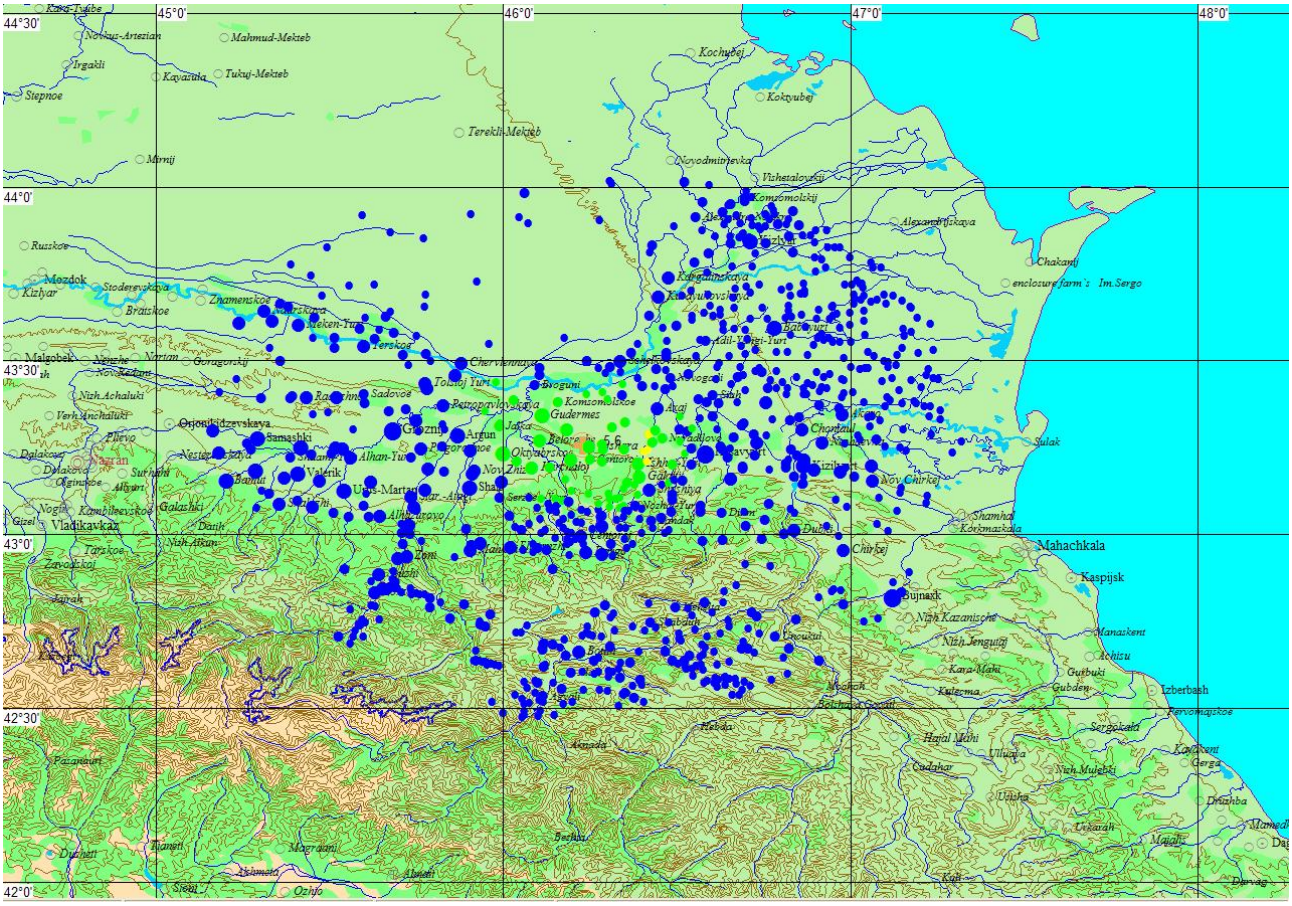

Fig.5.8. Results of possible loss assessment caused by October 11, 2008 earthquake in Russia: dots are settlements in the stricken area; colour of dots shows the average damage state of building stock (yellow: *d*=2, green : *d*=1, blue: no damage).

The results of computations are usually presented as maps and tables, where estimates of expected number of fatalities, injuries and homeless are given for the whole stricken area and for each settlement. The estimations are also given about the requirements in forces and resources needed for rescue and relief operations. **Fig.5.8** and **5.9** shows maps with the results of expected damage and loss computations for the earthquake occurred on 11 October 2008 in Russian Federation. Dots of different size and color show the settlements in the stricken area; the dot size stands for the number of

inhabitants; the dot color tells the expected "averaged" damage state of the buildings. The maps are of different scale: map on the **Fig.5.8** gives the general idea about the area where the earthquake was felt. In principal, there was no damage in the settlements shown by blue color on the map. In the settlements shown by green and yellow colors the average damage state was "light" (*d*=1) and "moderate" (*d*=2), but some buildings survived damage states "heavy" (*d*=3) and few even damage states "partial and total collapse" (*d*=4 and 5). The expected distribution of building stock, which survived various damage states, for definite settlements are usually given in the tables (**Table 5.5**). The reliability of loss computations in emergency mode depends on many factors [*Bonnin et al.,* 2002; *Bonnin et al.,* 2004; *Frolova et al.,* 2003a; *Frolova et al.,* 2003b; *Frolova et al,* 2007; *Frolova et al.,* 2009, *Frolova et al.,* 2010]. First of all, it is influenced by error the earthquake parameters determination by Seismological Surveys. The other factors that contribute to the reliability of output results are databases on elements at risk and parameters of simulation models used in the Extremum System.

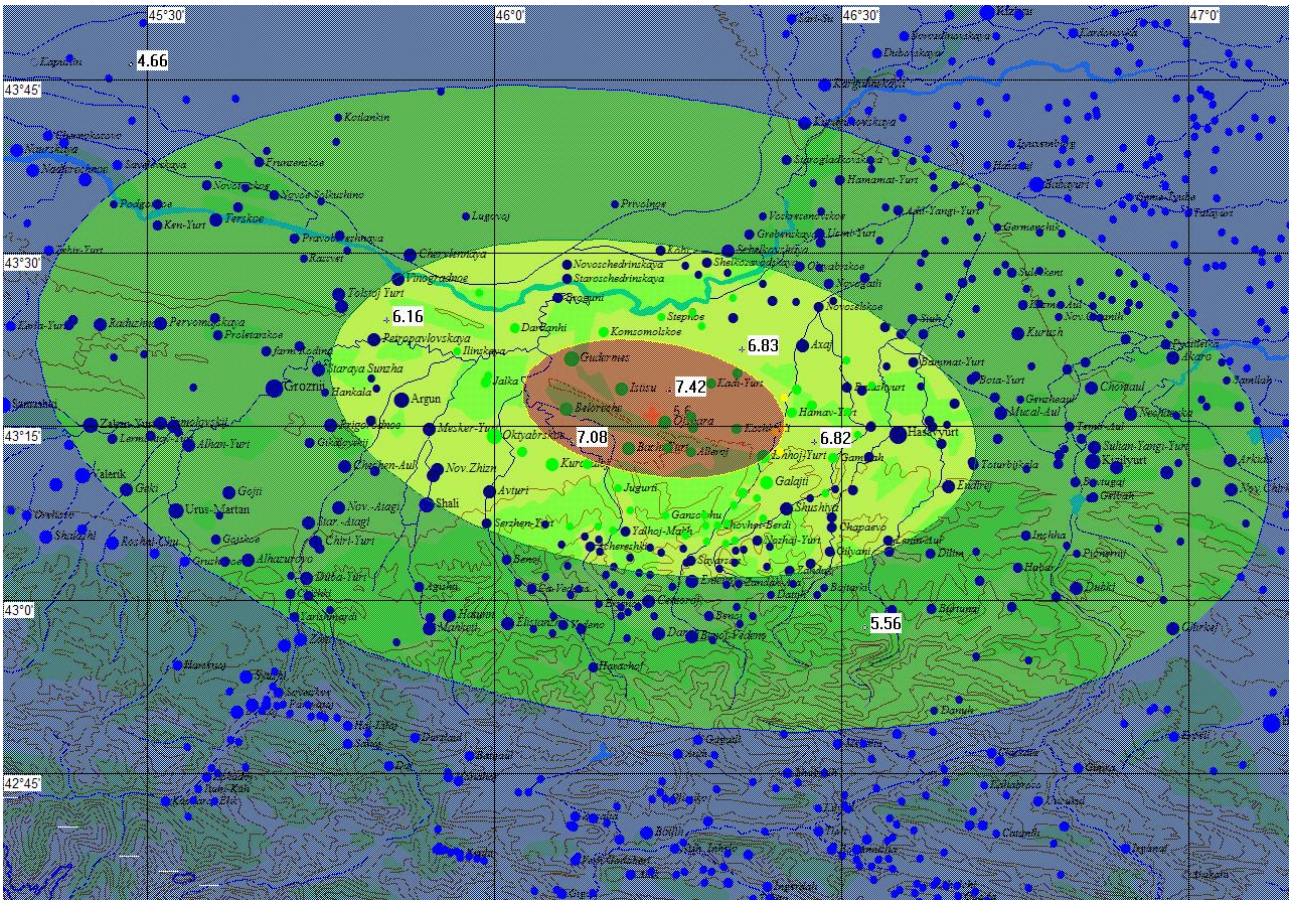

Fig.5.9. Results of possible loss assessment caused by October 11, 2008 earthquake in Russia: figures show the values of expected shaking intensities.

At the first stage of loss computations the shaking intensity is simulated (**Fig.5.9**). In order to take in to account the regional peculiarities of attenuation laws the computations are made with usage of various parameters of macroseismic field obtained by different researcher for the area under study. This information is accumulated in the knowledgebase of the Extemum system.

The simulated estimations of expected shaking intensities and losses are usually compared with observed macroseismic effect and reported damage. **Fig.5.3** shows the comparison of observed values of intensities and the results of computations with usage of different values of regional coefficients of macroseismic field: variant 1 – proposed by Shebalin [*Kondorskaya, Shebalin*, 1977] for Dagestan, variant 4 - proposed by Shebalin [*Kondorskaya, Shebalin*, 1977] for the Northern Caucasus, variant 5 - proposed by Shebalin [*Kondorskaya, Shebalin*, 1977] for the Caucasian States; variant 6 – proposed by Bystritskaya [*Bystistkaya*, 1978]; variant 7 – proposed by Lutikov [*Aver'yanova et al.,* 1996] for the

Chechen Republic; variant 12 - proposed by Shebalin [*Shebalin*, 2003]. The input parameters for computations according different variants are presented in **Table 5.6.** The circular isoseists obtained with Shebalin equation application are stretched along the active tectonic faults in order to take into account anisotropy of the medium and source line extension. Expected shaking intensity maps are computed taking into account various regional coefficient of macroseismic field, different orientation of ellipse axis (along the faults or they may be oriented at the angle according to the source mechanism solution), as well as empirical data about ratio k of ellipse major and minor semi-axis (for different value of k).

Table 5.5. List of the settlements in the affected area (fragment).

Settlement name		I_{exp}	Expected fatalities	Expected injured	Portion of buildings survived different damage states					Relative economic losses
English	Russian				d=1	d=2	d=3	d=4	d=5	
Gudermes	Гудермес	6.90	2-15	6-70	0.21	0.16	0.09	0.02	0.00	0.09
Istisu	Истису	7.19	1-11	5-41	0.21	0.16	0.10	0.04	0.01	0.12
Suvirov-Yurt	Суворов-Юрт	7.22	2-11	5-40	0.22	0.17	0.12	0.05	0.01	0.14
Bachi-Yurt	Бачи-Юрт	7.07	1-8	2-35	0.19	0.15	0.09	0.03	0.00	0.10
Beloreche	Белоречье	7.04	1-8	2-35	0.19	0.15	0.09	0.03	0.00	0.10
Hasavyurt	Хасавюрт	6.25	0-2	0-23	0.13	0.05	0.01	0.00	0.00	0.01
Centoroj	Центорой	7.12	1-5	2-19	0.21	0.16	0.10	0.04	0.01	0.12
Ishhoj-Yurt	Ишхой-Юрт	6.85	0-3	2-15	0.18	0.13	0.06	0.01	0.00	0.06
Kurchaloj	Курчалой	6.67	0-2	0-15	0.16	0.10	0.04	0.01	0.00	0.04
Koshkeldi	Кошкельды	7.05	1-4	3-12	0.19	0.15	0.09	0.03	0.00	0.10

Table 5.6. Input data for simulation of the Kurchaloj event consequences with the Extremum System application.

#	Event parameters	Regional coefficients in macroseismic field equation	Ratio k of ellipse semi-axis	Orientation of ellipse axis
1	43.276; 46.229; M=5.6; h=15 ; instrumental source, GS RAS	b=1,5; ν=3,6; c=3,1 for Dagestan (*Shebalin*, 1977)	k=1.5	Along faults
2	43.276; 46.229 ; M=5.6; h=15 ; instrumental source, GS RAS	b=1,5; ν=3,6; c=3,1 for Dagestan (*Shebalin*, 1977)	k=2	Along faults
3	43.276; 46.229 ; M=5.6; h=15 ; instrumental source, GS RAS	b=1,5; ν=3,6; c=3,1 for Dagestan (*Shebalin*, 1977)	k=4	Along faults
4	43.276; 46.229 ; M=5.6; h=15 ; instrumental source, GS RAS	b=1,6; ν=3,1; c=2,2 for NorthernCaucasus (*Shebalin*, 1977)	k=1.5	Along faults
5	43.276; 46.229 ; M=5.6; h=15 ; instrumental source, GS RAS	b=1,4; ν=3,5; c=4,2 for Caucasus (*Shebalin*, 1977)	k=1.5	Along faults
6	43.276; 46.229 ; M=5.6; h=15 ; instrumental source, GS RAS	b=1.52; ν=3.6; c=1.6 for Dagestan (*Bystristkaya*, 1978)	k=1.5	Along faults
7	43.276; 46.229 ; M=5.6; h=15 ; instrumental source, GS RAS	b=1.593; ν=3.41; c = 2.44 for Groznyj City (*Aver'yanova et al.,* 1996)	k=1.5	Along faults
8	43.3; 46.3; M=5.9; h=10 NEIC	b=1,5; ν=3,6; c=3,1 for Dagestan (*Shebalin*, 1977)	k=1.5	Along faults
9	43.47; 46.34; M=5.9; h=15 CSEM	b=1,5; ν=3,6; c=3,1 for Dagestan (*Shebalin*, 1977)	k=1.5	Along faults
10	43.37; 46.35; M=5.6; h=10 Verified, GS RAS	b=1,5; ν=3,6; c=3,1 for Dagestan (*Shebalin*, 1977)	k=1.5	Along faults
11	43.15; 46.10; M=5.6; h=15 macroseismic source, GS RAS	b=1,5; ν=3,6; c=3,1 for Dagestan (*Shebalin*, 1977)	k=1.5	Along faults
12	43.276; 46.229 ; M=5.6; h=15 instrumental source, GS RAS	b=1,5; ν=4; c=3,8 (*Shebalin*, 2003)	k=1.5	Along faults

In the case of the 2008 Kurchaloj earthquake more general parameters of macroseismic field equation (variant 12), which was proposed by *Shebalin N.V.*, allowed to simulate shaking intensity which proved to be close to observed values of shaking intensities (**Fig.5.10**).

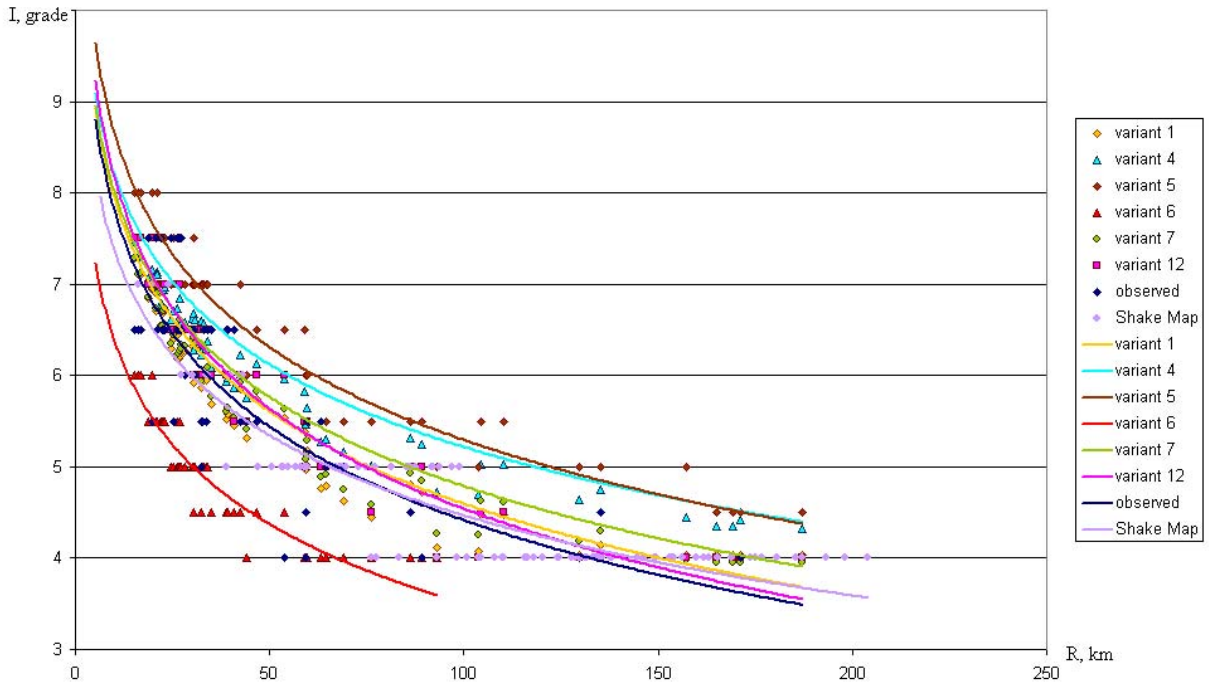

Fig.5.10. Comparison of simulated shaking intensities with application of different attenuation law parameters and observed values.

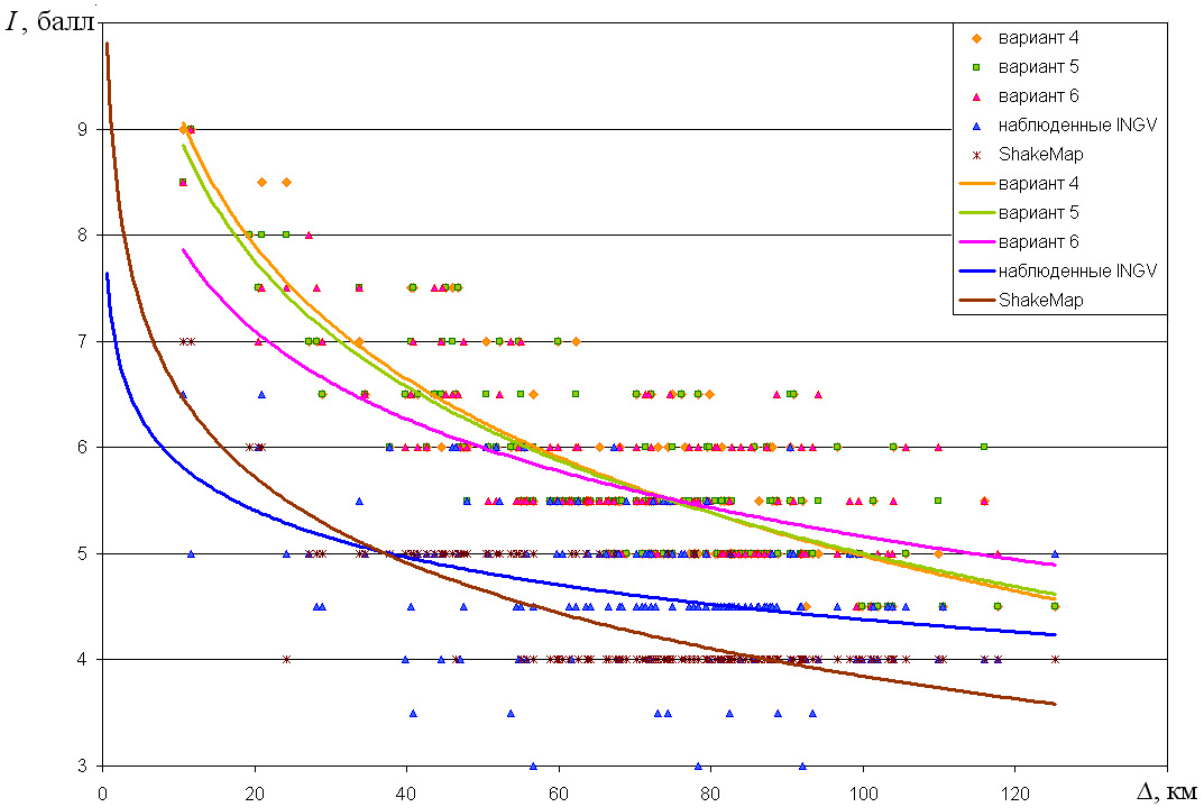

Fig.5.11. Influence of macroseismic field regional coefficients on simulated values of shaking intensities; INGV event parameters.

Table 5.7. Expected consequences assessment due to the L'Aquila earthquake in Italy.

Survey	Event parameters				Expected fatalities, persons
	Longitude	Latitude	M	h, km	
NEIC	13.334	42.334	6.3	8.8	280-1,400
EMSC	13.32	42.38	6.3	2	1,600-6,000
GS RAS	13.4	42.51	6.4	10	180-750

Table 5.8. Input data for simulation of the L'Aquila event consequences with the Extremum System application.

#	Event parameters	Regional coefficients of macroseismic field	Ratio *k* of ellipse semi-axis	Orientation of ellipse axis
1	43.334N; 13.334E M=6.3; h=8.8; NEIC	*b*=1,5; *ν*=3,5; *c*=3,0 (*Shebalin*, 1977)	k=1.5	Along faults
2	43.334N; 13.334E M=6.3; h=8.8; NEIC	*b*=1,5; *ν*=4,0; *c*=3,8 (*Shebalin*, 2003)	k=1.5	Along faults
3	43.334N; 13.334E M=6.3; h=8.8; NEIC	*b*=1,5; *ν*=4,0; *c*=3,8 (*Shebalin*, 2003)	k=3	Along faults
4	43.334N; 13.334E M=6.3; h=8.8; NEIC	*b*=1,5; *ν*=3,5; *c*=3,0 (*Shebalin*, 1977)	k=3	Along faults
5	43.334N; 13.334E M=6.3; h=8.8; NEIC	*b*=1,5; *ν*=3,5; *c*=3,0 (*Shebalin*, 1977)	k=3	Angle 127°
6	43.334N; 13.334E M=6.3; h=8.8; NEIC	*b*=1,5; *ν*=3,5; *c*=3,0 (*Shebalin*, 1977)	k=3	Angle 156°
7	43.334N; 13.334E M=5.8; h=8.8; INGV	*b*=1,5; *ν*=3,5; *c*=3,0 (*Shebalin*, 1977)	k=3	Angle 156°
8	43.334N; 13.334E M=5.8; h=8.8; INGV	*b*=1,5; *ν*=4; *c*=3,8 (*Shebalin*, 2003)	k=3	Angle 156°

In addition to estimations of expected shaking intensities, expected number of casualties (fatalities, injuries of different level, homeless), engineering situation (percent of buildings survived various damage states, length of blocked transportation systems, number of accidents at lifeline systems and so on) the Extremum System provides optionally information about the effective response measures for strong earthquakes. The estimations are given about the forces rescue operations (rescue mechanized teams, that of hand-operated debris disassembling, medical teams), that for urgent operations (fireman brigades, crash crew, policemen and so on), as well as about engineering devices needed for rescue and relief measures. The estimations are also made about the life-support for the people in the affected area: expected number of temporal shelters, heating devices in winter time and field kitchens; supply with water and food during the first days after the disaster. The estimations are made on the basis of empirical data about past events. The debris volumes and numbers of injured and homeless are used to assess the requirements in forces and resources. At present the relationship are reviewed in order to take into account new modern equipment used for rescue operations.

For the L'Aquila, Italy Earthquake of 6 April 2009 the expected loss computations in emergency mode were made with Extremum System application using the event parameters determined by three Seismological Surveys: NEIC, EMSC and GS RAS. **Table 5.7** shows the input data and the results of expected fatalities simulation.

When the data on source mechanism, reported macroseismic effect and damage become available the computations were repeated for different variants of input information (**Table 5.8**) in order to find the better agreement between simulated and observed effect.

Fig.5.11 shows the results of computation of expected intensity *I* for the earthquake parameters determined by INGV: φ=43.334N; λ=13.334E; M=5.8; h=8.8 km (variants 7 and 8). Simulation is made for different coefficients of macroseismic field according to [*Shebalin*, 1977] and [*Shebalin*,

2003]; and for macroseismic field orientation at the angle of 156° in accordance with source mechanism solution of GS RAS.

Fig.5.12. Map of active faults according to INGV (http://cnt.rm.ingv.it**)**.

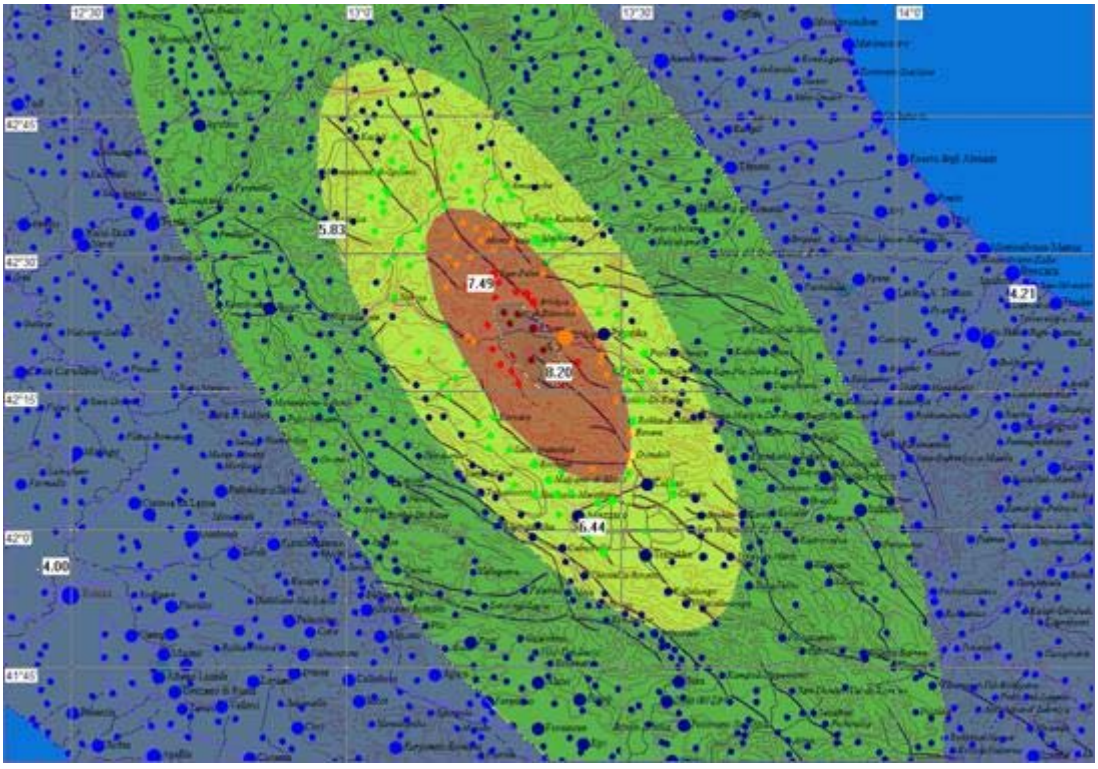

Fig.5.13. Results of possible loss assessment caused by April 6, 2009 earthquake in Italy; dots are settlements in the stricken area; colour of dots shows the average damage state (brown: *d*=4, red: *d*=3, yellow: *d*=2, green: *d*=1, blue: no damage); figures show the values of *I*.

Fig.5.12 shows active faults of the area under study, **Fig.5.13** shows the results of simulation of the L'Aquila earthquake consequences with the Extremum System application; input data are taken according to variant 7 (**Table 5.8**). The values of simulated intensities (pink, green and yellow curves in **Fig.5.11**) obtained with the Shebalin macroseismic field equation application [*Shebalin*, 1968] are higher than the observed values (blue curve in **Fig.5.11**), which were displayed at the INGV website

and were based on response of people who feel the earthquake. It was so called Internet intensities. The highest values of *I* were equal to 7 by EMS-98 scale for four settlements. It is possible to suggest that inhabitants whose buildings were severely damages or totally collapsed did not put their information about feelings at the INGV web site. According to the Preliminary Field Report [*Rossetto et al.,* 2009] by the UK Earthquake Engineering Field Investigation Team (EEFIT) at least in 2 settlements Onna and San Gregorio the engineering consequences for existing building stock were estimated as *I*=9 by EMS-98 scale, for other two settlements Malepasso and Paganica the effect was estimated as I=8, for L'Aquiala if was estimated between 7 and 8 on EMS-98 scale (**Fig.5.14**).

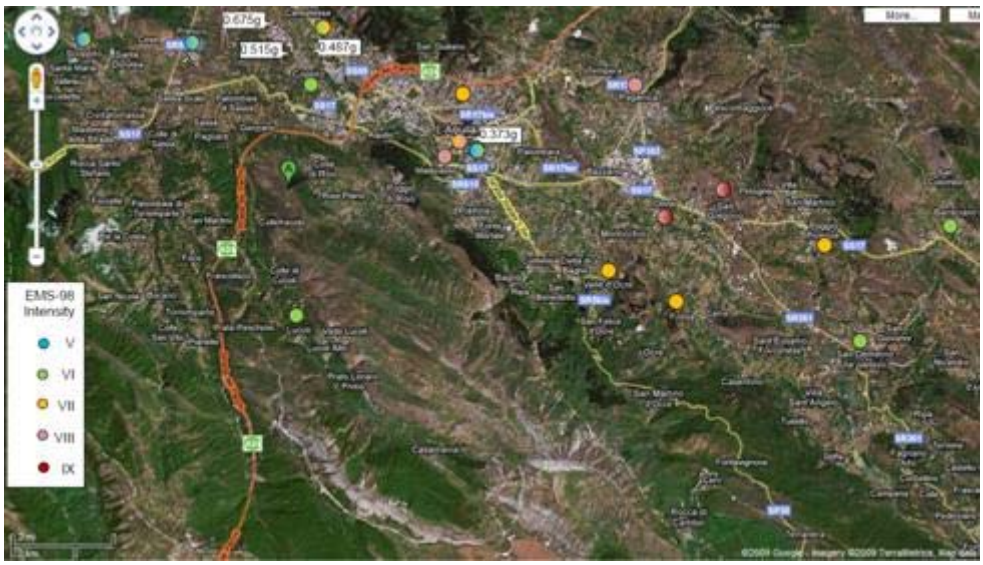

Fig.5.14. The results of EEFIT team survey of the L'Aquila event affected area [*Rossetto et al.,* 2009]: dots with two colors indicate the intensity lies between two values.

The information about buildings and structures behavior, about response measures published in the Preliminary Field Report by EEFIT [*Rossetto et al.,* 2009] and other similar publications will allow to verify data bases on elements at risk and impact knowledgebase of the Extremum System in order to determine more precisely the regional parameters of the simulation models for the area under consideration.

Fig.5.15 shows one more example of expected loss estimations due to the 12 January 2010 earthquake in Haiti. The computations were made for different input information about event parameters determined by GS RAS, EMSC and NEIC and two orientation macrosismic field according to the source mechanism solution.

The loss estimations obtained with NEIC parameters usage proved to be the closest to reported one, but the reported casualties will be changed by accumulation new information.

The 10 years experience of the Extremum System application for expected loss assessment due to strong earthquakes worldwide showed the merits and demerits of the System current version. Besides the error of Seismological Survey in event parameters determination in emergency mode there are other factors that contribute to uncertainties in results of computations. First of all, the data bases on elements at risk, impact data bases on past events should be verified and constantly maintained. It will allow to construct more accurate the regional attenuation laws and regional vulnerability functions for various elements at risk, as well to verify models for identification response measures taking into account new technological achievements in the field.

The analysis of simulation outputs and used input data allows to draw the conclusion that priority should be given to verification and standardization of data bases on elements at risk and impact data bases about past strong earthquakes, including information about the response measures, in order to increase the reliability of the results in emergency mode.

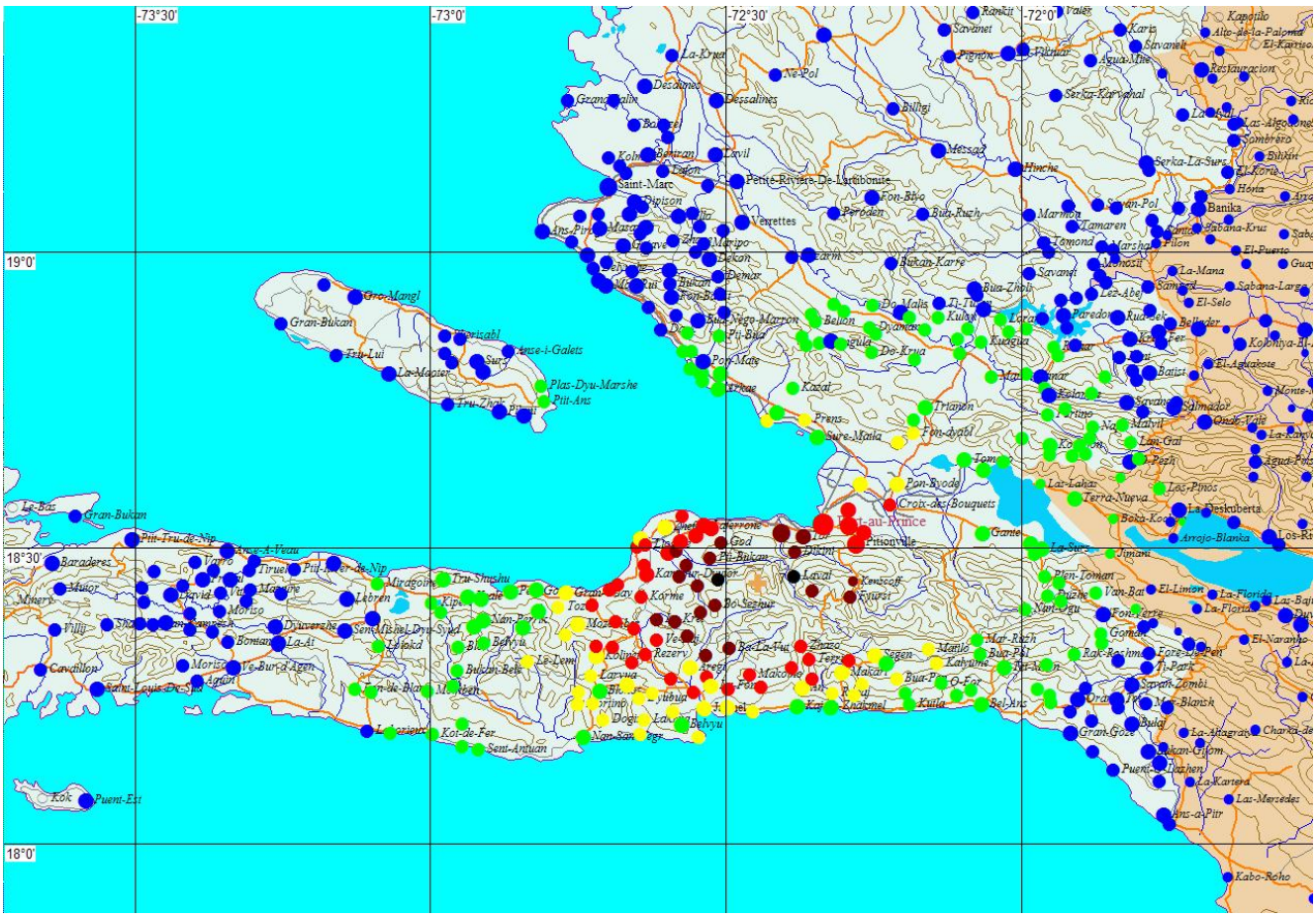

Fig.5.15. Results of possible loss assessment caused by January 12, 2010 earthquake in Haiti; dots are settlements in the stricken area; colour of dots shows the average damage state (black: d=5; brown: *d*=4, red: *d*=3, yellow: *d*=2, green: *d*=1, blue: no damage).

The last years experience of the Extremum System application also showed that there is a wide range for verification of simulation models used in the System at all stages from estimating shaking intensity to assessing the damage to different elements at risk and identification the effective response and relief measures. It is definite that the task is huge and hardly can be successfully solved in the nearest future without international efforts.

References

Aver'yanova V, Baulin Yu, Koff G, Lutikov A, Mindel I, Nesmeyanov S, Sevost'yanov V (1996), Complex estimation of seismic hazard for the Grozny city territory. Moscow: 48-51. (in Russian)

Bonnin J., Frolova N., Kozlov M., Larionov V., Sushchev S., Ugarov A. (2002), Experience of "Extremum" System Application for Operative Earthquake Loss Assessment. Proc. 28th General ESC Assembly, Genoa, Italy.

Bonnin J., Frolova N. (2004), Near Real-Time Loss Assessment Due To Strong Earthquakes: The State of The Art. Proc. XXIXth General Assembly of European Seismological Commission (ESC2004), Potsdam, Germany.

Bystristkaya Yu. (1978) Comparison of macroseismic and instrumental data (Dagestan earthquake): Seismicity and hydrogasgeochemistry for the Dagestan territory №2(17): 78-84.

Frolova N.I., Larionov V.I., Nikolaev A.V., Kozlov M.A., Ugarov A.N. (2003a), Analysis of Real Time Earthquake Information Applied For Possible Loss Assessment, *Proc. TIEMS2003 Conference*, Sofia Antipolis, France.

Frolova N., Kozlov M., Larionov V., Sushchev S., Ugarov A. (2003b), Extremum System for Earthquake Risk And Loss Assessment, *Proc. of SE-40EEE,* Skopje-Ohrid, Macedonia.

Frolova N., Larionov V., Bonnin J. (2007), Simulation-based information systems for multi-hazard risk and near real time loss estimations due to strong earthquakes, *Proc. TIEMS2007 Conference*, Trogir, Croatia.

Frolova N., Larionov V., Bonnin J. (2009), Challenges Of Global Earthquake Loss Estimation In Emergency Mode, Proc. TIEMS2009 Conference, Istanbul, Turkey.

Frolova N., Larionov V., Bonnin J. (2010), Data Bases Used In Worlwide Systems For Earthquake Loss Estimation In Emergency Mode: Wenchuan Earthquake, Proc. TIEMS2010 Conference, Beijing, China.

Kondorskaya N., Shebalin N., editors (1977) New catalogue of strong earthquakes for the USSR territory. Nauka, Moscow, 535P.

Larionov V., Frolova N. (2003a), Peculiarities of seismic vulnerability estimations. In : Natural Hazards in Russia, volume 6: Natural Risks Assessment and Management, Publishing House "Kruk", Moscow, pp.120-131. (in Russian).

Larionov V., Sushchev S., Ugarov A., Frolova N. (2003b), Seismic risk assessment with GIS-technology application. In : Natural Hazards in Russia, volume 6: Natural Risks Assessment and Management, Publishing House "Kruk", Moscow, pp. 209-231. (in Russian).

Methods of earthquake consequences forecast (2000), Moscow, VNII GOChS, Extreme Situations Research Center, Seismological Center ofIGE RAS, 2000, 27c. (in Russian).

Rossetto T., Peiris N., Alarcon J., So E., Sargeant S., Sword-Daniels V., Verrucci E., Del Re D., Free M. (2009). The L'aquila, Italy Earthquake of 6 April 2009 A Preliminary Field Report By Eefit, 53 P.

Shebalin N.V. (1968), Procedures of engineering seismological data application for seismic zoning. In: Seismic zoning of the USSR, Nauka, Moscow, pp.95-121 (in Russian).

Shebalin N.V. (1977). Reference earthquakes and macroseismic field equations// New catalogue of strong earthquakes for the USSR territory. Nauka, Moscow, pp.20-30 (in Russian).

Shebalin N. (2003) Macroseismic Problems. In: Computational Seismology, issue 34: 55-200 (in Russian).

6. Physics of seismic process and earthquake prediction

6.1. Earthquake physics and precursors

G. A. Sobolev, sobolev@ifz.ru**, A. D. Zavyalov,** zavyalov@ifz.ru**, A. V. Ponomarev,** avp@ifz.ru**,** *Schmidt Institute of the Physics of the Earth RAS. Str. Bol. Gruzinskaya 10. Moscow 123995, GSP-5, Russia.*

The following main results on physics of earthquakes and their forerunners were obtained in 2007-2010.

1. In the area of seismic regime analysis:

1.1. Medium-term earthquake prediction methods have been improved. The practical use of these developments is illustrated by the early prediction of the Simushir (Middle Kuril) earthquake with the magnitude of 8.2 on November 15, 2006. The consecutive stages of seismic quiescence, foreshock activation and appearance seismic event clusters with lower magnitude in the seismic focus zone of this earthquake have been traced. The successful prediction of the Simushir earthquake was noted as one of the most important achievements made by the Russian Academy of Sciences (RAS) in 2006.

1.2. Microseismic records from 5 IRIS wide-band seismic stations located at distances of 1-2 thousand kilometers from a seismic focus have been investigated. Non-standard programs for revealing hidden periodicities, signal coherence at various stations and asymmetry of oscillation amplitudes have been applied. In records from some stations, it has been found that 60 hours before the Sumatran earthquake there were periodic oscillations with cycles within 20-60 minutes that occurred after the Macquarie earthquake and lasted within 24 hours. 53 hours before the Sumatran

earthquake, the stations recorded the start of oscillation synchronization continuing until the time of the earthquake, and the dominant period gradually lengthened from a few minutes to tens of minutes.

1.3. Based on data from the Harvard catalog of seismic moments and the ISC worldwide catalog, the generalized vicinity of a strong earthquake has been obtained and studied. Statistically significant anomalies inherent to this vicinity have been shown up. A number of these anomalies (evolution of focal mechanism coherence, decrease in b-value of the magnitude-frequency relationship) agree with previously obtained results. A number of other anomalies are new, in particular, an effect of decrease in apparent stress values in the focus zone of a strong earthquake and an effect of primary "floating-up" of a focus in the region of a strong event. The obtained results indicate 1) probable presence of a fluid phase in the seismic focus and 2) evolution of a material softening effect in a quite wide space-time vicinity of a strong earthquake.

1.4. Assessments regarding spatial distribution of failure cycle parameters have been obtained based on data from seismic catalogs of northern California and Japan. These regions are characterized by pronounced tectonic features – tectonic displacement of the San Andreas Fault and a subduction zone of the Japanese Island Arc. The failure cycle length for the both regions in average does not virtually depend on earthquake magnitude. Average failure cycles for California and Japan last 6300 and 3100 years respectively.

1.5. RTL algorithm applicability in various regions was studied (by the example of Iran, north-east China and north-west India). It has been shown that, in various regions and in case of source catalogs which essentially differ from each other by their detail level, the algorithm is able to work even if a standard set of parameters is selected. Finer algorithm tuning makes it possible to improve contrast and, in some cases, a detail level of anomalies, however, the overall picture remains the same.

1.6. The seismicity structure before the two largest earthquakes in the territory of Russia, the 7.8 magnitude Kronotsky earthquake in 1997 and the 8.2 magnitude Simushir earthquake in 2006, has been investigated. Various algorithms were used to reveal seismic quiescence, foreshock activation, critical seismic acceleration and appearance of seismic event clusters. It has been found out that the seismic process evolved based on a common scenario. Several years before the earthquake, seismic quiescence appeared in the area of about 200 km adjacent to the epicenter. The area of further activation with the size of about 100 km included the earthquake epicenter. The time interval between the end of the activation stage and the earthquake was more than one year. Several days before the earthquake, a sharp increase in seismic event cluster number was observed near the epicenter.

1.7. Changes of seismogram shape and/or spectral content in acoustical activity groups have been studied during laboratory experiments and in swarms of natural earthquakes. In this connection, it was assumed that one of the reasons for swarm appearance is fluid penetration into the local volume of the seismically active zone.

1.8. A map of earthquakes expected in Greece ($M_L \geq 5.5$) for 2003-2009, which was plotted early in 2003, has been reviewed. In 2003-2008, there were 8 earthquakes with $M_L \geq 5.5$ and their groups in the studied region. Earthquakes with a focal depth not more than 50 km were taken into account. It turned out that 6 (75%) earthquakes occurring in the area of the expected earthquake map where the conditional probability level did not exceed 70%. This number includes the strongest earthquake with $M_L=6.5$ occurring on June 8, 2008 in the north-west part of Peloponnesus and a series of strong earthquakes on February 14-20, 2008 ($M_L=6.2$, 6.1, 6.0) in Leonidio, the south-west part of Peloponnesus. A version of a map of earthquakes expected in Greece for 2008-2014 has been designed using new methodical elements introduced to the expected earthquake map algorithm.

1.9. A scale transformation method has been developed and implemented for summation of data on the vicinity of various-magnitude earthquake combination. As a result of its implementation for the total of 500 vicinities of the world's strongest earthquakes, we have been able to obtain a large amount of statistical data required for reliable identification of premonitory, coseismic and postseismic characteristics of the seismic regime. The analysis of the plotted combination has confirmed a number of previously assumed characteristics of premonitory behavior (in particular, characteristic parameters of exponential foreshock cascade of seismic activity increase have been determined).

1.10. Individual provisions were developed for a fluid metamorphogenic (FM) model of seismogenesis and a model for realization and statistical description of power-series distributions (responsible for evolution of instability processes) in natural systems.

1.11. Within the framework of the "Physics of Earthquake Formation Process and Complex Analysis of Multiparameter Observation Data for Prediction Purposes" Project of the Long-Term Comprehensive Program of Cooperation in Science and Technology between Russia and India, prognostic anomalies of the seismic regime were revealed in the Western Himalayas.

1.12. Based on comparison between differential satellite interferometry data, surface geodetic data and seismic data, a contribution to the overall deformation of coseismic and aseismic (creep) processes (by the example of aftershocks of the Altai earthquake on 27.09.2003) has been assessed.

1.13. Several scenarios of seismic noise field multi-fractal parameters synchronization have been distinguished. Synchronization effects have been detected for low-frequency microseismic background parameters according to data from 77 wide-band F-net stations in Japan for the period from the beginning of 1997 to August 2009. The analysis was performed using vertical components with 1 sec sampling interval which were subsequently conversed by averaging and decimation into signals with 1 minute time intervals. The following 6 statistics have been taken as parameters: width of a multi-fractal singularity spectrum carrier, generalized Hurst index, singularity spectrum asymmetry factor, dispersion logarithm, spectral exponent and linear predictability index. These parameters were calculated based on realizations within successive 24 hour intervals. When a sliding time window equal to 1 year is used for assessment of multiple correlation measure, daily variations of background statistics median values from 5 spatial clusters of stations demonstrate sustained growth of synchronization degree not long before an earthquake on Hokkaido (25.09.2003, $M = 8.3$) with subsequent rise to a new level of high synchronization.

1.14. Evolution of multi-fractal singularity spectrum parameters of seismic records from an IRIS wide-band network (throughout the world, 2004-2005, 123 stations) has been analyzed in order to distinguish long-term trends (averaged both by stations of the whole network and its individual subgroups) and rhythms of change in statistical properties of microseismic oscillation field noises and compare the distinguished peculiarities with the seismic regime. An effect of global synchronization has been distinguished for singularity spectrum carrier width median variations for low-frequency microseismic records from 7 clusters of seismic stations covering the entire world. It was assessed in the sliding time window equal to 112 days (4 lunar months) that started 200 days before the disastrous earthquake on Sumatra on 26.12.2004.

1.15. Variations of Kamchatka stress state as a result of strong earthquakes (Kronotsky earthquake in 1997 and Simushir earthquake in 2006 in the Kuril Island Arc) have been assessed. The Simushir earthquake caused seismicity level oscillation synchronization in Kamchatka.

2. In the area of theoretical studies of failure processes and seismic regime:

2.1. Development of an Earth's crust Self-similar *Seismogenerating* Structure (SSS) model has been completed. The SSS model describes an Earth's crust common structure of the multi-fractal fields with consistent scalings that are directly involved in earth quake formation processes. Based on a direct multiplicative cascade procedure, we have developed the mathematical tool of the model which allows to quantitatively analyze natural fields and formulate, in particular, a generalized scaling law that connects scalings of individual fields.

2.2. Development of a phenomenological model for a process of seismic macrofracture formation from a fractal set of nucleating thermofluctuation microcracks has been completed. The model explains seismic macrofracture formation through multiscale avalanche-type coalescence of nucleating cracks by a reverse cascade type. We have deduced crack coalescence conditions connecting crack set fractal dimension values and crack coalescence concentration criteria required for start of multiscale avalanche-type crack coalescence into a macrofracture. Geometrical aspects of this process have been defined in terms of mathematics.

2.3. With use of model calculations, it has been shown that the method of phase trajectory averaging is applicable for restoring time variations of dynamical systems and improving an assessment of its numerical characteristics in case of superposition of both a high-dimensional process

(absolutely random process) and a small-dimension process (linear interpolation). The performed analysis of dynamical system variations for the purpose of recording relative deformations in different points of seismically active regions of China made it possible to assess the following dynamical parameters: phase space dimension (m=5-7) and correlation dimension varying in different observation points (d2=2.6-3.5).

2.4. We have developed a computer model that generalizes currently known geometrical features of the process of crack coalescence in rocks. The model consists of two computing procedures: 1) – generation of a microcrack set with realistic spatial relationship (which conforms to multi-fractal statistics), and 2) – crack coalescence simulation based on a scale-invariant coalescence criterion ("concentration" criterion analog).

The results of modeling indicate that, at really observed fractal dimension values for crack sets in rocks, the coalescence criterion at which cracks can coalesce into a single macrofracture shall not exceed 2 or, maybe, smaller. In case of multi-fractal microcrack distribution, large macrocracks appear in the places where microcracks are locally concentrated, and then, at next coalescence stages, large-size adjacent macrocracks rip large-size barriers between each other (simultaneously in many points along the future macrofracture pathway). So, in order to form a macrofracture of any length, microfractures may have arbitrarily small total length at the first stage of coalescence (theoretically, i.e. without notice of material structure). In this way, multiscale coalescence of the cracks arranged as a scale-invariant set principally differs from the coalescence process when cracks are characterized by uniform spatial distribution.

3. In the area of analysis of geophysical data sequences:

3.1. New approaches to analysis of geophysical time series from the perspective of a non-linear dynamical systems theory have been developed. Attention to use of non-linear dynamics approaches in analyzing complex geophysical fields is largely connected with clear physical meaning of the dynamical parameters assessed. Their values allows to estimate model relationships for the behavior of the phenomena under study. These parameters include phase space dimension of a dynamical system. The capability of assessing it based on a single time realization of a geophysical field has been reviewed on the example of data series of long-term observations over apparent resistivity and relative vertical displacement of surface.

3.2. Wavelet analysis of apparent resistivity series variations, volume deformation and Earth's surface tilts in North-East China has been performed. Anomalies which may be connected with a seismic process have been identified in the lower scales of wavelet diagrams (in a high-frequency part).

3.3. Analysis of long-term observations over geophysical fields of various nature (volume deformation, Earth's surface tilting, Earth's surface vertical displacements, water level in a well, apparent resistivity, etc.) as individual parameters of the dynamical system under study makes it possible to distinguish several components (usually two) in the structure of the observed process which corresponds to different dynamical systems. The parameters of dynamical system connectivity in different observation points indicate the existence of both a common component that corresponds to a global process and a local component that corresponds to the process occurring immediately in the observed area and is not related to local processes in other observation points.

4. In the area of geodynamics:

4.1. We have compared parameters of a field of tectonic stresses reconstructed based on seismic data with contemporary deformations of the surface based on GPS data for the territory of China. The comparison of horizontal components of principal direction deformation tensors based on the GPS data and seismic data for different depth intervals has shown their good convergence.

4.2. We have analyzed the relationships of sequential changes in deformation conditions and old phases, as well as contemporary one, of a single cycle of a deformation process near the southern boundary of the Siberian plate in the late Mesozoic. For this purpose, the field of tectonic stresses has been reconstructed based on both seismic data on seismic focal mechanisms and geological data on shear displacement vectors. Based on geological data for the Baikal rift area, six Earth's crust

deformation phases have been reconstructed to reflect sequential change in kinematics of regional mechanisms of the deformation process. The obtained results have made it possible to conclude that there is a sequential change in kinematic conditions of Earth's crust deformation in this region in the context when subhorizontal orientation along and across the Baikal rift area is maintained for two principal axes of the stress tensor throughout the reconstructed deformation cycle. The parameters of the deformation series are described by a model of smooth quasisinusoidal variation of stresses in time.

5. In the area of study of transient and trigger processes in the seismic regime:

5.1. As a result of joint analysis of in-situ aftershocks and their modeling in laboratory experiments, we have found out common regularities of a relaxation process. A delay of relaxation start (characteristic decay of activity) with regard to an exciting impact moment has been revealed. The laboratory results indicates that this delay increases with the level of effective stresses. The relaxation process power approximation parameter (Omori parameter) also increases with growth of effective stresses. As a possible explanation of the revealed relationships, we consider competition of excitation and relaxation processes which evolve in time with different velocities depending on a stress level and degree of material failure.

5.2. Peculiarities of acoustic emission (AE) generation have been studied in samples of rocks deformed with constant rate of 10^{-7} l/s in 160 MPa triaxial compression conditions under the uniaxial load modulated by sinusoidal oscillations. The samples used had preliminary shaped internal fracture surface where stick-slip phenomena appeared. AE catalogs containing tens of thousands events within the range of three energy orders have been reviewed. The studied model, in a first approximation, is considered as a model of seismic regime change under the influence of natural intermittent processes.

5.3. It has been shown that a periodic AE response synchronized with external force action occurs in a loaded sample. Response intensity varies with time. The intervals where an "induced" acoustic signal decays several times with the modulating load being constant have been identified. It has been found out that synchronization effects almost disappear (at constant AE detection threshold) during the period immediately after stick-slip phenomena and are gradually reestablished as loading further increases.

5.4. Based on a series of carefully set up laboratory experiments, regularities of excitation and relaxation have been revealed for the failure process in rock; similar regularities have been identified in full-scale conditions; a physical idea and its mathematical illustration have been proposed to explain the obtained experimental results.

The experiments were aimed at identifying the nature of excitation of the failure process initiated by an external impact and its relaxation with impact cessation depending on the level of effective stresses. The acoustic response that reflects the fracture propagation process is manifested in different ways at various rates of growth of an initiating deformation "step". At higher deformation rates, we observed a process that is similar to aftershock sequences, at lesser ones, seismic swarms were observed. Similar regularities have been identified in full-scale conditions based on data of an experiment for medium failure caused by water injection into a well (Soultz-sous-Forets, France). In order to explain the obtained experimental results, a hypothesis has been suggested that excitation and relaxation processes compete with each other. Corresponding mathematical modeling has confirmed the validity of this hypothesis.

5.5. Based on literature data analysis, assessments of dynamical characteristics of the best-known natural and anthropogenic processes initiating transient seismic regimes (reservoir filling, variations of water level in reservoirs, cyclones, luni-solar tides, waves from remote earthquakes, storm microseisms) have been collected in a summary. As dynamical characteristics of impact, we considered values of characteristic stresses, rates of their change in time, as well as gradients that are indicative of volume density of elastic forces.

5.6. Regularities of seismic regime variations have been revealed on the example of two swarms in the area of the Corinth rift. As a result of the analysis performed, the following characteristic variations of swarm seismic regime parameters have been identified: b-value of the magnitude-frequency relationship, fractal dimension d and parameter q characterizing distribution of medium life on a scale of failure. Variations of these parameters are different at stages of swarm seismic activity

increase and decay. At the activity increase stage (at the excitation stage), b decreases and d increases. At the activity decay stage (at the relaxation stage), the changes are reverse: b increases and d decreases. Variations of q indicate that the failure process evolves from smaller scales to higher ones at the excitation stage and vice versa at the relaxation stage.

6. In the area of seismic monitoring at mining facilities:

6.1. Focal mechanisms of seismic events have been studied at various mining facilities. In particular, 70 large seismic events occurring in 2004 at mines of the Verkhnekamskoe Potassium Salt Deposit (VKPSD) have been analyzed. Based on the results of fitting of equivalent concentrated seismic sources that most adequately describe the recorded wave shapes, it has been established that focal processes of the most events (66, or 94% of the total number) were rock slides. Thus, other possible dynamical processes, including a classic seismic focus in the form of a shear crack, were not confirmed in VKPSD conditions.

6.2. Techniques for assessment of stress state parameters (orientations of principal stress tensor components and ratios of their amplitudes) based on focal mechanisms of small seismic events have been tested for conditions of seismic monitoring at mining facilities. The use of such techniques is promising with regard to integration of seismic monitoring data and geomechanical model calculations in order to predict large-scale instabilities of developed rock massifs (mine-tectonic shocks).

6.3. Continuous instrumental monitoring via a Western Urals seismic stations network has provided an evidence that the natural component of seismic activity in the Urals region within the magnitude range from 1.5 to 4.5 is underestimated by at least one order.

The assessments supported by observations that were conducted within the last 10 years using a modern instrumental basis objectively indicate a higher seismic activity level which exceeds the level previously determined for the region based on historical data and episodic instrumental observations carried out until 1999.

Bibliography

Babushkin I.A., Glukhov A.F., Demin V.A., Malovichko D.A., Dyagilev R.A. A Hele-Shaw Cell-based Seismic Pick-up // Applied Physics. 2008. No. 3, P. 7 (in Russian).

Bogomolov L., Bragin V., Fridman A., Makarov V., Sobolev G., Polyachenko E., Schelochkov G., Zeigarnik V., Zubovich A. Comparative Analysis of GPS, Seismic and Electromagnetic Data on the Central Tien Shan Territory // Tectonophysics. 2007. Vol. 431, Issues 1-4, pp. 143-151.

Cherepantsev A.S. Determination of the Phase Projection of a Dynamic System from Strain Field Observations. Izv. Phys. of the Solid Earth. 2008. Vol. 44. No. 2. pp. 119-137.

Cherepantsev A.S. Dimension of the Phase Space of a Dynamic System from Geophysical Data. Izv. Phys. of the Solid Earth. 2007. Vol. 43. No. 12. pp. 1047-1055.

Cherepantsev A.S. Extraction of a Dynamic Component from Variations in Geophysical Fields Using the Convergence of a Sample Average. Izv. Phys. of the Solid Earth. November 2008. Vol. 44, No 11, pp. 883-897.

Kalab Z., Lyubushin A. Study of Site Effect using Mining Induced Seismic Events and Ambient Noise from Karvina Region // Acta Geodyn. Geomater. 2008. Vol. 5, No. 2 (150), pp. 105-113.

Levin B.V., Rodkin M.V., Sasorova E.V. Specific Features of the Seismic Regime in the Lithosphere: Manifestations of the Deep Aqueous Fluid Action // Izv. Phys. of the Solid Earth. 2010. Vol. 46, No. 5, pp. 451-460.

Levin B.W., Rodkin M.V., Sasorova E.V. Possible Nature of the Seismic Boundary at a Depth of 70 km // Earth Sciences Papers. 2007. Vol. 414, No. 1, pp. 578-581.

Liperovskaya E.V., Liperovsky V.A., Pokhotelov O.A., Rodkin M.V. About Disturbances in Ionospheric F-Region before Earthquakes // Geophysical Research. 2006. Issue 6, M.: IPE of RAS, pp. 51-58 (in Russian).

Lyubushin A.A. Mean Multifractal Properties of Low-Frequency Microseismic Noise // 31st General Assembly of European Seismological Commission. Short Papers. Hersonissos, Crete Island, Greece, 7-12 September, 2008. pp. 265-270.

Lyubushin A.A. Microseismic Noise in the Low Frequency Range (Periods of 1-300 min): Properties and Possible Prognostic Features. Izv. Phys. of the Solid Earth. 2008. Vol. 44, No. 4. pp. 275-290.

Lyubushin A.A. Synchronization Trends and Rhythms of Multifractal Parameters of the Field of Low-Frequency Microseisms. Izv. Phys. of the Solid Earth. 2009. Vol. 45, No. 5. pp. 381-394.

Malovichko A.A., Dyagilev R.A., Malovichko D.A. Earthquake Monitoring at Mines of the Verkhnekamskoe Potassium Salt Deposit // Mining Journal, 2008. P. 5 (in Russian).

Malovichko A.A., Malovichko D.A., Dyagilev R.A. Earthquake Monitoring at Mines of the Verkhnekamskoe Potassium Salt Deposit // Mining Journal, 2008. No. 10, P. 5 (in Russian).

Nikitin A.N., Kulakovsky A.L., Rodkin M.V., Yurchenko O.A., Ivankina T.I., Vasin R.N. About Some Mechanisms of Rock Permeability in connection with Geoecological Safety of Highly-Radioactive Waste Storages // Geophysical Research. 2006. Issue 6, M.: IPE of RAS, pp. 85-95 (in Russian).

Nikitin A.N., Vasin R.N., Rodkin M.V. Possible Influence of Polymorphic Transitions in Minerals (according to the Quartz Example) on Seismotectonic Processes in the Lithosphere. Izv. Phys. of the Solid Earth. 2009. Vol. 45, No. 4. pp. 338-346.

Petrov V.A., Anfu Niu, Smirnov V.B., Mostryukov A.O., Zhixiong Li. Field of Tectonic stresses from Focal Mechanisms of Earthquakes and Recent Crustal Movements from GPS Measurements in China. Izv. Phys. of the Solid Earth. 2008. Vol. 44. No. 10. pp. 846-855.

Pisarenko V.F., Rodkin M.V. Distributions with Heavy Tails: Appendices to Disaster Analysis // In Collect.: Computational Seismology, M.: GEOS. 2007. Issue 38, 240 p. (in Russian)

Pisarenko V.F., Rodkin M.V. The Instability of the Mmax Parameter and an Alternative to its Using. Izv. Phys. of the Solid Earth. 2009. Vol. 45, No. 12. pp. 1081-1092.

Rodkin M.V. Seismicity in the Generalized Vicinity of Large Earthquakes // Journal of Volcanology and Seismology. 2008. Vol. 2, No. 6, pp. 435-445.

Rodkin M.V. About a Seismic Focus Formation Process: New Data and a Stochastic Model of Instability Development // Physical Mesomechanics. 2007. Vol. 10, No. 1, pp. 39-46 (in Russian).

Rodkin M.V. About Seismic Activation Conditions in Generalized Vicinity of a Strong Earthquake // Physical Mesomechanics. 2008. Vol. 11, No.1, pp. 74-79 (in Russian).

Rodkin M.V. Typical Fore- and Aftershock Behaviour: an Insight from the Analysis of the Generalized Vicinity of Strong Earthquake. J. of Geology, Ser.B., No. 31-32, 2008. P. 337.

Rodkin M.V., Rukavishnikova T.A. Softening Processes in Vicinity of Strong Earthquakes and in Phase Transformation Zones in the Upper Mantle // Geophysical Research, Vol. 10, No. 3, M.: IPE of RAS. 2009. pp. 51-58 (in Russian).

Rodkin M.V., Rukavishnikova T.A. Softening Processes in Vicinity of Strong Earthquakes and in Phase Transformation Zones in the Upper Mantle // Geophysical Research. Vol. 10, No. 3, M.: IPE of RAS. 2009. pp. 51-58 (in Russian).

Smirnov V.B. Prognostic Anomalies of Seismic Regime. I. Methodological Fundamentals of Source Data Preprocessing // Geophysical Research. 2009. Vol. 10, No. 2. pp. 7-22 (in Russian).

Sobolev G.A. On applicability of the RTL Prognostic Algorithms and Energy Estimation to Sakhalin Seismicity // Journal of Volcanology and Seismology. 2007. Vol. 1, No. 3, pp. 198-211.

Sobolev G.A. Seismological Evidence for the Nucleation of Two Strong Earthquakes // Izv. Phys. of the Solid Earth. 2008. Vol. 44. # 11. pp. 873-882.

Sobolev G.A. Series of Asimmetric Pulses in the Low-Frequency Range (Periods of 1-300 min) of Microseisms as Indicators of a Metastable State in Seismically Active Zones. Izv. Phys. of the Solid Earth. 2008. Vol. 44, No. 4. pp. 261-274.

Sobolev G.A., Arora B., Smirnov V.B., Zavyalov A.D., Ponomarev A.V., Kumar N., Chabak S.K., Baidiya P.R. Prognostic Anomalies of Seismic Regime. II. Western Himalayas // Geophysical Research. 2009, Vol.10, No. 2, pp. 23-36 (in Russian).

Sobolev G.A., Kireenkova S.M., Morozov Yu.A., Smul'skaya A.I., Tsel 'movich V.A., Vettegren V.I., Kulik V.B. Nanostructures in the Deep Xenolite before and after Straining. Izv. Phys. Of the Solid Earth. 2009. Vol. 45, No. 9. pp. 731-739.

Sobolev G.A., Lyubushin A.A. Microseismic Anomalies before the Sumatra Earthquake of December 26. 2004. Izv. Phys. of the Solid Earth. 2007. Vol. 43. No. 5. pp. 341-353.

Sobolev G.A., Lyubushin A.A., Zakrzhevskaya N.A. Asymmetrical Pulses, the Periodicity and Synchronization of Low Frequency Microseisms // Journal of Volcanology and Seismology. 2008. Vol. 2, No. 2, pp. 118-134.

Sobolev G.A., Vettegren V.I., Kireenkova S.M., Kulik V.B., Morozov Yu.A., Smul'skaya A.I. Raman Spectroscopy of Nanocrystals in Rock. Izv. Phys. of the Solid Earth. 2007. Vol. 43, No. 6. pp. 447-454.

Stakhovsky I.R. Phenomenology of Seismic Macrofracture Formation. Izv. Phys. of the Solid Earth. 2008. Vol. 44. No. 7. pp. 570-576.

Stakhovsky I.R. Self-Similar Seismogenic Structure of the Crust: A Review of the Problem and a Mathematical Model. Izv. Phys. of the Solid Earth. 2007. Vol. 43. No. 12. pp. 1012-1023.

Tyupkin Yu.S., Rodkin M.V., Gvishiani A.D., Labuntsova L.M. A Nonequilibrium Process Center in Seismology and Geology of Subsurface Resources: Common Approaches and Simple Models // Geophysical Research. 2006. Issue 6, M.: IPE of RAS, pp. 23-34 (in Russian).

6.2. Mechanics of triggering instability in geosystems

G. G. Kocharyan, gevorgk@idg.chph.ras.ru, *Institute for Geospheres Dynamics RAS, 119334, Leninsky prospect, 38, 1, Moscow, Russia.*

Changes in stress conditions that trigger dynamic instability are often associated with short-term local fluctuations in the stress field or with the change of rock properties at the area of deformation localization. The probable sources of these short- and intermediate- term local fluctuations in stress conditions include deformation processes in the neighboring areas, impacts of earthquakes, tides, oceanic load, magmatic intrusions; anthropogenic activity such as filling reservoirs, mining operations, injecting and pumping out fluids, large explosions, and seasonal meteorological factors. If these changes are produced by a certain deterministic process the situation is considered as the normal development of deformation of a crustal segment. In seismology, the process of normal evolution is usually called the seismic regime. However, if some more or less short term impact causes an event, which otherwise could not have occurred or would have occurred substantially later, then it can be referred to as the initiation of the deformation process, or the trigger effect.

There are many reasons for studies of trigger processes to be fascinating. One of them is the fact that trigger phenomena provide a rare possibility for revealing the cause-and-effect relationships in large-scale geomechanics.

In 2007-2010 investigations of different aspects of the trigger effect were performed in Russia by several groups of researchers. A certain outcome of this stage was presented at the Workshop "Triggering in Geosystems", which was conducted in the Institute of Geospheres Dynamics of the Russian Academy of Sciences in June 2010 [*Trigger effects*, 2010]. More than 60 experts from more than 20 institutions presented forty oral talks and nine posters.

General approach to the problem of triggering dynamic instability in the Earth's crust is discussed in the review papers [*Kocharyan*, 2010; *Mirzoev et al.,* 2010; *Mukhamediev*, 2010; *Sobolev*, 2010]. It was noted that the facts of triggering are registered in the range of, at least, from 100 nano-stranes and above. Delays between the seismic wave arrival times and triggered events change from seconds to weeks and durations of triggered seismicity are from several minutes to several weeks. In many cases the triggered seismicity is accompanied by the increase of fault deformation rate.

Vibratory effects on a geological medium and the interrelation between fluids and seismicity were studied in laboratory experiments. In works of G. Kocharyan's group the opportunity is considered of realization of two mechanisms that can lead to the change of fault zone deformation

regime under low-amplitude dynamic stresses. The first mechanism is connected with the occurrence of residual deformations, when a stressed contact between blocks is deformed dynamically. The second one bases on redistribution of pore stresses during de-mudding of fractures that were blocked by colloidal films of aluminum silicates. The slow creep of appreciable amplitude and duration that is initiated by pulse dynamic actions on the fault zone makes an important contribution to the trigger effect. The effect of low-frequency seismic vibrations may turn to be an effective mechanism of changing the fluidal and dynamic regimes of the fault zone, and as a consequence, of local redistribution of pore stresses [*Kocharyan, Markov et al.,* 2010].

G.A.Sobolev and A.V.Ponomarev investigated the trigger effect of water on the dynamics of failure in long-term laboratory experiments. They found that fade-in and decay of acoustic emission after a step-wise mechanical load and after pouring water differ essentially. In the first case the Omori's law is true. In the second one the intensity of acoustic emission passes through a pronounced maximum. Triggering failure by a fluid results from the local decrease of strength near metastable fractures not on account of increasing the pore pressure, but due to the physical and chemical interactions [*Sobolev et al.,* 2010].

Field observations of the response of stressed sections of tectonic faults to mechanical disturbances were performed at several test sites. At all the objects nearly the same regularities of reaction of discontinuities to external disturbances were detected. The intensity of reaction or the amplitude of residual displacement depends on the geometry of block structure, the local stress-strain conditions and the strength characteristics. Though amplitudes of relative displacements of discontinuity sides are rather low, it was established reliably that even low-intensity disturbances can trigger residual deformations. It is important to emphasize that a principal difference is observed in deformations registered at fractures and at intact rock. At sections without macroscopic discontinuities no appreciable residual deformations are registered [*Adushkin et al.* 2009]. Interesting results were obtained in the frames of the integration project #20 of the Siberian Branch of RAS "Physical Modeling of Deformation Processes in the Lithosphere Basing on Investigations of the Ice Cover of the Lake of Baikal" (coordinated by S.G.Psakh'e) that is being carried out by several institutions of the Siberian Branch of RAS on Academician N.L.Dobretsov's initiative [*Ruzhich et al.,* 2009].

Some results of field experiments are shown in the summarizing plot in **Fig.6.2.1**.

The generalization of the results of laboratory experiments and field observations suggested new models of triggering dynamical events by seismic waves [*Kocharyan, Markov et al.,* 2010].

Numerical simulations were carried out by several groups. In IDG RAS the numerical model was elaborated of accumulation of weak disturbances in fault zones, based on the non-linear rheological characteristics of discontinuities [*Budkov, Pavlov*, 2010].

S.G.Psakh'e team successfully used numerical simulation by the movable cellular automaton method to investigate the possibility for estimating the closeness of stress conditions in the fault zone to a subcritical state according to the measurements of the fault's response to a low amplitude impact. They also considered the possibility of transfer of the regime of movements along a fault to the creep conditions and some other problems [*Filippov et al.,* 2006; *Shilko et al.,* 2009].

The results of processing the parameters of seismicity recorded before and after the firing runs of the magnetohydrodynamic (MHD) generator and dc current pulses were investigated in the works of V.A.Zeigarnik's team. They provided field borehole measurements of geoacoustic emission response to electromagnetic pulses generated by ERGU-600 power system located at Bishkek geodynamic test site (Northern Tien-Shan), as well as theoretical analysis of the processes of rock interaction with electromagnetic field. With the application of up to date methods of statistical data processing and the formalism of nonlinear dynamics it has been confirmed that the excitation of high power current pulses in the Earth's crust contributes to triggering weak seismic activity. Dynamics of relaxation processes in stressed rock samples after action of electromagnetic field was studied in detail in laboratory experiments (**Fig.6.2.2**). A possibility of change of stress relaxation rate at different stages of the sample loading was estimated. It was shown that the external physical action leading to the reduction of local structural stresses is possible at the linear section of $\boldsymbol{k}_{\mathrm{tr}}$ ($\boldsymbol{k}_{\mathrm{p}}$), while acting at the non-linear

loading section leads to sample macro-fracturing [*Avagimov and Zeigarnik*, 2008; *Bogomolov*, 2010; *Tarasov*, 2010].

An important component of investigations of the trigger effect is the study of regularities of space-time localization of seismicity [*Sherman*, 2009]. The obtained results suggest that the region, wherein active deformation takes place during preparation of medium earthquakes (M≤6.5÷7.0), includes a number of local «strips», each about 100 m in width. The latter size is comparable to the scale of technogenic capabilities of producing effects on geo-environment [*Kocharyan, Kishkina, Ostapchuk*, 2010].

Sh.A.Mukhamediev [*Mukhamediev*, 2010] has aptly noted that in the near future it is too early to consider the problem of prevention of a forthcoming strong earthquake as a practical task, otherwise, the results can prove to be very different from the desired ones. Nevertheless, it makes sense to continue studying this problem. The theoretical research and experimental investigation of the structure and properties of the regions where the prevention of a forthcoming strong earthquake is planned in the future are of primary importance.

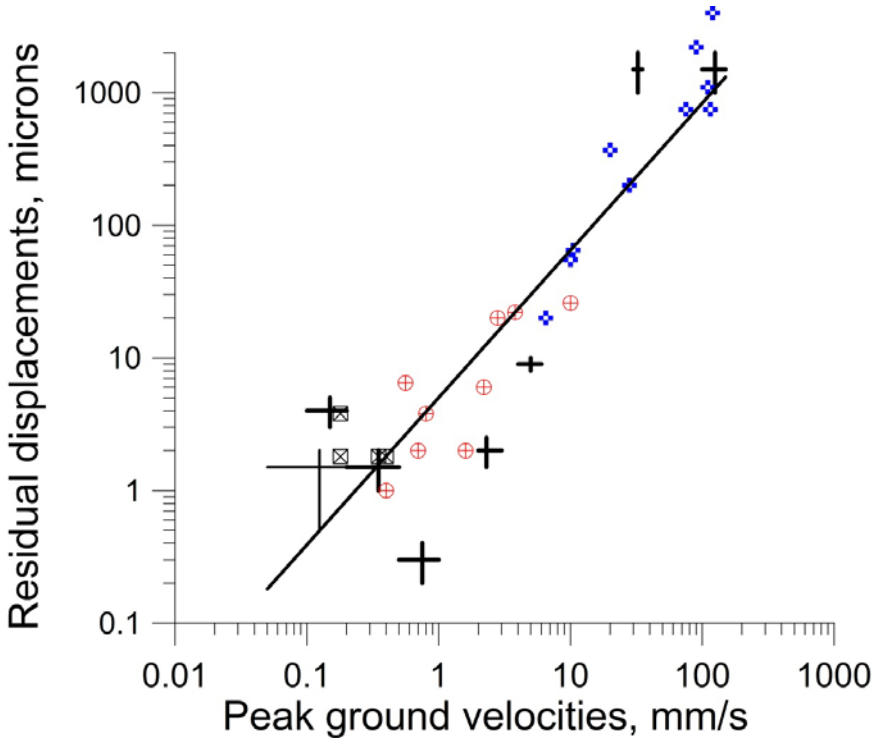

Fig.6.2.1. Registered residual displacements localized on fractures vs amplitude of dynamic disturbances. Signs are the data of measuring on various objects including natural tectonic fractures, the fractures in the wall of open pit, fractures in the concrete lining of a railway tunnel etc. The solid line corresponds to the regression relation $\Delta = 5.02 \cdot u_m^{1.1}$.

References

Adushkin V.V., Kocharyan G.G., Pavlov D.V., et al. (2009) Influence of Seismic Vibrations on the Development of Tectonic Deformations. Doklady Earth Sciences, Vol. 426, No. 4, pp. 588–590.

Avagimov A.A., Zeigarnik V.A. (2008) Estimation of the triggering effect energy in relation to model sample failure//Izvestiya Physics of the Solid Earth. V. 44. No. 1, pp. 69-72.

Bogomolov L.M. (2010) On a mechanism of electromagnetic influence on kinetics of microcracs and electro-stimulated variations of acoustic emission of rock samples// Phys. Mesomech.. V. 13, No.3. pp.39-56. (in Russian)

Budkov A.M., Pavlov D.V. (2010) Numerical simulation of the process of cumulating interblock displacements under low-amplitude dynamic disturbances. Phys. Mesomech.. V.13. No.2. pp.21-30. (in Russian).

Filippov A.E., Popov V.L., Psakh'e S.G., et al., (2006) On the Possibility of the Transfer of the Displacement Dynamics in the Block Type Media to the Creep Conditions, Pis'ma v ZhTF, vol. 32, No. 12, pp. 77–86. (in Russian).

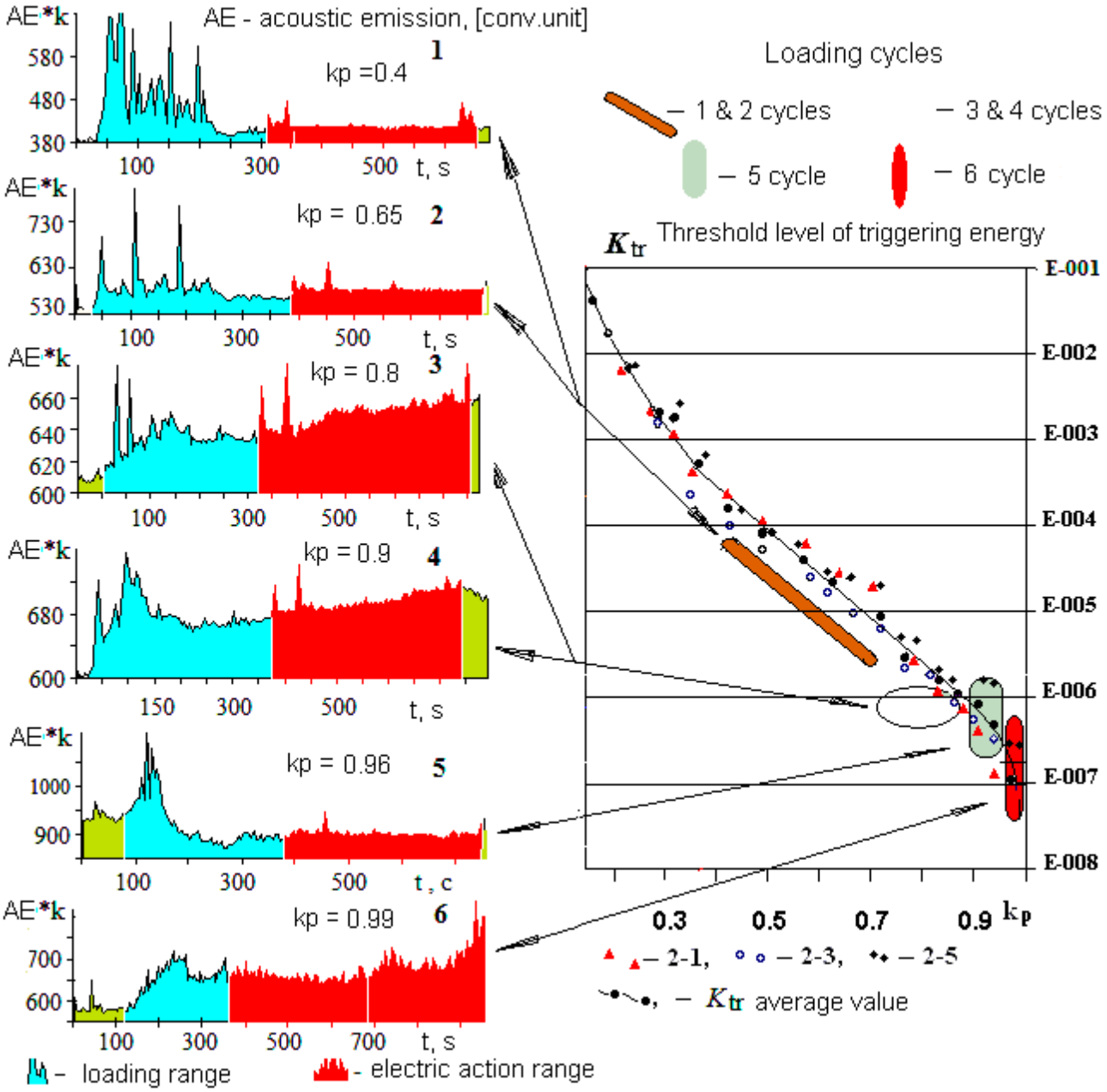

Fig.6.2.2. Response of acoustic emission to electric actions on the model rock samples under stressed condition. AE – acoustic emission (conventional units); $k_p=\sigma/\sigma_{max}$ – loading factor; $k_{tr}=(E_{AE}/N_{AE})_i/E_{pot}$ – relative energy of the sample relaxation.

Kocharyan G.G., (2010) Remote triggering of dynamic events. In Trigger effects in geosystems. V.Adushkin, G.Kocharyan eds. Moscow, GEOS. 2010. pp.18-30 (in Russian).

Kocharyan G.G., Markov V.K., Markov D.V. et al. (2010) Mechanics of the changing the regime of fault zone deformations by dynamic effects. In Trigger effects in geosystems. V.Adushkin, G.Kocharyan eds. Moscow, GEOS. 2010. pp.62-71 (in Russian).

Kocharyan G.G., Kishkina S.B., Ostapchuk A.A. (2010) Seismic picture of a fault zone. What can be gained from the analysis of fine patterns of spatial distribution of weak earthquake centers? Geodinamics & Tectonophysics V.1 No. 4, p.419-440. (in Russian)

Mirzoev, K.M., Nikolaev, A.V., Lukk, A.A., and Yunga, S.L. (2009) Induced Seismicity and the Possibility of the Controlled Discharging of the Accumulated Tectonic Stresses in the Earth's Crust, Fiz. Zemli, No. 10, pp. 49–68.

Mukhamediev Sh. (2010) A.Prevention of Strong Earthquakes: Goal or Utopia? // Izvestiya, Physics of the Solid Earth, Vol. 46, No. 11, pp. 955–965.

Sobolev G.A. (2010) The concept of earthquake predictability on the basis of dynamics of seismicity under trigger effects. In Extreme environmental hazards and catastrophes. M. IFZ RAN. pp.15-43.

Sobolev G.A., Ponomarev A.V., Maibuk Yu.Ya. et al. (2010) The Dynamics of the Acoustic Emission with Water Initiation // Izvestiya, Physics of the Solid Earth, 2010, Vol. 46, No. 2, pp. 136–153.

Tarasov N.T. (2010) An influence of strong electromagnetic fields on the rate of seismotectonic deformations //Doklady Earth Science. V. 433. No. 2. p.p. 1088-1091.

Trigger effects in geosystems (2010). Proceedings of Russian Workshop 22-24 June 2010. V.Adushkin, G.Kocharyan eds. Moscow, GEOS. 348p. (in Russian).

Ruzhich V.V., Chernykh E.N., Bornyakov S.A., Psakhie S.G., Granin N.G. (2009) Deformation and seismic effects in the ice cover of Lake Baikal Russian Geology and Geophysics. V. 50. № 3. pp.214-221.

Shilko E.V., Astafurov S.V., Ruzhich V.V., Psakhie S.G. (2009) On the feasibility of shear stress estimation at interfaces of block-structured medium. Physical mesomechanics. V. 12. № 3. pp.15-22.

Sherman S.I. (2009) Natural triggers in violating the fault and block crust metastability in real time. Journal of mining science, V.45, N5, p.438-451.

6.3. Intermediate-term prediction of the world largest earthquakes in real-time

V. G. Kossobokov, volodya@mitp.ru, *International Institute of Earthquakes Prediction Theory and Mathematical Geophysics RAS, Profsoyuznaya str., 84/32, Moscow 117997, Russia.*

In summary presented here we report the up-to-date statistics of the on-going real-time experimental testing of so-called M8-MSc predictions started officially in 1992 [*Healy et al., 1992; Kossobokov, 1997*] and demonstrate the most recent case-histories.

In semi-annual updates of the Global Test of M8-MSc predictions we use the M8 algorithm as an intermediate-term middle-range approximation which is explicitly defined in [*Healy et al., 1992*] and which code is available from IASPEI Software Library [*Kossobokov,* 1997]. This earthquake prediction method was designed by retrospective analysis of dynamics of seismic activity preceding the great, magnitude 8.0 or more, earthquakes worldwide, hence its name. Its prototype [*Keilis-Borok and Kossobokov,* 1984] and the original version [*Keilis-Borok and Kossobokov,* 1987] were tested retroactively. A short description of the original version of M8 is as follows:

Prediction is aimed at earthquakes from magnitude range $MM_0+ = [M_0, M_0 + \Delta m]$ where $\Delta m<1$. Overlapping Circles of Investigation, CI's, of the fixed size scan the territory of the seismic region under study. The diameter $D(M_0) = \exp(M_0 - 5.6) + 1$ in degrees of the Earth's meridian, i.e., about 5-10 larger than a source of the target magnitude MM_0+ events.

The sequence of earthquakes with aftershocks removed is considered within each CI. Sequences in different CI's are normalized to about the same pre-fixed average annual number of earthquakes $\bar{N}$ by selecting the lower magnitude cutoff $\underline{M} = M_{\min}(\bar{N})$.

For a given sequence several functions are computed in the trailing time window (*t-s, t*) and magnitude range ($\underline{M} \le magnitude < M_0$). These functions include (i) the number of earthquakes $N(t)$ of magnitude $\underline{M}$ or greater in time window (*t-s, t*); (ii) the deviation of $N(t)$ from longer-term trend, $L(t)$; (iii) linear concentration $Z(t)$ estimated as the ratio of the average source diameter to the average

distance between sources; and (iv) the maximum number of aftershocks $B(t)$. Each of the functions N, L, and Z is calculated twice with $\underline{M} = M_{\min}(\bar{N})$ for $\bar{N} = 20$ and $\bar{N} = 10$. As a result, the earthquake sequence is given a robust averaged description by seven functions $N1$, $N2$, $L1$, $L2$, $Z1$, $Z2$, and B. An alarm or a Time of Increased Probability, a TIP, is diagnosed when at least six out of seven functions, including B, show up "anomalously large" values within a narrow time window. The results of the TIP diagnosis are subject to semi-annual updates. Due to prefixed delay time the duration of TIP in a CI is about 5 years on average.

From a general viewpoint, the algorithm M8 uses traditional description of a dynamical system adding to a common phase space of rate (N) and rate differential (L) the parameters of dimensionless concentration (Z) and a characteristic measure of clustering (B). The algorithm recognizes criterion, defined by extreme values of the phase space coordinates, as a vicinity of the system singularity. When the trajectory of an area of investigation enters the criterion, probability of extreme event increases to the level sufficient for its effective provision and remains that high for a delay time after the trajectory departs from the criterion.

The middle-range accuracy of the M8 algorithm is far from ideal. Therefore, the Mendocino Scenario algorithm for reducing the area of alarm was designed [*Kossobokov, Keilis-Borok, Smith,* 1990] by retroactive analysis of the detailed regional seismic catalog prior to the Eureka earthquake (1980, M=7.2) near Cape Mendocino in California, hence its name abbreviated to MSc. Qualitatively, the MSc algorithm outlines such an area of the territory of alarm where the activity, from the beginning of seismic inverse cascade recognized by the first approximation prediction algorithm (e.g. by M8), is continuously high and infrequently drops for a short time, i.e. characteristic of *intermittency*. Such an alternation of activity must have a sufficient temporal and/or spatial span. The phenomenon, which is used in the MSc algorithm, might reflect the second (possibly, shorter-term and, definitely, narrow-range) stage of the premonitory rise of seismic activity near the incipient source of main shock.

Thus, in our practice, the M8 algorithm provides intermediate-term prediction in the first, middle-range, approximation, and the algorithm MSc, if the data permit, narrows down the area covered by alarm to a narrow or even exact location of the incipient target earthquake. Naturally, both apply to the null approximation delivered by identifying earthquake-prone zones, e.g. in terms of "seismic regions", "active fault zones", "D-intersections or knots", etc.

The overall performance of the M8-MSc predictions can be judged from the achieved statistics summarized in **Table 6.3.1** where the measure of alarm accounts for heterogeneous density distribution of seismic locus, and the confidence level tells how sure one can be that the achieved score does not happen by chance. For both magnitude ranges, the significance level estimates are far below 1% and, therefore, suggest rejecting the hypothesis of random guessing almost with certainty, i.e. with confidence of 99% or more. Table 1 provides statistics for the two test periods: (i) 1985-2010 includes the diagnosis in hindsight and (ii) 1992-2010 is documented pure control.

Table 6.3.1. Worldwide performance of earthquake prediction algorithms M8 and M8-MSc.

Test period	**Large earthquakes** Total	Predicted by M8	M8-MSc	**Measure of alarms,%** M8	M8-MSc	**Confidence level, %** M8	M8-MSc
Magnitude range M8.0+							
1985-2010	19	14	10	33.16	16.89	99.96	99.96
1992-2010	17	12	8	30.09	15.04	99.93	99.82
Magnitude range M7.5+							
1985-2010	65	38	16	28.73	9.32	99.99	99.98
1992-2010	53	28	10	23.14	8.31	99.99	98.89

Let us illustrate how the semi-annual M8-MSc predictions work with the recent history of application targeting magnitude range M8.0+:

Eight earthquakes that large shook the Earth in 2007-2010:

1) No alarm was identified for the epicenter area of **the 13 January 2007 great M8.2 earthquake EAST OF KURIL ISLANDS**. Note that the chain of correlated earthquakes [*Keilis-Borok et al., 2004*] was connecting this area with the M8-MSc prediction.

2) The M8 alarm was confirmed by epicenters of **the 01 April 2007 great M8.1 earthquake and its aftershocks on SOLOMON ISLANDS**. The second approximation by the MSc algorithm has identified correctly the location of the April 01, 2007 earthquake.

3) No alarm was identified for the area of epicenter of **the 15 August 2007 great M8.0 earthquake NEAR THE COAST OF CENTRAL PERU**. Note that the diagnosis of alarm in the area was next to critical: five functions (out of 6 required) did show up "anomalously large" values in July 2007.

4-5) Both of **the two 12 September 2007 great M8.5 SOUTHERN SUMATRA, INDONESIA and M8.1 KEPULAUAN MENTAWAI REGION, INDONESIA** earthquakes confirm the M8 alarms; the epicenter of the first one and its aftershocks fit nicely the prediction outlined by MSc algorithm in the second approximation, while the epicenter of the second one is located just outside this narrow-range area.

6) The disastrous 12 **May 2008 Wenchuan (EASTERN SICHUAN, CHINA) great M8.1** earthquake happened just in two circles of investigation at the periphery of Global Test area where no M8 alarm was identified.

7) **The 29 September 2009 great M8.1 earthquake and its aftershocks in SAMOA ISLANDS REGION** confirmed both the M8 and MSc predictions. It appears notable that the two 07 October 2009 significant M7.6 and M7.8 earthquakes on VANUATU and SANTA CRUZ ISLANDS separated by less than 16 minutes and 60 km, which scored the two "failures-to-predict" in the Global Test aimed at M7.5+ range, are next to the area M8-MSc alarm for M8.0+ (**Fig.6.3.1**).

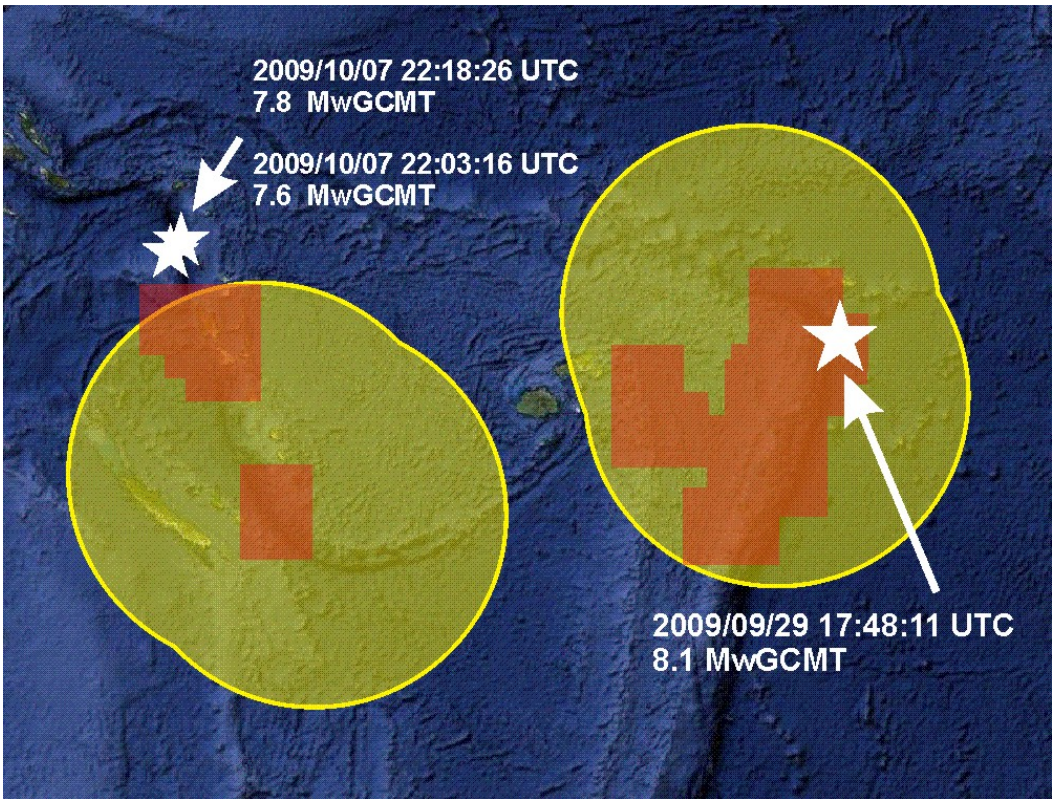

Fig.6.3.1. Global Test of the M8-MSc predictions aimed at M8.0+ (as of 01 July 2009): The 29 September 2009 great earthquake in SAMOA ISLANDS REGION and the two 07 October 2009 significant earthquakes on VANUATU and SANTA CRUZ ISLANDS.

8) The 27 February 2010 mega M8.8 earthquake OFFSHORE MAULE, CHILE ruptured the 600-km portion of the South American subduction zone inside a cluster of TIPs, which was recognized as capable of producing a magnitude M8.0+ event before mid-2012 (**Fig.6.3.2**). The earthquake epicenter missed the reduced area of alarm diagnosed in the second approximation by algorithm MSc. (The 27 February 2010 main shock and most of its first aftershocks fall inside a cluster of the M8 algorithm TIPs aimed at M7.5+ events as well).

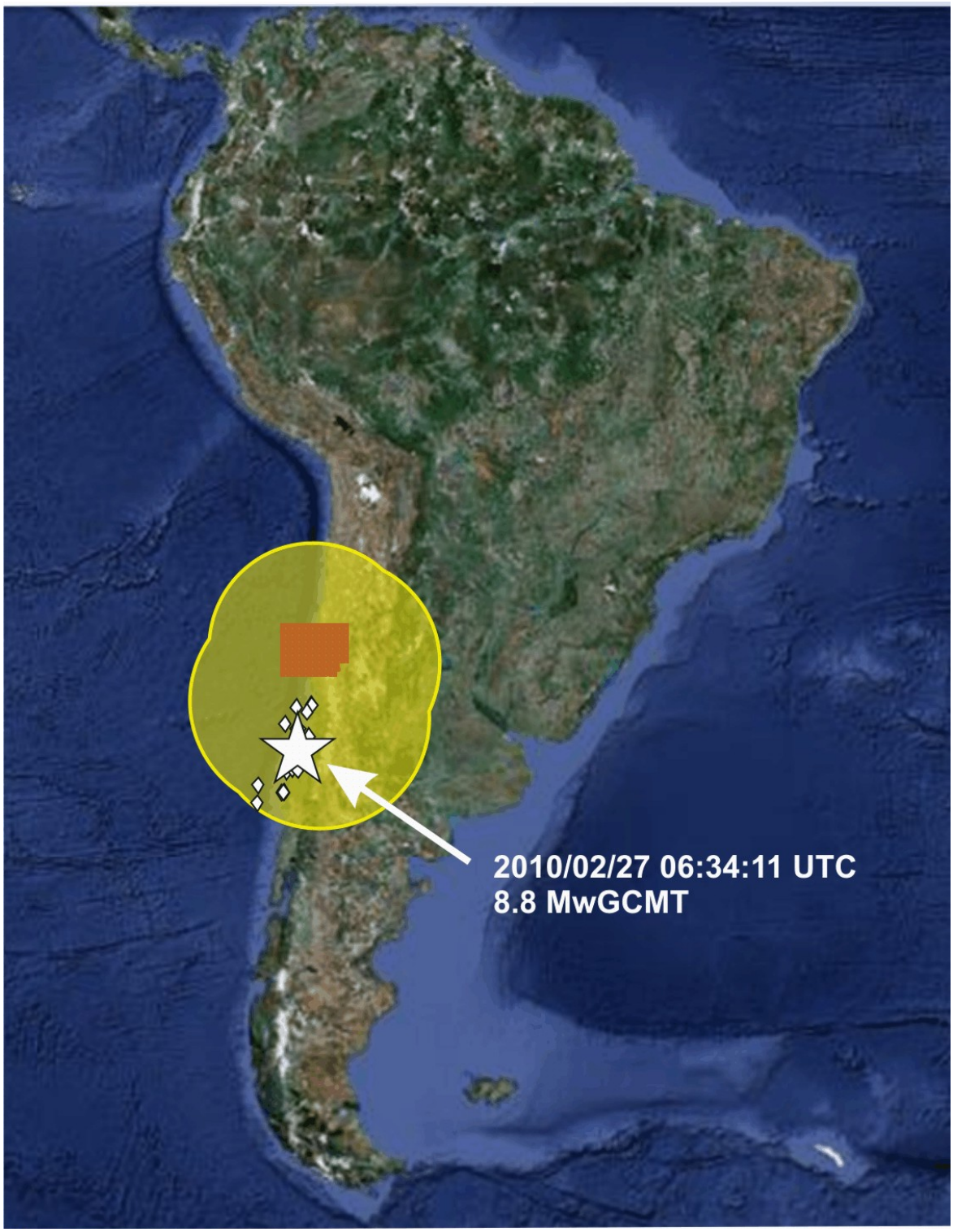

Fig.6.3.2. Global Test of the M8-MSc predictions aimed at M8.0+ (as of 01 January 2010): The 27 February 2010 OFFSHORE MAULE, CHILE mega-earthquake and its first aftershocks.

In regard to the 2010 Chile earthquake, it should be mentioned that after the 26 December 2004 Indian Ocean disaster, we expanded regular application of M8 algorithm *targeting mega-earthquakes*. In fact, the giant event happened to be the first indication that the algorithm designed for prediction of M8.0+ earthquakes and tested in applications aimed at lower magnitude ranges down to M5.5+ can be rescaled for prediction of extreme mega-earthquakes. Of course, the M8 methodology suggests using much larger circles of investigation when targeting mega-earthquakes like the 26 December 2004 M=9.2 Sumatra-Andaman, 28 March 2005 M=8.7 Nias, and 27 February 2010 M=8.8 Chile earthquakes, which ruptured the 1300-, 400-, and 600-km portions of subducting margins of the Indian and Pacific Oceans. An appropriate expansion of regular application of the M8 algorithm targeting M9.0+ earthquakes would have predicted the 2004 Sumatra-Andaman earthquake, however, in July 2004 it would lead to the area of alert that cover an extremely large portion of the Earth seismic belts [*Kossobokov,* 2005*; Romashkova et al.,* 2005].

The precursory seismic activation recognized by M8 algorithm and widespread globally in 2004 has decreased by 2008 to the four clusters of TIP's [*Kossobokov et al.,* 2008]: the largest includes Sumatra-Andaman and adjacent major seismic zones from Kashmir on the North-West to Timor Islands on the East, where 28 March 2005 Nias, M8.7 mega-earthquake and coupled 12 September 2007 Southern Sumatra, M8.5 and M8.1 great earthquakes have already confirmed the diagnosis of TIP's. One of the other three smaller clusters of TIP's located in South America (i.e., the circle centered at 31°S and 70°W) got the confirmation with the occurrence of the 27 February 2010 offshore Maule, Chile M8.8 mega-trust. The epicenters of the main shock (star) and its aftershocks (white diamonds) fill the 600-km portion of the South American subduction zone, which is about one half of the major seismic belt segment highlighted by TIPs diagnosed in the regular experimental testing aimed at magnitude M8.0+ (**Fig.6.3.2**, yellow outline) and M7.5+. As mentioned above, the regular update on January 1, 2010 the second approximation diagnosed by algorithm MSc (red outline) missed the earthquake epicenter. However, this failure of MSc algorithm appears natural, taking into account the linear extent of the rupture zone, which is about one half of the area alerted in the first approximation [*Kossobokov et al.,* 2010].

Naturally, we cannot get in our lifetime enough statistics required for ultimate justification of applicability and efficiency of predictions in magnitude ranges M8.5+ and M9.0+. However, same as the unique case history of retrospective diagnosis of the M8-type TIP in advance the largest "starquake" in a series of the 111 flashes of energy release radiated from the neutron star with celestial coordinates 1806-20 [*Kossobokov et al.,* 2000], the application aimed at mega-earthquakes appears to us very important both from theoretical and practical viewpoints.

The algorithms M8 and MSc are neither optimal nor unique. Their efficiency and accuracy could be improved by a systematic monitoring of the alarm areas and by designing a new generation of earthquake prediction technique. This requires more data of different nature being analyzed systematically to establish reliable correlations between the occurrence of extreme events and observable phenomena.

References

Healy, J. H., V. G. Kossobokov, and J. W. Dewey. A test to evaluate the earthquake prediction algorithm, M8, *U.S. Geol. Surv. Open-File Report* **92-401**, 23 p. with 6 Appendices, 1992.

Keilis-Borok V.I, Kosobokov V.G, 1984. Complex long-term precursors for the strongest earthquakes in the world. Earthquake and disaster prevention. 27-th International Geological Congress, 4-14 August 1984, Moscow. Colloquium C6. M.: Nauka, Vol. 61, pp.56-66 (in Russian).

Keilis-Borok, V.I., and V.G. Kossobokov, 1987. Periods of high probability of occurrence of the world's strongest earthquakes, *Computational Seismology* **19**, Allerton Press Inc., p. 45-53.

Keilis-Borok,V., P.Shebalin, A.Gabrielov, and D.Turcotte, 2004. Reverse tracing of short-term earthquake precursors. *Phys. Earth and Planet. Inter.*, **145**, 1-4: 75-85.

Kossobokov, V.G.; L.L. Romashkova; A.K. Nekrasova, 2010. Targeting the next mega-earthquake: the 27 February 2010 Chile case. *Eos Trans. AGU, **91**(26), Meet. Am. Suppl.*, Abstract U41A-06.

Kossobokov, V., Romashkova, L., Nekrasova, A., 2008. Targeting the next mega-earthquake.

Geophysical Research Abstracts, Volume 10, 2008. Abstracts of the Contributions of the EGU General Assembly 2008, Vienna, Austria, 13-18 April 2008 (CD-ROM), EGU2008-A-07303.

Kossobokov, V.G., 1997. User Manual for M8. In Healy, J.H., Keilis-Borok, V.I., and Lee, W.H.K. (Eds), *Algorithms for earthquake statistics and prediction*. IASPEI Software Library, Vol. 6. Seismol. Soc. Am., El Cerrito, CA.

Kossobokov, V.G., V.I. Keilis-Borok, and B. Cheng, 2000. Similarities of multiple fracturing on a neutron star and on the Earth. *Phys. Rev. E* **61**: 3529-3533

Kossobokov, V.G., V.I. Keilis-Borok, and S.W.Smith, Localization of intermediate-term earthquake prediction, *J. Geophys. Res*., 1990, **95**, No. B12, 19763-19772.

Kossobokov. V., 2005. Can we predict mega-earthquakes. *Geophysical Research Abstracts*, Vol. 7, Abstracts of the Contributions of the EGU General Assembly 2005, Vienna, Austria, 24-29 April, 2005 (CD-ROM): 05832.

Romashkova, L., A. Nekrasova, V. Kossobokov, 2005. Seismic cascades in advance and after 26 December 2004 Sumatra-Andaman and other mega-earthquakes, *Eos Trans. AGU*, 86(52), *Fall Meet. Suppl.*, Abstract U11B-0834.

6.4. An "umbilic" catastrophe as a model of rock failure in earthquakes

A. V. Klyuchevskii, akluchev@crust.irk.ru**,** *The Earth's Crust Siberian Branch RAS, Lermontov st., 128, Irkutsk, 664033, Russia*.

Physical and mathematical (including numerical) modeling of earthquake physics has been increasingly developing lately as a tool to predict ground motion in large seismic events [*Keilis-Borok*, 1950; *Vvedenskaya*, 1969; 1984; *Kostrov*, 1975; *Riznichenko*, 1976, 1985; *Myachkin*, 1978; *Rice*, 1980; *Nikolaevsky*, 1982; *Aki, Richards*, 1980; *Shebalin*, 1997; *Lee et al.,* 2002] and to search for precursors [*Sadovsky*, 1975; *Dobrovolsky*, 1991; *Sobolev*, 1993; *Sobolev, Ponomarev*, 2003; *Zavyalov*, 2006]. According to the present-day views, an earthquake is associated with elastic fracture as the principal driving process, and an outlook of an earthquake source, a key subject in seismology, is reduced to physics (mechanics) of subsurface rock failure. In this respect, predicting a large or great earthquake and its consequences consists in recognizing the conditions for energy accumulation in zones of stress concentration and in understanding the mechanism which governs the deep-seated origin of failure and its evolution in space and time.

Modeling an earthquake source in terms of dynamic theory implies obtaining a space-time distribution of stresses and forces which fit the best the observed parameters of seismic waves. The well-known classical studies by *Keilis-Borok* (1950), *Vvedenskaya* (1969; 1984), *Kostrov* (1975), etc. provide a solid background of how to deduce the information on an earthquake source from seismological data. Details of earthquake modeling issues, from point or dislocation sources to dynamic models, can be found in [*Kostrov*, 1975; *Rice*, 1980; *Aki, Richards*, 1980; and references therein]. Proceeding from the principles of physics (mechanics), the cited authors interpret the source of a tectonic earthquake as rapid break of continuity in rocks along a certain surface under the effect of stress associated with shear strain. However, the origin, nucleation, and effectuation of earthquakes and related changes in the state of material at the source are far from being properly understood. The very problem is even formulated in quite different ways in different publications.

Dynamics of failure process

The dynamic problems of fracture mechanics turned out to be mathematically irresolvable with the classical methods, and almost each problem required some particular method [*Vvedenskaya* 1969; 1984; *Kostrov*, 1975]. Propagation of failure in solids (earthquake sources) has been commonly investigated within the limits of physical concepts and interpretation approaches developed in fracture mechanics theory. For a long time, the studies aimed at determining the type and direction of a point source equivalent to an earthquake in the polarity and amplitude ratio of first arrivals. Yet, the choice of a point source and constraining its orientation is just a part of the problem: one has to relate the

parameters of the point source with some physical ideas and obtain the physical parameters of an earthquake. The need in a rupture propagation theory for seismological applications brought about a need in synthesizing the knowledge of brittle failure mechanics and in developing techniques for solving the respective dynamic problems [*Vvedenskaya*, 1969; 1984; *Kostrov*, 1975].

Earthquakes are modeled through kinematic or dynamic problems which describe, in different ways, the same process of rock failure along some discontinuity. In kinematic modeling, slip is specified as a function of time and coordinates while dynamic models describe failure as a crack for which the user specifies the stress distribution on its surface, the interaction law of its faces, and some physical propagation laws. Earthquake failure mechanics is a field of fracture mechanics concerned with fast propagation of rupture and related generation of seismic waves. Continuity break is assumed [*Kostrov*, 1975] to be a universal mechanism of catastrophic release of shear stress but discontinuity becomes an earthquake source only when it is rapidly propagating. Sudden (catastrophic) stress release occurs by formation of a narrow zone of strain concentration at some surface which, macroscopically, is indistinguishable from the discontinuity that forms in an earthquake. The fact that an earthquake is sudden is evidence of local loss of stability in the deformation process. Unlike the stability loss that is a common subject of continuum mechanics, the cause of seismic instability lies with the properties of rock material. Note that it is only some layer that becomes unstable, with its thickness being controlled by inhomogeneity of the involved piece of crust. Unstable deformation may be physically ductile (plastic), and an earthquake source in this case can be presented as a giant Luders band in plastic material; or, it may be an unstable phase in a creep process. *Sharov* (1992) suggested a mechanism of rock failure implying four successive phases in a model of a nonequilibrium thermodynamic process.

The positive and negative signals that are characteristically present in natural earthquake seismograms can appear in synthetic seismograms in the case of discontinuous failure. The maximum displacement in the wavelet G_1 associated with a ring exceeds that in the wavelet G associated with an inclusion [*Vvedenskaya*, 1984]. It means that the failure process within a ring is physically different from that within an inclusion. At each point along the inclusion/ring boundary, alternating positive and negative inertia forces excite discrete elementary perturbations of opposite directions which produce oppositely directed signals when overlap at the observation point. The positive and negative signals in seismograms correspond to discrete stick-slip motions of the crack faces due to inhomogeneity of rocks [*Kostrov*, 1975].

Linear elastic fracture mechanics attributes the real strength loss in solids to the presence of numerous cracks (flaws), whose catastrophic propagation leads to failure. This theory describes brittle fracture as resulting from growth of a crack in the absence of significant plastic strain at its tip, when stress and strain are asymptotic and the crack propagation problem can be formulated in terms of stress intensity factors. However, the concept of stress factor looses sense in the case if there is a plastic zone at the tip of the crack that reaches 20% of the crack length, which places the behavior of deformed solid into the domain of plastic strength [*Parton*, 2007]. In this formulation, it is the domain of nonlinear fracture in which all models assume the presence of a rather well developed plastic zone at the crack tip. The dynamic modification of Griffith's failure criterion is

$$G = \frac{1}{2\mu}\left\{\frac{v^2}{c_2^2 R_*(\delta_1,\delta_2)}\left[\delta_1 K_I^2(t) + \delta_2 K_{II}^2(t) + \frac{1}{\delta_2} K_{III}^2(t)\right]\right\}, \tag{6.4.1}$$

where G is the released elastic energy, μ is the shear modulus, v is the failure rate, $\delta_i = \sqrt{1-(v/c_i)^2}$ (i=1, 2), c_1 and c_2 are the dilatational and shear elastic waves, respectively; the function $R_*(\delta_1,\delta_2)$ denotes the Rayleigh function $R_*(\delta_1,\delta_2) = 4\delta_1\delta_2 - (1+\delta_2^2)^2$; $K_I(t), K_{II}(t), K_{III}(t)$ are the stress factors for three types of cracks (*Parton*, 2007). Equation (1) is the energy balance equation, which is a dynamic equivalent of the relationship between the force and energy parameters of failure.

There are two basic postulates of the model of dynamic fracture mechanics:

i. Stress fields at the crack tip are described via stress factors;
ii. The criteria of the start, stop, and crack propagation are derived from energy balance equation

(6.4.1).

The appropriateness of the model is evaluated from experimental stress factors according to the fit between real and theoretically predicted conditions of start, propagation, and stop of crack growth. This comparison, however, casts doubt on the theory. For instance, it follows from the energy balance equation that the stop conditions are inverse with respect to the start conditions: a fixed crack is starting while a propagating crack stops at the same critical stress factor. However, the critical stress intensity factors of start or stop never coincide in practice, and the energy balance equation by no means implies the possibility of crack branching which is a common case in nature.

Topology (geometry) of the process. The calculated and observed displacement fields in *P*, *SH* and *SV* seismic waves are characterized by the geometry and spatial position of nodal planes at the points where one of the three wave types has zero displacement. In an early study [*Vvedenskaya*, 1969], the displacement field was sought, within the limits of the elasticity theory, as a wave equation solution at specified dynamic conditions on the failure surface. The nodal plane of the *P*-wave displacement field is a second-order cone with its vertex at the origin of the coordinates and an elliptical (or circular [*Vvedenskaya*, 1984] guide line. As the displacement direction changes, the conical surface splits into two planes while the cone may degenerate and become imaginary. The nodal planes of *SH* and *SV* waves are the conical surfaces of the second and third orders, respectively, with their vertices at the coordinates' origin. The *P* nodal plane is a hyperbolic cone with its axis orthogonal to the vectors $\bar{\mathbf{n}}$ and $\bar{\mathbf{b}}$ directed along the normal to the failure plane and along the displacement jump [*Kostrov*, 1975]. The rays corresponding to positive and negative *P* arrivals are separated in real earthquakes by a pair of mutually orthogonal nodal planes, which is possible only in the case of zero separation.

In the current practical seismology, an earthquake source has been commonly simulated by a point source which, at a large distance, gives a wave pattern equivalent to the observed one. The point-source model can be either a double pair of forces without moment (double dipole) or a set of such double pairs oriented in difference directions in space. These models correspond, respectively, to an earthquake mechanism with two nodal planes and relative displacement directions along these planes and a centroid moment tensor (CMT) solution [*Arefiev*, 2003; *Rebetsky*, 2007]. In the classical approach, the main focus in analysis of seismograms is on the polarity of picked *P* first arrivals with their signs fitting a quadrant distribution in the double-dipole model. A CMT solution is provided when analyzed is the wave field as a whole. With a system of coordinates related with the hypocenter and an earthquake source encircled by a unit-radius sphere, one can construct Cauchy hyperbolic surfaces which divide the sphere into domains of positive and negative *P* arrivals (**Fig.6.4.1**). In the double-dipole source model, the hyperbolic surfaces degenerate into two orthogonal planes.

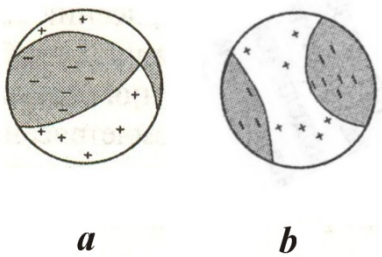

Fig.6.4.1. Point source models of an earthquake mechanism: (a) double dipole; (b) *CMT* solution. Lower hemisphere projection. Modified after (*Rebetsky*, 2007). Light gray color marks compressional first arrivals corresponding to sourceward motion, negative (–); white color marks tensile waves corresponding to stationward motion, positive (+).

Results

The rapid advance of earthquake source studies and, especially, the advent of methods for estimating the physical parameters of slip, calls for a single system of logically consistent concepts, instead of separate models and solutions. Such a system, which may account for new data on processes at an earthquake source, can stem from catastrophe theory, nonlinear fracture mechanics, and the respective ideas of seismology.

Table 6.4.1. Representativeness of the sample of $K_P \geq 10$ ($M_{LH} \geq 3.5$) earthquakes in the Baikal region with known focal mechanisms.

K_P	10	11	12	13	14	15	16	17	All shocks
n	2700	791	284	99	37	5	8	2	3926
n_1	53	72	61	43	24	4	6	2	265
n_1/n, %	2.0	9.1	21.5	43.4	64.9	80	75	100	6.7

Note: n is the number of shocks recorded in the Catalog of Earthquakes in the Baikal Region for 1950–1998; n_1 is the number of shocks with known focal mechanisms for 1950–1998; $n_1/n \times 100$, % is the data representativeness, in percent.

Even purposive studies of earthquakes in the Baikal region [*Klyuchevskii et al.,* 2009] provided estimates of source parameters for less than 10 % of $M_{LH} \geq 3.5$ ($K_P \geq 10$) events (**Table 6.4.1**). The earthquake mechanism data cover only a minor part of moderate shocks, though the representativeness increases with earthquake magnitude to exceed 50 % for $M_{LH} \geq 5.5$ ($K_P \geq 14$) events. This greater percent mainly accounts for the fact that reliable constraining the nodal planes requires a great number of body-wave first arrivals which, in an invariable observation system, is possible for relatively large events only. The source parameters of almost 40% of $M_{LH} \geq 5.5$ ($K_P \geq 14$) events in the Baikal region remain, however, undetermined. The use of the same input data in the source parameters modeling practice for the Baikal region often drives at ambiguous solutions, even if there are enough seismic stations [*Melnikova, Radziminovich*, 1998] Judging from the published evidence, the situation is similar in other active seismic areas elsewhere if the source parameters are inferred from first arrivals of body waves [*Shirokova*, 1985]. This may be due to some uncertainty in solutions based on *P* arrivals, possibly, related also with the interpretation of the geometry and position of nodal planes, i.e., with the topology (geometry) of rock failure in earthquakes.

The processes in earthquakes are generally agreed to be catastrophic. A catastrophe is most often meant as being related with very large displacement, velocity, and acceleration of ground motion in a short time, i.e., with the dynamics of the process. Note that jump-like changes in the variables of state commonly result from a particular topology of nonlinear dynamic systems [*Malinetsky, Potapov*, 2000] whose behavior is described in terms of catastrophe theory. According to this theory, there is a physical system which rapidly minimizes the potential while the latter changes as a function of govern parameters (the minimization is local). As the parameters change, some local minimums may disappear, and these are the related catastrophic changes that gave the name to the theory. In this respect, there is much freedom for geometrical intuition supported by diverse pictures which one can draw when there are no more than three active variables (the sets of parameter values at which a catastrophe occurs). In the case of less than five active variables, one can obtain a small list of polynomials (René Thom's seven catastrophes), at which almost any potential function can be driven through local substitutions in the vicinity of the origin [*Poston, Stewart*, 1978]. At some conditions, a system insensitive to small perturbations can be simulated locally using one of the seven elementary catastrophes.

Catastrophe theory is quite a well advanced field of the general theory of nonlinear dynamic systems, which has received much recent interest. It concerns with self-organizing dynamic systems whose hierarchic structure maintains their stability, interaction with the environment, and evolution. The natural and unavoidable character of the elementary catastrophes follows from the universality of catastrophes in Thom's list. Thom suggested to model the sudden changes in natural phenomena using the topological theory of dynamic systems, which descends to the works by H. Poincaré, and noted the special importance of structural stability in this consideration. The methods of catastrophe theory play a certain (though not universal) role in natural sciences. They are applicable directly to self-organizing systems in which some function is minimized or maximized (e.g., energy and entropy, respectively) at each moment of time as the situation is changing, while the energy and stress release in an earthquake

is a way to minimize these parameters. The Earth' lithosphere as a whole can be interpreted as a self-organizing system [*Sadovsky et al.*, 1987; *Keilis-Borok*, 1990; *Sornette et al.,* 1990], and the lithosphere of the Baikal rift in particular shows a behavior of a nonlinear system with bifurcations corresponding to large earthquakes [Klyuchevskii and *Klyuchevskaya*, 2010; *Klyuchevskii*, 2010].

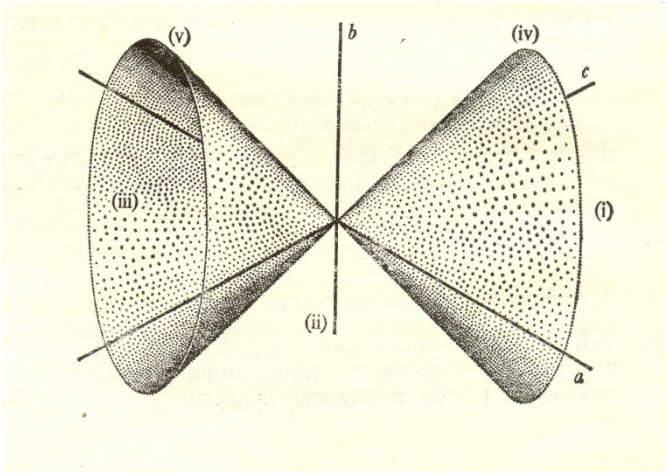

Fig.6.4.2. A geometrical interpretation of the quadric discriminant cone.

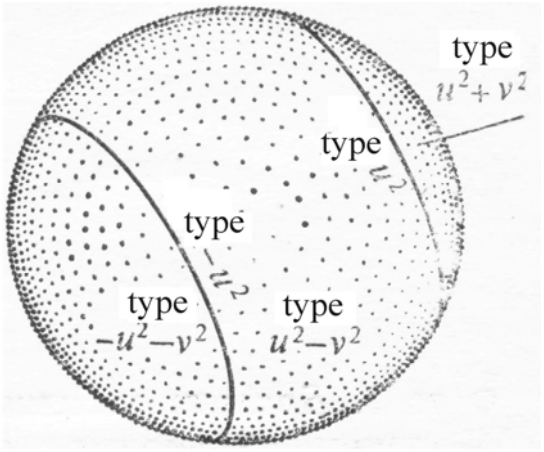

Fig.6.4.3. A geometrical interpretation of the quadric discriminant cone in a unit sphere.

Fig.6.4.2 and **Fig.6.4.3** are given in same notations as in [*Poston, Stewart*, 1978].

A quadratic equation with two active variables

$$g(x,y)=ax^2+bxy+cy^2 \tag{6.4.2}$$

can be interpreted geometrically as a quadric discriminant cone (**Fig.6.4.2**) in which *g* is zero. One can transform this picture into one of Fig. 3, for the case of unit sphere

$$\{(a,b,c): a^2+b^2+c^2=1\}, \tag{6.4.3}$$

with its center at the origin, draw two circles on the sphere as in **Fig.6.4.2**, and construct cones below them with their vertices at the origin (Poston and Stewart, 1978). The two circles are quadric forms (*a*, *b*, *c*) that lie on the unit sphere and satisfy the condition of the discriminant cone $b^2=ac$. Comparing **Fig.6.4.1b** and **Fig.6.4.3** shows that the nodal surfaces are positioned on the sphere in the same way as the surfaces of the cone. Therefore, the *P*-wave nodal surfaces have a discriminant cone geometry, which is consistent with the seismological theory and practice [*Vvedenskaya*, 1969; 1984; *Kostrov*, 1975].

This geometry in the manifold *M* is appropriate only of elliptical and hyperbolic umbilics of Thom's seven elementary catastrophes. Hyperbolic umbilic catastrophe is given by [*Poston, Styuart*, 1978]

$$V_{abc}(x,y)=x^3+y^3+axy+bx+cy, \tag{6.4.4}$$

where *a*, *b* and *c* are the active variables (govern parameters). The catastrophe manifold *M* is defined by the pair of equations

$$0=\frac{\partial}{\partial x}V_{abc}(x,y)=3x^2+ay+b, \tag{6.4.5}$$

$$0=\frac{\partial}{\partial y}V_{abc}(x,y)=3y^2+ax+c. \tag{6.4.6}$$

Fig.6.4.4. An umbilic bracelet Tim Poston cut out of hard maple [*Poston, Stewart*, 1978].

After the Taylor expansion at the point corresponding to the manifold M and subsequent transformations, the quadratic part of the series degenerates at the discriminant cone. The cubic terms of the Taylor series likewise lie on the same cone and have a single real root straight line. There are points of a fold catastrophe on the cone, except for the straight line where the cusp and double cusp catastrophes lie, and the Morse points lie outside the cone. Using a projection onto the govern space, one can find a bifurcation set in the form of fold, cusp, and double cusp elementary catastrophes. The elliptical umbilic structure is generally similar to that of hyperbolic umbilic [*Poston, Stewart*, 1978]. An umbilic surface can be described as a "twisted rotation surface" that results from motion of a three-cusp hypocycloid that rolls within a circle (at each moment, the circle is orthogonal to the hypocycloid plane at its center). While it is rolling, the hypocycloid rotates in its plane and can do one third of a full revolution [*Poston, Stewart*, 1978]. *Zeeman* (1976) who was the first to investigate this surface (**Fig.6.4.4**) called it *umbilic bracelet*. Proceeding from the study of *Johnston* and *Linde* (2002), one may assume that the size of the initiation domain in which an umbilic catastrophe is realized does not exceed several tens of meters and does not depend on the earthquake magnitude. The directivity of motion defines the slip geometry at the source.

Discussion

According to the today's views, the source of a seismic wave field is not necessarily required to be a two-parameter set of points. However, the reported results have a clear physical ground rooted in catastrophe theory and thus support the idea of the earthquake physics developed in seismology. The catastrophe theory allows a new outlook on the classical results, which may be useful as a basis for further advance. A catastrophe has universal dynamics (sudden jumps) and topology (critical points), and in both cases, this is a degenerate critical point corresponding to the absolute minimum (or maximum for entropy). The maximum delay principle in this theory implies that a system undergoes a catastrophe only when it has no other choice. This means that the equilibrium-state path replaces a sheet on the surface only having passed through a catastrophe, while the list where it occurs "disappears": catastrophic jumps happen when smooth small changes in the govern parameters cause abrupt changes of state. This is, however, not the only way: minor path dissimilarities may cause major difference in the state without any jump, even if the paths start and finish at the same points. The system can pass from one state to another either smoothly or through a jump depending on its path, i.e., on the govern parameters (active variables).

It follows from equation (4) that in both hyperbolic and elliptical umbilic catastrophes, the potential function depends on three active variables. Two of them may represent stress and strain in rocks and the third parameter may be responsible for rock rheology. Note that the fold points continuously fill the discriminant cone (except for the cusp and double cusp straight line) and divide the space into the domains of positive and negative P first arrivals in seismograms. The crack propagation front is also known [*Parton*, 2007] to have the form of a fold catastrophe; the vicinity of this front is a zone of greatest stress concentration where local failure occurs. As for the cusp and double cusp catastrophes, they can generate the alternating positive and negative signals and define the recorded waveforms. It is the universal character of umbilic catastrophes that may be responsible for the self-similarity of the amplitude spectra of earthquakes [*Aki, Richards*, 1980].

The failure dynamics can be described using the variational principle of critical action from catastrophe theory. According to this principle, among all other paths with the same ends, failure takes the one which is extreme stationary (i.e., is a minimum, a maximum, or another critical point) with respect to resistance against its propagation. The applicability of variational principles in the classical mechanics is explicable with the example of quantum mechanics where variations have the physical sense [*Poston, Stewart*, 1978]. In this approach, the most probable path defined by the stationary conditions will be the actual failure path. This assumption is satisfactory as far as this stationary path of the action (energy or time) remains a non-degenerate critical point.

Conclusion

Thus, the methods of catastrophe theory can be applied to interpret the topology (geometry) of rock failure in earthquakes. With this approach, an earthquake source is hypothesized to reflect the properties of a universal umbilic catastrophe as the manifold of the latter corresponds to a discriminant cone formed by *P* first arrivals associated with seismic failure. This hypothesis can account for the sudden character of earthquakes, the geometry of slip, the alternation of positive and negative signals in seismograms, and the self-similarity of earthquake amplitude spectra.

The study was supported by grants 08–05–90201–Mong_a and 09–05–00014_a from the Russian Foundation for Basic Research.

References

Aki, K., Richards, P., 1980. Quantitative Seismology. Freeman and Co., New York.

Arefiev, S.S., 2003. Epicentral Seismological Studies. Akademkniga, Moscow (in Russian).

Dobrovolsky, I.P., 1991. The Theory of Earthquake Nucleation. OIFZ, Moscow (in Russian).

Johnston, M.J.S., Linde, A.T., 2002. Implication of crustal strain during conventional, slow, and silent earthquakes. In: Lee, W.H.K., Kanamori, H., Jennings, P.C., Kisslinger, C. (Eds.), International Handbook of Earthquake and Engineering Seismology, Part A. pp. 589-605.

Keilis-Borok, V.I., 1950. Studying sources equivalent to earthquake foci. Transactions, Geophysical Institute, AN SSSR, Izd. AN SSSR, Moscow-Leningrad, No. 9 (136), 20-42.

Keilis-Borok, V.I., 1990. The lithosphere of the Earth as a nonlinear system with implications for earthquake prediction. Rev. Geophys. 28, 19–34.

Klyuchevskii A.V., 2010. Nonlinear geodynamics of the Baikal Rift System: an evolution scenario with triple equilibrium bifurcation. J. Geodyn. 49 (1), 19–23.

Klyuchevskii, A.V., Klyuchevskaya, A.A., 2010. Stress-associated synchronization and desynchronization in geologic and biologic systems. Izvestia, Atmospheric and Oceanic Physics, 46 (7), 81–92.

Klyuchevskii, A.V., Dem'yanovich, V.M., Dzhurik, V.I., 2009. Hierarchy of earthquakes in the Baikal rift system: implications for lithospheric stress. Russian Geology and Geophysics, 50 (3), 206–213.

Kostrov, B.V., 1975. Mechanics of an Earthquake Source. Nauka, Moscow (in Russian).

Lee, W.H.K., Kanamori, H., Jennings, P.C., Kisslinger, C. (Eds.), 2002. International Handbook of Earthquake and Engineering Seismology. Part A. Academic Press, Amsterdam, Boston, New York, Tokyo.

Malinetsky, G.G., Potapov, A.B., 2000. Current Problems of Nonlinear Dynamics. URSS, Moscow (in Russian).

Melnikova, V.I., Radziminovich, N.A., 1998. Mechanisms of action of earthquake foci in the Baikal region over the period 1991-1996. Russian Geology and Geophysics, 39 (11), 1597-1606.

Myachkin, V.I., 1978. Earthquake Nucleation Processes, Nauka, Moscow (in Russian)

Nikolaevsky, V.N., 1982. Earth's crust, dilatancy, and earthquakes: A review, in: Nikolaevsky, V.N. (Ed.), Mechanics of an Earthquake Source [in Russian]. Mir, Moscow, pp. 133–217.

Parton, V.Z., 2007. Mechanics of Fracture: from Theory to Practice. LKI, Moscow (in Russian).

Poston, T., Stewart, I., 1978. Catastrophe Theory and its Applications. Pitman, London, San Francisco, Melbourne.
Rebetsky, Yu.L., 2007. Tectonic Stress and Strength of Natural Rocks. Akademkniga, Moscow. (in Russian).
Rice, J., 1980. The Mechanics of Earthquake Rupture, in: Dziewonski, A.M., Boschi, E. (Eds.), Proc. Intern. School of Physics. Italian Physical Society, pp. 555–649.
Riznichenko, Yu.V. (Ed.), 1976. Treatise on Earthquake Physics. Nauka, Moscow (in Russian).
Riznichenko, Yu.V., 1985. Problems of Seismology [in Russian]. Nauka, Moscow.
Sadovsky, M.A. (Ed.), 1975. Earthquake Source Physics. Nauka, Moscow (in Russian).
Sadovsky, M.A., Bolkhovitinov, L.G., Pisarenko, V.F., 1987. Deformation of the Geophysical Medium and the Seismic Process. Nauka, Moscow (in Russian).
Sharov, V.I., 1992. A tectonic earthquake as a nonequilibrium thermodynamic process of rock failure (On the change of paradigm in seismology). Izv. RAN, Fizika Zemli, No. 5, 121–127.
Shebalin, N.V., 1997. Large Earthquakes. Selected Works. Izd. Akad. Gorn. Nauk, Moscow (in Russian).
Shirokova, E.I., 1985. Non-shear earthquakes. Izv. AN SSSR, Fizika Zemli, No. 3, 29–40.
Sobolev, G.A., Ponomarev, A.V., 2003. Earthquake Physics and Precursors. Nauka, Moscow (in Russian).
Sobolev, G.A., 1993. Fundamentals of Earthquake Prediction. Nauka, Moscow.
Sornette, D., Davy, P., Sornette, A., 1990. Structuration of lithosphere in plate tectonics as a self-organized critical phenomenon. J. Geophys. Res., 95 (B11), 17,353-17,361.
Vvedenskaya, A.V., 1969. Stress and Rupture in Earthquake Sources in Terms of Dislocation Theory. Nauka, Moscow (in Russian).
Vvedenskaya, A.V., 1984. Seismodynamics. Nauka, Moscow (in Russian).
Zavyalov A.D., 2006. Medium-term Earthquake Prediction: Fundamentals, Methods, Implementation. Nauka, Moscow, 256 p. (in Russian).
Zeeman, E.C., 1976. The umbilic bracelet and the double cusp catastrophe, in: Hilton, P.J. (Ed.), Structural Stability, the Theory of Catastrophes, and Applications in Sciences. Lecture Notes in Mathematics. Springer, Berlin and New York, pp. 328 – 366.

7. Induced seismicity and its monitoring

7.1. Induced seismic activity. The effect of production induced factors on fine seismicity structure

A. V. Nikolaev, nikavs@ifz.ru**,** *Schmidt Institute of the Physics of the Earth RAS. B. Gruzinskaya 10. Moscow 123995, GSP-5, Russia.*

The investigations of induced seismicity and the factors, natural and production induced impacts, affecting it now broadly expand experimental studies and provide rethinking of geological and physical representations of processes proceeding inside the Earth basing on their results. Active promotion of the geophysical medium model, its expansion and extension in the scientific mind proceeds. In part of development of geological grounds, geological structural models, dynamics of natural medium and geological and physicochemical processes proceeding in it become increasingly complicated. In terms of development of the physical notions on the induced seismicity, the scientific efforts are focused at combined effect of natural and production induced factors of different origins on it. New hypotheses based on the ideas of the effect of degassing and dehydration of the Earth crust and mantle on seismicity, interaction of processes of different nature, metastable states, remote actions of production induced and natural factors, including planetary and astronomic ones, are investigated. Paradoxes discovered in the experiments, not clear yet, are studied. And the ideas and methods of seismicity study and earthquake forecast interpenetrate.

The effect of natural processes on seismicity manifests in natural variations of endogenous seismic noises, nano- and microearthquakes and the ones from low to the highest magnitudes. These variations are directly associated with changes in the stress-strain state and tectonic movements. An indirect connection is due to nonlinear properties of the geologic environment, which are processes of a different nature.

Stress-strain state changes and their mediated effect on seismicity. Numerous reports made at the Meeting held by Institute of Dynamics of Geospheres in 2010 [*Adushkin*, 2010; *Kocharyan*, 2010; *Levina*, 2010; *Molcanov*, 2010; *Tarasov*, 2010; *Avagimov*, 2010; *Astafurov*, 2010] and a number of papers [*Tarasov*, 2009a,b; 2010; *Mirzoev*, 2009] concerned these problems.

Block structure of the medium, elastic interblock fault zones, their hierarchic heterogeneity, and energy saturation are basic geological and tectonic concepts of the structural model of the Earth crust and the upper mantle. These elements control intermotions of blocks, their tectonic activity manifested in creep and endogenous seismic noise (the frequency range 100 Hz or higher, kilohertz) and earthquakes with a broad range of magnitudes: from negative, around -4 ÷ -6, nanoearthquakes with predominant frequencies from 20 to 2000 Hz via medium magnitude (-2 to 5, 0.02 to 100 Hz) and high magnitude earthquakes to catastrophic events with the magnitude up to 9 or higher and frequencies from zero (residual deformations) to 100 Hz or higher (acoustic and ambient seismic noise), which accompany geotectonic movements. These processes proceeding in the real medium are studied by seismic, acoustic and geological deformation methods, as well as by electrical logging, magnetic and electromagnetic measurements. The effect of changes in characteristics of seismic wave field (elastic and inelastic parameters, induced electric, magnetic and electromagnetic fields) with parameters of dynamic impacts from seismic generation sources [*Levina*, 2010; *Mirzoev*, 2009; *Gokhberg*, 2010; *Rebetskiy*, 2010; *Turuntaev*, 2010; *Sherman*, 2010; *Avagimov*, 2010; *Lavrikov*, 2010; *Sycheva*, 2010; *Kuptsov*, 2010; *Mirzoev*, 2010].

Degassing and dehydration, embrittlement of rocks. Degassing processes proceeding in lithosphere are associated with embrittlement of the material, reduction of strength and destruction. This is accompanied by emission of elastic strain energy in the form of stress relaxation, creep, seismic noises and earthquakes. Degassing, dehydration and hydration can be decisive factors in earthquake preparation. Until recently, models of earthquake focus preparation and development were built with no respect to changes in rheological properties of the matter due to degassing, dehydration and hydration, which are accompanied by changing elastic and inelastic modules of rheological properties of rocks. Consideration of these processes will make the origin of events proceeding inside the Earth, seismicity, first of all, much more understandable: changes in characteristics of seismic wave fields of elastic and inelastic parameters and metastable state of the matter [*Gusev*, 2007; *Gufeld*, 2007; 2008a,b; 2010].

The change in potential of the bottom layer of atmospheric electricity due to radon exhalation along fault zone correlates well with microseismic noise intensity anomalies (increasing) that testifies the effect of radon degassing on increasing activity of microseism and acoustic strain noise [*Kuptsov*, 2007; *Shuleikin*, 2008].

Water property variations are due to its structuring, cluster formation accompanied by variations in density, electric conductivity and viscosity. Thus, water present in the interior of the Earth, bound or free, is able to change physical and chemical properties of rocks irrespective of other physical impacts on them, i.e. water itself is able to affect the physical properties of rocks and the processes proceeding inside the Earth. There as experimental evidences that changes in water are induced by processes associated with the Sun, the Moon and the planets motion [*Volkov*, 2008a,b]. It is obvious that water effect should touch upon geodynamic processes, seismicity and its manifestations in other hypostasis.

Long-range action of initiating factors is due to several reasons. This is the amazing sensitivity of rocks, earthquake preparation and initiation in permanently changing energy saturated and nonlinear geophysical medium subject to variations of seismic and electromagnetic noise level and present in the metastable state. At the same time, there are tenable evidences of hyperdistant-range influence of

cosmic factors, such as planetary motion of planets by the coelosphere and gravitational radiation of pulsars.

Other astrophysical and physical phenomena were detected under special conditions by a device, which registers small changes in the Earth velocity at some specific moments of time – morning and evening crossing of the horizon line by the Sun, the Moon giant planets Jupiter and Saturn and their passing over upper and lower culminations. For a short period of time about 10-15 minutes, the background of endogenous microseismic noise, nanoseismisity, increased [*Vasiliev*, 2008; *Lezdynsh*, 2008]. In case of specific, favorable quincunx, relatively intense earthquakes with magnitude 5 or higher were detected, their foci occurring in the regions with increased tectonic strain, i.e. in places, where earthquake conditions were formed. As confirmed by observation, detected regularities may be applied to the earthquake forecast, on any hand, for Kamchatka region [*Lezdynch*, 2008].

Summing up this section of the review, note that the influence of natural processes on seismicity is high anywhere and manifests not only in increased seismic hazard in a broad range of frequencies, energy and other manifestations, but also in temporary reduction of the seismicity level. These changes are characterized by interference of many acting factors, are unstable in some manifestations and widely used in attempts to forecast earthquakes.

The influence of industrial processes. Historically, construction of impounded bodies and high dikes and strong earthquakes in the vicinity of them became the initial experimental fact, which called attention to the problem of induced seismicity. The following are facts of increasing seismic potential of fault zones in the areas of fluid injection, nuclear subsurface bursts, production of gas, oil and solid mineral resources, launches of heavy missiles, near high vibration sources of hydraulic plants, industrial borrows, mining of coal, rock salt and other solid minerals.

Permanent geophysical monitoring is carried out near impounded bodies and high (over 100 m) dams, in oil and gas fields and large industrial borrows, where strong blasts are used [*Adushkin*, 2008; 2010; *Mirzoev*, 2009, 2010; *Eremenko*, 2010; *Avagimov* 2010; *Adushkin*, 2010; *Gokhberg*, 2010].

Vibration and electric impacts are significant initiators of seismicity in a wide range of its manifestations. Technologically, they are implemented by high power seismic vibrators noisy hydraulic power plants, powerful electric magnetogas dynamic (MGD) generators discharging powerful current pulses to the ground. The pulse length is 4-5 s with the power of 10^7 -10^9 J. The effect of electric impacts on seismicity is studied. It is found that electric impact most clearly manifests in initiation of the 5-km upper layer. Depending on physical properties of the upper Earth crust and MGD generator power, its distance of action is 100 to 1000 km. The effect of impacting the Earth crust is not only initiation of moderately strong earthquakes, but also their unexpected localization, acceleration of slow tectonic displacements, the creep [*Bogomolov*, 2010; *Tarasov*, 2010a,b,c; *Sycheva*, 2010; *Sychev*, 2010; *Tarasov*, 2007; *Tarasov* 2008a,b,c; *Tarasov*, 2009].

Industrial impacts inevitably occur at the background of natural processes and their combined effect can be planned in advance, if, for instance, one of background natural impacts is the earth tide or cyclonic activity, solar storm and/or burst (eruption), a strong earthquake or creep – they increase geodynamic or seismic activity. Seismicity is often reduced by sea storms, weather phenomena, and occurrence of intense microseisms. The same effects are induced by some industrial impacts: formation of strong and weak vibration fields, mass bombing, chemical and nuclear bursts, oil and gas production, fluid industrial waste injection. For combined impacts, complex simultaneous impacts can be chosen, nonlinear type of their combination giving in many instances unpredictable result [*Adushkin*, 2010; *Kocharyan*, 2010ab; *Gokhberg*, 2010; *Mirzoev*, 2010; *Turuntaev*, 2010; *Zeigarnik*; *Kuptsov*, 2007; *Shuleikin*, 2008; *Lezdinsh*, 2007; *Vasiliev*, 2008; *Volkov*, 2008a,b; *Adushkin*, 2008; *Mirzoev*, 2009; *Tarasov* 2010c; *Gusev* 2007; *Gufeld*, 2008a,b; *Zeigarnik*, 2009; 2010].

This, to the full extent, relates to the earthquake forecast: a complex interference of natural and industrial impacts frequently leads to mistakes in predictions, creates pessimism of the investigators and increases the number of opponents, who persuade scientists, scientific community and administration not to beat the air forecasting the earthquakes.

In any case, the use of combined natural and industrial impacts requires preliminary investigations – field, laboratory, physical and mathematical simulation, and application of the entire stockpile means of experimental and theoretical science. Thus, opportunities and effects of combined impacts are extremely numerous. It is already seen that the variety of conditions and nature of impacts cause great difficulties in the investigation of this subject, and sometimes make a positive result impossible – in many cases, the result will appear unclear, glimmering.

As a matter of fact, the situation is not so pessimistic. As we see, the fundamental problem, which investigation leads to a success at the wide scientific front, is the study of induced seismicity and geophysical fields and processes in conditions of simultaneous complex action of these factors. The fundamental research of induced seismicity will bring us to success in natural and exact sciences, which investigate the geodynamic process and seismicity, in particular.

References

Adushkin V.V., Spichak A.A. Tidal force of geophysical processes // Trigger effects in geosystems. Editors V.V.Adushkin and G.G.Kocharyan. Transactions of seminar - conference. Moscow, GEOS, June 23-24, 2010. P. 8-17.

Adushkin V.V., Turuntaev S.B., Kulikov V.I., Strom A.L. Industrially induced catastrophic processes in the Earth crust // Changes of the environment and climate: natural and relates industrial catastrophes. Vol. 1. Seismic processes and catastrophes. M.: IFZ RAN. 2008. P. 283-296.

Astafurov S.V., Shilco E.V. Grigoriev A.S. Influence of constrained conditions of the geologic medium deformation in active fault zones at initial stages of activation // Trigger effects in geosystems. Editors V.V.Adushkin and G.G.Kocharyan. Transactions of seminar - conference. Moscow, GEOS, June 23-24, 2010. P. 167-174.

Avagimov A.A., Zeigarnic V.A., Okunev V.I. Dynamics of the triggering processes of deformation and fracturing by energetic impact on model samples // Trigger effects in geosystems. Editors V.V.Adushkin and G.G.Kocharyan. Transactions of seminar - conference. Moscow, GEOS, June 23-24, 2010. P. 159-166.

Bogomolov I.M. Influence of electromagnetic impulses of rupture formation at different structure scale levels. // Trigger effects in geosystems. Editors V.V.Adushkin and G.G.Kocharyan. Transactions of seminar - conference. Moscow, GEOS, June 23-24, 2010. P. 42-51.

Gohberg M.B., Kolosnitsyn N.I. Triggering mechanisms of earthquakes // Trigger effects in geosystems. Editors V.V.Adushkin and G.G.Kocharyan. Transactions of seminar - conferenct. Moscow, GEOS, June 23-24, 2010. P. 52-61.

Gufeld I.L., Afanas'ev A.V., Afanas'eva V.V., Novoselov O.N. Trigger effects of seismotectonic process in dynamically changing geological medium // Doklady RAN. 2010. V. 433. No. 1. P. 92-96.

Gufeld I.L., Gavrilov V.A., Korol'kov A.V., Novoselov O.A. Endogenous activity of the Earth and decompression origin of seismic noise // Doklady RAN. 2008. V. 423. No. 6. P. 811-814.

Gufeld I.L. Physicochemical mechanics of strong crust earthquakes // Vylkanologia I Seismologia. 2008. No. 1. P. 62-65.

Gufeld I.L. Seismic process. Physicochemical aspects // Korolev: TsNIIMash. 2007. 160 p.

Gusev G.A., Gufeld I.L. Seismic process in extremely energy-saturated geological medium and earthquake forecast // Vylkanologia I Seismologia. 2007. No. 6.

Kocharyan G.G., Markov V.K., Markov D.V. et al. Mechanics of the processes of changing the regime of fault zone of deformation by dynamic effects // Trigger effects in geosystems. Editors V.V.Adushkin and G.G.Kocharyan. Transactions of seminar - conference. Moscow, GEOS, June 23-24, 2010. P. 62-70.

Kocharyan G.G. Remote trigger of dynamic events // Trigger effects in geosysnems. Editors V.V.Adushkin and G.G.Kocherian. Transactions of seminar - conference. Moscow, GEOS, June 23-24, 2010. P. 18-30.

Kuptsov A.V., Marapulets Yu.V., Mishchenko M.A. et al. On connection of high-frequency seismic noise and electric field in the surface layer of the atmosphere // Vulkanologia I Seismologia. 2007. No. 5. P. 71-76.

Levina E.A., Ruzhich V.V. Earthquake migration as demonstration of wave deformations of the earth crust // Trigger effects in geosystems. Editors V.V.Adushkin and G.G.Kocharyan. Transactions of seminar - conferenct. Moscow, GEOS, June 23-24, 2010. P. 71-77.

Lezdinsh A.Ya. Astroseismology – a short message. // The "Planet Earth" System (Nontraditional problems of geology) XIVth Scientific Seminar, 2008. M.: Geological Department, MSU. P. 221-225.

Makarov P.V. Self-organized criticality and seismic processes // Trigger effects in geosystems. Editors V.V.Adushkin and G.G.Kocharyan. Transactions of seminar - conference. Moscow, GEOS, June 23-24, 2010. P. 78-86.

Mirzoev K.M., Nikolaev A.V., Lukk A.A. et al. // Induced seismicity and possibility of controllable discharge of accumulated tectonic strains in the Earth crust // Fizika Zemli. 2009, No. 10. P. 49-68.

Mirzoev K.M., Nikolaev A.V., Lukk A.A. et al. Method of elastic energy withdrawal for earthquake prevention // Trigger effects in geosystems. Editors V.V.Adushkin and G.G.Kocharyan. Transactions of seminar - conference. Moscow, GEOS, June 23-24, 2010. P. 87-95.

Novikov V., Vorontsova E., Bragin V., Sycheva N. Regional geomagnetic field variations and seismicity activity of the Northern Tian Shan // Abstract 106-TUE-P1700-1279, IAGA-2009, Sopron, Hungary, August 23-30, 2009.

Novikov V., Vorontsova E., Bragin V., Sycheva N. Triggering impact of geomagnetic field variations on earthquake occurrence considering the earthquake source mechanisms // Abstract 106-TUE-P1700-1282, IAGA-2009, Sopron, Hungary, August 23-30, 2009.

Novikov V., Zeigarnik V. Development of basic physics of artificial electromagnetic impact on deformation processes in the Earth crust // Proc. of VIII General Assembly of European Seismological Commission, Montpellier, France, September 6-10, 2010.

Novikov V, Zeigarnik V. Earthquake electromagnetic triggering phenomena: field and lab observations//Proc. of EMSEV Workshop-2010, Chapman University, Orange, CA, USA, 406 October, 2010.

Novikov V, Zeigarnik V, Konev Yu, Rickman V. (2009). Electric Triggering of Crack Formations in the Fault for Release of Tectonic Stresses // *Eos Trans. AGU, 90(52)*, Fall Meet. Suppl., Abstract S51C-1447.

Novikov V, Klyuchkin V, and Okunev V. Experimental Study of Electromagnetic and Dynamic Triggering Phenomena at the Spring-Block Facility // Proc. of EMSEV Workshop-2010, Chapman University, Orange, CA, USA, 406 October, 2010.

Novikov V. Electromagnetic triggering of earthquakes: natural and man-made phenomena and their application for earthquake hazard mitigation // Eos Trans. AGU, 91(26), Meet. Am. Suppl., Abstract NH32A-03, The Meeting of Americas, 8-12 August 2010, Foz do Iguassu, Brazil.

Rebetsky Y.L. Physical processes body determining its metastable states and possibility of triggering effect // Trigger effects in geosystems. Editors V.V.Adushkin and G.G.Kocharyan. Transactions of seminar // Trigger effects in geosystems. Editors V.V.Adushkin and G.G.Kocharyan. Transactions of seminar - conference. Moscow, GEOS, June 23-24, 2010. P. 105-116.

Shuleikin V.N., Reznichenko A.P., Pushchina L.V. On relation of methane, hydrogen and radon of subsurface air to electric field of the surface layer of the atmosphere // Proceedings of All-Russian Conference "The Earth degassing: geodynamics, geofluids, oil, gas and their parageneses", M.: GEOS. 2008. P. 544-547.

Sychev V.N., Bogomolov L.M., Rybin A.K. et al. Influence of the Earth crust electromagnetic probing on the seismicity of the Bishkek geodynamic test site // Trigger effects in geosystems. Editors V.V.Adushkin and G.G.Kocharyan. Transactions of seminar - conference. Moscow, GEOS4, June 23-24, 2010. P. 316-325.

Sycheva N.A., Bogomolov L.M. Sychev V.N. Solar flare, Seismic noise level variations and North Tian Shan seismicity // Trigger effects in geosystems. Editors V.V.Adushkin and G.G.Kocharyan. Transactions of seminar - conference. Moscow, GEOS, June 23-24, 2010. P. 326-335.

Tarasov N.T., Tarasova N.V. Imitative electromagnetic influence on the Earth crust deformation processes: strain relaxation, active monitoring possibility in order to earthquake forecast // Trigger effects in geosystems. Editors V.V.Adushkin and G.G.Kocharyan. Transactions of seminar - conference. Moscow, GEOS, June 23-24, 2010. P. 136-143.

Tarasov N.T., Tarasova N.V. Changes in spatial and energetic seismicity parameters at crust irradiation by high-power electromagnetic pulses // Geodynamics and geoecology of high-mountain regions in XXI century. Ed. Dpm Monzhikov B.Ts. Moscow-Bishkek: "Kantskaya Tipografia", 2008. Iss. 3. P. 58-66.

Tarasov N.T., Tarasova N.V. Increase of seismotectonic deformation rate in the course of deep electric probing using MGD-generator // Electromagnetic surveys of the Earth. Ed. V.V. Spichak. M.: IFZ RAN, 2009. P. 154.

Tarasov N.T., Tarasova N.V. Relaxation of elastic strains in the crust affected by strong electromagnetic fields, changes of the seismic process as a nonlinear dynamic system // VIII International School-Seminar "Physical grounds of rock destruction forecast". 2010. Saint-Petersburg: "Pradikom". P. 84 (Thes. Rep.).

Tarasov N.T., Tarasova N.V. Seismicity variations at crust irradiation by high-power electromagnetic pulses // Report on the Plenary Meeting of the Exhibition "Russian Geology from Congress to Congress", VI All-Russian Congress of Geologists. 2008.

Tarasov N.T., Tarasova N.V. The effect of strong electromagnetic fields on the seismotectonic deformation rate and possibility of active monitoring for the purpose of earthquake forecast // VIII International School-Seminar "Physical grounds of rock destruction forecast". 2010. Saint-Petersburg: "Pradikom". P. 85 (Thes. Rep.).

Tarasov N.T., Tarasova N.V. Variations of energetic and fractal characteristics at crust irradiation by high-power electromagnetic pulses // Fundamental basis of new technologies in oil and gas industry. Theoretical and applied aspects. Theses of reports of the All-Russian Conference. M.: GEOS, 2007. P. 231-232.

Tarasov N.T. The effect of electromagnetic fields on the seismotectonic deformation rate // Doklady RAS. V. 433. 2009. No. 5. P. 680-692.

Tarasov N.T. Variations of the seismic process at crust irradiation by high-power electromagnetic pulses // Chapter from the monograph (p. 177-195): Modern methods of treatment, analysis and interpreting of electromagnetic data. Ed. V.V. Spichak. M.: URCC, 2008. 278 p.

Turuntaev S.B., Melchaeva O.Yu. An analysis of triggered seismic processes by means of non-linear dynamics methods // Trigger effects in geosystems. Editors V.V.Adushkin and G.G.Kocharyan. Transactions of seminar - conference. Moscow, GEOS, June 23-24, 2010. P. 124-135.

Vasiliev S.A. A series of articles on the nature of long-range action // The "Planet Earth" System (Nontraditional problems of geology) XIVth Scientific Seminar, 2008. M.: Geological Department, MSU. P. 93-221.

Volkov Yu.V. Penetrating solar radiation and its effect of the Earth // The "Planet Earth" System (Nontraditional problems of geology) XIVth Scientific Seminar, 2008. M.: Geological Department, MSU.

Volkov Yu.V. The effects of water // The "Planet Earth" System (Nontraditional problems of geology) XIVth Scientific Seminar, 2008. M.: Geological Department, MSU. P. 66-78.

Zeigarnik V.A., Konev U.B., Novikov V.A. Thermal effect of a powerful current on saturated porous media // Trigger effects in geosystems. Editors V.V.Adushkin and G.G.Kocharyan. Transactions of seminar - conference. Moscow, GEOS, June 23-24, 2010. P. 202-208.

Zeigarnik V.A., V.A. Novikov V.A., Avagimov A.A., Sobolev G.A., Ponomarev A.V., Nikolaev A.V., Tarasov N.T., Tarasova N.V., Bogomolov L.M. Earthquake Hazard Mitigation Based on Release of Tectonic Stresses in the Earth Crust By Controlled High Power Electromagnetic Pulses // Book of Abstracts, Indo-Russian Workshop on Mitigation of Natural and Human Induced Disasters, March 4-6, 2009, New Delhi, India, pp. 12-13.

7.2. Seismic monitoring of large-scale karst processes in a potash mine

D. A. Malovichko, mal@mi-perm.ru, **R. A. Dyagilev,** dr@mi-perm.ru, **D. Y. Shulakov,**
P. G Butyrin. *Mining Institute, Ural Branch RAS, 78-a, Sibirskaya Str., Perm 614007, Russia.*

In October 2006 a serious accident happened in Berezniki-1 mine of the world's second largest Verkhnekamskoye potash deposit. The integrity of the waterproof stratum which separates mine workings from aquifers was broken and an uncontrolled flooding of the mine had begun. The accident resulted in the appearance of several potential problems associated with karst processes in the rock mass above the mine, i.e. hazardous subsidence of the earth's surface and formation of a sinkhole. The exact position of the water inflow zone was unknown due the inaccessibility of the excavations within the problematic part of the mine. This aggravated the situation seriously. The applied complex of geophysical and geotechnical methods made it possible to localize the inflow zone, to estimate the size of the expected sinkhole and to monitor its development in time. Seismic monitoring played an essential role in these investigations.

From October 2006 to July 2007 the karst processes had no visible manifestations. However, the several techniques pointed to significant variations of the controlled characteristics and properties (i.e. gradual decrease of seismic wave velocity for different horizons within the risk area, anomalous subsidence (with rates up to 270 mm/month) in the eastern part of the risk zone, formation of local areas with high concentration of methane in soils).

At 3 PM of 28 July 2007 a sinkhole had appeared on the earth's surface 150 m to south-west from the center of the risk zone. The initial size of the sinkhole was 55 x 80 m (**Fig.7.2.1a**). A huge gas and rock blowout had happened next morning.

During the following several months the sinkhole had actively grown mostly in the northern and north-eastern directions toward the federal railway. The growth decelerated significantly during the winter months, but nevertheless the eastern slope of the sinkhole reached the old federal railway in December. During February and April 2008, a short-time increase in the rate of the sinkhole expansion was noted in the eastern and southeastern directions.

At the end of 2008 the flooding of Berezniki-1 mine was completed and the growth of the sinkhole virtually stopped. Its size had stabilized at approximately 440x320 m (**Fig.7.2.1b**).

a) **b)**

Fig.7.2.1. A sinkhole appearance at 28 July 2007 (a) and its view at 29 November 2008 (b).

To monitor the risk zone a local seismic network based on ISSI hardware and software were promptly (in few days after inflow beginning) installed. The network have been changed sometimes and included from 14 to 30 geophones deployed both in boreholes at the depths of 10 and 50 m and on the surface. Continuous quality control over the performance of the new system was maintained remotely from the central site.

From October 2006 till May 2008 the monitoring systems had registered more than 10 000 seismic events which could be associated with karst processes in the risk zone. It was efficient to divide those seismic events in two groups:

1) Events of the 1st type distinguished by clear arrivals of P waves and relatively high frequency content (30-60 Hz) (**Fig.7.2.2a**). The arrivals of S wave are hardly identifiable event for tri-axial sensors. We associate this kind of events with fracturing at the level of mining openings or in the consolidated part of the overlaying rock mass.

2) Events of the 2nd type characterized by low frequency (5-20 Hz) long-duration (several seconds) signals without clear arrivals (**Fig.7.2.2b**). We associate this sort of events with fracturing in the soft part of the rock mass (slopes of the sinkhole, near-surface layers) or rockfalls from roof and walls of karst cave(s). A not karst- or mining-related origin of these events is not excluded in some cases, i.e. they may be caused by failures in foundations of surface buildings due to their extensive deformation.

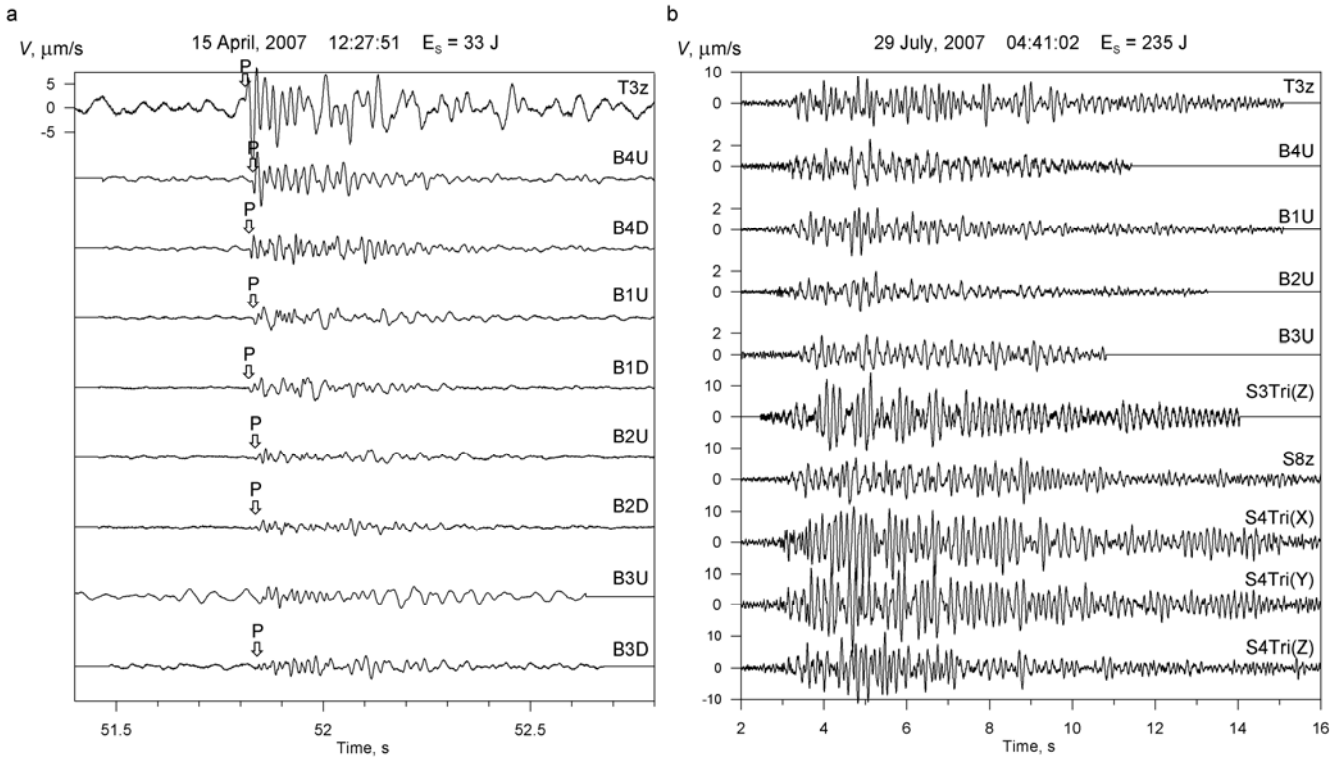

Fig.7.2.2. Examples of registered in the risk zone seismic events of the 1st (a) and 2nd (b) type.

The described classification of the events is not strict – sometimes events possessing the features of both types were observed.

On October 2006 only 3 of the registered seismic events were reliably located. The depth of the sources was in the 150-300 m range. Therefore, they were associated with fracturing in a consolidated rock mass above of the mining excavations.

These results were obtained within a 10 days period after discovering the loss of integrity of the waterproof stratum in the mine. The positions of the sources were in general agreement with the anomalous rock mass properties (velocities of P waves) and rock mass behavior (intensive subsidence) as revealed by other techniques. This made it possible to localize the area of the waterproof stratum desintegration and to identify the zone of expected karst processes (the risk zone).

Until the appearance of the sinkhole, the level of seismic activity in the risk zone was low (**Fig.7.2.3a**). Most of located events were of the 1st type. Their sources were generally within the risk zone, close to its western part. The depth of the sources was more than 140 m. Three events had been ascribed to the 2nd type and one to the mixed type. Two events had occurred out of the risk zone and one of them, which had happened 13 June 2007 had its source on the earth's surface. So the later event was associated with foundation destruction of a building.

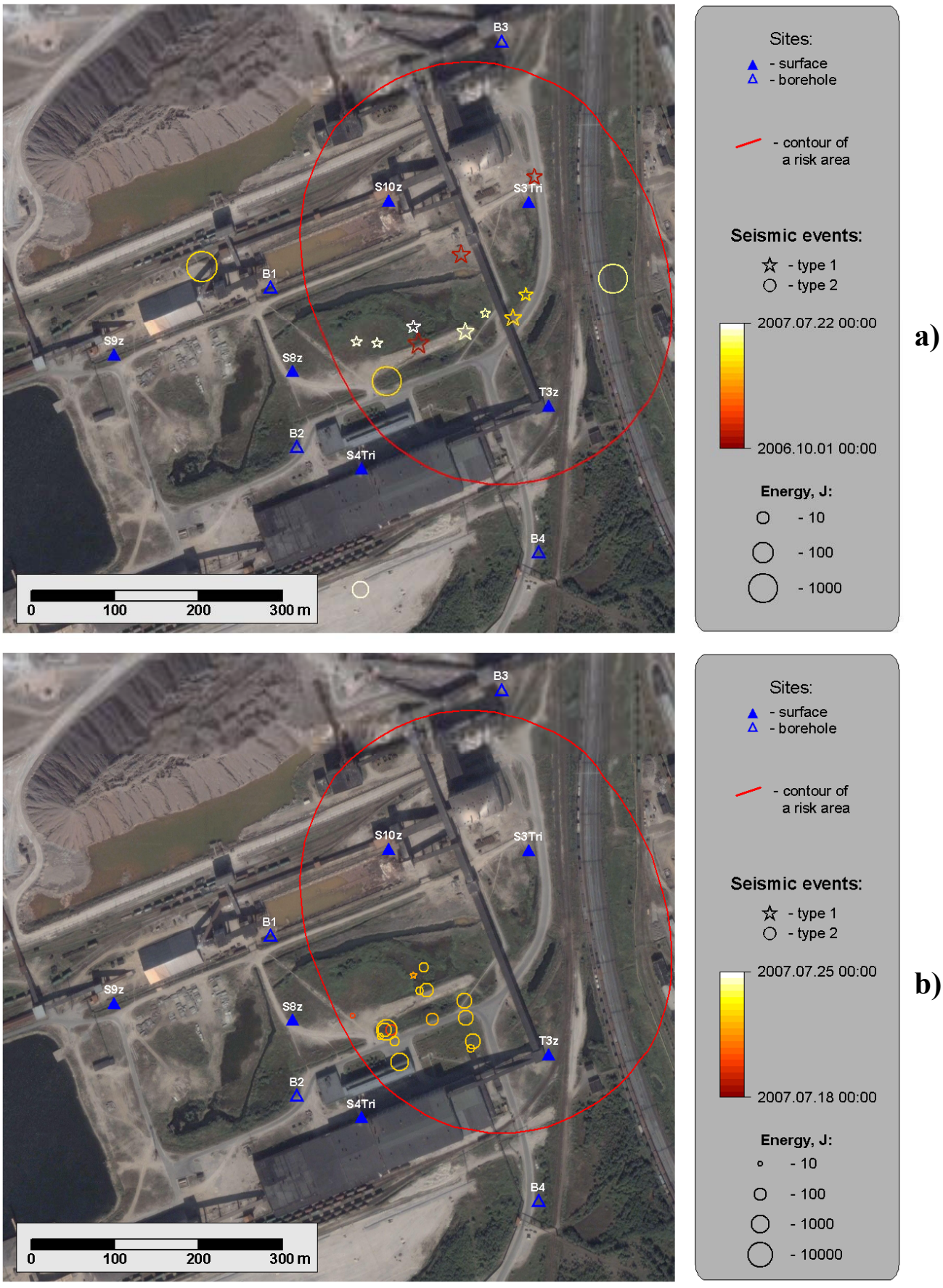

Fig.7.2.3. Seismic activity in the risk zone before 22 July 2007 (a) and from 16 to 22 July 2007 (b).

Anomalous seismic activities have been detected during the two weeks before the formation of the sinkhole. The anomalies took the form of swarms of events of the 2nd type with huge rate (100 and more events per hour) and overall duration up to several hours (**Fig.7.2.4**). Initially it was assumed that all these events are associated with fracturing in near-surface layers (having depth less then 100 m) or with structural damage of foundations of buildings situated in the risk zone. The post processing of the events made it possible to determine their locations more precisely. All of them had occurred in the south-western part of the risk zone (**Fig.7.2.3b**) where the sinkhole was formed initially.

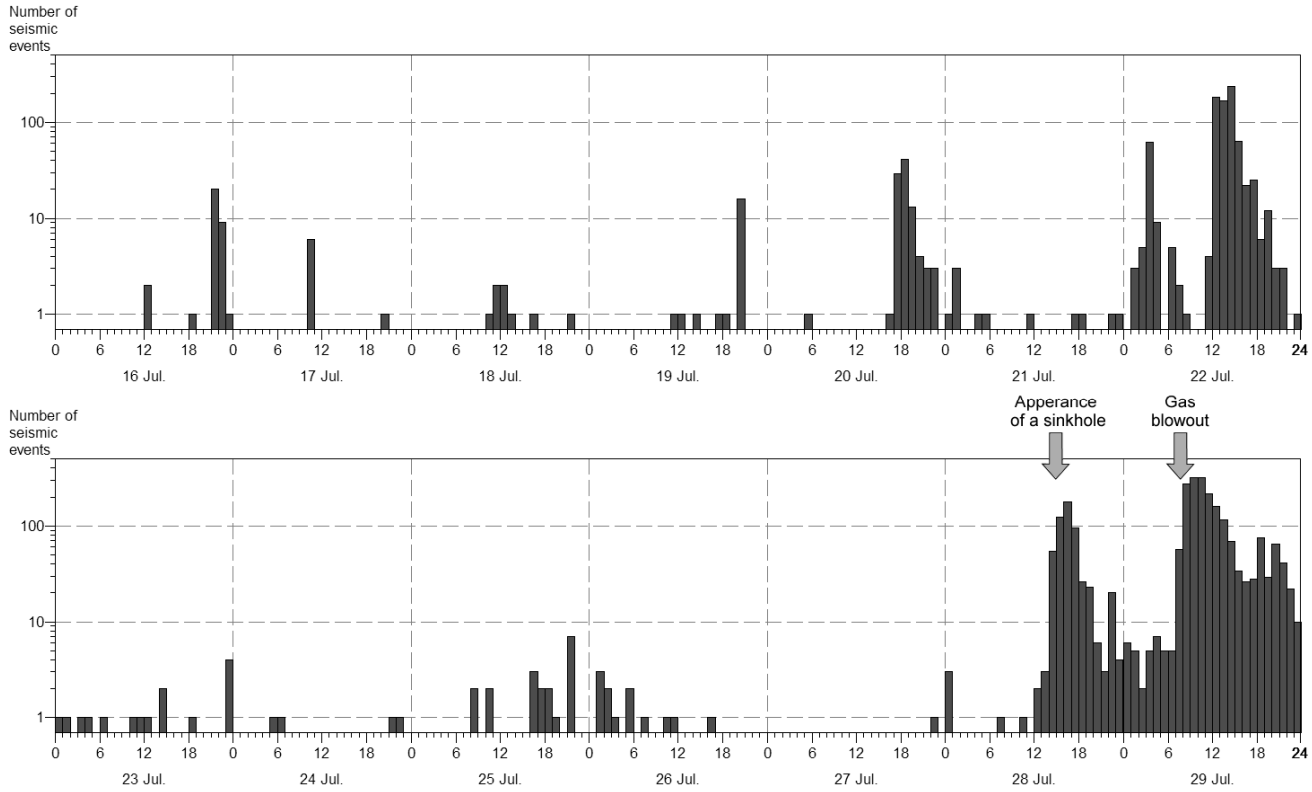

Fig.7.2.4. Time history of seismic activity in the risk zone from 16 to 29 July 2007.

During the 5 days before the appearance of the sinkhole the rate of the seismic activity was low. At 2 PM of 28 July the seismicity increased sharply (figure 4). Most of events in this swarm were of the 2nd type. At 3:30 PM the sinkhole was visually discovered (figure 1a). Next day (29 July) the seismic activity had risen again and this burst was accompanied by a blowout of gas and rocks from the sinkhole.

Therefore at this stage it had become obvious that bursts of seismicity (especially events of the 2nd type) preceded by a period from several minutes to hours the onset of the sinkhole development. This fact has forced us to switch over to around-the-clock monitoring to ensure an immediate response to any bursts of seismic activity in the risk area. Triggering of 10 events on eight sensors within 10 minutes was set up as an alarm criterion. When this criterion was met the emergency services of the mine and railway station (which manage train operations in the vicinity of the risk area) were notified.

The alarm criterion was met 10 times in August and September 2007 and every time the duration of the alarm condition was less then 8 hours. Almost every alarm was followed by an acceleration of the sinkhole growth sometimes accompanied by blowout or emission of gas.

Both the intensity and the frequency of the seismic activity bursts decreased in September 2007. From October 2007 till the end of 2008 the alarm criterion was never met. In total, the level of seismic activity in the risk zone gradually decreased. In the first half of 2008 the average rate of seismicity was 20-40 events per day (i.e. 10 times lower then in August and September of 2007). In the end of 2008 the rate was several events per day and almost decreased to zero to the end of 2010.

The event location results revealed a space-time correlation of seismicity and direction of the sinkhole growth. More than once the sinkhole ‘responeded’ to the grouping of seismic sources in

clusters by a directional expansion. For instance, in the beginning of August 2007, the events were clustered near the eastern slope of the sinkhole. And in the following weeks this was followed by an accelerated growth of the sinkhole eastward (**Fig.7.2.5**). Then the sources migrated eastward and again the sinkhole followed them.

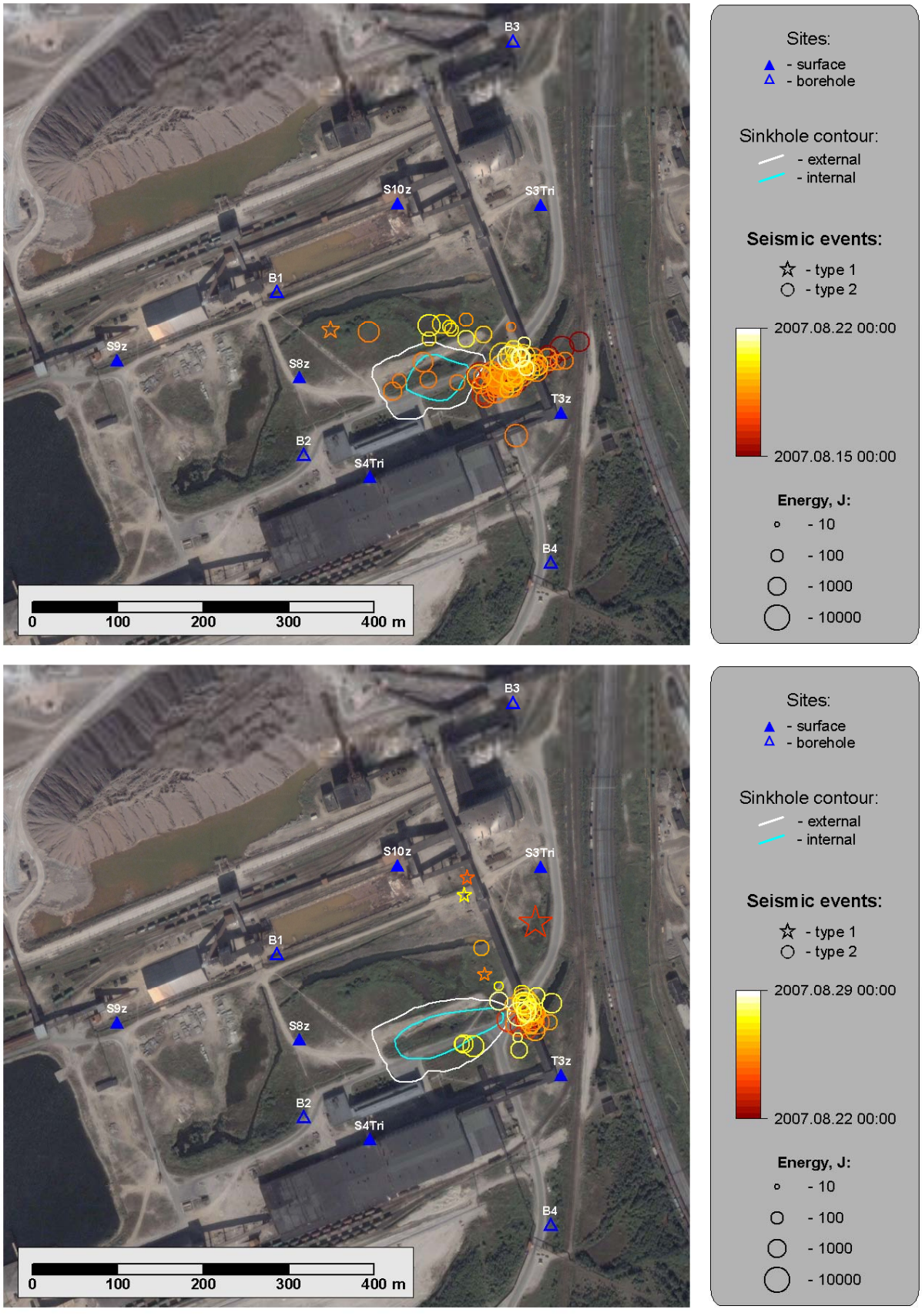

Fig.7.2.5. Seismic activity in the risk zone during 2 weeks in August 2007.

Analysis of several samples of such space-time correlations has revealed that the time delay between the clustering of seismicity and the directional sinkhole growth can be from several days to 2 weeks.

The acquired experience of seismic monitoring of karst processes in Berezniki-1 mine is of considerable practical value. According to numerical modeling of solution processes in the mine an intensive dissolving of carnallite pillars is expected in several areas, one of which is within the populated part of Berezniki town. An intensive deformation of the undermined strata was predicted for these areas which may result in hazardous subsidence of the earth's surface. A variety of geotechnical methods was employed in the monitoring of rock mass deformation and for identifying potential karst processes within the new risk zones. During the summer of 2008 a seismic monitoring system based on 12 tri-axial borehole sites was commissioned in one of the most hazardous zones. The practical skills obtained during monitoring of the old risk zone are applied now when processing and interpreting seismic monitoring data of new system.

References

Malovichko D.A., Dyagilev R.A., Shulakov D.Y., Butyrin P.G., Glebov S.V. Seismic monitoring of large-scale karst processes in a potash mine // Controlling seismic hazard and sustainable development of deep mines. V.2. New York: Rinton Press, 2009. P. 989-1002.

Malovichko A., Dyagilev R., Shulakov D., Butyrin P., Malovichko D., Glebov S. Seismic monitoring of karst processes accompanying flooding of mine at Upper Kama potash deposit // Proceedings of 32nd General Assembly of European Seismological Society. Montpellier, 2010. P. 61-62.

7.3. Mining-induced seismicity monitoring in the Kola peninsula

A. A. Kozyrev, kozar@goi.kolasc.net.ru, **V. I. Panin, Yu. V. Fedotova**, julia@goi.kolasc.net.ru, *Mining Institute, Cola Scientific center RAS, 24, Fersman Str., Apatity 184200, Murmansk region, Russia.*

In recent years the most actual problem in large mining regions and also in areas of large mining-induced impacts of other sort, for example, under construction of unique hydraulic engineering or underground objects, has been so-called induced (mining-induced) seismicity which essentially raises hazard of mining operations and leads to considerable material losses.

As an illustration of such catastrophic events in the mining practice we can call a large dynamic event on 21st January, 1960 at the Coalbrook mine, SAR [Bryan, 1994], with a following 3.2 km^2 destruction and fatal injuries of 437 miners; a seismic event with M≈5.2 in 1977 at the Klerksdorp deposits, SAR; a seismic event with M≈5.3 in March 2005, when 2 miners were killed [*Durrheim*, 2007]. A seismic event with M=5.4 destructed 6km^2 area of the German salt mine Werra on 13th March, 1989 [*Knoll P.,* 1990]. On 21st January, 1993 the Book Cliffs coal mine, USA [Swanson, 1995] experienced destruction of 15,000 m^2 pillars. On 5th January, 1995 the II Solikamskiy mine in Russia [Baryakh, 1996] was exposed to a simultaneous failure of the rib pillars and interbedding roofs at 300,000m^2 area followed by immediate surface subsidence to 4.5 m. On 3rd February, 1995 a seismic event with M≈5,1 caused failures at 2 km^2 area of the US Solvay mine [*Kozyrev*, 1996].

Rockbursts and mining-induced earthquakes have become real when mining ore deposits in Russia. The Kirovsky mine of JSC "Apatit" was exposed to the seismic events on 16th April, 1989 (M≈4.2-4.3), on 25th July, 1989 (M≈3.0), on 17th November, 1993 (M=2.0-2.5), on 9th and 12th December, 1993 [*Syrnikov*, 1990]. The Tsentralny mine experienced a seismic event on 26th October, 1995. The Kirovsky mine was exposed to a seismic event with M=3.4 on 21st October, 2010. The Northern Ural and South Ural bauxite mines experienced a seismic events with M~3.0 (on 5th October, 1984) and M~3.5-4.0 (on 28th May, 1990) [*Kolesov*, 1993; *Lomakin*, 1993]. A seismic event with M~3.0-3.5 occurred on 12th August, 1984 at the Tashtagolskoe iron-ore deposit, Gornaya Shoriya, Russia [*Shrepp*, 1993]. On 17th August, 1999 a seismic event (M=4.0-4.2) occurred at the Umbozero

mine, Lovozerskoe deposit, Russia. The comprehensive information on the deposits prone to tectonic rockbursts and mining-induced earthquakes is given in the papers [Aitmatov, 1987; Johnston, 1989].

The mining-induced earthquakes can be recorded during open mining operations in the high stress rock massive as well. According to the data [*McGrarr*, 2002], an earthquake with M≈3.3 occurred during open-pit quarrying operations nearby the Wappingers Falls, New York. The event occurred under the open-pit floor (0.5-1.5 km deep) with length more than 1.0 km. The high horizontal stresses were recorded on the deposit close to surface (up to 50m).

During 1992–1997 a range of mining-induced earthquakes was recorded on the open workings in the Cacoosing Valley, near Reading, PA, directly below a quarry [McGrarr, 2002]. The strongest event with M≈4.3 was registered in January, 1994, with fracture activation on the depth up to 2.0 km directly under the mining operations.

One more example of the mining-induced seismicity is the Belchatow region in Poland, where a seismic event with M≈4.6 was recorded at the open-pit coal mining [*McGrarr*, 2002] having dimensions 1×2 km^2 and 100 m depth. In the period from 1981 to 1995 in the USA, California, the Lompoc diatomite mine had experienced 4 seismic events with M≥3 [*McGrarr*, 2002]. The length of the open pit excavation exceeded 1000m. On the pit bench appeared a fracture relating to the California zone active by tectonic events.

In Australia during the BHP Billiton Nikel Wests nickel deposit developing the seismic events were registered under the open-pit when operating in the rock mass with high horizontal stresses [*Sweby*, 2006].

In Russia the seismic shocks and dynamical cleavage of plates occurred in the granite open pits of the Vyborg region, Leningradskaya Oblast, caused by high horizontal stresses acting. The pits depth was 30 – 50 m [*Kozyrev*, 2007].

The large seismic events occurred at the open pit of the Tsentralny mine belonged to JSC Apatite where volumes of the rock mass extracted exceeded 350 mln m^3. The events with M≥3.0 were recorded on 26th October, 1995, 24th September, 2004 and 25th May, 2009 [*Kozyrev*, 2002; *Kozyrev*, 2005; *Melnikov*, 2010].

The represented data indicate that tectonic rockbursts occur at the all deposits where are revealed abnormal high natural stresses in the rock mass whatever the type of tectonic structure (stable shields, mobile platforms, mobile mountain-folded areas). The mining-induced earthquakes occur, as a rule, at the deposits where the large areas are excavated, and significant volumes of rock mass are extracted and removed. According to our data [Melnikov, 1995], geodynamical behavior of regional geological environment is disturbed only under extraction of certain volume of the rock mass and creation of overstressed zone having considerable area. Then arises a situation which is similar to one of forming and realizing induced seismicity during water reservoirs filling [*Nikolaev*, 1977].

The tectonic rockbursts can be regarded at a first approximation as foreshocks or aftershocks of the mining-induced earthquakes. At that, as the experience shows the depth in the high stressed rock massive where tectonic rockbursts occur is minimal. This fact indicates that natural stress field is indeed the first course of tectonic rockbursts and mining-induced earthquakes with mining-induced event being a trigger.

According to existing conceptions [*Gupta*, 1979; *Kozyrev*, 1994], mining-induced earthquakes are similar to the natural ones, but differ by a behavior of seismic energy released under the mining-induced factors influence. The factors are characterized by a large number of foreshocks (or tectonic rockbursts) prior to a maximal earthquake, by slow decrease of aftershocks, and increased seismic magnitude due to shallow location of an earthquake source. For mining-induced earthquakes to occur during mining operations a combination of a set of conditions is required as follows:

- High level of horizontal tectonic stresses in the rock mass determined by a corresponding tectonic – physical environment (i.e. existence of zones with heavy gradients of the most recent tectonic movements rates),
- Existence of friable high-strength rocks with tectonic discontinuities within a working zone,
- Favorable geomorphologic environment (massifs relief),
- Large-scale mining (excavation area, working depth, volume of excavated and removed rocks),

- Blasting impact in driving workings and ore breaking.

Manifestation of the most recent movements results in redistribution of stresses in the earth crust which has an impact on separate blocks behavior, and the latter is expressed in slow (creep) or stick-slip (shocks) movement on faults.

Human engineering activity can be considered to be an additional external impact on the complicated chain of natural interrelated processes acting as trigger for accumulated elastic energy releasing. Due to cascade energy release close to geomechanical mine space the total level of natural stresses in the rock mass decreases, and maturing of the largest possible earthquake for the region is of low-probability. In the zone of mining-induced impact where considerable rock mass volumes are excavated and removed and considerable mined-out spaces are formed (**Fig.7.3.1**), the rate of rocks deforming increases compared to natural one (sometimes in order of magnitude) [*Melnikov*, 1995; *Kozyrev*, 1994] and large dynamical impacts from bulk blast are superposed. This leads to the disturbance of source formation process (maturing source time), early initialization of weaker shocks due to the contacts failure between blocks or interaction of contiguous fractures and faults. Energy released in a mining-induced earthquake is proportionate to volume of mined-out space and cannot exceed energy of maximum natural earthquake for the area of interest.

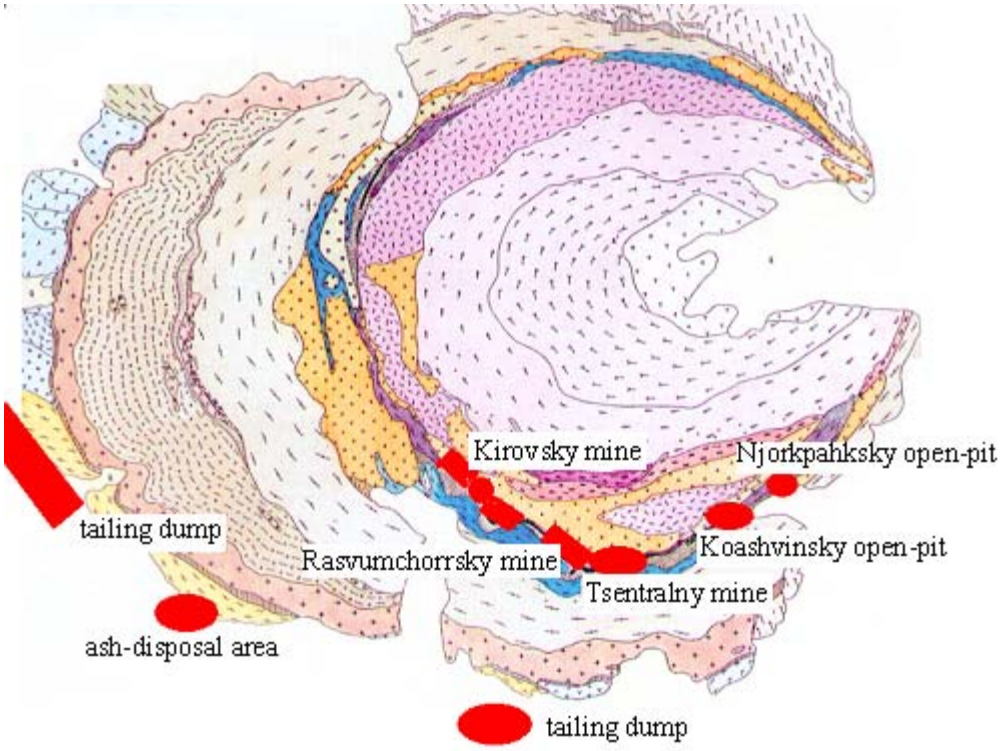

Fig.7.3.1. The chart of natural-technical system "Apatity."

To search precursors of the large dynamical events and control efficiency of preventive measures the systems of geodynamical monitoring are created, including the Khibiny apatite - nepheline mines [*Kozyrev*, 2002]. The monitoring system at Khibiny mines consists of three major blocks: monitoring of stresses and deformations, seismic monitoring and seismologic control. The first subsystem includes stresses measurements by unloading method, periodical leveling and light distance measurements, continuous deformation control by quartz strainmeters and dipmeters. The seismic monitoring is carried out in active and passive mode, including seismic transmission of source zones in the Khibiny massif with use of industrial blasts as a source of elastic vibrations, and seismic tomography and transmission in the mining workings on the high stressed mine field's parts. The largest dynamic events in the Khibiny and Lovozero massifs as well as mining-induced and natural earthquakes are registered by the seismic station "Apatity" belonged to the Kola Branch Geophysical Survey RAS which is a part of the united seismic stations system of the Northern Europe.

The Khibiny rock massif seismicity control within the United Kirovsky (UKM) and Rasvumchorrsky mines is managed by JSC "Apatite" seismic station with the using of automated monitoring systems of mining-induced seismicity (AMSMS) (**Fig.7.3.2**).

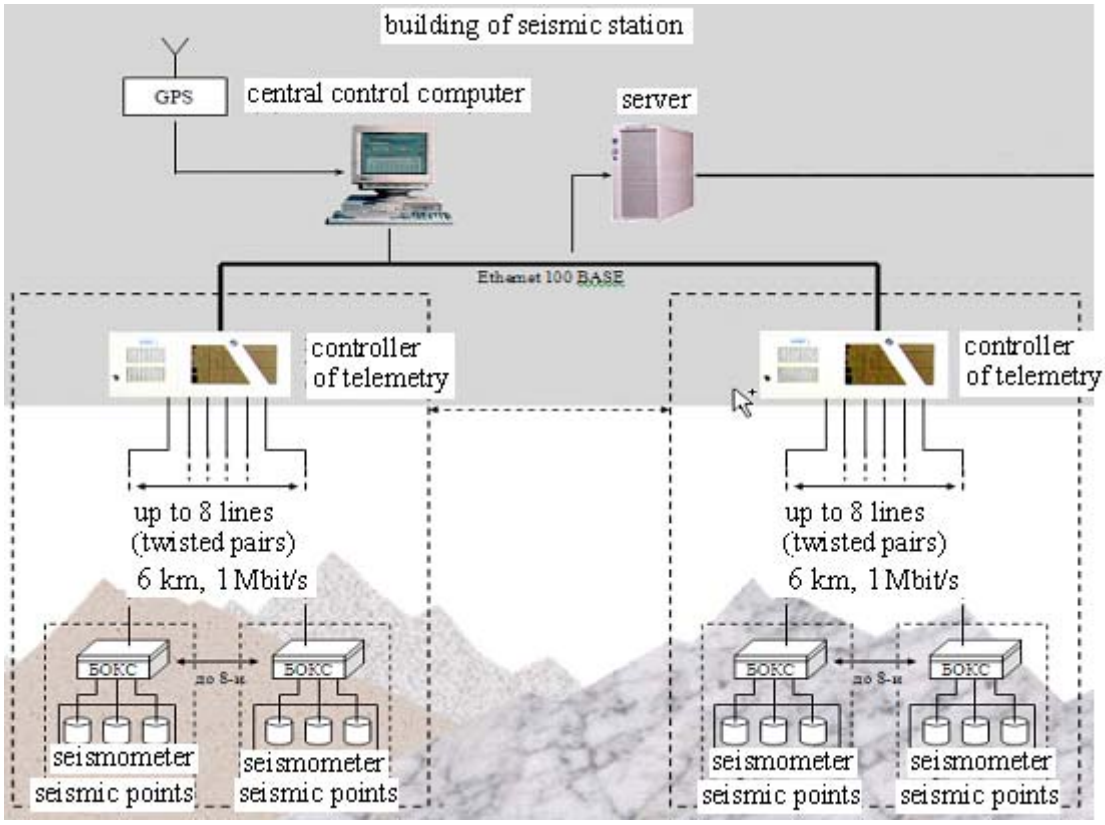

Fig.7.3.2. Layout of AMSMS of geophysical monitoring center JSC "Apatit."

UKM is monitored by AMSMS–UKM system installed on the base of telemetric system of seismic information gathering (TSG) made by SIE "Systemotechnika" (Ivanovo). Seismic points of AMSMS–UKM are located in the underground workings. The distance between them is 300 – 400m. The seismic point contains a 3 component seismometer, a telemetric box, an electrical power unit and accumulators to provide uninterruptible power supply in the power cutoff. Telemetric box provides frequency filtering of seismometer's signals, preamplification, analog-to-digital conversion and data transmission on a seismic controller. Concentrators unite signals from different blocks to transmit data through one radio-frequency cable. The seismic network uses seismometers made by The Schmidt Institute of Physics of the Earth (Moscow), such as S1073 accelerometers and S2123 velocimeters. At that, the velocimeters are installed in the outlying districts to register seismic waves from remote sources. The results of the regional prediction are transferred to the mine service of prediction and prevention of rockbursts (SPPRB).

The Rasvumchorrsky mine subsystem AMSMS–R manages a zone of joining with an open-pit, an ore pass №6 zone, and a northern-western highwall of the Tsentralny mine. It contains a network of seismic points deployed in the underground mine workings, cable communication lines and a telemetry controller. To connect the seismic points with seismic station building a radio frequency cable is used. Range of boxes communication Geos kft (Hungary) without retranslation is 1000m. Surface program – hardware complex AMSMS–R is located in the mine administration building, and is a remote automated center of seismic data gathering and preliminary scrapping. The files of wave forms of seismic events registered by AMSMS–R are transferred through fiber-optic communication lines into the seismic station where they are processed by a geophysicist. The results of the regional prediction are transferred to the SPPRB.

Analysis of seismic events flow shows that at least half their sources are internal destructions in the rock in situ which are not manifested in the mine workings and this fact was also noted at the Northern Ural bauxite mines [*Petukhov*, 1984]. The main factors determining manifestations of the seismic events in the massif rock as well as rockbursts and mining-induced earthquakes are zones of concentration of natural stresses in the intact massif, stresses nearby stope faces and tectonic disturbances, bulk blasts, and inflows in the mine workings. The large technological blasts in a number of cases induce an event of mining-induced aftershock seismicity since they act as trigger mechanisms for different dynamic events in the massif rock.

Analysis of the investigations performed to date has shown that the parameters of seismic behavior of rock massif and rock deformation behaviors are the most perspective predictive precursors of tectonic rockbursts.

Disturbance process develops in space and time, and so criteria of seismic prediction, first of all, must take into account just space-time parameters of microseismicity. At that are used single one-parameter criteria such as tangents of angle of seismic events recurrence graph, concentration parameter, parameter of fractal dimension of seismic events spatial distribution, average length of fractures and etc.

Prediction effectiveness by separate criteria, as a rule, exceeds slightly prediction effectiveness by random guessing. World experience and our investigations show that the complex analysis of different precursors increases greatly the prediction reliability [*Melnikov*, 2010].

The results of the mine seismicity monitoring in the Khibiny massif for last 5 years (2006–2010) are presented below.

Fig.7.3.3 shows a distribution according to years of a number of seismic events registered at the Rasvumchorrsky and United Kirovsky mines of JSC "Apatit" for this period. The graph in **Fig.7.3.3** shows decline of values in 2007 as against 2006 both for this mines. A less number of events at the Rasvumchorrsky mine were registered in 2010. This can be related to failure of some seismic points (and as a result recording abilities of the monitoring system decreased). Currently a reconstruction of AMSMS–R is being carried out.

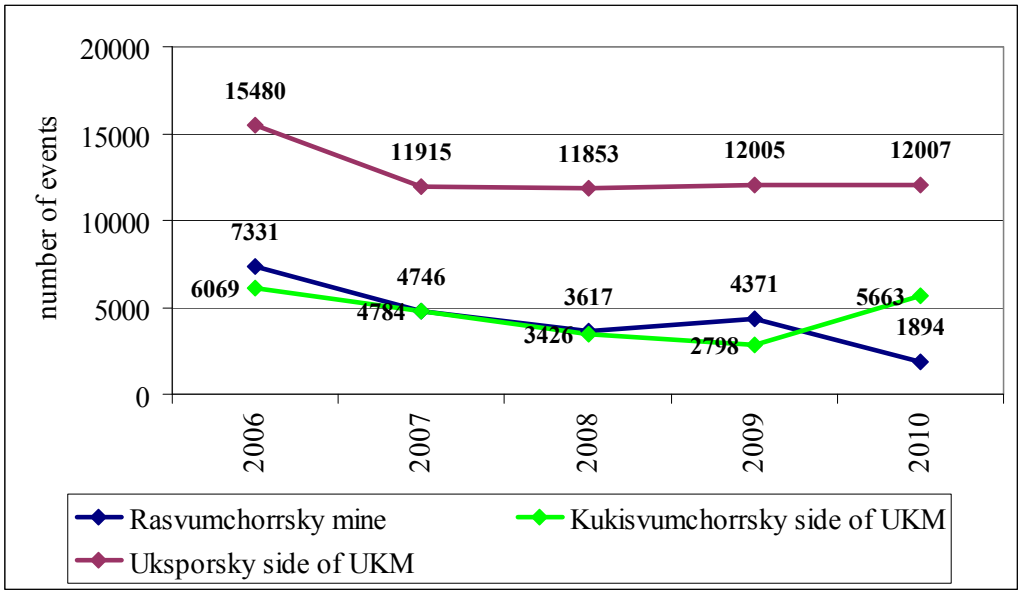

Fig.7.3.3. Number of registered seismic events by years.

The Kukisvumchorrsky side of UKM presents decrease of values till 2009 and almost double increase of those in 2010. It is connected with a fact that since the end of 2008 and during 2009 the mining operations were less intensive than in 2010. The Uksporsky side of UKM doesn't record considerable changes of a number of events starting from 2007.

Also the distinctions are noticed according to total energy released in the mines (**Fig.7.3.4**). At the Rasvumchorrsky mine the value of total energy released didn't exceed 10^8 J in 2006 but since 2007

there are recorded values higher 10^8 J. The Uksporsky side of UKM demonstrates a decline of values on 2 orders of magnitude in 2010 as against 2006.

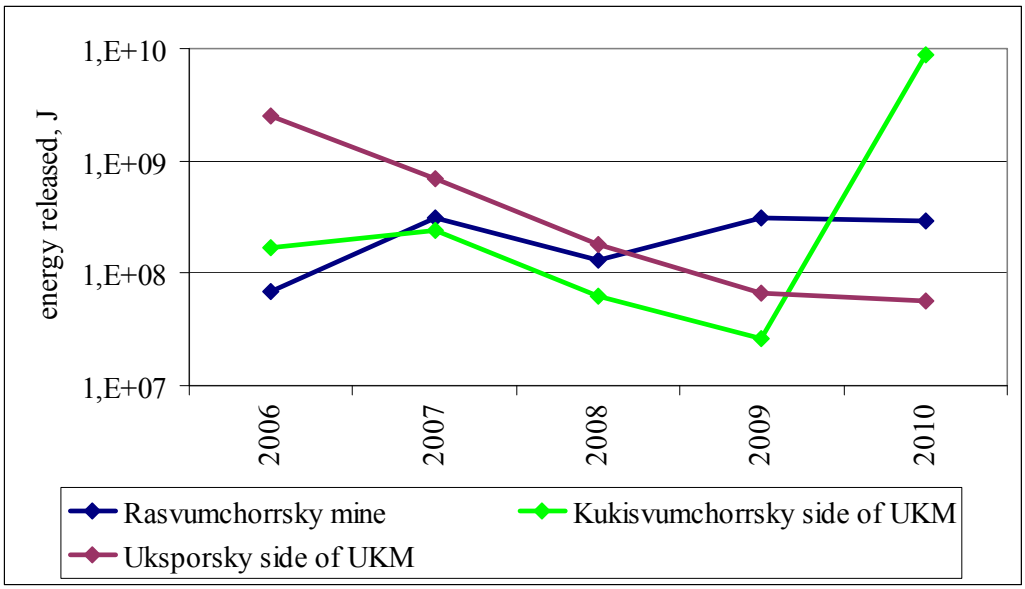

Fig.7.3.4. Total energy released.

The diagram made for the Kukisvumchorrsky side of UKM demonstrates a slight increase in 2007 related to a fracture intergrowth in the hangwall and partial failure of the roof rocks. Then you can see a gradual decline till 2009 and a maximum peak in 2010. This peak is related to a mining-induced earthquake with $E=10^9$ J recorded on 21st October, in the mining zone of the Kukisvumchorrsky side. The foreshocks prior to the main event in this region were not registered. The aftershocks were noticed for a week after the main event.

Fig.7.3.5a,b,c presents monthly distribution of a number of events and total released energy for the Rasvumchorrsky mine, the Kukisvumchorrsky and Uksporsky sides of UKM. As can be seen, all the mines record the increase of seismicity level during the periods of rain and intensive snow melting.

For the period under study there were recorded the following events:

On 12th July, 2008 a micro rockburst was recorded at the Rasvumchorrsky mine caused by high tectonic stresses acting in the massif rock, existence of bearing pressure zone due to stoping operations at the working level, and under bearing pressure of overlying rocks console. The event resulted in the total ore outburst approximately $15m^3$. On 14th October, 2008 another micro rockburst was recorded at the Rasvumchorrsky mine. The event was also caused by high tectonic stresses acting in the massif rock, existence of zone with bearing pressure due to stoping operations at the overlying working level, impact of non-caved overlying rocks, and close location of drill haulage crosscuts. The seismic event caused destructions with total volume of $20m^2$ on the 30m section.

On 4th February a tectonic rockburst was registered at the Rasvumchorrsky mine which was induced by shearing of weakly spreustein rocks but heavily fragmented rocks along the steeply inclined shallow zone (0,2m). As a result 20 m^2 area of the monolith concrete excavation support was disturbed.

On 13th May, 2009 a micro rockburst was registered at the Kukisvumchorrsky side of UKM. It was caused by influence of stress concentration zone formed close to a boundary of stoping zone, an existence of monchikite dyke, and changing of rock massif stress strain state due to ore drawing on the underlying level. After this seismic event a $12m^2$ rock mass outburst was recorded in the 8m of mine with disturbance of sprayed concrete excavation support.

On 25th May, 2009 an increase of seismic activity in the Khibiny massif was registered at the mine Tsentralny area. The seismic event with $E=5*10^{10}$ J occurred at 12:05 p.m. The increased seismicity in the region of interest is caused by a long mining-induced impact during mining operations at the Plato Rasvumchorr and Apatitoviy Tsirk deposits. The seismicity activization was induced by a temporary decrease of the rocks strength in the zones with tectonic disturbances because

of water filling during snow melting. The source of the mining-induced earthquake was rock shearing along a fault in the Draznyashchee Ekho valley.

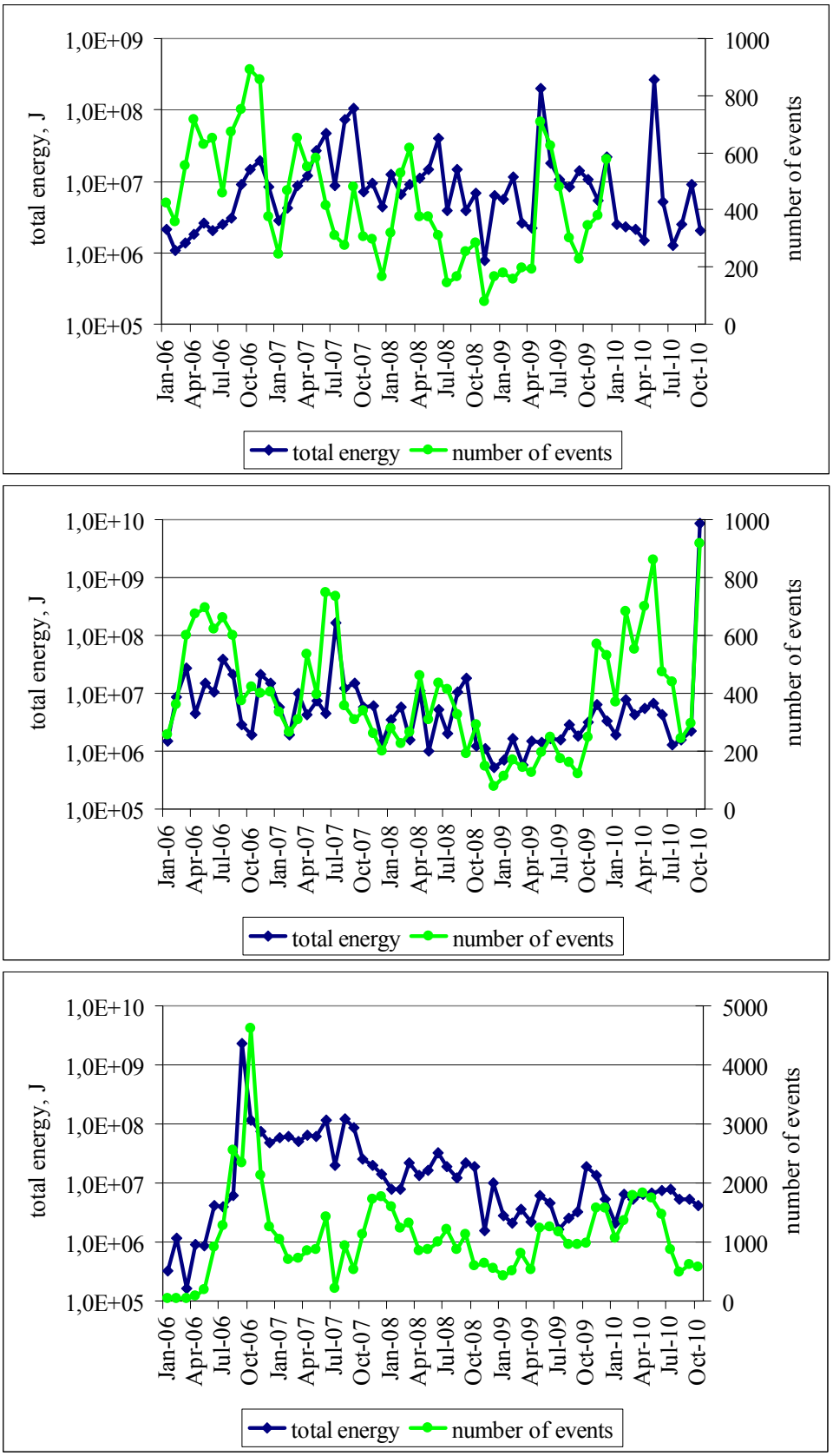

Fig.7.3.5. Monthly distribution of values of total energy released and a number of events for the JSC "Apatit" mines: a) the Rasvumchorrsky mine; b) the Kukisvumchorsky side of UKM; c) the Uksporsky side of UKM.

On 18th November, 2009 at the Rasvumchorrsky mine a micro rockburst was registered within an mine located in the zone of bearing pressure from the boundary of overlying level breaking and stoping operations at the level. The rockburst occurred during drilling wells unloading line. As a result of the event there occurred a rock mass outburst by total volume $10m^3$ in the mine. The seismic event was triggered by loading of the border part of unloading line in the highly-stressed rock mass.

At the end of 2010 the background level of seismicity according to the mines made up:

- the Rasvumchorrsky mine $3*10^4$ J
- the Kukisvumchorrsky side of UKM $7*10^3$ J
- the Uksporsky side of UKM $6*10^3$ J

For the Rasvumchorrsky mine and Uksporsky side of UKM the background level was calculated on the beginning of November, 2010. For the Kukisvumchorrsky side of UKM the background level was calculated on the beginning of October, 2010.

In October there occurred a mining-induced earthquake; therefore one can observe a sudden increase of energy characteristics of seismic behavior for the Kukisvumchorrsky side. Average value of energy released during October was $9*10^6$ J.

So, mining-induced seismicity is a reflection of evolution of the geological environment stress strain state in the natural-technical systems as well as tectonic seismicity is a consequence of accumulated high stresses discharging in the separate lithosphere parts. The changing of parameters of mining-induced seismicity at the apatite mines because of increasing the depth and volume of mining operations and corresponding complication of the geomechanical conditions in the Khibiny mining technical system is a convincing evidence of the above said.

Prediction and preventive measures of the mining-induced seismicity are based on the strategic and tactical measures. The strategic measures involve studying of tectonics and stress state of the mining technical system geological environment, small-scale numerical modeling of stress strain state of mining technical systems geomechanical space and organization of complex geodynamical monitoring of mining technical systems geomechanical space. The tactical measures involve large-scale numerical modeling of problem parts of geological environment in the mining technical system, instrumental control for rocks properties and state in the mining workings, and determination of optimal sequences of mining operations development and rational methods of rock mass stress state decrease, as well as a choice of rational methods of mining workings supporting.

References

Aitmatov I.T. Geomechanics of ore deposits of the Central Asia. Frunze. – Ilim, 1987. –246 p.

Baryakh A.A., Konstantinova S.A., Asanov V.A. Saliferous rocks deformation. Ekaterinbourg, UB RAS, 1996. 204 p.

Bryan A., Bryan J.G. and Fouche. Some problems of strata control and Support in pillar Workings. The Mining Engineer. 1994. # 2– P.238-266.

Durrheim R.J., Anderson R.L., Cichowich A., Ebrachim-Trollope R., Hubert G., Kijko A., McGarr A., Ortlepp W.D., Van der Merwe N. The Risks to Miners, Mines and the Public Posed by Large Seismic Events in the Gold Mining Districts of South Africa. // Challenges in Deep and High Stress Mining. – Australian Centre for Geomechanics, Perth, 2007. P.33-40.

Gordon Sweby. What's shocking your pit? Newsletter. Australian Centre for Geomechanics, 2006. P.12.

Gupta H., Rastogi B. Dams and earthquakes. – Moscow: 1979

Johnston I.C. Rockbursts from a global perspective // Gerlands Beitrage zur Geophysik. – Leipzig, 1989. – Band 98. – Hefl 6, – P. 474-490.

Knoll P. The Fluid-induced Tectonic Rockburst of March 13, 1989 in the "Werra" Rotash Mining District of the GDR (first results), Gerlands Beitrage zur Geophysik. – Leipzig, 1990. – 99(6),. P.239-245.

Kolesov V.A. State of activities on rockburst problem at the "Sevuralboksitruda" mines // Rockbursts under developing ore and industrial mineral deposits. – Apatity: KSC RAS, 1993. P.50-57.

Kozyrev A.A., Panin V.I., Ivanov V.I. et al. Rock pressure management in the tectonically stressed rock mass (2 volumes). Apatity KSC RAS, 1996. V.1 – 159 p. V2. – 162 p.
Kozyrev A.A., Panin V.I., Savchenko S.N. Maltsev V.A., et al. Seismicity at mining operations. Apatity: KSC RAS, 2002. 325 p.
Kozyrev A.A., Savchenko S.N. Maltsev V.A. On reasons of tectonic earthquake during open mining of the Khibiny apatite deposits // Journal of Mining Science (Fiziko-teknicheskie problemy pazpabotki poleznykh iskopaemykh), 2005. # 3. P.11-16.
Kozyrev A.A., Savchenko S.N., Maltsev V.A. Development of methodical approaches to diagnose tectonic stresses in the earth crust's upper part with aim of managing rock pressure dynamical manifestations. - Apatity: KSC RAS, 1994, 64 p.
Kozyrev Anatoly, Lovchikov Alexander, Savchenko Stepan. On tectonic stresses Occurrence in Rock Masses Near the Day Surface // The Role of Geomechanics in the Stability on Development of Mining Industry and Civil Engineering. – Bulgariy, Nesserbar, 2007. P. IV-11 – IV-19.
Lomakin B.S., Yunusov F.F. Operative method of seismologic observations at the mines. // Rockbursts under developing ore and industrial mineral deposits. – Apatity: KSC RAS, 1993. P.63-76.
McGarr A., Simpson D., Seeber L. Case Histories of Induced and Triggered Seismicity. International Handbook of Earthquakes and Engineering seismology Volume 81A. Part A. Edited by William H.K.Lee, Hiroo Kanamori, Paul C. Jenings and Karl Kisslinger. Published by Academic Press for International Association of Seismology and Physics of the Earths Interior. – Amsterdam, Boston, London, New York, Oxford, Paris, San Diego, San Francisco, Singapuro, Sydney, Tokio, Copyright 2002. P.647-661,
Melnikov N. N., Kozyrev A. A., Fedotova Yu. V., Zhuravleva O. G. Seismic hazard assessment of rock mass under mining-induced impact of mining operations by complex of prediction criteria // Fundamental challenges of mining-induced geosphere formation. –Novosibirsk, 2010. P. 15-19.
Melnikov N.N., Kozyrev A.A., Panin V.I. Geodynamical test area during large-scale mining operations for the prediction and prevention of mining-induced earthquakes and tectonic rockbursts // Mining Bulletin (Gorniy Vestnik), 1995. – # 4. – P. 6-11.
Melnikov N.N., Kozyrev A.A., Panin V.I. Induced Seismicity in Large-scale Mining in the Kola Peninsula and Monitoring to Reveal Informative Precursors. – PAGEOPH, 1996. V.147. # 2 – P.263-276.
Nikolaev N.I. On state of studying problem of induced earthquakes related to engineering activity // Influence of engineering activity on seismic behavior. – Moscow: Nauka, 1977. – P.8-21.
Petukhov I.M., Egorov P.V., Vinokur B.Sh. Prevention of rockburst at the mines. Moscow, Nedra, 1984, 230 p.
Shrepp B.V., Mozolev A.V., Norkhin A.M. et al. Activity to solve rockburst problem on the Tashtagolsky ore deposit // Prediction and prevention of rockbursts in the ore deposits. – Apatity: KSC RAS, 1993. – P.32-36.
Swanson P.L., Boler F.M. The Magnitude 5.3 Seismic Event and Collapse of the Solvey Trona Mine: Analysis of Pillar / Floor Failure Stability. Open File Report 86-95, U.S. Department of the Interior Bureau of Mines. 1995. – 82 p.
Syrnikov N.M., Tryapitsyn V.M. On mechanism of mining-induced earthquake in the Khibiny. – RAS USSR, 1990. V. 314. # 4 – Pp.830-833.

7.4. Induced processes in the Earth crust

V. V. Adushkin, adushkin@idg.chph.ras.ru**, S. B. Turuntaev,** turunt@postman.ru**.** *Institute of dynamics of geospheres RAS, 38, Leninsky prospect, build. 1, Moscow 119334, Russia.*

High heterogeneities of the Earth crust and high mobility of some crust blocks along existing faults result in non-linear respond of geosystem on industrial actions even if these actions are low enough in comparison with tectonic forces. In 2007-2010 an analysis of man-made seismicity related with various types of industrial activities was continued, peculiarities of induced seismicity occurrence, development and spreading were continued to be studied. The main attention was paid to

influence of fluid injection and extraction related seismicity and to mining seismicity and its relation with ore blasting.

Climate change is one of the main modern problems. To eliminate greenhouse gas pollutions, use of geothermal energy and CO_2 sequestration in underground deep collectors are considered as the possible methods. Meanwhile, fluid injection in geothermal power plants as well as in oil fields leads often to induced seismicity. Induced earthquakes (even of minor magnitudes) may cause building damages and human victims because their hypocenters are situated usually directly at places of human industrial activity. An increase of seismic activity due to water injection into deep wells on geothermal power plants resulted in stop of Bazel project, Switzerland, in which millions euro were invested. The same reason threaten to stop hundred million euro projects in the south of Germany and in others Europe countries. CO_2 sequestration is also accompanied by induced seismicity that leads to that project stopping too. So, the greenhouse pollution problem occurred to be related with the induced seismicity problem, which is needed to be studied. Some of the questions arouse in relation with induced seismicity problem could be divided into three groups:

- how to discriminate natural and man-made seismicity?
- how to forecast induced seismicity, what highest earthquake magnitude can be expected?
- what are industrial action limitations to prevent catastrophic seismic events, is it possible to control induced seismicity?

To discriminate natural and induced seismicity and to estimate stability of seismic regimes under industrial actions, non-linear dynamics methods were used. Study of seismic regime variations was made by means of the phase portrait reconstructions and their parameters (embedding space dimensionality and an attractor correlation dimensionality, if that one exists). The data on seismicity in the region of Romahkino oil-field, Tashtagol iron ore deposit, Severouralsk bauxite mines, the Geysers power plants, powerful explosions on Burlykia and Uch-Terek river, powerful electro-magnetic source actions, vibrations were studied.

It was found that in all considered cases, the actions lead to increase of the seismic activity deterministic component if compered with natural seismicity. The results showed, that, from one hand, the induced seismicity is more predictable, than the natural one, and from the other hand, a possibility to create a technology of the seismic activity control to prevent catastrophic earthquakes is looks to be real.

In the followings, some samples of non-liner method applications to analysis of various types of induced seismicity are presented.

Method.

The seismic activity time variations were analyzed with the help of Grassberger-Procaccia method of correlation integral calculation for different embedding space dimensions. The integral was calculated as follows:

$$C(\varepsilon) = \frac{1}{N^2} \int_{i,j=1}^{N} \theta(\varepsilon - \|z_i - z_j\|),$$

where $\vec{z}_i$ is the vector describing position of a point in phase space at the moment of time $t_i = t_0 + i\tau, i = 1...N$, τ is the time delay (lag), N is the sample volume, $\theta(x)$ is the Heaviside's function: $\theta(x) = \begin{cases} 1, x \geq 0; \\ 0, x < 0. \end{cases}$, m-dimensional vectors $\vec{z}_i$ are obtained by shifting of the original time series x_i by a fixed lag τ. $z_t = \left\{ x_t, x_{t+\tau}, x_{t+2\tau}, ..., x_{t+(m-1)\tau} \right\}$.

At small ε the correlation integral $C(\varepsilon) \propto \varepsilon^d$ therefore the attractor dimension d can be estimated by a slope of linear dependence of $\ln C$ on $\ln \varepsilon$: $\ln C(\varepsilon) \cong d \ln \varepsilon + c$. Usually dimensionality d depends on phase space dimensionality m. One can consider change of attractor dimensionality with increase of m. If the dependence of d versus m is declined from straight line

beyond some reasonable small *m*, the system represented by the time series should possess an attractor [*Babloyantz, et al.*, 1985]. The correspondent values *d** and *m** are regarded as an estimation of the dimensionality of the attractor and embedding space. Parameters of the time delay were chosen based on autocorrelation functions.

Data characteristics.

a. The Geysers.

The Geysers is a complex of 22 geothermal power plants, drawing steam from more than 350 wells, located in north of San Francisco, California. Commercial development of The Geysers started in the middle of 1950s.

Historical data on steam production and water injection volumes in The Geysers area is shown in **Fig.7.4.1.** Between 1995 and 1997, the injection volumes remained more or less constant. In 1997, the Lake County-Southeast Geysers Effluent Pipeline Project begins operations. The 29-mile underground pipeline started to deliver eight million gallons of water to The Geysers everyday to be injected into the geothermal resource.

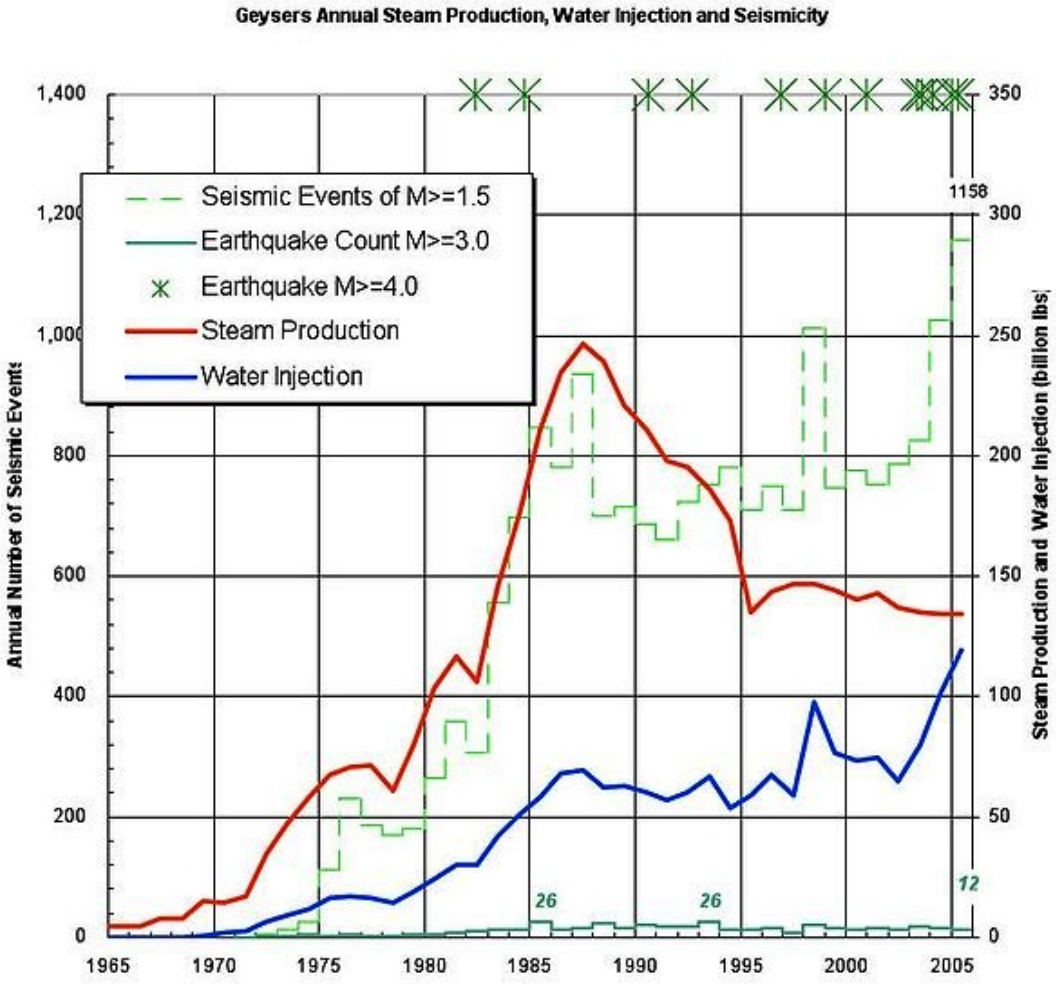

Fig.7.4.1. The Geysers annual steam production plotted with the earthquake activity, and water injection. Adopted from http://esd.lbl.gov

The area is intensely seismically active and generates many small earthquakes every day (see **Fig.7.4.1**). In the presented research, the Calpine Geysers seismic catalogue was used. It includes 86 483 earthquakes with magnitudes M=0.1-3.3 registered from 1.01.1995 till 12.31.1998.

To study possible influence of intensive water injection, which began in 1997, the earthquake catalogue was divided into two parts of the same durations: 1995-1996 (50156 earthquakes) 1997-1998 (36327 earthquakes). As a characteristics of seismic regime, seismic activity was used, which was calculated as a sum of cubic roots from energies of seismic events occurred during a day.

b. Bishkek test site.

Bishkek test site is located in seismically active area of Kyrgyzstan (**Fig.7.4.2**). A powerful electromagnetic source (an electro prospecting installation ERGU-600-2) starts to work there in the beginning of 2000. Probing pulse of ERGU-600-2 represents a series of periodic sign-changing square pulses of a current with amplitudes 600-800A and the period 10 sec. Duration of one session was about 20 minutes. The total duration of the experiment was 6 years (since 2000 till 2005). The details of the experiment were published by *Velikhov et. al.,* 2006. The analysis of seismic activity was made on the basis of local seismic network data (KNET, **Fig.7.4.2**). The catalog contains 6623 earthquakes with magnitudes M=1-6, registered from 6.01.1994 till 12.30.2008 on the area with coordinates φ=37.35-45.77 N; λ=68.67-82.24 E. The earthquake catalog was divided into two parts of the same durations: before EM excitations and during the excitations. The considered area of possible EM excitation influence was 200x200 km in size with the center coincident with EM source position.

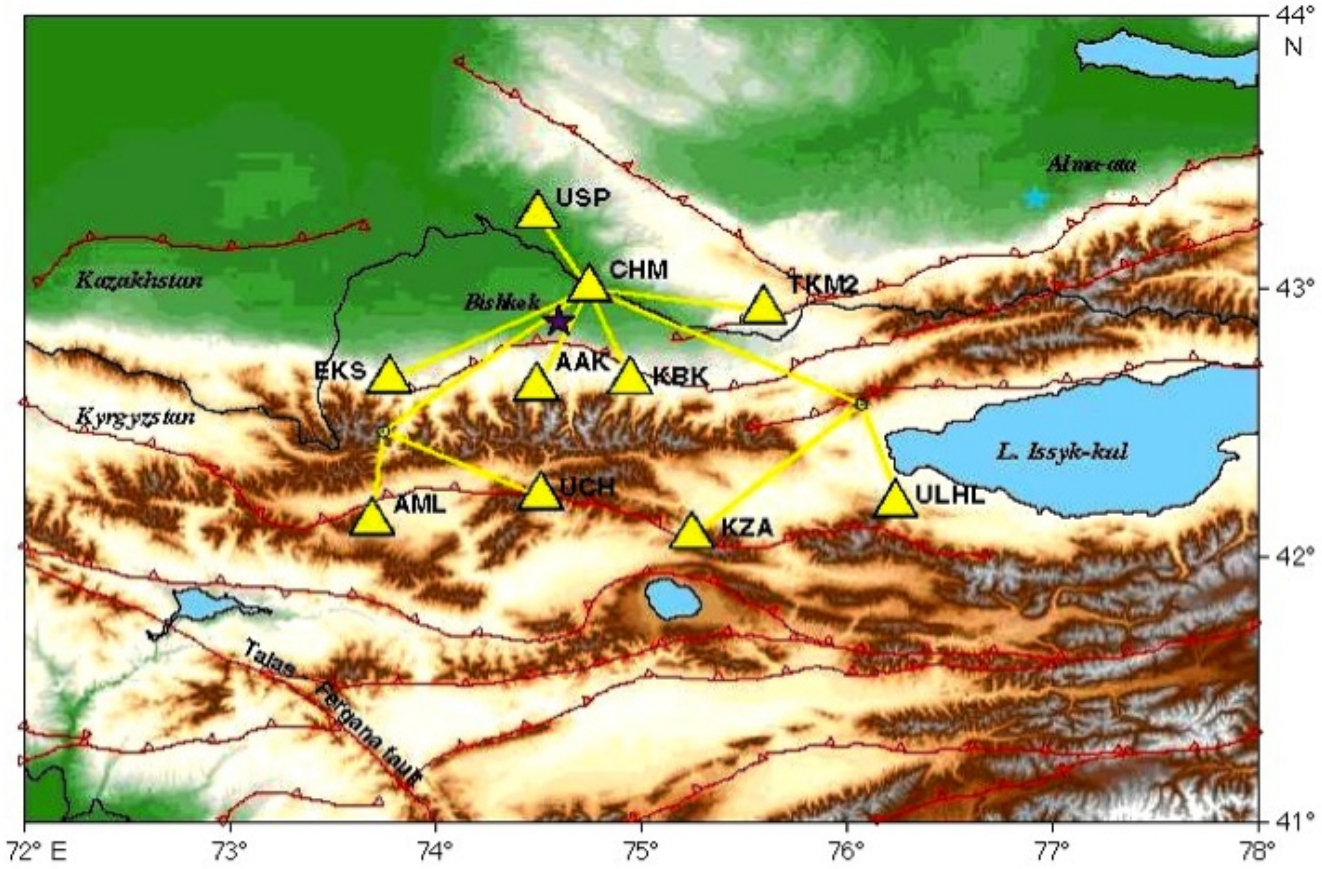

Fig.7.4.2. Map of the studied region and KNET seismic station locations. Yellow lines show telemetry links.

c. Romshkino oil-field

According to the map of seismic zoning the south – east part of Tatarstan, where Romashkino oil field is located, is considered to be a seismically quiet area. In 1982-83 in the region of Almetjevsk citizens noticed city seismic events with intensity III-IV. A local seismic network was installed in 1985. An increase in seismic activity was recorded at the end of 1986 – beginning 1987, in the middle of 1988, and at the end of 1991. The earthquake on September 29, 1986 had intensity VI in epicenter (magnitude M=3.8, hypocenter depth 5-10 km) and that on September 19, 1988 had intensity up to V.

On October 28, 1991 an earthquake with M=4, intensity in epicenter VI and a hypocenter depth 6 km [*Iskhakov*, 1992] occurred in the region of Almetjevsk.

Romashkino oil field is the biggest oil field in Russia. Its maximal dimension is about 70 km. Amplitude of structure crest high of Devon sediments is 50-60 m, reservoir depth is 1600 – 1800 m. Oil-bearing formation is formed by quartz sandstone with thickness between 10 and 30 m and carbonates. The permeability of the sandstone layers ranges from 200 to 420 mD, the porosity is between 18.8 and 20.4%, oil-saturation is 69.4–90.5%. The initial reservoir pressure is 160 to 180 atm.

In July, 1948 oil was produced for the first time. Water injections in the oil field started in 1954. On 01.01.1976, volume of injected fluid was 2.13×10^9 m^3, which was at that time equal to 104.7% of extracted fluid in reservoir conditions [*Muslimov*, 1979].

Most of earthquake epicenters are situated along Altunino – Shunaksky depression structure, seismic activity distribution on the area does correspond to tectonic faults, revealed by *Belousov et al.,* 1994.

Results of non-linear analysis.

The Geysers.

The seismic activity variations in the considered area are shown in **Fig.7.4.3**. It can be seen that besides high-frequency oscillations of the activity, there are some variations of the activity with respectively low frequency – the period of the variations is near 1.5 years. To avoid possible influence of that low-frequency variations on results of the study, these variations were eliminated by subtraction of polynomial averaging of the data from original activity data set.

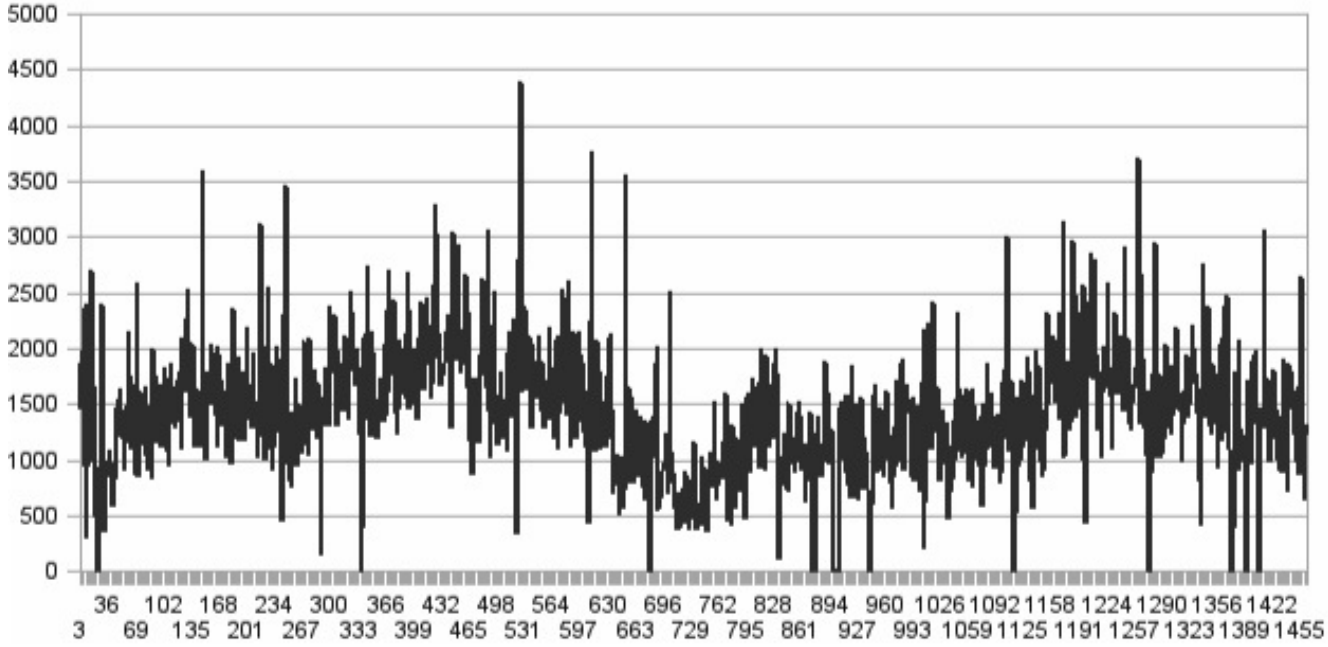

Fig.7.4.3. The variations of the seismic activity in the region of the Geysers in time.

The autocorrelation functions of the detrended seismic activity are shown in **Fig.7.4.4** for two periods separately (before start of the injection in the scope of Lake County-Southeast Geysers Effluent Pipeline Project and after its start). Based on these autocorrelations, the time delay value was chosen to be 5.

For data on seismic activity, the correlated dimensions *d* were calculated as it was described in previous section. It was found (**Fig.7.4.5**), that for the period of time before the injection project start, the correlated dimension shows no intent to decline from the direct dependence on embedding space dimension *m* (beyond *m*=3), while for the period after the injection project start, the dependence of *d* vs. *m* looks to saturate at the point *m*=6-8, *d*=4.2-4.5. It means that the increase in injection volumes resulted in change of the seismic regime in the region of The Geysers geothermal area and lead to an

increase of deterministic component of the seismic regime, which looks like an attractor appearance with fractal dimensionality 4.2-4.5 embedded in space with dimensionality 6-8.

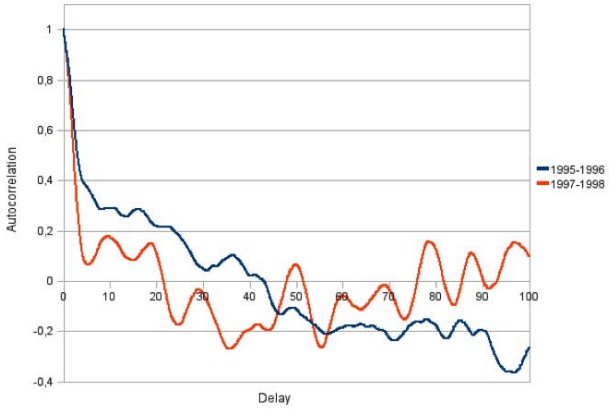

Fig.7.4.4. Autocorrelation functions.

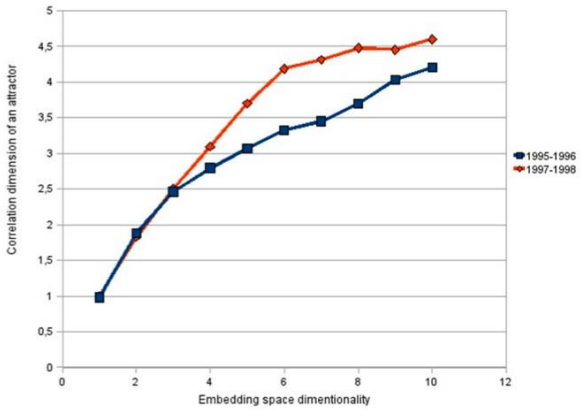

Fig.7.4.5. An attractor dimensionality estimation.

Bishkek test site.

The variations of the seismic activity in time are shown in **Fig.7.4.6** for the time periods before EM action start and during actions of EM source.

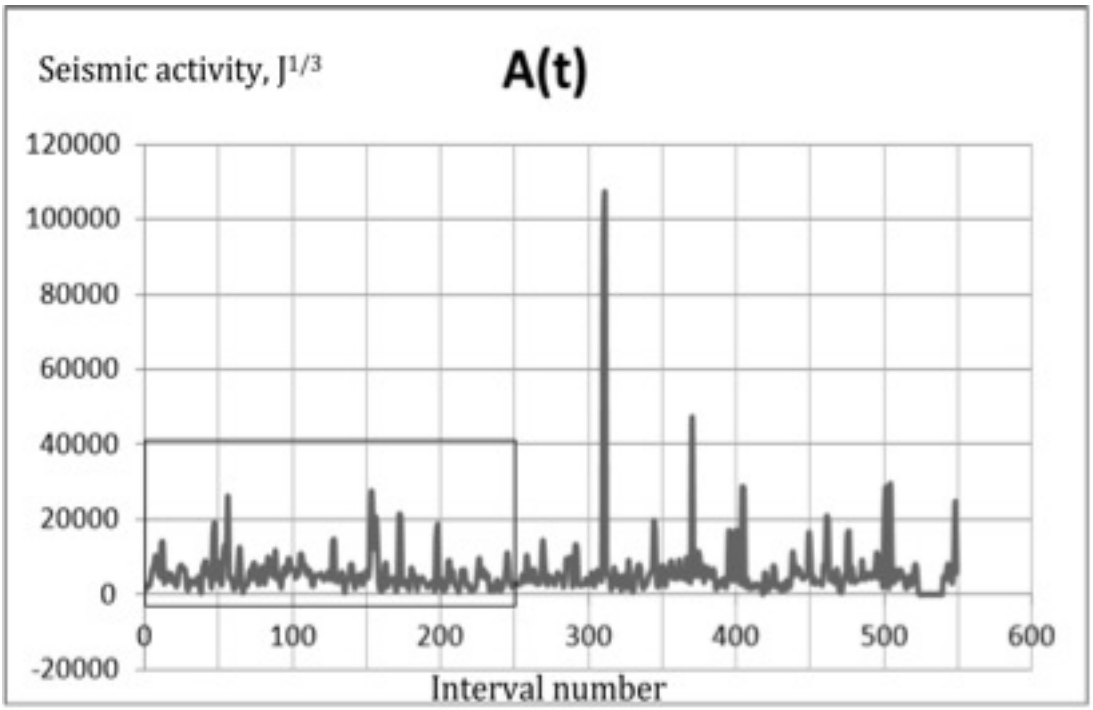

Fig.7.4.6. Change of the seismic activity in time before (left graph) and after (right graph) EM action start. On the X-axis the numbers of consecutive intervals for which the seismic activity was calculated are postponed.

The correlation integral was calculated for several dimensions of embedded space, which were varied from 1 to 20. Obtained relations between the fractal correlation dimensionality and the dimensions of the embedded phase space are shown in Fig.7.3.7. Dimensionless time delay values (or lags - the value of shifting the time interval used for seismic activity calculation) were chosen based on autocorrelation function local minimums; their meanings are shown in **Fig.7.4.7**. It can be concluded that during EM actions the correlation dimensionality diminishes from 7.4-7.8 to 4.7-5.2, the embedded space dimensionality decreases from 14 to 6.

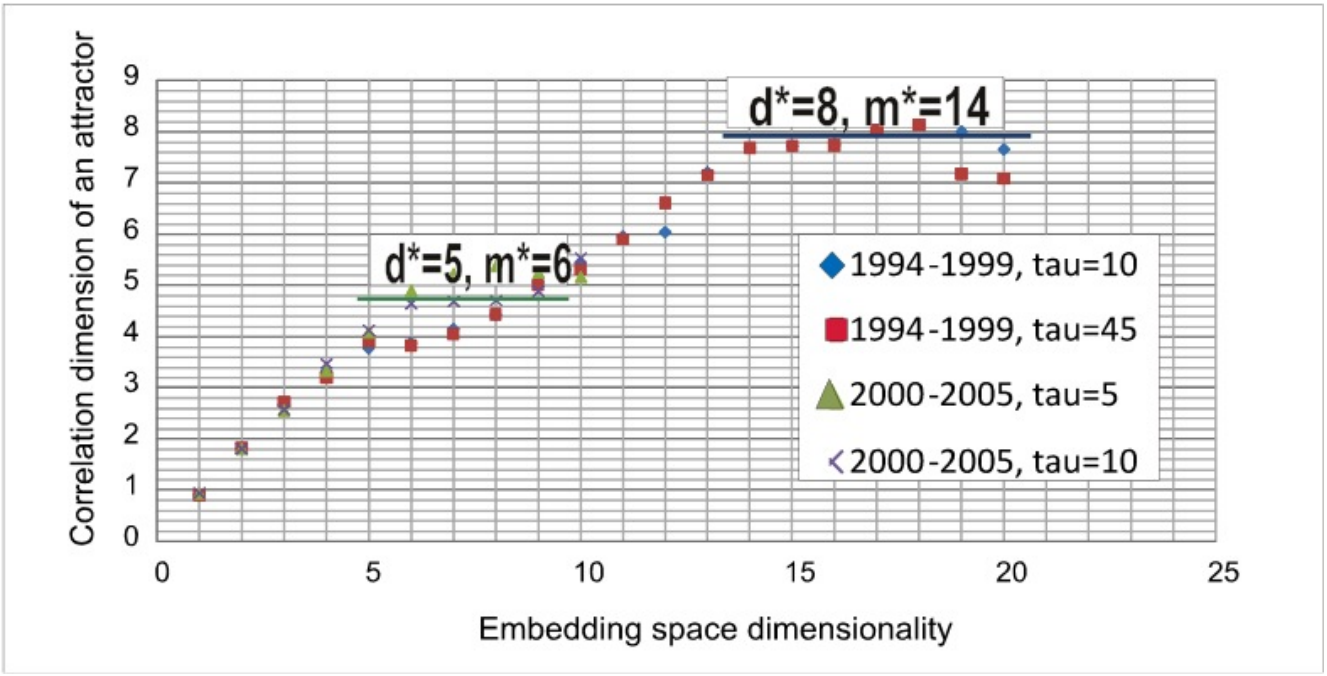

Fig.7.4.7. Fractal correlation dimension vs. embedding space dimensionality of the seismic activity before and during EM actions.

One can suppose that some natural perturbations of seismic regime could influence on the above results. To avoid it, the calculations were made for the periods of observations, which have no significant peculiarities. The periods are shown in **Fig.7.4.6** by rectangles. Dependences of the correlation dimensionality on the embedded space dimensions were calculated. It was found, that before the EM action start, the seismic process didn't show any stable state indications while during EM action the seismic process gains an attractor of dimensionality 5.6-6.0.

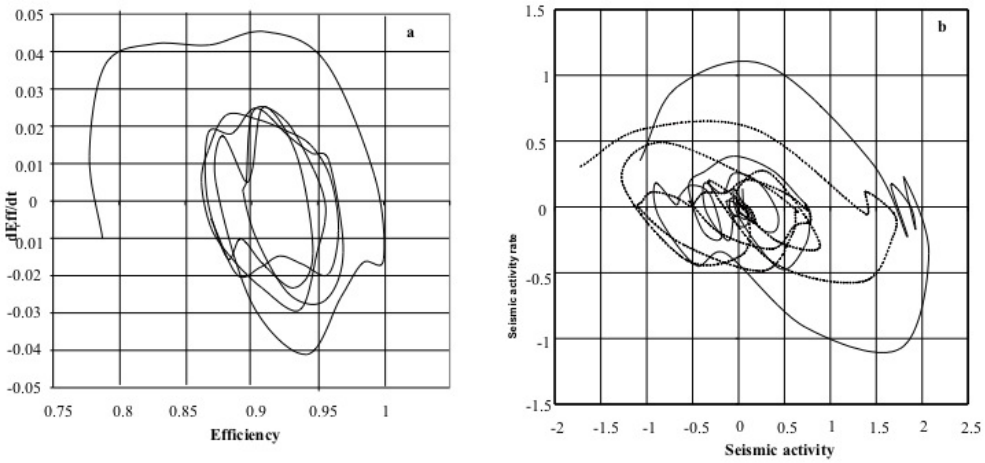

Fig.7.4.8. Two-dimensional phase portrait of injection efficiency (left figure) and phase portrait of the seismic activity (right).

Romashkino oil-field

In **Fig.7.4.8** the dependence of attractor dimensionality versus phase space dimensionality is presented for smoothed data on seismic activity in the region of Romashkino oil-field. One can see that the time series looks like derived from the system, which possessed an attractor of 2.7 fractal dimensionality, and which can be described with the help of 5 variables. The calculations of correlation integral were made also for ratios of volumes of produced fluid to injected water in four

most seismically active areas of Romashkino oil field before and after the year of the first increase of the seismic activity there.

The ratios were calculated for monthly values and then smoothed by moving window. It is interesting, that the attractor dimensionality and phase variables number became higher after 1986. The attractor dimensionality for the first period was near 1.5 that corresponds to two-dimensional curve. Unfortunately the length of data set does not allow us to make a reliable estimation of phase space dimensionality greater than 5 or 6. We can just estimate that the attractor dimensionality of the second period of the studied value changes is of the same magnitude, as the dimensionality of the seismic activity.

If there is a correlation between seismic activity and parameters of oil production, there have to be a similarity between phase portraits, which can be derived from these data sets. The correlation between Romashkino oil-field exploitation parameters was studied and discussed in the paper [Adushkin et al., 2000]. We can use a ratio of volumes of produced fluid to volumes of injected water as a measure of injection efficiency, and as one of the phase coordinates. The rate of injection efficiency changes can be used as another phase variable. To construct a phase portrait of seismic activity (see [Adushkin et al., 2000], we can use the seismic activity, as one of the phase coordinates, and rate of the seismic activity change, as another phase coordinate. Two-dimensional phase portrait of injection efficiency is shown in **Fig.7.4.8a**. The injection efficiency and its rate of changes were smoothed undependably by moving averages. One can see that the phase portrait of the injection efficiency bears similarities to the phase portrait of the seismic activity, which is presented in **Fig.7.4.8b**.

Seismicity in the region of Hydrocarbon Production in the North-Eastern Part of Sakhalin Island.

Over last decade there was an intensive development of oil and gas industry in the Sakhalin Island. Many of the offshore oil and gas fields in the north-eastern part of the island are located in the vicinity of tectonic active faults. Over last two decades about 10 earthquakes with magnitude $M \geq 5$ occurred in this tectonic active area, in particular the catastrophic 1995 Neftegorsk Earthquake (M_W 7.2).

Many types of seismic events associated with oil and gas production have been recognized or hypothesized over the past decades. There are many cases for which a connection between unusual seismicity and oil and gas production activities has been suggested in the scientific literature [*Segall et al.*, 1994; *Adushkin et al.*, 2000, *Adushkin, Turuntaev*, 2005, *Suckale*, 2009;]. The seismic response to oil and gas production is highly variable from field to field. So, it is important to monitor seismic activity to advance scientific understanding of this phenomenon as its relation to oil and gas production.

Detailed seismological observations by permanent seismic local network were started in 2006, September in the northern-eastern part of Sakhalin Island. Six seismic stations were equipped by KS-2000/SP short-period seismometers and SMART-24R recorders produced by Geotech Instruments, Dallas, Texas, USA. The seismic equipment was installed in the proximity to the Sakhalin-1 and Sakhalin-2 offshore production areas. The main objective of the local seismic network is to monitor and assess the potential effects of hydrocarbon production on the seismic activity.

SEISAN software [Havskov*, Ottemoller*, 2000] is applied for earthquake data processing. Unified database of registered seismic events and waveforms has been created. More than 500 seismic events with local magnitude $M_L \geq 1.0$ have been localized from 2006, September to 2010, March. Significant number of earthquake clusters including microearthquakes is related to main active faults in the Northern Sakhalin and associated with a natural background seismicity corresponding to the regional tectonic stresses.

Over last five years a few moderate earthquakes occurred in the proximity to the offshore Piltun Astoskhskoye field, which is developing since 1999: 2005.06.12 M_W 5.6, 2005.09.05 m_b 4.1, 2009.08.22 m_b 4.8 (according NEIC). It seems like unusual seismicity pattern and is currently discussed among seismologists in terms of triggered seismicity due to hydrocarbon production [*Tikhonov*, 2010]. The summarized key arguments, which seem reasonable, are the following:

1. Time interval: level of seismic activity increases 10-20 years after beginning the oil and gas field development.
2. Spatial distribution: triggered earthquakes occur in the proximity to the oilfield production areas.
3. Frequency magnitude relation: variation of b-value.

We have analyzed the spatial-temporal and frequency magnitude distributions of seismicity according to the seismic monitoring data from 2006 to 2010 and regional catalogue from 1905 to 2005. The comparison of results showed that earthquake source distribution in the magnitude range $2 \leq M \leq 4$ is characterized by stable level of seismic activity at Northern Sakhalin including offshore oilfield production areas and may be considered as natural background seismicity. There is no significant activation of small to moderate earthquakes in examined areas.

It should be noted that activation of moderate earthquakes with magnitude greater than 4 over last two years is related to seismogenic areas at distances more than 100 km away from oilfield production areas. It cannot be associated with induced or triggered seismicity. This phenomenon should be probably described in terms of natural seismicity activation in 2009-2010 at a whole northern part of the island.

Study of an influence of blasting on mine seismicity.

The underground mines widely utilize blasting with different charge capacities. The relation between ore blasting and seismicity in mines is considered based on data on seismicity variations after explosions in Tashtagol Iron-Ore Mine (Russia). The seismic monitoring station Tashtagol records annually to 1500 seismic events in average. To analyze an influence of blasting on the seismicity, two cumulative catalogues were created, one by overlapping one-week periods after each blast, another by overlapping one-week periods before each blast. In the catalogues, the time and location of each seismic event were recalculated relatively to time and position of the corresponding explosion. As the seismicity characteristics, variations of the seismic event positions and time of occurrence as well as changes of seismic activity in space and time were considered. The seismic activity was calculated as sum of cubic roots from energies of the seismic events occurred during some time period. It was found that summarized energy of seismic events occurred during an hour increased by a factor of 20-40 after blasting. The seismic activity returned to background value in 0.5-1 day. The linear regression analysis of the explosion energy effect on the number and energy of seismic events within a week after the blasting showed their relation (on the significance level 99%) with the correlation factors 0.6–0.7. The post-blasting seismic events concentrated at the blast site area. Within three days after the blasting, the average distance between the epicenters of the seismic events and the explosion gradually enlarged and finally became background.

References

Eremenko V.A., Eremenko A.A., Rasheva S.V., Turuntaev S.B. Blasting and the man-made seismicity in the Tashtagol mining area // Journal of Mining Science, Vol. 45, No. 5, 2009.

Konovalov A.V., Turuntaev S.B. Induced Seismicity due to Hydrocarbon Production in the North-Eastern Part of Sakhalin Island: Weak Motion Monitoring and Further Prospects // Proceedings of the European Centre for Geodynamics and Seismology. Luxembourg. 2010. V.30.

Melchaeva O.Yu., Turuntaev S.B. Non-linear analysis of seismicity change under electromagnetic action // European Seismological Commission 32nd General Assembly Abstract Book. ESC2010. p.159.

Turuntaev S.B., Eremeeva E.I., Zenchenko E.V. Laboratory study of temporal-spatial peculiarities of microseismicity spreading due to pore pressure change // European Seismological Commission 32nd General Assembly Abstract Book. ESC2010. p.198.

Turuntaev S.B., Eremeeva E.I., Zenchenko E.V. Laboratory study of temporal-spatial peculiarities of microseismicity spreading due to pore pressure change // Proceedings of the European Centre for Geodynamics and Seismology. Luxembourg. 2010. V.30. P.123-130.

Turuntaev S.B., Melchaeva O.Yu. An analysis of triggered seismic processes with the help of non-linear dynamics methods // Triggered effects in geosystems. Moscow: GEOS. 2010. P.124-135. (in Russian)

Turuntaev S.B., Melchaeva O.Yu. Non-linear analysis of seismic regime response to electromagnetic powerful source actions // Proceedings of the European Centre for Geodynamics and Seismology. Luxembourg. 2010. V.30. p.48-56.

Turuntaev S.B., Zenchenko E.V., Eremeeva E.I. Laboratory experiments on relation between pore pressure change and acoustic (microseismic) emission // Rock mechanics in civil and environmental engineering. CRC Press / Balkema. 2010. p.99-103.

Turuntaev S.B., Zenchenko E.V., Eremeeva E.I. Laboratory study of microseismicity caused by pore pressure change // Short Papers of 31st General Assembly of the European Seismological Commission, Hersonissos, Crete, Greece, 7-12 September 2008. P.210-218

Turuntaev S.B., Zenchenko E.V., Eremeeva E.I. Permeability evaluation from microseismic data (laboratory study) // 80th Annual International Meeting SEG, Expanded Abstracts. SEG Publications. 2010. 1342–1345.

Turuntaev S.B., Zenchenko E.V., Eremeeva E.I. Temporal behavior of microseismmicity as a characteristic of local pore pressure change // SEG 2009 Conference Expanded Abstracts. SEG Publications P.1642-1646.

Turuntaev S.B., Zenchenko E.V., Novikov A.V. Microseismic characterization of pore pressure change in laboratory experiments // SEG 2008 Conference Expanded Abstracts. SEG Publications P.237-241.

8. Nanocrystals in geomaterials (experimental works of Russian scientists in 2007-2010)

S. M. Kireenkova, ksm@ifz.ru, *Schmidt Institute of the Physics of the Earth RAS. B. Gruzinskaya, 10. Moscow 123995, GSP-5, Russia.*

Based on results of numerous studies in other fields of since, it is known by now that nanocrystals have unique properties different from those of macroscopic-size crystals. This refers, in particular, to strength, defect rate and spatial structure of nanocrystals. However it is known that the processes causing destruction of solid bodies (including rocks) and the destruction processes themselves, for all sizes (from nano- to macro-), begin with formation and coalescence of nanodefects and "nucleating" cracks which also are nanosized. In this connection, the task of studying physical properties of nanocrystals and a mechanism of failure in rocks assumes fundamental importance in seismology.

The presented paper considers one of the aspects of this problem: experimental determination of nanostructures in rocks and minerals of various depth, their identification, determination of nanocrystals physical properties and their change in the process of deformation in different p–T conditions.

The first results of such studies were given in a number of papers published in 2005-2007 [*Kireenkova, Sobolev*, 2005; *Sobolev et al.*, 2006, 2007a, 2007b; *Chanturiya*, 2006; *Yushkin*, 2005]. In the past three years, the range of publications on this problem widened insignificantly, and this report presents the studies that were carried out in continuation of the work previously commenced by the abovementioned authors.

It has been shown in the first papers [*Sobolev et al.*, 2006, 2007a] that the physical method applied for study of nanostructures, namely a Raman spectroscopy method, allows to detect nanocrystals in rock, estimate their dimensions and internal stresses. In order to obtain spectra, rock samples in the form of 3-4 mm thick plates were installed on a specimen stage of a Ramalog 5 spectrometer. Spectra were recorded in a photon-counting mode at the scattering angle of ~180°. Polarization of diffused light was not analyzed. Spectra were excited using an Ar^{++} 16508 (Spectra Physics) argon laser, the line being 488 nm in the study of thinly laminated arcose sandstone and

xenolith samples and 514.5 nm in the study of pseudotachylite. The laser beam focused on sample surface gave a spot with the diameter of ~ 30 μm. The light diffused in backward direction was directed to a monochromator entrance slit using a mirror and a focusing optical system. There it was spread out into a spectrum by two holographic arrays and recorded by a TE-104 TS photomultiplier cooled down to -30 °C (in order to reduce thermal noise). The signal from the photomultiplier was sent to a computer for accumulation during rerecording and further analysis.

In order to more exactly determine frequencies of band peaks and their shifts, simultaneously with spectra registration the spectrum was recorded in the range of frequency of the exciting light the band of which was used as a benchmark. Consequently, an error in determining peak frequency and width of the studied bands in the spectrum did not exceed 0.2 cm^{-1}. In order to reduce the influence of instrument function on band shape, the spectral width of the slit was taken as 2 cm^{-1}. Since the band width was, at least, 4 times larger than the spectral width, spectra were not adjusted for accounting of instrument function. The scanning speed did not exceed 1 cm^{-1}/min for the purpose of dynamic distortion minimization.

When arcose sandstone was studied, the bands corresponding to anatase, α-quartz and plagioclase crystal lattice vibrations were observed in rock spectra. It has been found out that spectrum peaks for 10-20 nm nanocrystals of quartz, anatase and plagioclase were shifted to the high-frequency area in comparison with macrocrystal spectra and broadened. This indicates the presence of additional internal stresses [*Sobolev et al.*, 2007a].

A selected sample of deep-seated rock was mantle xenolith from the Obnazhennaya kimberlite pipe located in the north of the Yakut kimberlite province [*Morozov, Kireenkova, Sobolev et al.*, 2008; *Sobolev et al.*, 2009]. The rock was composed of 40-50% garnet, 45-55% clinopyroxene and 10-15% orthopyroxene. With regard to chemical composition, the rock is between peridotites and eclogites and close to garnetiferous pyroxenites, the difference from eclogites being in lesser content of Al_2O_3. The xenolith sample was put into quasi-hydrostatic compression up to 2.5 GPa in a cylinder-piston unit with simultaneous recording of longitudinal and transverse wave travel time using an ultrasonic pulse method according to a known procedure [*Kireenkova, Safarov*, 1979].

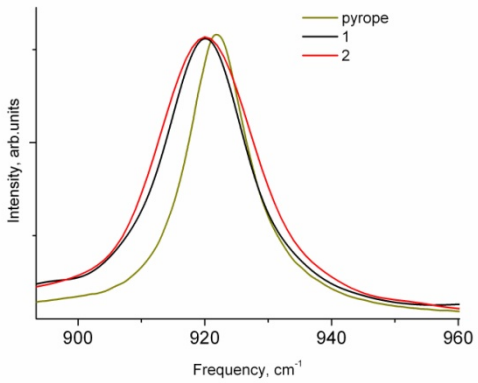

Fig.8.1. Shapes of bands in 920 cm^{-1} area in Raman spectra of xenolith samples (1 and 2) and macroscopic-size pyrope monocrystal.

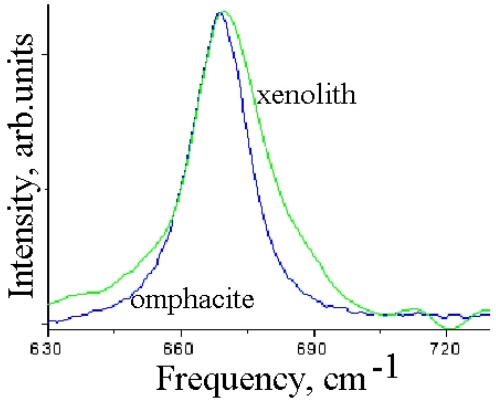

Fig.8.2. 670 cm^{-1} band in Raman spectra of xenolith and omphacite monocrystal.

Nanocrystals of pyrope and omphacite have been detected in xenolith samples using the Raman spectroscopy method. In order to determine pyrope nanocrystal sizes in a xenolith sample surface layer, the position and shape of the bands attributed to valence vibrations of Si-O bonds in 926 cm^{-1} pyrope and 670 cm^{-1} omphacite crystals were analyzed. **Fig.8.1** shows spectra of a pyrope monocrystal and an undeformed xenolith sample in 920 cm^{-1} band. Xenolith spectra peaks are shifted toward low frequencies and asymmetrically broadened. **Fig.8.2** presents the same comparison for an omphacite monocrystal and an undeformed xenolith sample in 670 cm^{-1} band. Here we can observe the shift of a xenolith spectrum peak toward high frequencies and also its asymmetrical broadening. As a result of spectral analysis, sizes of nanocrystals in mantle xenolith have been estimated as follows: pyrope

nanocrystals with size of ~18 nm and omphacite nanocrystals with size of ~13 nm. In addition, it has been established that crystallographic cell dimensions are larger in nanocrystals than in macrocrystals. The estimated value of the internal tension stresses which might have caused these changes is equal to ~1.1 GPa.

As noted above, the xenolith samples were deformed at quasi-hydrostatic pressure up to 2.5 GPa. The detailed analysis of spectral bands has shown that peaks and shape are different in samples before and after compression. **Fig.8.3** gives a band attributed to valence vibrations of pyrope nanocrystals in xenolith before (1) and after (2) deformation under pressure. After quasi-hydrostatic compression stress, the vibration frequency decreased by ≈0.5 cm^{-1}, and the band width (at half-maximum intensity) decreased by ~1 cm^{-1}. It can be seen from the calculations that after hydrostatic compression crystal sizes remained the same and crystallographic cell dimensions increased. This increase corresponds to the hydrostatic tension stress of ≈0.6 MPa. While the spectrum shape for pyrope nanocrystals before and after pressure application changed only in terms of quantitative variables, the spectra of pyroxene demonstrated differences. Instead of the single band of ≈670 cm^{-1}, two bands appeared. According to [*Burzo*, 2006], only one type of SiO_4-tetrahedron chains and therefore one vibration mode exist for clinopyroxenes (monoclinic crystal lattice). Whereas there are two types of such chains positioned at some angle to each other and having different average Si–O bond length in orthopyroxenes (orthorhombic lattice). Therefore orthopyroxenes are characterized by to vibration modes which are close to each other in frequency. For pyroxenes, band splitting was attributed to change in a crystal lattice space group of symmetry [*Burzo*, 2006; *Rull*, 2004]. When the applied pressure was increased (>3.5 GPa), the authors observed transition from orthopyroxenes to clinopyroxenes; in case of pressure reduction, the transition was reverse. This was done for macrocrystals. It appears that no such studies have been carried out for nanocrystals. In our experiment with xenolith samples, deformation occurred at the quasi-hydrostatic pressure of 2.5 GPa. It is known that internal stresses within the crystal lattice of nanocrystals may be several times higher than external stresses applied to the sample. It was recorded, for example, in a study of α–β transition in quartzite using neutron diffractometry methods [*Sobolev et al.*, 2004]. Nevertheless, the preliminary conclusion about the transition of clinopyroxenes to orthopyroxenes at the nanocrystal-scale level under compression requires a more detailed experimental study.

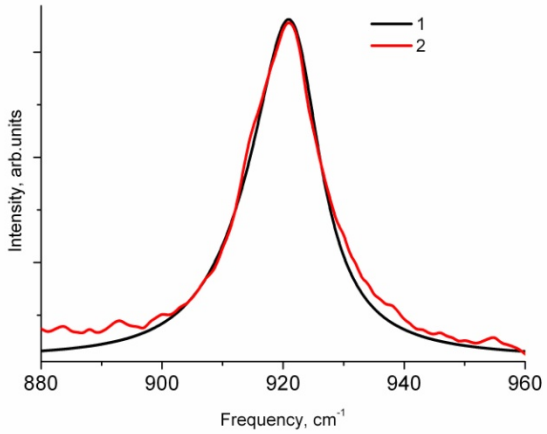

Fig.8.3. Band attributed to valence vibrations of pyrope in xenolith before (1) and after (2) deformation under pressure.

The above listed works were logically continued by the studies in which rock was not only compressed, but also heated to high temperature [*Vettegren et al.*, 2010]. The most commonly encountered group of rocks in the Earth's crust, granites, has been selected as a subject of research, and a product of their maximum intense crushing in the seismogenic fault zone, apogranite pseudotachylite, is investigated in this study. Pseudotachylite is a rock in which fragments of bedding material are cemented by dark grey microcrystal mass. It consists of quartz, feldspars and ore minerals. The rock undergone the complex evolution comprising the following stages: magmatic stage – granite formation; cataclasis – crushing and weak texturing under compression and shear conditions; recrystallization of cataclastic chips into quartz [*Morozov*, 1991, 2002]. All the stages of rock

evolution following the magmatic one took place under low-temperature conditions and therefore did not lead to complete rock transformation. Samples in the form of cylinders and right-angle prisms were prepared for measurement purposes. The samples were primarily grey with separate areas of white color. The spectral analysis was carried out using the Raman spectroscopy method. Spectra were recorded in several points of the samples. Information about nanocrystals sizes can be obtained based on the results of studying the shape of bands in Raman spectra attributed to the crystal lattice vibrations [*Zbinden*, 1964; *Tiong et al.*, 1984; *Shen, Pollak*, 1984; *Richter et al.*, 1981]. The detailed analysis of the results has shown that the bands attributed to quartz vibrations have maximum intensity in the Raman spectra of the surface layer of grey rock areas. At the same time, in the Raman spectra of white rock areas, maximum intensity was observed for the bands attributed to feldspar crystal lattice vibrations. As an example, **Fig.8.4** and **8.5** show fragments of Raman spectra for non-deformed pseudotachylite samples. The same figures present macrocrystal spectra for quartz and low-temperature (stable at temperatures below 400°K) albite modification. The observed bands are symmetrical in quartz macrocrystal spectra and asymmetrically broadened toward high frequencies in rock spectra, and the frequency of their peak is shifted. The bands have symmetrical dispersion shape in the Raman spectra of albite macrocrystals and are asymmetrically broadened toward low frequencies in the spectra of the examined rock. It is known [*Tiong et al.*, 1984; *Shen, Pollak*, 1984; Richter et al., 1984] that asymmetrical broadening occurs due to scattering of vibrations at nanocrystal edges. This means that quartz and albite crystals are nanosized in pseudotachylite. It can be seen from the calculations that linear dimensions of quartz and albite nanocrystals in pseudotachylite vary within ≈4-25 nm and ≈ 8-30 nm respectively.

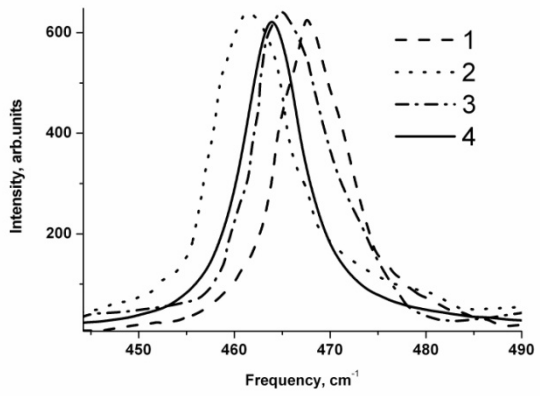

Fig.8.4. A_1 vibration band for the crystal lattice of quartz in Raman spectra of rock (1–3) and macrocrystal (4).

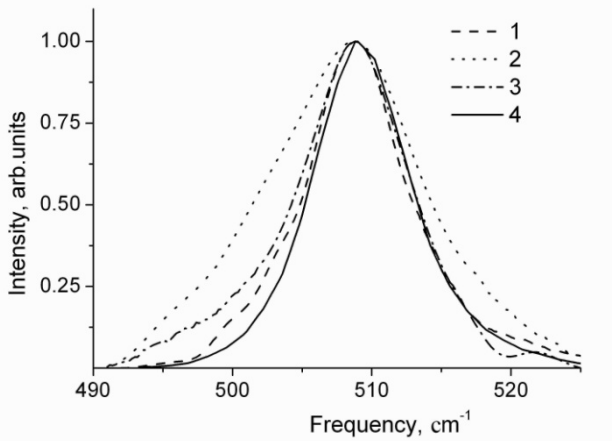

Fig.8.5. Band of the valent T–O–T (T – atom of Si or Al) bonds symmetrical to vibrations in Raman spectra of albite macrocrystal (4) and the examined rock (1-3).

The crystal lattice frequency shift is driven by lattice deformation, and the shift value is proportional to the stress that may have caused this deformation. The ratio between shift and stress in known for quartz [*De Boer K. et al.*, 1996], which made it possible to estimate an effective stress value. It has turned out that it varies for different pseudotachylite areas from –300 MPa (compression) to +480 MPa (tension). In order to find out if the quartz nanocrystal lattice deformation effect is cased by residual stresses after the action of high pressures and temperatures, the Raman spectra of two samples subjected to hydrostatic compression at high temperatures have been studied using a solid-phase modified Bridgman anvil-type unit. The first sample was held under pressure at 470-500°C for 10 minutes, the second one – at 550-600°C for 16 minutes. It has turned out that linear dimensions of quartz nanocrystals decreased by about two times under the action of pressure and high temperature. At the same time, tension stresses in them increased up to ≈ 800 MPa.

The fact that nanocrystals with deformed crystal lattice have been detected in the examined rock from a focal zone of an earthquake repeats the situation in case of a higher hierarchy level where

millimeter quartz grains formed in conditions of both compression and decompression exist. This may indicate the conjunction of processes in nano- and macroscales.

Bibliography

Burzo E. Inosilicates. Berlin: Springer Berlin Heidelberg. 2006. 569 p.

Chanturiya V.A., Trubetskoi K.N., Viktorov S.D., Bunin I.Zh. Nanoparticles in the Process of Opening-up and Destruction of Materials. M.: 2006. 216 p. (in Russian).

De Boer K., Jansen A.P.J., van Santen R.A. et al. Free Energy Calculations of Thermodynamic, Elastic and Structural // Physical Review. B. 1996. V.54. N.2. P.826–835.

Kireenkova S.M., Safarov I.B. Simultaneous Measurement of Longitudinal and Transverse Wave Velocities in Rocks under High Pressures // Izv. of USSR Academy of Sciences. Earth Physics Series. 1979. No. 12. P.93–98. (in Russian).

Kireenkova S.M., Sobolev G.A. About Capability to Study Natural Processes at Nanoscale Level in Earth Physics // Geophysical Research. 2005. Issue 1. P.108–115. (in Russian).

Morozov Yu.A. Compression-Decompression Model of Deformational-Real Transformations in the Earths Crust // In Collect.: Mechanisms of Structure Formation in the Lithosphere and Seismicity. M.: IPE of RAS. 1991. P.179–181. (in Russian).

Morozov Yu.A. Structure-Forming Role of Transpression and Transtension // Geotectonics. 2002. No. 6. P.3–24. (in Russian).

Morozov Yu.A., Kireenkova S.M., Sobolev G.A., Smulskaya A.I., Tselmovich V.A., Vettegren V.I., Kulik V.B., Pikulin V.A. Experimental Study of Rock Nanostructures after Quasi-Hydrostatic Compression // In Collect.: Tectonophysics and Topical Issues of Earth Sciences (Abstracts of All-Russian Conference on October 13-17, 2008). M.: IPE of RAS, 2008. V.2. P.157–158. (in Russian).

Richter H., Wang Z.P., Ley L. The One Phonon Raman Spectrum in Microcrystalline Silicon // Solid State Commun. 1981. V.39. P.625–629.

Rull F., Martinez – Frias J., Sansano A., Medina J., Edwards H. G. M. Comparative Micro – Raman Study of the Nakhia and Vaca Muerta Meteorites. // J. Raman Spectrosc. 2004. V.35. P.497–503.

Shen H., Pollak F.H. Raman Study of Polish-Induced Surface Strain in <100>GaA_S and InP // Applied Phys. Letters. 1984. V.45. P.692–694.

Sobolev G.A., Kireenkova S.M., Morozov Yu.A., Smul'skaya A.I., Tsel 'movich V.A., Vettegren V.I., Kulik V.B. Nanostructures in the Deep Xenolite before and after Straining. Izv. Phys. of the Solid Earth. 2009. Vol. 45, No. 9. P.731-739.

Sobolev G.A., Ponomarev A.V., Nikitin A.N., Balagurov A.M., Vasin R.N. Dynamics of the Polymorphic α–β-Transition in Quartzite from Data of Neutron Diffractometry and Acoustic Emission. Izv. Phys. of the Solid Earth. December 2004, V. 40, No 10, P.788-797.

Sobolev G.A., Vettegren V.I., Kireenkova S.M., Kulik V.B. Morozov Yu.A., Smulskaya A.I. Experimental Study of Nanostructures in Rocks // In Collect.: Physicochemical and Petrophysical Studies in Earth Sciences (International Conference Proceedings) M.: IPE of RAS. 2006. P.67–68. (in Russian).

Sobolev G.A., Vettegren V.I., Kireenkova S.M., Kulik V.B. Morozov Yu.A., Pikulin V.A. Smulskaya A.I. Experimental Study of Nanostructures in Rocks // Geophysical Journal. 2007b. V.29. No. 3. P.10–14. (in Russian).

Sobolev G.A., Vettegren V.I., Kireenkova S.M., Kulik V.B., Morozov Yu.A., Smul'skaya A.I. Raman Spectroscopy of Nanocrystals in Rock. Izv. Phys. of the Solid Earth. 2007a. Vol. 43, No. 6. P.447-454.

Tiong K.K., Amirtharagj P.M., Pollak F.N., Aspness D.E. Effects of A_S^+ Ion Implantation of the Raman Spectra of GaA_S: ”Spatial Correlation” Interpretation // Applied Physics Letter. 1984. V.44. P.122–128.

Vettegren V.I., Kulik V.B., Mamalimov R.I., Sobolev G.A., Genshaft Yu.S., Kireenkova S.M., Morozov G.A., Smulskaya A.I. Study of Nanocrystals in Apogranite Pseudotachylite using Raman and

Infrared Spectroscopy Methods // In Collect.: Physicochemical and Petrophysical Studies in Earth Sciences (International Conference Proceedings) // M.: IPE of RAS. 2010. P.68–71. (in Russian).

Yushkin N.P. Ultra- and Fine-Dispersed State of Mineral Matter and Problems of Nanomineralogy // In Book: Nanomineralogy. Ultra-Dispersed State of Mineral Matter. Saint Petersburg. Nauka. 2005. P.10-61. (in Russian).

Zbinden R. Infrared Spectroscope of Polymers. N.Y.&L. Academic Press. 1964. 264 p.

9. Modeling of geodynamic processes

V. P. Trubitsyn, trub@ifz.ru, *Schmidt Institute of the Physics of the Earth RAS. B. Gruzinskaya, 10. Moscow 123995, GSP-5, Russia.*

Main driving force of global geodynamics processes in the Earth is mantle convection. This convection is coupled with floating continents, sinking lithospheric plates and upewlling plumes.

In 2007-2010 Russian scientists maid an contribution to numerical modeling of mantle convection with moving continents and modeling of mantle convection with generation and evolution of lithospheric plates. Comparison with available in word literature results are included.

9.1. Mechanical and thermal effects of floating continents on the global mantle convection

Numerical models are presented that simulate mantle convection coupled with superimposed continents. The continents and main islands are modelled as thin rigid spherical caps with non-slip boundary conditions and continuity conditions for temperature and heat flux at their bottom. Additional repulsive forces prevent overlap of the continents in the case of their collision. The initial temperature distribution in the mantle is calculated based on seismic tomography data. The evolving mantle model implies 10% basal and 90% internal heating and uniform viscosity. Mechanical coupling leads to near horizontal convection currents under continents and consequently to a noticeable decrease of the mantle temperature under them in spite of the thermal blanket effect. The modelling results show that a long-term evolution of the free convection model and of the model with implemented continents leads to principally different structures. Several common stages of the continental evolution are revealed. Back-arc basins at the active continental margins are closed at the first stage. In the next stage of the modelled evolution the convection pattern is reorganized and the main downwellings start to move to the south pulling the continents, which tend to assemble a new super-continent around Antarctica. Due to the repulsive forces the continents rotate and adjust to each other. The calculated structure of mantle flows, temperature distribution, and position of continents are presented for a time moment 100 Myr in the future.

Modelling is based on results of previous studies of Trubitsyn et al. A system of coupled differential equations was obtained in [*Trubitsyn*, 2000] for a quantitative description of mantle convection with coupled continents including equations of translational and rotational motion of continents.

The mantle was modeled by a viscous fluid located in a spherical shell. Continents were considered as thin spherical caps floating on the mantle. Impermeable free-slip boundary conditions with a fixed temperature were set at the mantle–core interface. The mantle was assumed to be heated by internal radioactive sources; the amount of heat generated by them was ten times larger than the heat supplied by the Earth's core. The upper surface of the mantle, unoccupied by continents, was considered free, with a fixed zero temperature. At all points of bases of continents, viscous flow velocities are equal to the velocity of a continent and the continuity condition should be valid for the temperature and heat flux. The temperature at the upper surface of a continent is equal to zero. The effect of thermal screening by continents (corresponding to thick continents) was taken into account.

Forces acting on a continent were calculated as the integral of viscous cohesion forces over the lower surface of the continent. A detailed analysis is given in [*Trubitsyn*, 2008; *Trubitsyn et al.*, 2008].

The present-day positions of six continents and the nine largest islands are taken as an initial state. The contemporary temperature distribution in the mantle is calculated according to the data of seismic tomography. The 3-D distribution of seismic wave velocities is converted into the density distribution and then into the temperature distribution. The Stokes equation is numerically solved for flows in a viscous mantle with floating continents for the given initial temperature distribution. In this way, the velocities of convective flows are determined in the entire present-day mantle and the surface distribution for the Earth's heat flux is obtained. The reliability of the calculated flows in the mantle is estimated by the comparison of the calculated velocities of the contemporary continents and oceanic lithosphere with data of satellite measurements.

Fig.9.1.1 shows result of one step calculation of mantle convection with initial temperature distribution, taken from tomography data and continental positions from geography map. With initial condition after one step calculation the mantle and continental velocity arose, which are similar to GPS data.

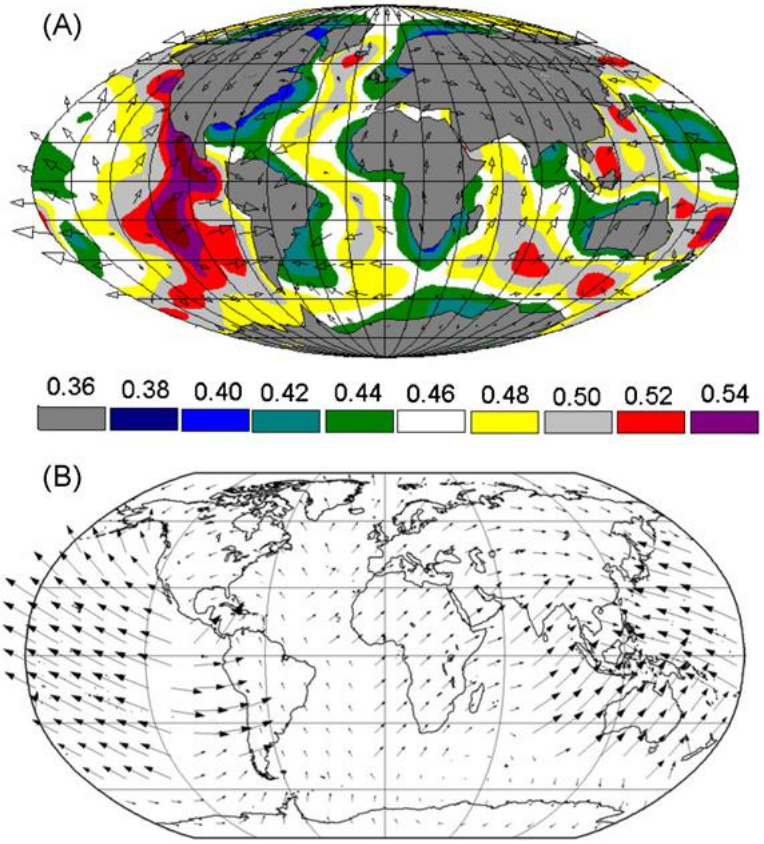

Fig.9.1.1. (A) dimensionless temperature at a depth of 100 km and mantle/continental. Velocities, calculated after the initial time step for the mantle with the initial lateral temperature variations obtained from tomography data. Temperature is shown by color, velocities – by arrows with the maximal value (dimensionless) – $2*10^3$. **(B)** Plate velocities according to the REVEL model based on GPS data. Maximal value is equal to 10 cm/year.

Father calculations show the evolution of the system mantle and continents. Continents drift and due to thermal and mechanical interaction with mantle change mantle flow. Positions of drifting continents in future till 100 Ma are shown in **Fig.9.1.2.**

Calculated final positions of continents, mantle velocities and temperature are shown in **Fig.9.1.3**.

The results similar to presented were carried out in [*Phillips, Bunge*, 2005, 2007]. These models are analogous to the models calculated early in [*Trubitsyn*, 2000, 2004; *Trubitsyn, Rykov*, 2001] but involve a number of simplifications; thus, they do not provide for the calculation of rotation of continents and do not take into account repulsive forces of continents and use disk like continent instead of their real figures.

Presented results show the first fully selfconsistent calculation of mantle convection with floating continent with real their figures and initial temperature distribution of present-day Earth.

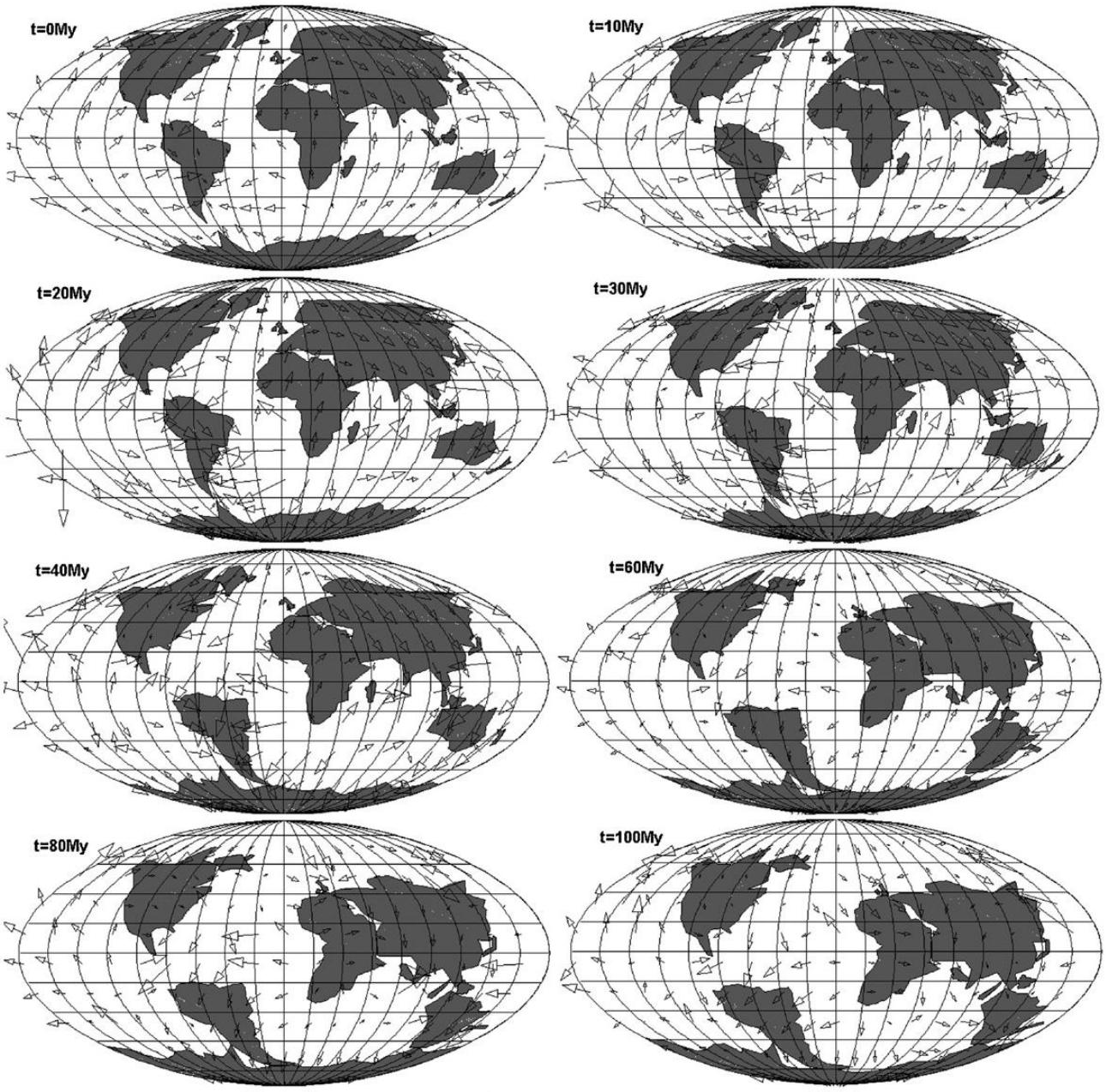

Fig.9.1.2. Positions of the continents and mantle velocities for different time steps from 0 through 100Ma. Dimensionless velocities are shown by arrows (maximal value $Vmax=2*10^3$).

References

Phillips, B.R., Bunge, H.-P., 2005. Heterogeneity and time dependence in 3-D spherical mantle convection models with continental drift. Earth Planet. Sci. Lett. 233, 121–135.

Phillips, B.R., Bunge, H.-P., 2007. Supercontinent cycles disrupted by strong mantle plumes. Geology 35 (9.), 847–850.

Trubitsyn, V.P., 2000. Principles of the tectonics of floating continents. Izvestiya Phys. Solid Earth 36 (9), 708–741.

Trubitsyn, V.P., Rykov, V.V., 2001. A numerical evolution model of interacting continents floating on a spherical Earth. Russ. J. Earth's Sci. (Electronic) 3 (2), (http://www.agu.org).

Trubitsyn V.P. 2004. Evolutionary Models of Floating Continents, Russ. J. Earth Sci. (electronic) 5(6), 31–322 (http://www.agu.org).

Trubitsyn V.P,. 2008. Seismic Tomography and Continental Drift Izvestiya, Physics of the Solid Earth, 2008, Vol. 44, No. 11, pp. 857–872. Pleiades Publishing, Ltd., 2008.).

Trubitsyn V., M. Kaban, M. Rothacher. Mechanical and thermal effects of floating continents on the global mantle convection. Physics of the Earth and Planetary Interiors 171 (2008) 313–322

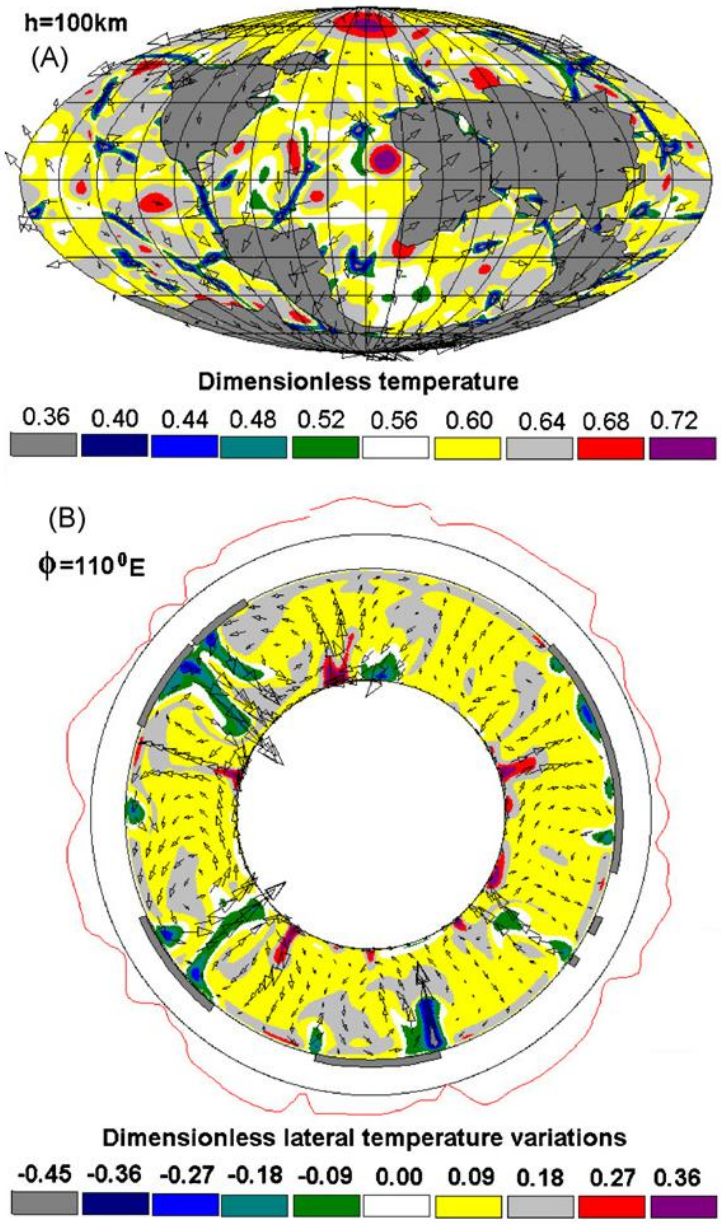

Fig.9.1.3. (A) Mantle convection pattern and positions of the continents at a time of 100Ma. Dimensionless temperature at a depth of 100 km is shown by color, dimensionless velocities—by arrows (maximal value $Vmax=2*10^3$). **(B)** The same for a sample cross-section. The red line around the sphere represents the calculated heat flux (grey, reference level).

9.2. A numerical experiment reproducing convection in the mantle with the generation and evolution of lithospheric plates

The results of a numerical experiment are presented for a layer of a heated viscid fluid similar to the matter of the Earth's mantle. The numerical solution of the equations of the mass, heat, and momentum conservation demonstrate that thermal convection with a high viscosity lithosphere developed in a layer of fluid with a temperature jump of 4000 K without any additional conditions. The modeling reveals that the mantle currents divide the lithosphere into a set of individual rigid plates limited by ridges and subduction zones. The plates submerge into the mantle, and their substance participates in the convective circulation. Plumes are periodically generated at the bottom of the mantle and ascend. The results of selfconsistent numerical experiment can be an experimental basis for the theory of the plate and plume tectonics on the Earth and make possible revealing new properties of the mantle convection.

Mantle was modeled by a layer of viscous liquid in a box with a size of 15000x 3000 km heated similarly to the heating of the Earth's mantle with the Rayleigh number equal to 10^7. The viscosity depends on temperature and pressure by diffusion creep and on stress by formula $\eta_\tau = \tau_y/e$. Here, e is the invariant of the deformation velocity tensor and τ_y is the critical value of the transition stress from creeping to plasticity. Stress τ_y can be called the effective strength of the lithosphere [*Moresi, Solomayov*, 1998; *Kneller et al.*, 2005].

For the effective lithosphere strength equals to τ_y=50 mPa plates appear with the sizes comparable with the thickness of the mantle [*Trubitsyn*, 2010]. The results for one of the moments of convection evolution are shown in the **Fig.9.2.1**. The calculated distribution of horizontal velocities at the mantle surface is shown in the upper part of the figure. The dependence of velocity on the horizontal distance appears piecewise constant. This means that rigid plates appeared, each of which moves as a whole with a velocity up to 10 cm/yr. The plates are numbered from 1 to 6. The plates at the junctions either converge and then submerge into the mantle (subduction zones) or diverge, and the matter from the mantle is entrained into them (oceanic ridges). The distribution of temperature in the mantle is shown in the lover part of the figure (the scale is shown on the right) together with the velocities of mantle flow with the scale of the arrow equal to 12 cm/yr. Cold plates descending in the subduction zones (dark blue, x=2800 km and x =12000 km) are sink deep in the mantle. Their negative buoyancy is the main driving force of convection. Near the ridge (x =7500 km) the plates are thinner and become thicker with the distance from this ridge. Red color shows the hot regions of the mantle. Some plumes are seen ascending from the bottom of the mantle at x=7000 km and x=135000-14300 km.

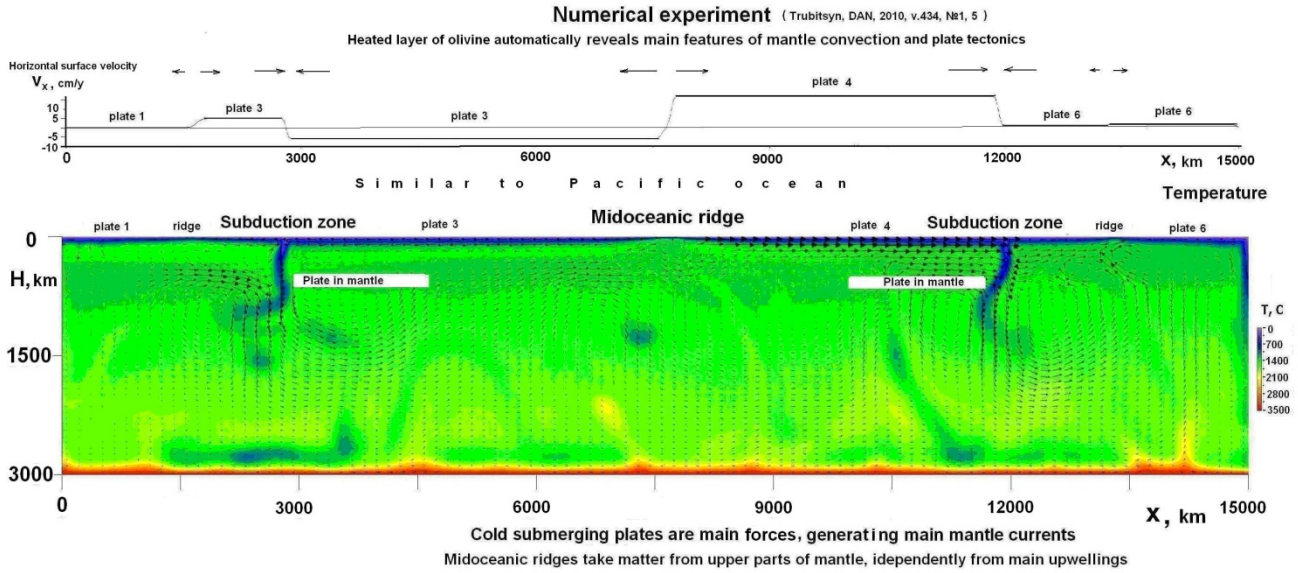

Fig.9.2.1. Calculated temperature and velocities of mantle flow for Ra=107 and for the effective lithosphere strength τ_y =50 mPa.

The distribution of viscosity is shown in **Fig.9.2.2** (the scale is on the left). The generated lithosphere has a viscosity up to 10^{25} Pa. Its mean thickness is approximately 40 km. It is clearly seen in the lithosphere that viscosity is lower in the ridges (owing to higher temperature) and in the subduction zones (owing to softening during the transition into the plastic state). It is also seen that the lithospheric plates of high viscosity (dark blue) are accumulated in the lower parts of the lower mantle. The numerical mathematical experiment is based on solution of the classical equations of energy, mass, and momentum conservation using verified methods; therefore, it can have the sense of a physical experiment. It is surprising that the variety of complex processes of plate and mantle plume tectonics in the Earth can appear only due to the simple heating of a homogeneous fluid layer, in which viscosity depends on the temperature, pressure, and stresses corresponding to the mantle substance without any additional special initial or boundary conditions.

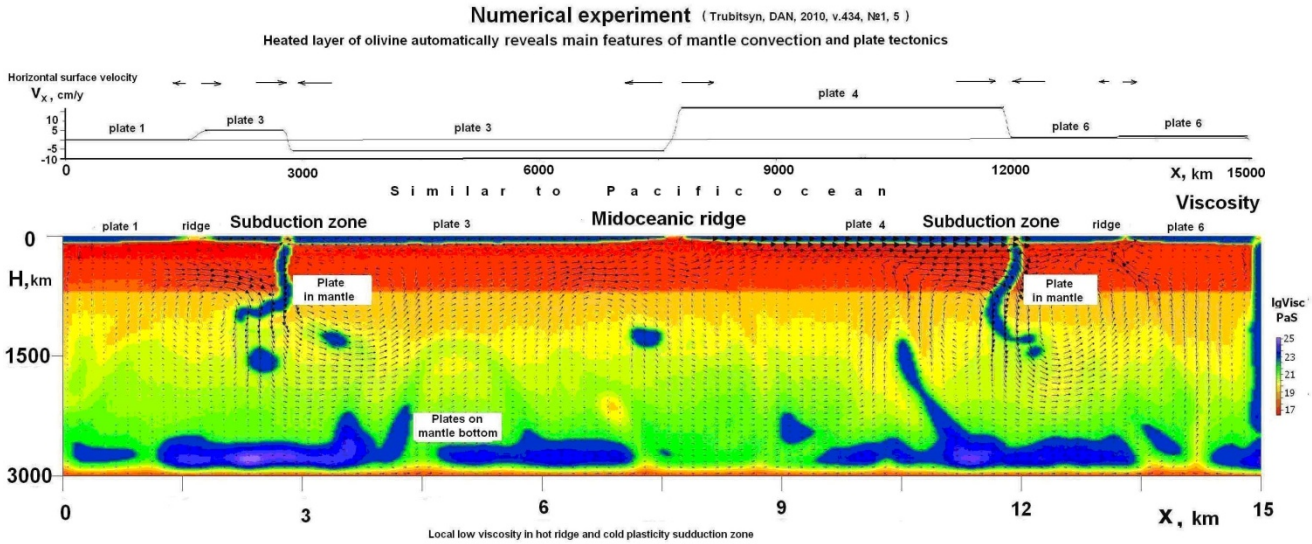

Fig.9.2.2. Calculated viscosity and velocities of mantle flow for Ra=107 and for the effective lithosphere strength τ_y =50 mPa.

References

Moresi L.N. and V. Solomatov. (1998), Geophys. J. Int. **133**, 669–682.
Kneller E., P. Keken, Sh. Karato, and J. Park. (2005), Earth Planet. Sci. Lett. **237**, 781–797.
Trubitsyn V.P., 2010. A Numerical Experiment Reproducing Convection in the Mantle with the Generation and Evolution of Lithospheric Plates, Plumes, and Superplumes, Doklady Earth Sciences, 2010, Vol. 434, Part 2, pp. 1370–1372. © Pleiades Publishing, Ltd., 2010.

10. Pattern Recognition Techniques in Geophysics

A. D. Gvishiani, gvi@wdcb.ru, **A. A. Soloviev, R. Sidorov, S. M. Agayan, S. R. Bogoutdinov.**
Geophysical Center RAS, str. Molodezhnaya, 3, 119296 Moscow, Russia.

Nowadays geophysics has to deal with great data arrays, and this corresponds to many directions of geophysical field data recording, processing and analysis. Modern software technologies developed by the leading research laboratories help to arrange, keep, process and study the registered data. Nevertheless there are some problems featuring lack of formalization, automatic data analysis and so on. A special problem concerns modeling an interpretation process in terms of human logic – this means to make an automated data interpretation process as close to the one performed by a human expert as possible. Geophysical Center RAS (GC RAS) has developed several algorithms using the fuzzy logic and discrete mathematical analysis techniques intended for automatic data analysis close to the positions of a human interpreter. Actual systems of detection of anomalies developed at GC RAS in 2007-2010 include Fuzzy Comparison Algorithm for Recognition of Signals (FCARS) [*Bogoutdinov et al.,* 2007; *Gvishiani et al.*, 2008a], Difference Recognition Algorithm for Signals (DRAS) [*Gvishiani et al.,* 2007], Fuzzy Logic Algorithm for Recognition of Signals (FLARS) [*Gvishiani et al.*, 2007], SP and SPs algorithms for recognition of spikes on time series [*Bogoutdinov et al.*, 2010]. A characteristic feature of these algorithms is a more comprehensive use of so-called fuzzy comparisons introduced by the authors [*Gvishiani et al.*, 2008b].

In investigating the data represented by time series, two successively solved problems are distinguished: the signal detection against the background of noise and recognition of abnormal fragments of the signal detected. In investigations connected with retrospective analysis and estimation of possible occurrence of various natural phenomena the initial information consists of observable time series of geophysical data. A new approach developed by the authors is oriented toward the investigation of anomalies (zones of increased activity). Here, an attempt is made to model discrete

analogues of fundamental concepts of mathematical analysis, for example, limit, continuity, smoothness, connectivity and monotony, extremum, inflection, convexity, etc. This give ground to use the term "discrete mathematical analysis" (DMA) in the substantiations of new algorithms constructed below. The starting point of this modeling is a sufficiently "soft" character of perception of discreteness properties by man. In fact, an experienced researcher, as a rule, efficiently clusterizes and detects thickenings and traces and finds anomalies in two- or three-dimensional arrays and in small-size time series. The objective of DMA is to extend the execution of these operations to higher dimensions and larger sizes of processed data. The technical basis of DMA consists of fuzzy mathematics and fuzzy logic that possess expressive capabilities for translation of human ideas and speculations into a formal computer language. **Fig.10.1** presents the scheme of our approach to the construction of DMA. The three upper blocks of the scheme are specific to the formal foundations of DMA and conclude with the definition of a finite limit. Note that, of course, we consider that the introduced definition of a finite limit is only one of possible definitions. The density construction based on it allows one to introduce a new interpretation of the concept of a thickening, a cluster, and a trace in multidimensional discrete spaces. To date, DMA has important geological-geophysical and geodynamic applications that include the investigation of anomalies in seismic, geoelectric, geomagnetic, and gravitational records, search for magnetic anomalies, monitoring of volcanoes, geodynamic applications, and geoecological investigations of places for possible radioactive waste disposal sites. At the same time, the sphere of applications of DMA is essentially wider. In particular, the algorithms described below can be used in analyzing time series of various natures.

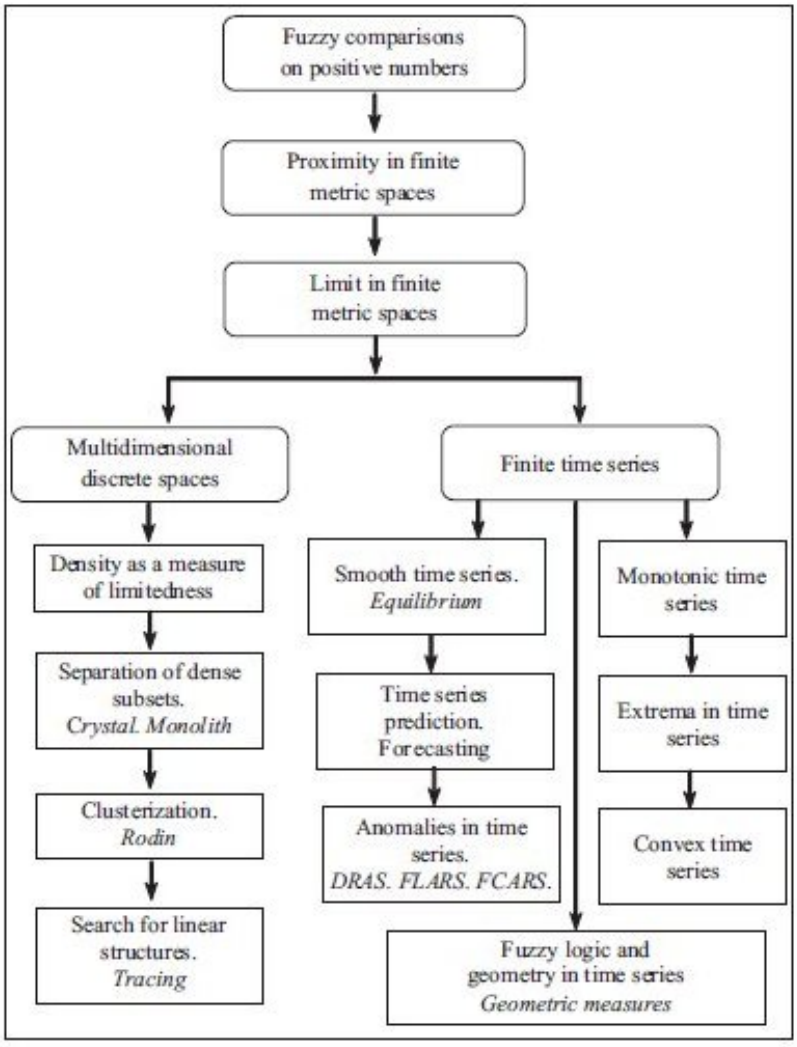

Fig.10.1. Scheme of construction of DMA.

Generally accepted algorithms of anomaly detection are mostly based on a combination of the statistical approach and the spectral-time analysis (STA). The latter is a method of statistical analysis designed for the study of frequency characteristics of a stationary random process with discrete time or a time series. The STA is based on a combination of diverse spectral, asymptotic, and functional techniques that is often strongly constrained by the physical essence of events studied and, for this reason, is fairly illustrative. Examples of commonly used algorithmic systems are: SESMO1 for real-time detection of short-period seismic anomalies; autoregressive moving average (ARMA) models based on the use of adaptive and matching filters; Maximum likelihood based on the use of maximum likelihood filters are difficult to be utilized for real-time detection of anomalies; Recognition with training which deals with STA analysis of known anomalies in a region of interest to construct a set of typical patterns with the following. comparison of them with the available patterns based on a coherence value specified for several levels of the signal intensity; and, finally, Neural networks approach which consists in the modeling of researcher's capabilities by means of a specially constructed neural network [*Gvishiani et al.*, 2007].

The DMA-based algorithms DRAS and FLARS [*Gvishiani et al.*, 2007] are an alternative approach to modeling of human reasoning and actions in search for anomalies. These algorithms yield estimates for boundaries of sought anomalies and subdivide them morphologically into initial, central, and final stages, identifying strong and weak phases in the central stage. The algorithms are rather versatile due to a wide set of "rectifications" arising in modeling interpreter's work. In a simplified form, work of an interpreter detecting an anomaly by visual inspection of a record is understood here as follows. Initially he looks over the record, estimating activity of its fragments in terms of positive numbers and mentally assigns the inferred numerical estimates to the fragments or their centers. Thus, the interpreter passes from the initial record to a nonnegative function that can be naturally called "rectification" of a record. Actually, larger values of this function (rectification) will correspond to record points that are more active from the standpoint of sought signals. Further, the interpreter searches for rises in the record rectification that correspond to the most active record fragments. Thus, the interpreter works at two levels, local (rectification of a record) and global (search for rises in the rectification).

An anomaly in a record (time series) is an ambiguous notion changing its form both from one record to another and within one record. Similarly to other intuitively clear mathematical notions (e.g., an element of a set), we do not attempt to give its strict definition. Anomalous nature is clear from examples given by experts. In terms of the DMA approach, a set of rectifications open for updating is applied for adequate modeling of "anomalies" (higher activity zones). The algorithmic implementation of this logic at a global level divides algorithms into the DRAS and FLARS families and enables differentiation between concrete implementations within each family [*Gvishiani et al.*, 2007].

The DRAS algorithm uses the strict definition of an anomaly in terms of the theory of fuzzy sets and includes a number of parameters enabling its adjustment to the recognition of different types of anomalies [*Bogoutdinov et al.*, 2007]. In DRAS, a record is first divided into background (quiet) and potentially anomalous (disturbed) parts. The interpreter's work can be divided into two stages. At the first stage, he successively inspects short segments of a record, assessing the anomalousness level of each segment. At the second stage, it examines the most active segments of the record and mentally clusters the identified active segments. Similarly, the DRAS algorithm has two levels, local and global. DRAS enables reliable recognition of anomalous segments of a record but is not capable of classifying them into different types. The discrimination between anomalies performed by an expert is time- and labor-consuming and cannot ensure complete uniformity in processing of large data sets due to significant factors both subjective (replacement of experts, involuntary changes in expert conceptions during continuous work, and so on) and objective (for example, lack of time).

Connected regions in the disturbed part serve as bases (platforms) of rises. Farther, DRAS identifies undoubtedly anomalous fragments on the platforms. Free parameters of DRAS are the rectifying functional and the following positive values: the local survey window, the vertical level of background, the global survey window and the horizontal level of background.

At the local level, a short record segment centered at a point t is considered for each time moment $t = kh$ and the initial record $y(t)$ is transformed to a positive function $\Phi_y(t)$ defined in the same time interval of the initial record under consideration. We call $\Phi_y(t)$ the rectification function for a record (time series) described by a discrete function $y = \{y_k = y\,(kh), k = 1, 2, 3, \ldots\}$. We may set $h = 1$ without loss of generality. We also introduce a local survey parameter (a natural number Δ). By the local survey fragment, we mean the following segment of the time series y centered at the point k:

$$\Delta^k y = \{y_{k-\Delta}, \ldots, y_{k+\Delta}\} \in \mathbb{R}^{2\Delta+1}$$

The rectification function $\Phi_y(k)$ of the record y is constructed with the help of a nonnegative (rectifying) functional Φ defined on the set of time series segments $\{\Delta^k y\}$ and converting anomalous segments of the time series into uplifted segments in the plot of the function $\Phi_y(k) = \Phi(\Delta^k y)$.

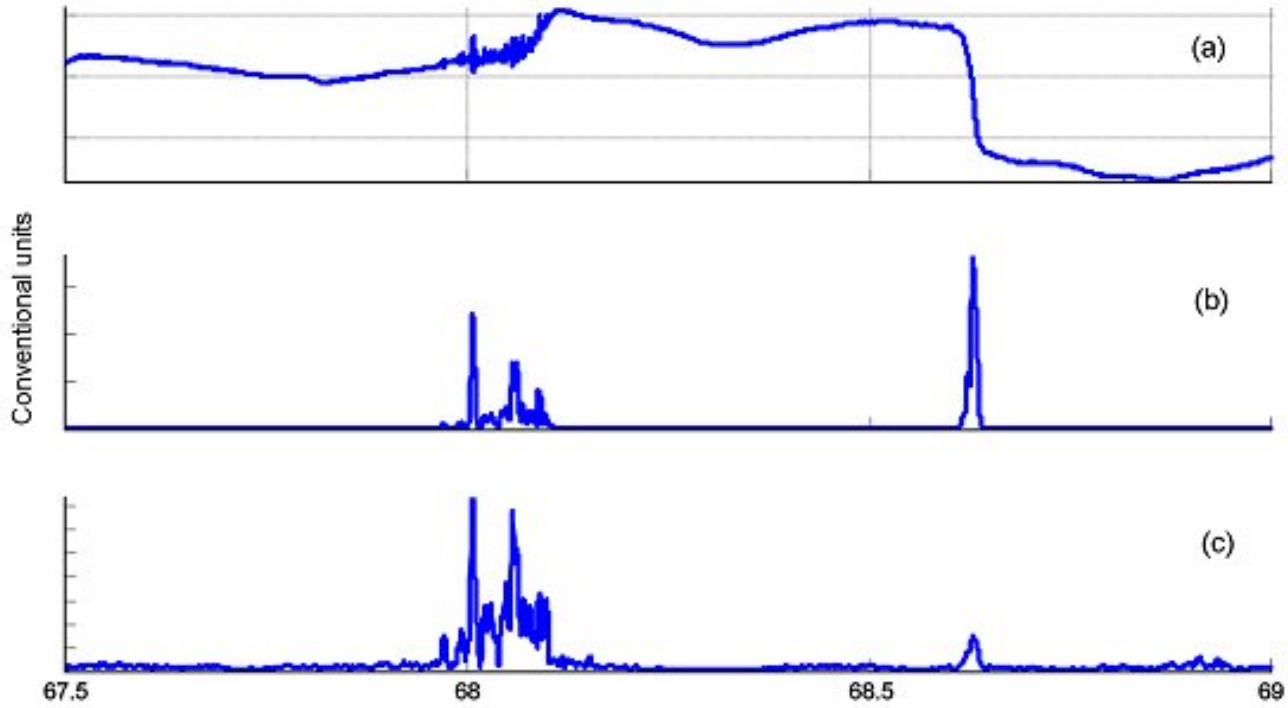

Fig.10.2. Rectification examples: (a) record of the electric self-potential near La Fournaise Volcano (Reunion Island, France; N–S DON station, 8–9 March 1998); (b) the same record rectified by the energy functional; (c) result of rectification by the length functional.

Depending on the concrete problem, the DRAS algorithm can use the length of the survey segment, the energy of the survey segment, or the deviation of the survey segment from its regression of the nth order as a rectifying functional. **Fig.10.2** shows an example of applying the rectifications at the segment of the E–W record obtained at the DON station over the period from March 8 to 9, 1988 (a), and its rectification with the help of the energy (b) and length (c) So it is clear that a rectification topography can be rather complex. The activity of anomalies cannot be invariably high and they can be inhomogeneities (activity intervals are several and they are divided by "quiet" points). The corresponding rectification intervals are oscillating rises. "Uplifts" in rectification time intervals where values of $\Phi_y(t)$ are sufficiently large compared to the remaining segments of the series are sought at a global level. At the global level, the graph of the rectification function can be really complicated and, therefore, the analysis of the ordinates $\Phi_y(t)$ is insufficient by itself to recognize the «hills»; anomalies may indeed have high ordinates but short durations, active segments may be separated by short calm intervals (in the last case the rectification function has the appearance of oscillating hills. Taking these observations into account, DRAS explores the problem at the global level in two steps. In the first step the record $y(t)$ is represented as a union of background (calm) and potentially anomalous parts. In the

second step, the algorithm applies a procedure which searches for real anomalous fragments inside the potentially anomalous part of the record. The basic role in this process is played by the introduction of left and right measures, $L\Phi_y(t)$ and $R\Phi_y(t)$. These measures are interpreted in DRAS as membership functions of the fuzzy set of sufficiently calm (non-anomalous) points of the initial time series $y(t)$ More specifically, the fuzzy membership functions $L\Phi_y(t)$ and $R\Phi_y(t)$ characterize how much calm a recording is on the left side and on the right side of a point t. The difference $D\Phi_y(t)$ and $R\Phi_y(t)= L\Phi_y(t) - R\Phi_y(t)$ appears to be a crucial parameter to discriminate a genuine anomalous point t among the potentially ones. As a result of DRAS application, the domain of definition of the time series $y(t)$ is represented as the union of three sets of points t. The first set contains calm (non-anomalous) points, the second set contains potentially anomalous points, and the third set contains really anomalous points.

Free parameters of DRAS are the rectifying functional and the following positive values: the local survey window $\Delta \ll |T|$, the vertical level of background α, the global survey window $\Lambda > \Delta$, and the horizontal level of background $\beta \in [0.5, 1]$ [*Gvishiani et al.,* 2007].

As an example of application of DRAS for geophysical data processing, we address the recognition of electrotelluric (ET) anomalies during the monitoring of the La Fournaise Volcano. Time series of self-potential (SP) activity periods from the DON station record were obtained from March 15, 1997, to December 31, 1998. The DON record segment from April 25 through June 13, 1997, is presented in **Fig.10.3**. The activity periods recognized by the DRAS algorithm can be divided into two groups: (1) periods containing intense high frequency oscillations with a relatively small amplitude (up to 100 mV/km over a few minutes) and (2) periods representing high amplitude jumps and transitions (up to 1000 mV/km or more over tens of minutes). Showers disturb the electric field, and therefore, we may assume that these two groups of activity periods had different origins and that anomalies of the second group were probably caused by rains. Using the available daily pluviometric data, we repeated the analysis only for those days when precipitation did not exceed 10 mm (**Fig.10.3b, 10.3c**) because it is believed that rainfalls below this threshold do not affect the record. After the removal of rainy days, the record fragments were connected by linear segments.

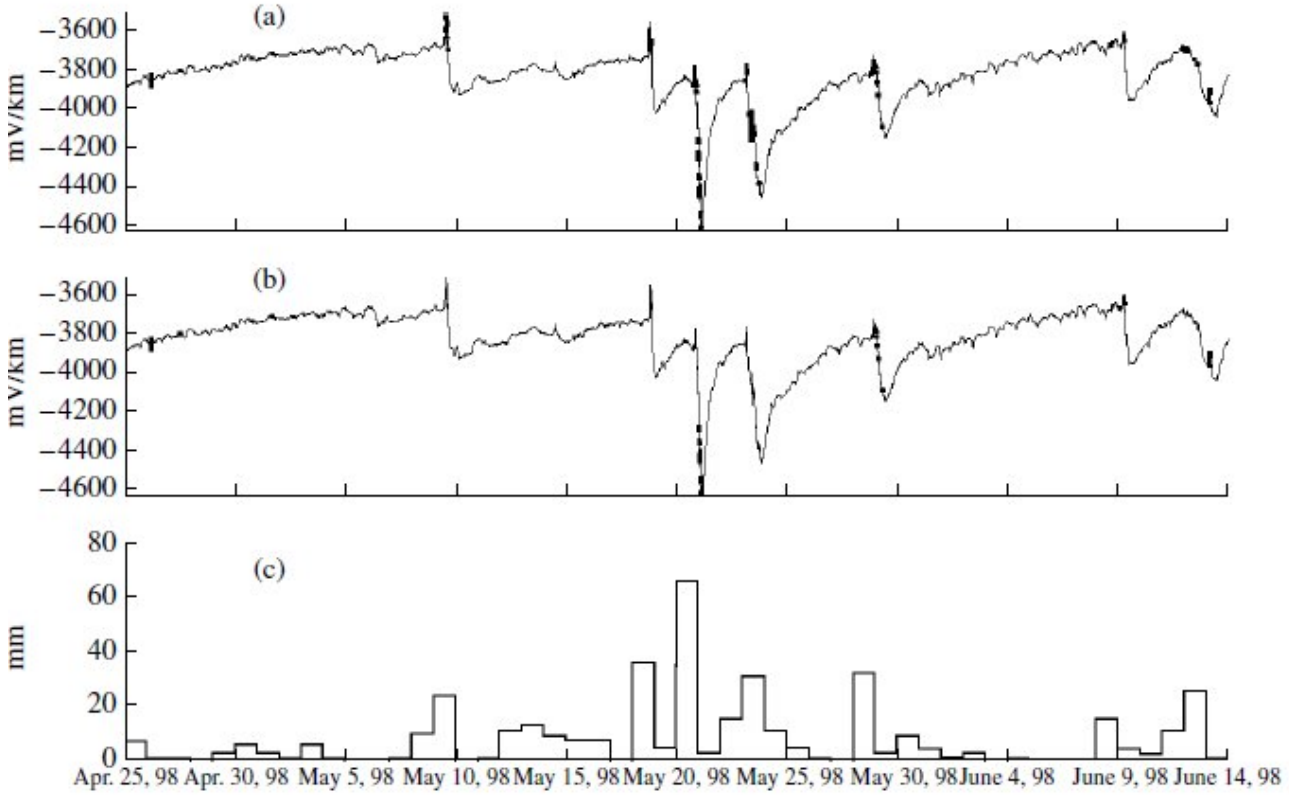

Fig.10.3. Anomalies recognized in an E–W record segment obtained at the DON station from April 25 to June 13, 1998: (a) with regardfor rainy days; (b) without rainy days; (c) precipitation level.

The DRAS analysis of the modified record did not reveal high amplitude jumps and transitions, which means that the latter occur on rainy days. On the contrary, the majority of anomalies represented by low amplitude high frequency oscillations were preserved and even new (weaker) anomalies were resolved. This is a weighty argument in favor of the relation between these signals and precipitation. Two types of SP anomalies are encountered most often in the analysis of time series of ET data: anomalies of the first type have high amplitudes (a few tens of mV/km) and are morphologically represented by a rapid decrease in a signal with its subsequent recovery. These anomalies generally occur synchronously at a few stations. Anomalies of the second type have smaller amplitudes and higher frequencies and can be recorded by one or several stations. In the latter case, they have a phase delay depending on the station. The analysis of the occurrence conditions of the two types of anomalies showed that anomalies of the first type are generally caused by heavy precipitation, while anomalies of the second type are associated with hydrothermal and volcanic activity. These two types of anomalies do not exhaust the possible diversity of anomalous ET signals. Therefore, the algorithm proposed for signal recognition must be easily adjustable to the detection of signals of various morphologies [*Bogoutdinov et al.*, 2007]. As it was shown, there could be successful DRAS applications for different tasks of electromagnetic and seismic monitoring or for any tasks featuring time series of geophysical data.

As distinct from DRAS, the FLARS algorithm first identifies significantly anomalous intervals and then the set of these intervals is supplemented with potentially anomalous intervals, thereby forming an "aureole" of an identified anomaly. Thus, FLARS divides, in two stages, the recording interval into three subsets ($T = A \cup P \cup B$) denoted as follows: A, anomalous points; B, quiet background points located sufficiently far from the anomaly; and P, potentially anomalous, disturbed points covering a rather long interval. FLARS forms the set of anomalous points A, using the search for extreme values on a Φ_y topography with the help of a fuzzy extremality measure $\mu(k)$ taking values from the interval $-1 \leq \mu(k) \leq 1$. The measure is constructed on Φ_y on the basis of fuzzy comparisons and the vertical extremality level $\tau \in [-1,1]$. Free parameters of FLARS are the rectifying functional and the following positive values: the local survey window, global survey window and vertical level of extremality [*Gvishiani et al.*, 2007].

Like DRAS and FLARS, FCARS uses at a local level the rectification procedure. At a global level, the FCARS search for oscillating rises in a rectification can be described as follows. Significant vertical spikes are first detected in the rectification. Their fairly dense clusters and adjacent features are of interest. Points lying inside such clusters are considered as anomalous without regard for values taken by the rectifying function at these points. Small rectification values at these points can imply only a short-term weakening of a signal due to its inhomogeneity. Such points form central parts of rises in accordance with clusters of the aforementioned vertical spikes.

Points lying to the left and to the right of the dense clusters can be of two types: these are either quiet, background points near a given cluster or disturbed points of the record that are not necessarily extremal in the rectification and form the initial and final stages of the signal. Bases of the anomalies are connected sets in the initial recording interval that consist of points extremally horizontally close to vertically extremal points of the rectification. Precisely this definition of a rise serves as a basis for the FCARS global level. FCARS modeling is based on fuzzy comparisons and monolithicity. Fuzzy comparisons are instrumental to a correct formulation of the notion of vertically extremal spikes in a rectification. The degree of extremal horizontal proximity to the spikes is described in terms of proximity measures. Further, likewise with the help of fuzzy comparisons, the shell of the rise (anomaly) base is formed by filling gaps in dense clusters of vertically anomalous spikes with horizontally extremal points.

In case of vertical subdivision, the vertical measure of anomalousness $\mu^v(k) \in [-1, 1]$ at the point k is defined as a fuzzy comparison of $\mathrm{Im}\Phi_y$ with the rectification value at this point:

$$\mu^v(k) = n\left(\mathrm{Im}\Phi_y, \Phi_y(k)\right),$$

where *n* is the binary, gravitational, or τ--extension of the fuzzy comparison $n_{\gamma,\nu}(a,b)$ [*Gvishiani et al.*, 2007; *Gvishiani et al.*, 2008b].

Let α_s (α_w) be the strong (weak) level of extremality with respect to the modulus of $\mathrm{Im}\Phi_y$, that is α_s (α_w) is the solution of the equation $n\left(\mathrm{Im}\Phi_{y,}\alpha_s\right) = 1/2$ ($n\left(\mathrm{Im}\Phi_{y,}\alpha_w\right) = 0$).

Here we have to introduce the definitions of types of points.

1. Point k is of the vertically background type if $\mu^v(k) < 0 \Leftrightarrow \Phi_y(k) < \alpha_w$.

2. Point k is vertically anomalous if $\mu^v(k) \geq 1/2 \Leftrightarrow \Phi_y(k) \geq \alpha_s$.

3. Point *k* is vertically potentially anomalous if $\mu^v(k) \in [0,\frac{1}{2}) \Leftrightarrow \Phi_y(k) \in [\alpha_{w,}\alpha_s)$.

Let *vB*, *vA*, and *vP*, denote respective sets of vertically background, vertically anomalous, and vertically potentially anomalous points. Then the recording period under consideration can be represented as T = *vB* + *vA* + *vP*.

For performing a horizontal subdivision, we introduce the left and right measures of proximity to the vertically anomalous subset *vA* in the model of local survey $\delta_k\left(\bar{k}\right) = \frac{\Delta+h-h|\bar{k}-k|}{\Delta+h}$ of a fragment $\Delta^k y$. For any $k \in T$, fuzzy disjunction $\mu_{vA}(k) = \max\left(L_{vA}\Phi_y(k), R_{vA}\Phi_y(k)\right)$ will be a measure of the concentration of vertically anomalous points from *vA* around it. Let β be its weakly maximal level: β is the solution of equation $n(\mathrm{Im}(\mu_{vA}),\beta) = 0$. Now we are to make a similar definition of horizontal anomality levels. Point *k* is horizontally anomalous if $\mu_{vA}(k) \geq \beta$, potentially anomalous if $\mu_{vA}(k) < \beta$ and $\mu_{vA+vP}(k) \geq \beta$ and background if $\mu_{vA+vP}(k) < \beta$. Horizontal division is the following: $T = hB + hA + hP$.

The further actions of the FCARS algorithm include final division of a record *y* into three types of points using the results of vertical and horizontal subdivisions.

As distinct from DRAS, the FLARS algorithm first identifies significantly anomalous intervals and then the set of these intervals is supplemented with potentially anomalous intervals [*Gvishiani et al.*, 2007]. The FCARS algorithm is successfully applied for the recognition of anomalies in geophysical records of various natures along with algorithms FLARS and DRAS.

The choice of the specific algorithm depends on the type of observed geophysical fields and a priori form of the sought anomalous intervals of records. In this case, FCARS is the most adaptive algorithm among those listed above. The algorithms of artificial intelligence developed by the authors of this article are the basis of an automated system for processing electrotelluric and electromagnetic observations of the Russian–French project of monitoring volcanic activity in Kamchatka [*Gvishiani et al.*, 2008a] and on Reunion Island, where the recognized anomalies accompany the eruption of La Fournaise Volcano on March 9, 1998. This eruption confirms the fact that redistribution of liquid fluids owing to the generation and manifestation of volcanic activity necessarily leads to variations in the natural potential of telluric currents.

Fig.10.4 illustrates the results of applying the FCARS algorithm to a seismic signal: background zones are shown in blue, potentially anomalous zones are green, and anomalous parts of the record are red. The testing of FCARS on seismic data proves that the technique of anomaly recognition with this algorithm appears to be very helpful in seismic data processing. This refers not only to seismic activity monitoring. As it is known, exploration seismology (seismic survey) deals with great data sets, so a possible application of the FCARS algorithm could be useful during the stage of seismic signal processing and can improve the quality of the processed data. It also can be used in some special tasks of interpretation of common depth point (CDP) seismic data, such as the "bright spot" technique, attribute analysis and similar tasks in which the way of anomaly detection depends mainly on human interpreter's logic and experience.

Automated systems of pattern recognition at time series which have been developed at the GC RAS find their specialized applications in different issues of geophysical data processing.

The algorithms *SP* and *SPs* were designed for detection of artificial disturbances on the magnetic field records provided by the worldwide International Real-time Magnetic Observatory Network (INTERMAGNET). The recording instruments of the INTERMAGNET observatories are

subject to external effects that affect the quality of the records. These anomalies (artifacts) generally arise for the following reasons:

1. natural phenomena;
2. anthropogenic phenomena, including displacements of large volumes of metal;
3. calibration of the measuring instrument;
4. distortion of data during their transfer from observatories to information nodes via the Internet.

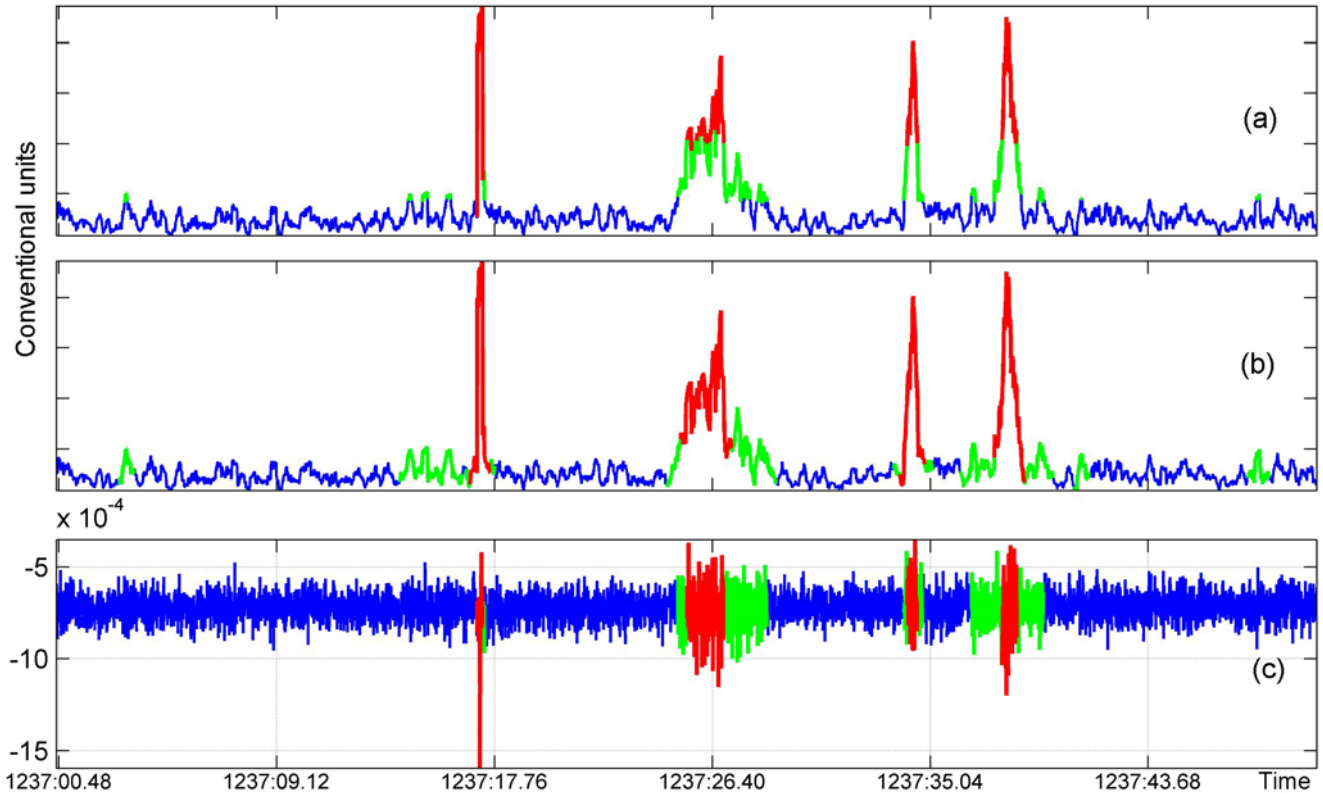

Fig.10.4. FCARS processing of a seismic record (2 June 2006): (a) vertical subdivision of the record; (b) horizontal subdivision of the record; (c) identification of the beginning and end of the anomaly.

Natural phenomena primarily include thunderstorms which induce electric currents inside the Earth and cause transient changes of the natural behavior of the Earth's magnetic field. Examples of natural phenomena include pulsations of magnetic field caused by solar activity. Anthropogenic phenomena occur due to the proximity of large cities, airports, railways, and power lines. An important aspect of spike recognition is the fact that manual (visual) spike identification is not only laborious but also often not objective. Indeed, in the manual processing of large information arrays, the approach taken by an expert necessarily changes with time, directly affecting its objectivity. Tiredness or external impacts may be a reason for an expert to miss the desired events or interpret differently analogous potential anomalies at different processing times.

Based on the task to be solved, the created algorithm is called SPIKE (*SP*); it substantially alleviates the subjectivity of manual processing. It is suited for automated and uniform spike identification in any large arrays of time series, such as in INTERMAGNET databases or magnetogram archives of worldwide data centers. The accumulated experience, skills, and knowledge of experts appear to be incorporated into the algorithm at the learning stage. The *SP* algorithm should not be considered as merely applicable for recognition of anthropogenic errors on magnetograms. By applying the *SP* algorithm to spike-free records, we proceed to the recognition of physical time anomalies, i.e., pulsations. Spikes of a particular origin are characterized by a specific morphology.

A spike is considered as a chain of interrelated singular record fragments representing disturbances that are substantial vertically and insignificant horizontally and that do not lead to a shift of the recording level. In analogy with other algorithms mentioned in [*Gvishiani et al.,* 2008a,b], the

algorithm for spike recognition in the record constructed here has two levels. The local level procedures identify singular fragments, and global level procedures analyze singular fragment combinations for the presence of a shift in the recording level.

A record (a magnetogram) will be interpreted as a time series $y = \{y_t = y(t)\}$, specified on the segment (recording period) T of the discrete halfaxis $R_h^+ = \{t = kh, h > 0, k = 1, 2, \ldots\}$, where h is the discretization step and k is the observation node. Without loss of generality, we let $h = 1$.

At the local level a singular fragment on the record $y = y(t)$ is a record disturbance, significant in the vertical direction (singular in value) and insignificant in the horizontal direction (singular in time and shortterm). Examples of elementary dynamics are shown in **Fig.10.5**. Since the dynamics are transient horizontally and singular vertically, the segment will necessarily contain points with derivatives that are significant in absolute value. Using the horizontal parameter $\Delta \in R_h^+$, fuzzy comparison n, and two (very large α and considerable β) vertical singularity levels, we formalized the notion of singular fragment (elementary dynamics) d_t on the $y(t)$ record. A local level final is the set of elementary dynamics $\{d_t,\ t \in \boldsymbol{A}\}$. Precisely these, at the global level, will in sum lead to spikes [*Bogoutdinov et al.*, 2010].

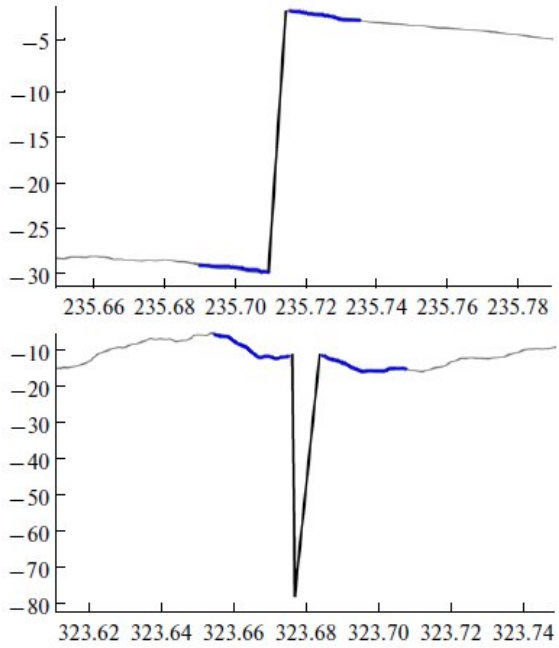

Fig.10.5. Examples of singular harmonics (shown in black) with the $\Lambda^-(s)$ and $\Lambda^+(s)$ sets (shown in blue). The bottom harmonic is a spike according to our definition.

At the global level we define the spike s on $y(t)$ as a chain of quite closely lying elementary dynamics d_k that do not lead to a shift of the base level $y(t)$. One more parameter $\Lambda \in R_h^+$ is a parameter of sufficient closeness of the dynamics d_k in the spike s: $\Lambda > \Delta$, with Δ and Λ being the results of the preliminary analysis at the learning stage. The spike s is defined by the union $\cup_{k=k*}^{k**} d_k: |e_k - b_{k+1}| \le \Lambda, k = k*, \ldots, k** - 1$ and represents a fragment of the $y(t)$ record, starting at b_{k*} and ending at e_{k**}: $s = y|_{[b_{k*}, e_{k**}]}$.

We will now define the wings $\Lambda^-(s)$ and $\Lambda^+(s)$ of the spike. They will help to express the singularity of the vertical spike at the global level, thereby completing the formalization of s. We let $\Lambda^-(s) = y|_{[b_{k*}, -\Lambda, b_{k*}]}$, $\Lambda^+(s) = y|_{[e_{k**},\ e_{k**}+\Lambda]}$. The fact that the spike preserves the base level of the $y(t)$ record means that the record is quiet at the union of $\Lambda^-(s)$ and $\Lambda^+(s)$ in comparison with s which is formalized with the fuzzy comparison n. **Fig.10.5** illustrates the $\Lambda^-(s)$ and $\Lambda^+(s)$ sets location.

So, as follows from a mathematical description, a specific implementation of the *SP* algorithm is determined by the choice of the following free parameters: $\Delta \in R_h^+$ is a parameter of survey of the dynamics, $\Delta \in \Lambda > \Delta$ is a parameter of the sufficient closeness of the dynamics, $\alpha \in [0.75, 1]$ is the level of extreme oscillation, $\beta \in [0.5, 1]$ is the level of a significant derivative. Every set of free

parameters will be denoted through $\pi = (\Delta, \Lambda, \alpha, \beta)$, and their totality through $P \subset R^4$. Thus, the *SP* algorithm, constructed in the framework of the introduced mathematical model, makes a uniform formalized spike identification on time series of an arbitrary nature.

The *SP* algorithm was studied at four of the above mentioned levels using 25 magnetograms recorded at 7 INTERMAGNET observatories (*BNG, BOU, DOU, FRD, GUA, HRN, MMB*) in the period January 1 – December 31, 2007 [*Bogoutdinov et al.*, 2010]. The magnetograms represent the preliminary data records. As the data resolution is 1 minute per sample, the length of each magnetogram is 525 600 points of digital recording on the time axis. The chosen observatories are located at different latitudes of the northern hemisphere and so they are representative from the viewpoint of the nature of the recorded data.

The internal exam consists of applying the optimal *SP* algorithms directly to the fragments of the learning sample. The corresponding *SP* algorithm, which was applied to 25 selected magnetograms, had identified 290 events, only 275 of which were expert-identified spike events. **Fig.10.6** represents the examples of spike identification, and **Fig.10.7** displays typical examples of spikes. Type 1 errors are absent. Thus, the probability of missing an event (type 1 errors) is 0.0 in this case, and the probability of a false alarm (type 2 errors) is as small as 0.055. **Fig.10.8** displays examples of false alarms.

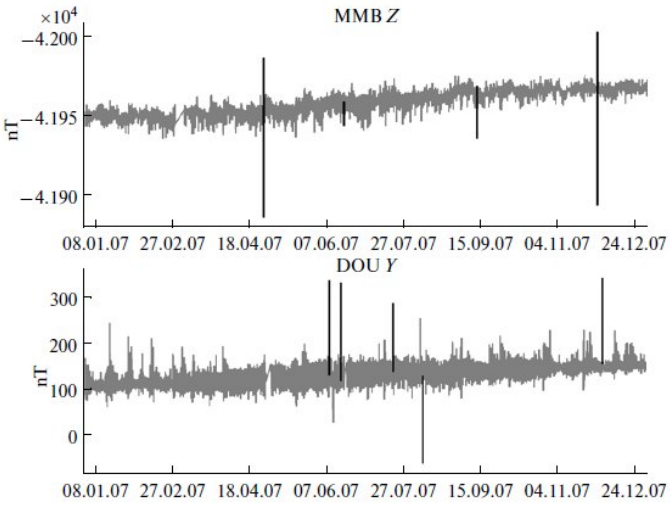

Fig.10.6. Examples of spike identification (shown in black) at the INTERMAGNET observatories.

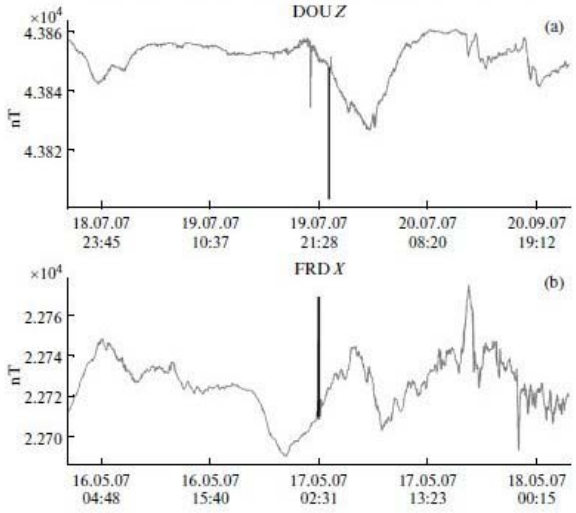

Fig.10.7. Examples of characteristic spikes.

The external (independent) exam consisted of applying the optimal *SP* algorithms directly to the records not belonging to the learning sample. These results of the independent exam of the *SP* algorithm should be considered highly successful [*Bogoutdinov et al.*, 2007]. As the observatories chosen for the *SP* learning are located in very diverse parts of the globe and at different distances from the magnetic poles, the initial data are sufficiently representative and allow us to conclude from the results of the internal and external exams on the reliability of the created formalized method of spike recognition on the magnetograms.

The *SP* algorithm is constructed using the methods of fuzzy logics and, as such, is notably adaptive and universal. It can be used for spike recognition on time series of any nature. The specifics and morphology of the data will be translated into the learning results (the values of free parameters).

There are seemingly two reasons why, at this research stage, the *SP* algorithm should be used in a semi-automated mode, i.e., in parallel with the work of experts. First, there are difficult spike events, unrecognizable by this *SP* algorithm version. For instance, they exist among the spikes with an amplitude less than 30 nT (**Fig.10.7a**). Second, the use of *SP* in such a mode favors the accumulation of statistics necessary for thoroughly estimating the reliability of the results of *SP* algorithm runs and the possibility of passing to automatic spike recognition.

The algorithm *SPs,* created as a modification of *SP* for the spike recognition at magnetograms of 1-second resolution, consists of three blocks: "Λ-analysis", "Construction of quasi-spikes" and "Selection of spikes". Initial record y is assumed to be given on an interval of discrete positive semiaxis.

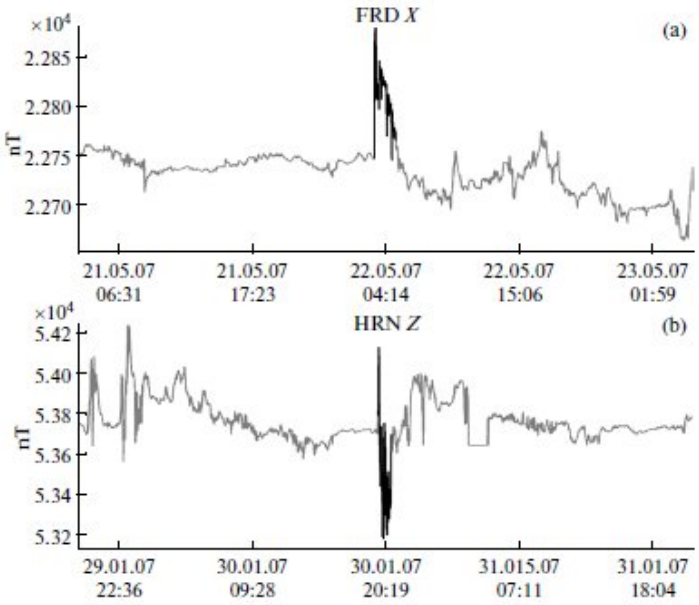

Fig.10.8. Examples of false alarms.

"Λ-analysis". While searching for spikes we have to distinguish between calm and sharp fragments on a record y. In turn, sharp fragments need a further classification for increasing and decreasing ones. Indeed, spikes are surrounded by calm fragments, or its wings, and represent combinations of either sharp increases and decreases, or sharp decreases and increases. Calm, energy, increase and decrease have to be defined in the most general, stochastic situation, since a nature of a record y is quite arbitrary. For classifications in the *SPs* algorithm we use linear regression. It allows solving these tasks simply and effectively by its angular coefficient: the sign is responsible for increase and decrease, and the module is responsible for calm and sharpness.

"Construction of quasi-spikes". We illustrate this block by an example of a positive quasi-spike (for a negative one the description is analogous). Let us clarify its definition: a fragment $S = y|_{[c,d]}$ on a record y is a positive quasi-spike, if inside $[c,d]$ there is a point $t = t(S)$ (a top of S), which divides S into sharply increasing left part $S^l = y|_{[c,t]}$ and sharply decreasing right part $S^r = y|_{[t,d]}$.

The algorithm *SPs* starts searching for a positive quasi-spike with its top at point t. As a top it naturally chooses this or that maximum on y. Then, by selecting sharp increasing fragments, the algorithm builds a left slope of a quasi-spike ending at a point t. From the right side, starting with a point t, the algorithm builds a right slope of a quasi-spike from sharp decreasing fragments. Thus, the block "Constriction of quasi-spikes" uses "increase-decrease" and "sharpness" classification results of Λ-analysis and constructs quasi-spikes starting from their tops and continuing in both directions along their left and right parts.

"Selection of spikes". The last task is to distinguish spikes among quasi-spikes. The selection logic has been already mentioned above: spikes should be accompanied with calm wings. In the algorithm *SPs* they are defined adaptively: for a quasi-spike its left wing has the same length as a quasi-spike's left slope. In the same way a quasi-spike's right wing has the same length as its right slope. A wing of a quasi-spike is considered to be calm, if it can be represented as a union of calm

fragments. Thus, the block "Selection of spikes" uses the last result of Λ-analysis, namely "calm" classification. Calm wings make quasi-spike a spike.

The analysis of difficult recognition cases makes us optimistic that the *SP* algorithm can be further modified to identify all spikes recognized by experts including those whose amplitude is less than 30 nT, while at the same time discarding the false alarm spikes. Moreover, the *SP* algorithm may facilitate a more detailed analysis regarding the presence of low-amplitude pulsations on the magnetograms. After being properly updated, the *SP* algorithm can be recommended for use at regional INTERMAGNET Geomagnetic Information Nodes (GINs). The implementation of the system of automatic data quality control will render the filtering process more objective and universal in character and, thereby, will improve our understanding of the magnetic field of the Earth.

The *SPs* algorithm was tested on raw one-second data acquired at the Easter Island magnetic observatory in July 2009. Each 1-day 1-channel record registered with 1 Hz frequency consists of 86 400 points of registration. Once the free parameters were fixed, we tested the algorithm by applying it to the second part of the testing dataset, from 21 to 31 July 2009.

The blind test of the *SPs* algorithm involved data recorded from 1 to 31 August 2009 with no *a priori* expert opinion. The results of the recognition by the algorithm $SPm = SPm(\pi^*)$ were evaluated by data experts from the Easter Island magnetic observatory. The evaluation details are given in **Tables 10.1, 10.2**. The probability of missed targets for *X* component is 3.72%, that of false alarms is 0.68%, to be compared with 5.9% of missed targets and 6.0% of false alarms for the 21/07-31/07 time interval. It confirms that the algorithm is able to detect most of the spikes, and shows that there is some variability from one day/week/month to the next.

Table 10.1. Results of external exam of the *SP*(Π, Ω) algorithm, obtained in the case of learning at the global level.

Observatory	Component	Expert-identified spikes	*SP*-identified events	Type 1 error (missed target)	Type 2 error (false alarms)
BOU	*X*	7	7	0	0
	Y	6	6	0	0
	Z	10	10	0	0
	F	7	7	0	0
DOU	*X*	9	9	0	0
	Y	15	15	0	0
	Z	12	11	1	0
GUA	*X*	3	4	0	1
	Y	3	4	0	1
	Z	3	4	0	1
	F	19	19	0	0
HRN	*X*	0	0	0	0
	Y	0	3	0	3
	Z	0	3	0	3
MMB	*X*	1	1	0	0
	Y	1	1	0	0
	Z	6	6	0	0
Total		102	110	1	9

So, the fuzzy logic algorithms applications for disturbance detection show good results at processing geomagnetic data of 1-minute and 1-second resolution. Involving these techniques into preliminary data studying at INTERMAGNET observatories will certainly improve their productivity and will be a helpful tool for the interpreters.

One of the recent developments of DMA techniques in application to geophysical data processing is a new approach to the smoothing procedure - the so-called gravitational smoothing method.

Table 10.2. Results of application of the algorithms $SPs(\pi_X^*)$, $SPs(\pi_Y^*)$, $SPs(\pi_Z^*)$ and $SPs(\pi_F^*)$ to the records obtained from 1 to 31 August 2009 and their assessment by experts.

Channel	Spikes recognized by experts	Events recognized by the algorithm	Missed spikes	Extra events	Probability of an error of the 1st kind	Probability of an error of the 2nd kind	Quality criterion $K_{0.8}$
X	2122	2057	79	14	0.0372	0.0068	0.031
Y	2143	2150	23	30	0.0107	0.0140	0.011
Z	1786	1780	104	98	0.0582	0.0551	0.058
F	1963	1996	39	72	0.0199	0.0361	0.023

Let us define a space of time series *BP*[*a,b*] on a discrete interval [*a,b*]. For a time series $y \in BP[a,b]$ there is a task of building of its smoothing.

Let z be a series of *BP*[*a,b*]. The approximation is formed by a RMS fuctional $Sc(z \mid y) = \| z - y \|^2$ and smoothness is formed by an nonnegative quadratic form *CGr*(*z*) which will be called a residual of gravitational smoothing. The less are the values of *Sc*(*z*|*y*) and *CGr*(*z*), the more is the reason to consider *z* as a smoothing of *y*. Thus a constituent and synchronic minimization of *Sc*(*z*|*y*) and *CGr*(*z*) functionals required, so their nontrivial convex combination is as following:

$$SM_\lambda(z|y) = \lambda CGr(z) + (1-\lambda)Sc(z|y), \lambda \in (0,1),$$

and the search for a smoothing *x* = *Sm y* is equivalent to the minimization of $SM_\lambda(z|y)$ on *BP*[*a,b*] with a suitable value of $\lambda \in (0,1)$. So, in terms of a smoothing *Sm y* a group of smoothings $\{Sm_\lambda y, \lambda \in (0,1)\}$ appears. For calculating a gradient, first we introduce an nonnegative at *BP*[*a,b*] *Gr* operator producing a residual of a gravitational smoothness *CGr*(*z*) = (*Gr z, z*). Briefly, the result is:

$$x = Sm_\lambda y \Leftrightarrow (\lambda Gr + (1-\lambda)E)x = (1-\lambda)y.$$

If $\lambda \in (0,1)$ then the $\lambda Gr + (1-\lambda)E$ operator is positive at *BP*[*a,b*], and thus, it is invertible. Hence, a smoothing $x = Sm_\lambda y$ always exists; is defined in a unique way for any $y \in BP[a,b]$; and is a result of application of an operator $(1-\lambda)(\lambda Gr + (1-\lambda)E^{-1}$.

The residual of smoothness is based on a particular feature of a continuous function which has a discrete definition. In terms of DMA a deviation of this feature by a time series *x* must be described with a quadratic form (*Gx, x*) as a zero residual level [*Agayan*, 2009].

An operator of discrete continuity is a result of a discrete interpretation of a mathematical continuity definition. To define continuity in terms of DMA we should introduce a model of survey in a point.

The nearness $\delta \leftrightarrow(\delta_i(j))$: $\delta_i(j)$, a fuzzy structure on the interval [*a,b*], is a nearness measure point t_j to point t_i at an interval [*a,b*]. $\delta_{t_k}(t_j)$ is a level of closeness of a point t_j to a point t_k on [*a, b*]. It is always true that $\delta_{t_k}(t_j) \in [0,1]$ and that $\delta_{t_k}(t_k) = 1$.

Now we connect a square matrix of *n*th order to δ: $A = A(\delta) = (a_{ij}) \in Mat(n)$, $a_{ij} = \frac{\delta_i(j)}{\sum_{k=1}^n \delta_i(j)}$. Then a discrete formula for a gravitational smoothing of a series *x* in its sample t_i is an equality $x_i = \sum_{j=1}^n a_{ij}\, x_j$, and its deviation *CGr*(*x*)(t_i) is to be considered as a gravitational continuity residual of *x* in t_i: $CGr(x)(t_i) = (x_i - \sum_{j=1}^n a_{ij}\, x_j)^2$.

Examples of the application of this smoothing technique are shown at **Fig.10.9–10.11**. At **Fig.10.9** there is a comparison of a gravitational smoothing result of an input signal with a wavelet smoothing of this signal (6th order Dobeshi's wavelet). According to [*Agayan*, 2009], the gravitational smoothing procedure produces a closer approximation but wavelet smoothing is easier for calculation.

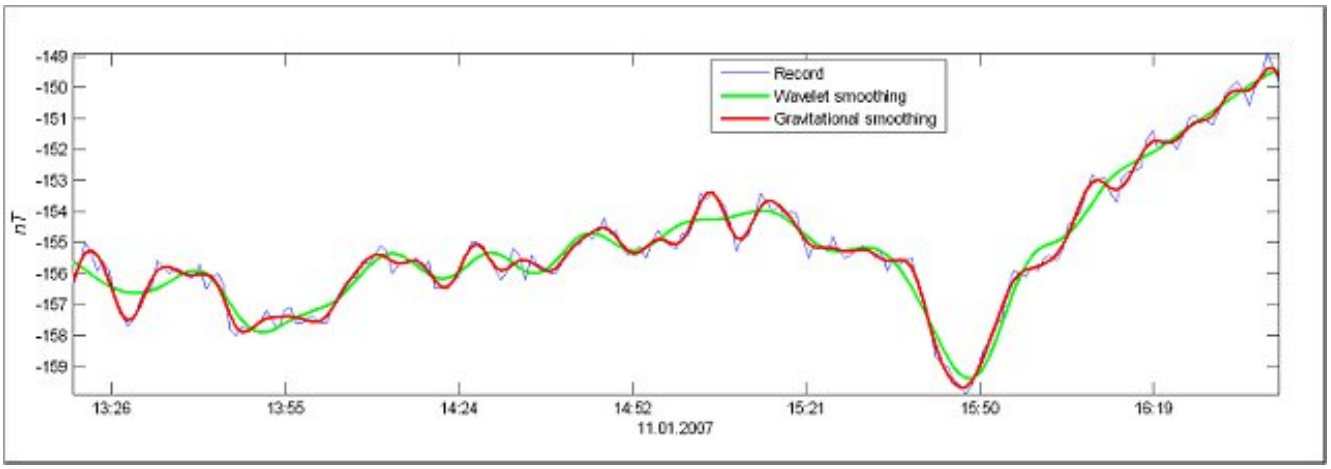

Fig.10.9. A comparison of gravitational smoothing to a Dobeshi's wavelet smoothing. The initial signal is shown in blue. The green line is the result of wavelet smoothing of the signal, and the red line is the result of the gravitational smoothing.

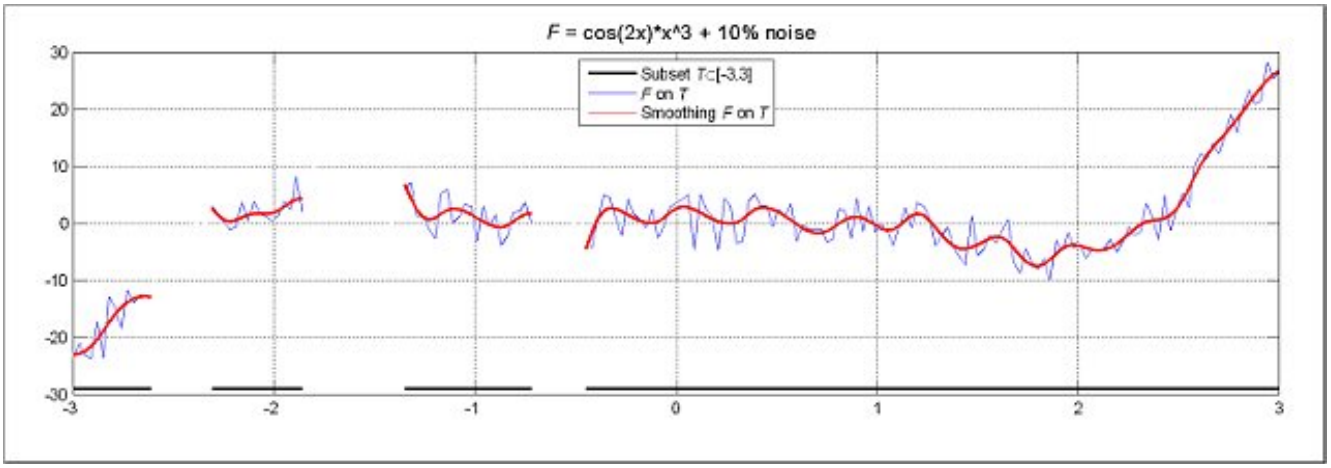

Fig.10.10. Non-regular signal smoothing.

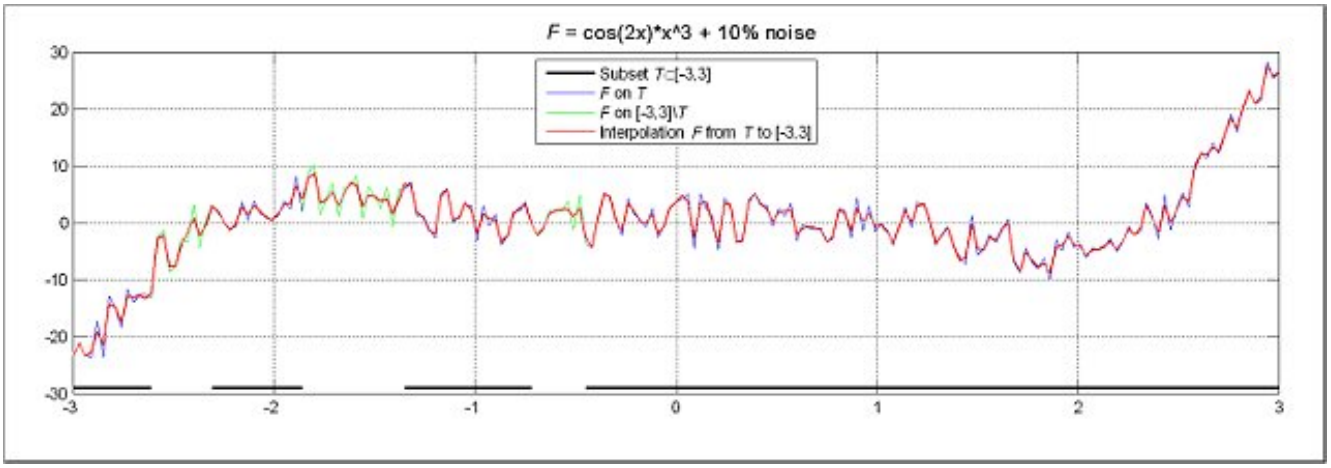

Fig.10.11. An example of gravitational interpolation.

Fig.10.10 displays a smoothing of an artificial signal with intervals of missing data (this is an attempt to model a typical situation of geophysical hardware failure). This describes a case of non-regular signal smoothing. The next **Fig.10.11** displays a procedure of gravitational interpolation of the previous singal example. Here the missing data is restored into a time series by interpolation. Another tool developed in CGRAS is also aimed at signal processing and also deals with fuzzy logic techniques. This is an approach for building the borders of time series on an interval. In fact this is another approach to smoothing or spline building for a time series [*Kagan*, 2009].

Scalar fuzzy borders of time series. Let $B = \{b_i\}|_l^m$ be a finite numeric set. Using mathematical induction, we shall define the values $S_k^+ = S_k^+(B)$, $S_k^- = S_k^-(b)$ and the subsets B_k^+, B_k^-. At the start of induction, when $k = 0$, $s_0^+ = s_0^- = s(B)$; $B_0^+ = \{b \in B: b \geq s_0^+\}$; $B_0^- = \{b \in B: b \leq s_0^-\}$; for a hypothesis of induction there are the values $s_k^+, s_k^-, B_k^+, B_k^-$. With induction we define a top fuzzy border of the *k*-th order $S_k^+ = S_k^+(B)$, and a bottom fuzzy border of the *k*-th order $S_k^- = S_k^-(B)$ for a set *B*. These are the scalar fuzzy borders.

Now we shall define the linear fuzzy borders. If *y* is a time series on an interval [*a, b*] and *y* has values in points t_i, i=0, …, n, $t_0 = a$, $t_n = b$, and *t* is an any point, let us define a value Δ – a local survey parameter. Then $r(y|t, \Delta)$ is a local linear regression for *y* at $[t - \Delta, t + \Delta]$. Now, using induction again, we shall define linear fuzzy borders $r_k^+(y|t, \Delta)$ and $r_k^-(y|t, \Delta)$. At the start when *k*=0, $r_0^+(y|t, \Delta) = r_0^-(y|t, \Delta) = r(y|t, \Delta)$. The induction hypothesis is the existence of the values $r_k^+(y|t, \Delta)$, $r_k^-(y|t, \Delta)$. The step of induction in this case is:

$$r_{k+1}^+(y|t, \Delta) = r(\max(y, r_k^+(y|t, \Delta))|t, \Delta); r_{k+1}^-(y|t, \Delta) = r(\max(y, r_k^-(y|t, \Delta))|t, \Delta)$$

Thus, we come to a conclusion of existence of the top and bottom fuzzy borders for a time series.

The next step includes the definition of a measure based on a difference between the maximal and minimal values of a discrete signal and, thus a difference between the borderlines built for this signal. Let us call it the envelope width. An analogous width definition appears for a *n*-th order fuzzy borders. Another base for building a stochastic envelope is based on another signal feature is its smoothness. Here we must introduce one more local survey parameter Λ [*Kagan*, 2009].

Like in the previous case, we get the formulas for one-side top amd bottom borders of the *k*-th order for the stochasticity width and come to the full continuity measure of the *k*-th order for a time series *y* in *t*.

Fig.10.12 displays the measure of continuity for a signal. A stochastic envelope built around the signal graph contains the zones of different morphology: the zones of fast alternation (so-called fast dynamics of a signal) are marked with red; the zones of lower speed of alternation are green; correspondingly slow dynamics are blue.

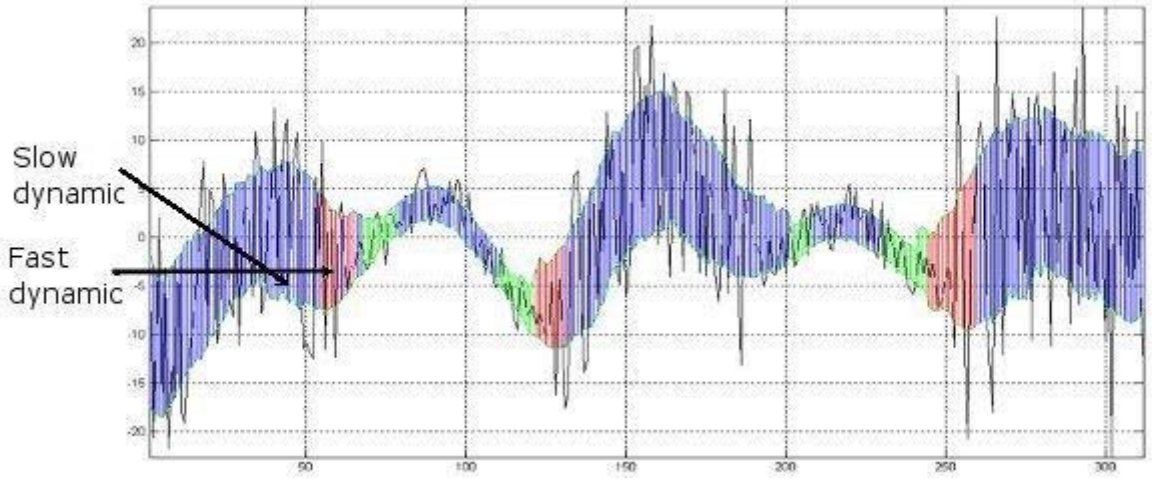

Fig.10.12. Measures of continuity and smoothness for a stochastic envelope.

Since the two latter tools are the recently developed ones, they have not been involved in any practical geophysical applications yet. Nevertheless, as they deal with the signal analysis (smoothing, interpolation, noise level control, vertical dynamical subdivisions of a signal), they will have possible application in some special tasks of data processing. Even nowadays many data processing software systems operate with signal smoothing and filtering based on polynomial regressions and least-square approximations which helps to build a smooting of a signal somehow. However in the tasks requiring precise approximations (not only in scientific activity but even in exploration geophysics – for example in reservoir modeling using seismic signals) the smoothing results of this software sometimes lack scanning (not enough close to an initial signal). That is the reason to apply more precise techniques in those fields of activity. It is important to note that an initial signal can be easily restored from a smoothing result, therefore this tool is invertible, and this appears to be the basic difference from other smoothing techniques.

Gravitational smoothing is an alternative for traditional methods in some complicated cases of signal processing (when the signal and noise components have the same features in the frequency domain, so that we cannot use just bandpass filtering). Gravitational interpolation appears to be useful for restoring geophysical data in some problems of data interpretation and geomodeling. The stochastic envelope building could be possibly useful in the analysis of complex geophysical signals (for example, seismic and electromagnetic signals).

So, this is an adaptive tool with soft logic modeling, like in all algorithmic developments based on DMA. As it was said, fuzzy logic methods of anomaly recognition represent a reliable technology to be applied for the salvation of various problems in the geophysical data analysis. That concerns especially particular tasks of data interpretation where human logic and experience must be applied.

References

Agayan S.M., Bogoutdinov Sh.R., Gvishiani A.D., and Kagan A.I. Smoothing of time series by the methods of Discrete Mathematical Analysis // Russian Journal of Earth Sciences, Vol. 11, RE4001, doi:10.2205/2009ES000436.

Bogoutdinov Sh.R., Agayan S.M., Gvishiani A.D., Graeva E.M., Rodkin M.V., Zlotnicki J., Le Mouël J.L. Fuzzy logic algorithms in the analysis of electrotelluric data with reference to monitoring of volcanic activity // Izvestiya, Physics of the Solid Earth. 2007. Vol. 43. P.597-609.

Bogoutdinov Sh.R., Gvishiani A.D., Agayan SM., Solovyev A.A., Kihn E. Recognition of Disturbances with Specified Morphology in Time Series. Part 1: Spikes on Magnetograms of the Worldwide INTERMAGNET Network // Izvestiya, Physics of the Solid Earth. 2010. Vol. 46, No. 11, pp. 1004–1016.

Gvishiani A.D., Agayan S.M., Bogoutdinov Sh.R. Fuzzy Recognition of Anomalies in Time Series // Doklady Earth Sciences, 2008a, Vol. 421, No. 5, pp. 838–842.

Gvishiani A.D., Agayan S.M., Bogoutdinov Sh.R., Graeva E.M., Zlotnicki J., Bonnin J. Recognition of anomalies from time series by fuzzy logic methods // Russian Journal of Earth Sciences, Vol. 10, ES1001, doi:10.2205/2007ES000278.

Gvishiani A.DAgayan., S.M., Bogoutdinov Sh.R., Zlotnicki J., Bonnin J. Mathematical Methods of Geoinformatics. III. Fuzzy Comparisons and Recognition of Anomalies in Time Series // Cybernetics and Systems Analysis, Vol. 44, No. 3, 2008b, pp. 309-323.

Kagan A.I., Agayan S.M., Bogoutdinov Sh.R. Definition of stochastic continuity by fuzzy logic methods and geophysical applications // Materials of the International Conference Electronic Geophysical Year: State of the art and results. 3–6 June 2009, Pereslavl-Zalessky, Russian Federation. P.48.

11. Network geoinformation technology for research of spatio-temporal seismo-tectonic processes

V. G. Gitis, gitis@iitp.ru**.** *Kharkevich Institute of information transmission problems RAS, Bol. Karetnyi per., 19, 127994 Moscow, GSP-4, Russia.*

Geoinformation technologies have been widely applied for years to Earth science research. They are based on methods of intelligent data processing and knowledge acquisition. In the 90's the rapid growth of Internet information space led to integration of network tools for geographical information (GI) storage and search into web-server based solutions [*Kraak and Brown*, 2001]. Web-based GIS's such as ArcIMS ESRI, GeoMedia WebMap Intergraph, MapGuide Autodesk, MapXtreme, MapInfo have become largely widespread. However, client-side user interface of these systems, as a rule, lacks interactivity. Analytical operations and visualization primitives (scale change, shift, palette change etc.) demand extensive interaction with the server that practically hampers interactive data research. Thereby it has become critical for GIS's oriented on scientific research to provide interactivity of the data analysis. The analytical operations have to be accompanied by visual exploration. Putting together methods of analytical and visual research constitutes the foundation of spatial and spatio-temporal cognitive modeling. It significantly simplifies the understanding of the problem under research and enhances the efficiency of the problem solutions. Therefore we believe that the network technologies realized within client-server architecture are more perspective for scientific research. They usually take advantage of Java framework, e.g. GeoProcessor (*Gitis et al.*, 1998, 2004), Lava Magma (the Netherlands, Berg et al, 1999), CommonGIS (Fraunhofer, Germany, Andrienko and Andrienko, 2002), GeoTime 2.0, [http://www.geo.iitp.ru/geotime/index.htm, IITP RAS, *Gitis et al.*, 2005], GIS UPC (http://www.unidata.ucar.edu/, Unidata Program Center, USA).

The aim of this paper is to present network geoinformation technology for research of spatio-temporal seismo-tectonic processes, which realized in web-GIS GeoTime 2.0. The system and several sample GIS-Projects for a number of regions are available online at http://www.geo.iitp.ru/geotime/index.htm.

1. GIS GeoTime

Web-GIS GeoTime 2.0 develops the ideas of the former desktop version (*Gitis et al.*, 1994). It is implemented as a Java application. It is loaded via Java Web Start which evolved from Java Applet technology. Java Web Start applications benefit both from the important positive aspects of the Java Applet technology (e.g. easy distribution of the application over the Internet and a guarantee of using the latest available version of the application), and advantage of starting the system outside the web browser. The latter feature allows to get rid of the negative effect of a web browser on the system functioning; in particular, to eliminate additional restrictions imposed by the web browser on the memory allocation which is critical as long as a considerable volume of spatio-temporal geographical data to be processed is concerned. The system can dynamically load distributed data and plug-ins, and store the user output. GeoTime supports parallel multithreaded data processing on multiprocessor/multicore front-end computers.

GeoTime can jointly handle 2D, 3D and 4D multitype spatial and spatio-temporal data: 2D and 3D polygons, 2D lines, 4D earthquake catalogues, 2D, 3D and 4D the grid-based layers, 2D and 3D vector fields, the geographically localized time sequences, and WMS images.

One can visualize 3D grid-based layer as animated 2D projections on three standard planes. Visualization of spatio-temporal layers can be done in the following planes: *XY* (the longitude-latitude plane, time varies as a discrete parameter and the step is consistent with the corresponding grid step), *XT* (the longitude-time plane, the latitude is a parameter) and *YT* (the latitude-time scale, the longitude is a parameter). Similar operations are supported for spatial 3D grid-based layers in projections *XY*, *XZ* and *YZ*. Vector data can be visually differentiated by color, line thickness, size of the point objects, type of the icons, and text formats. Often in seismological applications a layer of points represents an earthquake catalogue, in which the points are usually described by four co-ordinates. Animated visual exploration of this data can be done in all possible basic projections *XY*, *XZ*, *XT*, *YZ*, *YT*, *ZT*. For example, when visualizing the seismic process in the projection *XY* it is possible to fix some depth interval ΔZ and move interval ΔT uniformly. As result we will observe animated development of the

seismic process within the depth interval ΔZ (**Fig.11.1**). The movie can be saved as GIF-file or AVI-file.

Analytical conversions allow GeoTime to extract new properties of spatial and spatio-temporal data. In addition to the majority of operations adopted from GeoProcessor, there are several new ones like isoline curvatures and filtering with user defined kernel function. Sometimes it might also be handy to represent 2D and 3D grid-based layers as a bunch of isolines or, alternatively, in the form of arrows aligned with the gradient.

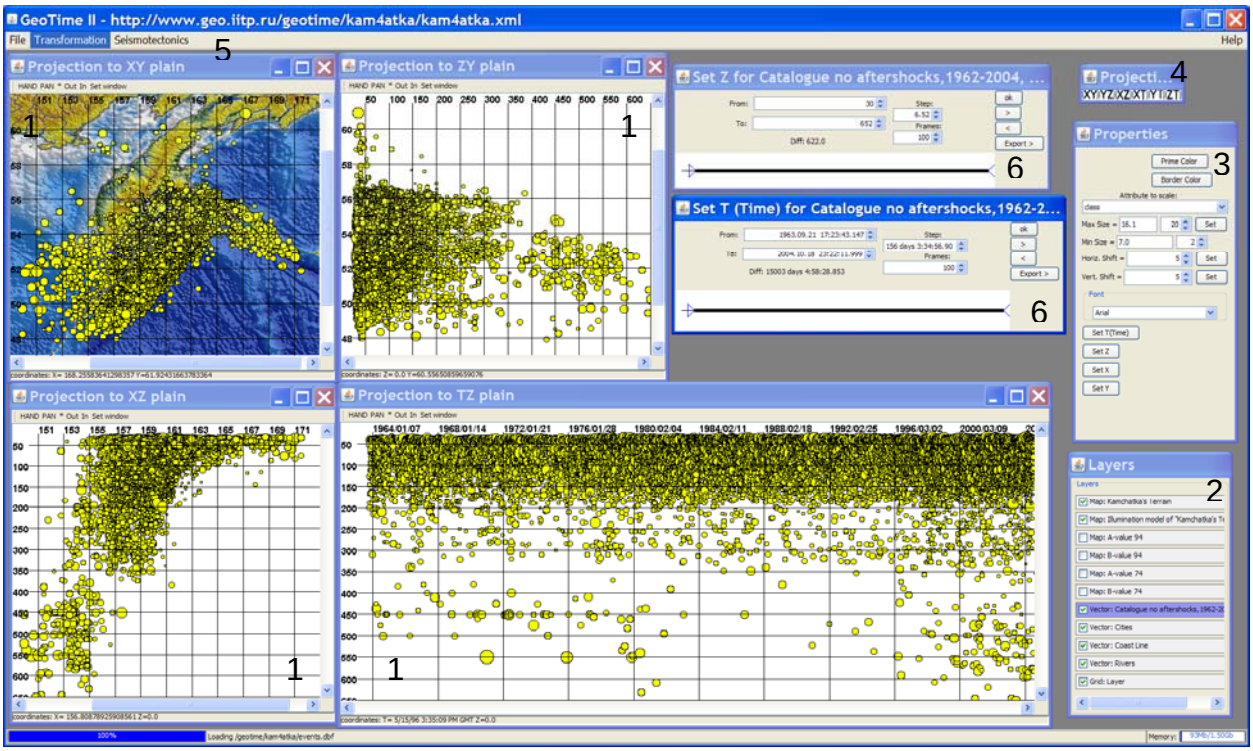

Fig.11.1. The main window of GeoTime with Kamchatka 4D earthquake catalogue: 1 are earthquakes in projections *XY*, *XZ*, *YZ*, *ZT*, where *X* is longitude, *Y* is latitude, *Z* is depth, *T* is time; 2 is the layer window; 3 is the attribute window; 4 is the panel of the plane projections; 5 is the operation management panel; 6 are the windows of animated visualization management.

The current version of GIS GeoTime is basically oriented on solving problems related to seismo-tectonic processes analysis, particularly to earthquake precursor analysis [*Gitis et al.*, 2005]. Detection of earthquake precursors in GeoTime technology relies on the assumption that the geological environment is inhomogeneous in space but has a stationary dynamics in the normal state, which is violated during the preparation of a geological disaster.

The system includes the following three groups of methods.

The first group is aimed to evaluate the major characteristics of seismic process in space and in time: the minimum representative magnitudes, b-value, seismic activity, and RTL criterion.

The second group of operations realizes methods for nonstationarity (anomaly) detection. The problem is approached by analyzing time-series of 3D fields. In order to detect the nonstationarity, the current observation interval is divided into two consecutive sub-intervals. The duration of both sub-intervals is determined by the researcher. The mean value within the back interval over the time characterizes a quasi-stationary background. The back interval duration T_1 is selected big enough for more exact estimate. The values within the front interval T_2 can be either thought to be alike those in the background or attributed to an anomaly. As a part of the process of detecting an anomaly, a statistics equal to the difference between the means divided on its standard deviation is estimated. In the absence of anomaly in the front interval the value of statistics will fluctuate with zero mean and unit variance. In the presence of abnormal values in the front interval one can expect significant

positive or negative deviations. GeoTime provides three methods of anomaly detection: for the model with independent Gaussian sequences, for the Markov process, and the method of empirical estimation.

The third group of methods is used to estimate the parameters of an expected catastrophe (earthquake) by 3D grid-based field of spatio-temporal anomalies. It is assumed that the anomaly amplitude is maximal in the centre of the seismic source preparation zone and exponentially decreases in space towards the edges. For each moment in time (a cut in 3-dimensional raster) GeoTime estimates the location and the spatial span of an anomaly, its amplitude and the degree of confidence associated with it. This is done by finding a Gaussian that approximates the anomaly in the best possible way (exploiting FFT as an optimization). Then the estimated parameters are plotted against the time, and one can accept only those anomalies with degree of confidence exceeding some desired threshold.

Users may extend the basic GeoTime functionality by means of connecting the problem-oriented subsystems realized in the form of plug-ins according to GeoTime API.

2. GIS GeoTime case studies

Analysis of Dynamic Interaction between Seismic and Earth Surface Deformation Fields

Research of interaction between seismicity and modern horizontal movements is usually based on spatial fields of seismicity and average velocities according to GPS. In [*Sobolev et al.*, 2010]) GeoTime was used to research this relationship not only in space, but also in time.

The research is fulfilled under the data received from the Bishkek polygon of the Scientific Station RAS (Tien Shan). Earthquake catalogue KNET (1994-2008, 708 events, K≥7, epicenter depths <25 km) and GPS data (horizontal displacements in 14 stations, 23.07.1997-5.25.2007, mean interval of measurements is 19 days) are used. The analysis is fulfilled in several stages.

Stage 1: analysis of the seismic catalogue. The analysis has shown that the seismicity of territory is inhomogeneous and must be divided into three zones.

Stage 2: interpolation of GPS time sequences in time series, smoothing, and calculation of horizontal velocity components.

Stage 3: interpolation of the GPS velocity time series in 3D grid-based fields East-West (V_x) and North-South (V_y).

Stage 4: calculation of the 3D fields of deformation velocities $\partial V_x/\partial x$, $\partial V_y/\partial y$, $\partial V_x/\partial y$, $\partial V_y/\partial x$ and their invariants: divergence div$\mathbf{V}=\partial V_x/\partial x+\partial V_y/\partial y$, rotor rot$\mathbf{V}=\partial V_x/\partial y-\partial V_y/\partial x$, and shear deformation sh$\mathbf{V}=0.5\cdot((\partial V_x/\partial x-\partial V_y/\partial y)^2+(\partial V_x/\partial y+\partial V_y/\partial x)^2)^{0.5}$.

Stage 5: analysis of spatio-temporal interaction between the fields of the deformation velocity invariants and seismicity.

The analysis has shown that strong earthquakes with K>10 during 1998-2006 basically occurred in vicinities of extremes div$\mathbf{V}$ and rot$\mathbf{V}$. It is shown that with probability more than 0.99 it is possible to consider that during these periods the strong earthquakes occurred not accidently. Earthquakes occurred before and after the extremes div$\mathbf{V}$ and rot$\mathbf{V}$. It testifies that extreme variations of normal and tangential tectonic stresses can cause a strong earthquake. On the other hand the stresses vary after a strong earthquake that can cause changes div$\mathbf{V}$ and rot$\mathbf{V}$. Both these phenomena can be a consequence of some regional or global process.

Fig.11.2 represents some elements of analysis. GPS stations are shown as triangles; earthquake epicenters from 1994 for 2008 are shown as yellow circles. In projection *XY* the vectors of horizontal Earth surface velocities and South-North component of the velocity on 10/12/2002 are shown. Projection *XT* represents a South-North component of the velocity for the co-ordinate Y=42.76º. Three plots are shown on the right side of the figure: the upper plot is the time sequence of the South-North displacement component recorded by the station *iv07*, the middle plot shows how the divergence of the deformation velocity changes in time (corresponding to the point in the vicinity of the station *iv07)*, the lowest plot depicts the sequence of earthquakes taken place in the zone around the same point with the radius of 10 km.

Detection of earthquake precursors

Earthquake prediction relies on the fact that earthquake preparation process is accompanied by spatio-temporal anomalies in the geological environment in the vicinity of the future event. The principal idea behind the analysis offered in GeoTime consists in complementing the traditional analysis of separate time series with the analysis of 3D grid-based fields having two spatial and one temporal co-ordinates. Thus, for each point of a spatial slice of the 3D field there is a corresponding time series. 3D spatio-temporal fields are calculated from earthquake catalogues or time series provided by geophysical, hydro-geological, geochemical and geodetic monitoring stations. Data presentation in the form of spatio-temporal rasters enables the user to observe the processes developing in time and in space, in a more comprehensive way.

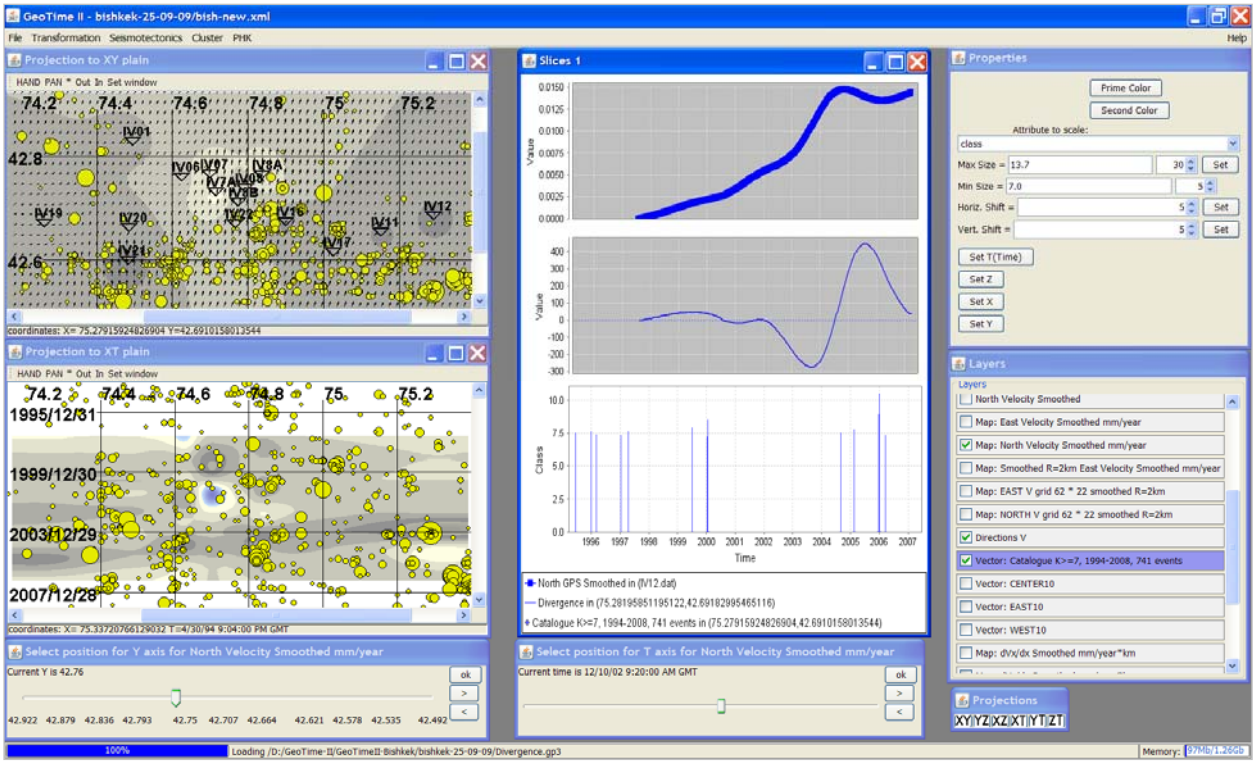

Fig.11.2. The main window of GeoTime with an example of visual exploration of GPS monitoring data for the West flange the North-Tien-Shan seismogenerating zone (the site of Scientific Station of the RAS in Tien Shan). Triangles denote GPS stations, yellow circles denote earthquake epicenters from 1994 for 2008.

Let us consider the case study of spatio-temporal analysis of Tangshan earthquake precursors. Tangshan earthquake with magnitude M=7.8 occurred at North-Eastern China on July 28, 1976. The input data comprise 10 daily time series of geophysical and hydro-geological measurements from 01.01.1972 to 27.07.1976 [*Ponomarev et al.*, 1999].

On the first step the time series have been normalized and standardized. Thereafter the time series were interpreted uniformly: as a response to the change of geological environment tension. On the second step the time series were interpolated and spatio-temporal 3D grid-based field $z(\lambda,\varphi,t)$ was calculated using the method of inverse distances. On the third step 3D grid-based field of anomalies $u(\lambda,\varphi,t)$ was estimated. Apparently, for a stationary process the statistics $u(\lambda,\varphi,t)$ has zero mean and the standard deviation less than 1. If the statistics deviates from zero by $(2\div3)\sigma$, it attests to the presence of an anomaly.

The slices representing the anomaly before of the Tangshan earthquake in projections to planes *XY*, *XT*, *YT* are shown by the orange color on the **Fig.11.3**. Stations of geo-monitoring are shown as white circles. The red circles denote the earthquake epicenters with $M \geq 6.8$. Along with the anomaly

immediately preceding the Tangshan earthquake, on projections *XT*, *YT* also shown are the regional anomalies caused by seasonal cycles.

Let us consider the case study of detection of Suusamyr earthquake precursors.

Suusamyr earthquake occurred on 19.08.1992. The energy class of the earthquake was K=17 (it corresponds to the earthquake magnitude M=7.2), the epicenter co-ordinates are λ=73.63°E and φ=42.06°N. For the analysis we used the catalogues that had been cleaned up from aftershocks. The catalogue spans over the region from 40.4°N to 44°N and from 71°E to 81°E and corresponds to the time period from 1980 to 2001. In the catalogue there are 16329 events of energy class K from 7 to 17. For research of the Suusamyr earthquake precursors we used the sub-catalogue with cut-off at the day before the earthquake occurred.

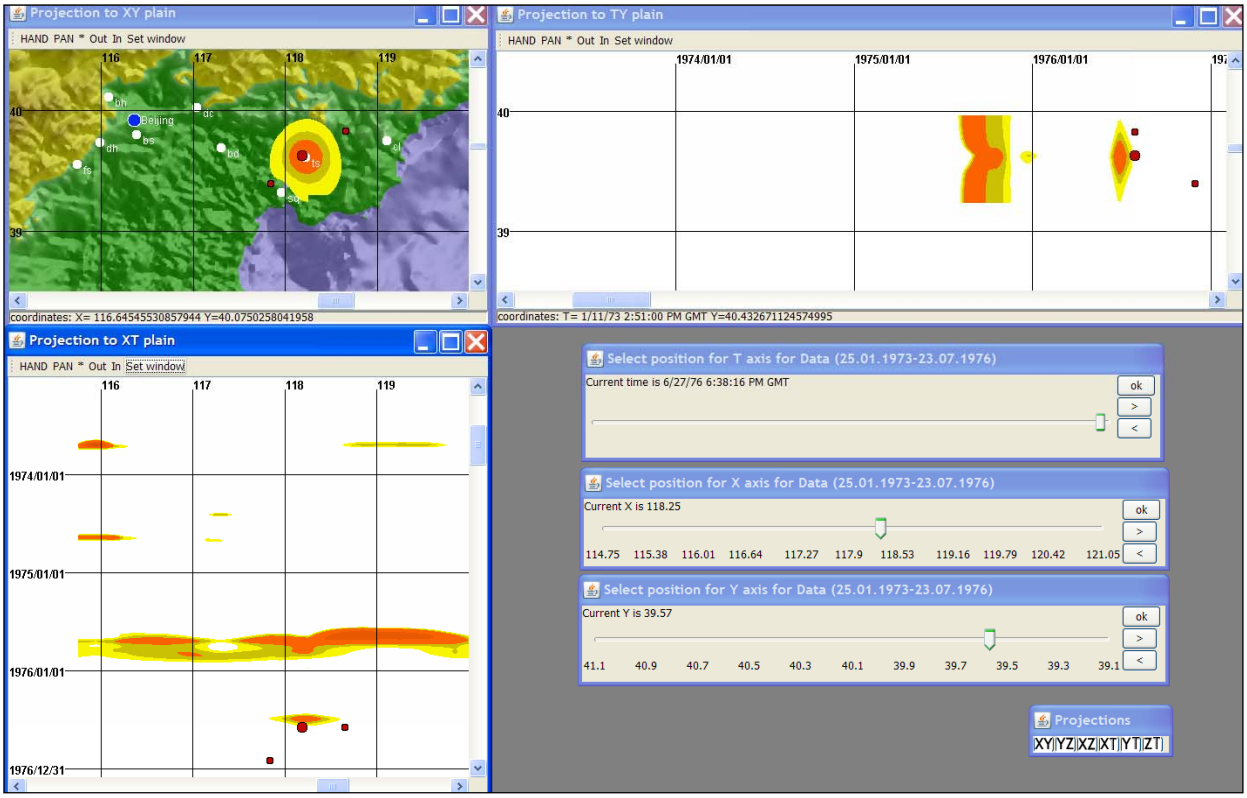

Fig.11.3. The main window of GeoTime with the pattern of Tangshan earthquake precursor in *XY*, *XT*, *YT* projections (the orange area close to Tangshan earthquake epicenter). White circles denote stations of geo-monitoring. Red circles denote earthquakes with $M \geq 6.8$. Besides the Tangshsn earthquake precursor, the regional seasonal anomalies are visible on *XT* and *YT* planes.

Again, we applied earthquake epicenter density model for the analysis. The following parameters of the cylindrical moving window were used: the radius equal to 100 km, the time interval equal to 10 days. The 3D grid-based layer of the earthquake epicenter density was computed on the grid with steps for the longitude $\Delta\lambda=0.3°$, for the latitude $\Delta\varphi=0.2°$ and for the time $\Delta T=10$ days. Then the grid-based layer of anomalies $u(\lambda,\varphi,t)$ was estimated based on the statistical model with independent Gaussian sequences.

On the following step the parameters of the anomaly layer were estimated. The method of estimating anomaly parameters is based on several assumptions: the anomaly amplitude is maximal in the centre of the seismic source preparation zone and exponentially decreases in space towards the edges; the time is discrete with step Δt; at each point in time there can be at most one source preparation zone, its center coinciding with one of the nodes on the grid: $k = 1, 2, ..., K$.

On the **Fig.11.4** the coordinates of the Gaussian centers with the confidence degree exceeding 0.5 are shown as white circles in the projections *XY*, *TY* and *XT* (the size of the circles is proportional to the confidence degree). Projection *XY* reveals an extensive negative anomaly. The epicenters of the

most severe earthquakes with $M \geq 5.5$ are shown in all projections as red circles. The biggest red circle corresponds to the Suusamyr earthquake. On **Fig.11.4** one can see two areas with anomalies. Small white circles correspond to a positive anomaly that is not attributed to a strong earthquake. Big white circles correspond to negative anomaly that precedes the Suusamyr earthquake. Moreover, that the most significant anomalies (big white circles) show up *just before* the earthquake. We believe that this approach can be used for earthquake prediction.

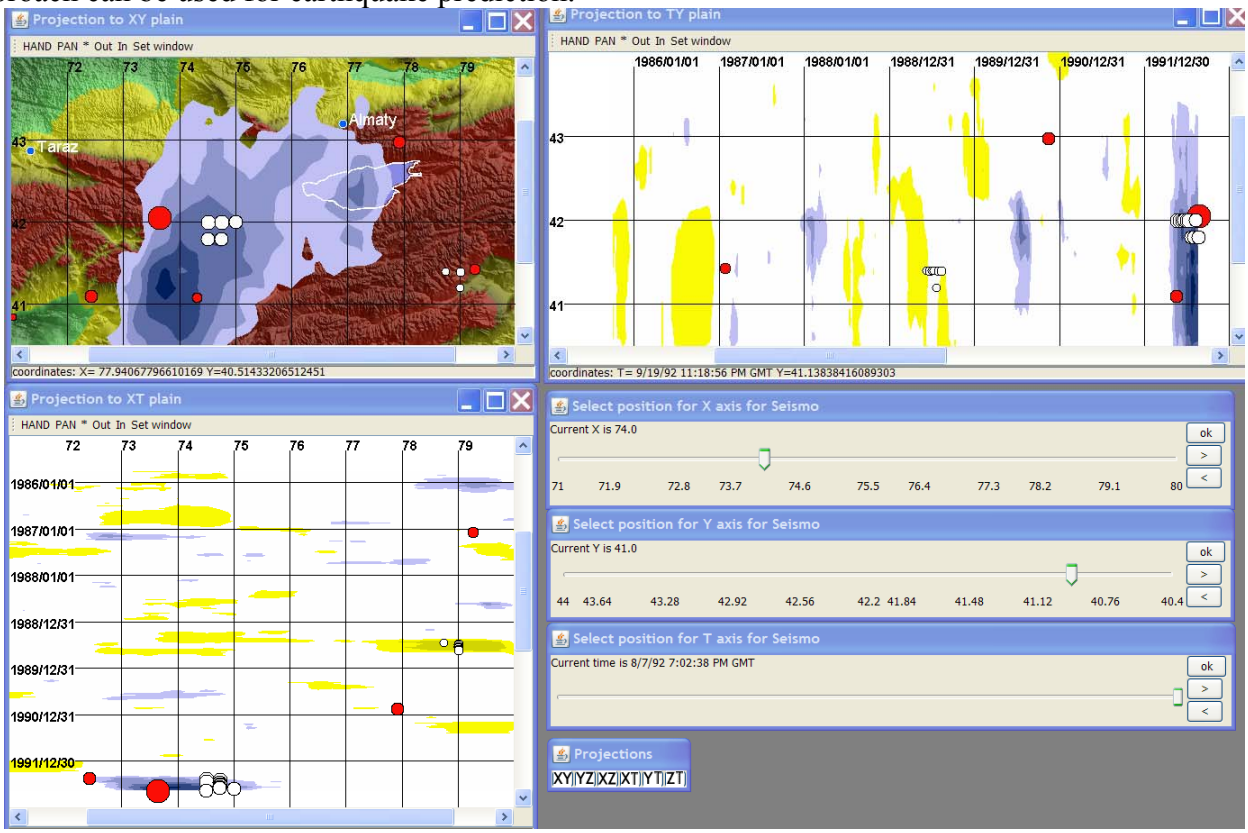

Fig.11.4. The main window of GeoTime with the pattern of Suusamyr earthquake precursor. Windows *XY*, *XT*, *YT* display projections of the 3D anomaly field. Yellow and blue colors correspond to significant values of negative and positive anomalies. Tint corresponds to increasing of the anomaly value. Projection *XY* corresponds to T=28.07.1992 (21 days before earthquake), projection *XT* corresponds to Y=41°, projection *YT* corresponds to X=74°.

Conclusion

We have outlined the network geoinformation technology and web-GIS GeoTime 2.0 which can be applied for the research of spatio-temporal seismo-tectonic processes, seismic hazard analysis. The major features of the technologey are: (1) the network access to geographical information, which can be distributed over network servers or reside on the user PC, (2) the modern methods of knowledge acquisition from spatial and spatio-temporal data, (3) high interactivity and clarity of visualization boosting a decision-making efficiency.

The next step in development of geoinformation technologies for Earth science research should be a response to the growing demand on handling the huge streams of multityped geodata being collected from natural and anthropogenic spatio-temporal processes. The amounts of data to handle are constantly growing due to the great progress in development of the Earth monitoring systems. Nowadays we face a challenging problem of building a multi-user computer environment for on-line integrated processing of distributed streams of geodata. A modern approach to the solution consists in imbedding the analytical toolkit of geoinformational network systems into the GRID-infrastructure.

Bibliography

Andrienko, N. and Andrienko, G. 2002. Intelligent Support for Geographic Data Analysis and Decision Making // Journal of Geographic Information and Decision Analysis, v.5 (2). P. 115-128.

Berg, C., Tuinman, F., Vijbrief, T., Meijer, C., Oisterom, P., Uitermark, H. 1999. Multiserver Internet GIS: standartization and practical experiments // Goodchild M., Egenfofer M., Feageas R., Kottman C. (eds) Interoperating Geographical Informatin Systems. Boston: Kluwer Academic Publishers. P. 365-377.

Gitis, V., Dovgyallo, A., Osher, B., Gergely, T.: GeoNet: an information technology for WWW on-line intelligent Geodata analysis // Proceedings of the 4th EC-GIS Workshop. Hungary. Joint Research Centre of European Commission. 124-135. (1998).

Gitis, V.G., Osher B.V., Pirogov S.A., Ponomarev A.V., Sobolev G.A., Jurkov E.F.: System for Analysis of Geological Catastrophe Precursors. // Journal of Earthquake Prediction Research, vol. 3, 540-555. (1994).

Gitis, V., Yurkov, E., Pirogov, S., Petrova, E., Weinstock, A., Derendiaev, A., Metrikov, P. Web-GIS for complex analysis of spatio-temporal processes // Abstracts of the General Assembly of IASPEI, Santiago, 2005.

Kraak, M., Brown, F.: Web Cartography // Taylor & Francis, 214. (2001).

Ponomarev, *A*., *Sobolev*, *G*., *Gitis, V., Chgan Chaochen*, *Van Gusuan*, *Chin Sinsi*: Complex analysis of geophysical fields for detection of spatio-temporal earthquake precursors // Vestnik OGGGGN RAN, 4 (10). (1999). URL: http://www.scgis.ru/russian/cp1251/h_dgggms/4-99/komp-an.zip (in Russian).

Sobolev, G.A., Zakrzhevskaya, N.A., Akatova, K.N., Gitis, V.G., Derendyaev, A.B., Bragin, V.D., Sycheva, N.A., Kuzikov, S.I. Dynamics of Interaction between Fields of Seismicity and Surface Deformations (Bishkek Geodynamic Test Area) // Izvestiya Physics of the Solid Earth, Vol. 46, No. 10, pp. 817–838. © Pleiades Publishing, Ltd., 2010. Original Russian Text © published in Fizika Zemli, 2010, No. 10, pp. 15–37.